UNIVERSITY OF LIVERPOOL

NPL National Physical Laboratory | QMI Quantum Metrology Institute

Construction of a Rubidium Fountain Atomic Interferometer for Gravity Gradiometry

Thesis submitted in accordance with the requirements of the University of Liverpool for the degree of Doctor in Philosophy by

Jonathan Neil Tinsley

February 2019

Abstract

Atomic interferometry is a highly precise metrological technique of interest to both fundamental and applied physics. One field in which atomic interferometry is of particular interest is gravimetry, where instruments based upon the controlled manipulation of atomic states have superseded the performance of classical devices. In such devices, a standing wave derived from laser beams with well-defined phase difference are used to impart momentum to atoms undergoing free fall, generating spatial superpositions along the axis of gravity, before returning the atoms to an overlapped final state for recombination. This thesis presents the design and experimental progress towards a gravity gradiometer based upon the interference of ^{87}Rb atoms, cooled and launched in a fountain configuration.

The fountain is leveraged from a decommissioned frequency standard, which has been repurposed and redesigned for use as a combined absolute gravimeter and gravity gradiometer package. It is capable of loading 10^8 atoms in 100 ms and then cooling and launching these atoms in a moving molasses configuration, with a final temperature of 5 μK. Furthermore, the process can be quickly repeated, with a second cloud subsequently launched, reaching its apogee at the same time as the first cloud, allowing for the possibility of simultaneous measurement at different heights and, in the future, the inference of the gravity gradient. Control of the fountain is provided by a stable and miniaturised optical setup, allowing for use with a future transportable or field-based device.

A Raman beam system to perform the interferometry sequence has been constructed and characterised, likewise designed in a minaturised and stable manner. The Raman beams simultaneously generated Ramsey interference fringes on two independent clouds of atoms – one launched to a height of 0.7 m and the other to 1 m. Such fringes were clearly observable after 200 ms of evolution time. Mach-Zehnder interference fringes were also demonstrated for dropped and launched atoms, providing the capability for gravimetric measurements to be made once the system has been fully characterised. The principle causes of noise in the Mach-Zehnder cases were identified as arriving from a lack of atoms and the phase noise of the Raman beams. To overcome these challenges, a new Raman beam system has been preliminary designed and tested and a new iteration of the fountain, moving towards quantum degeneracy, has been planned.

Acknowledgements

All of the work presented within this thesis would not have been possible without the efforts of a great number of people. This is true not only of those directly involved in the research or in the more general sense by which science is an inherently collaborative discipline, but also true of all those upon whom such research is predicated, especially the facilities management and administrative staff who provide and ensure a suitable working environment. Additionally, all of the social support and relief received outside of the work environment, from family and friends, is inestimably important in providing the platform upon which a functioning professional life is predicated.

Specific thanks, however, should firstly go to my supervisors for providing me with both the opportunity and support required to make this thesis viable. I'd like to thank Jonathon Coleman at the University of Liverpool for his unwavering belief and encouragement and Yuri Ovchinnikov at the National Physical Laboratory for his daily guidance and expertise.

Many further colleagues at both my host institutions deserve mention. At Liverpool, David Morris, Joe Heffer and Oliver Burrow welcomed me to the laboratory and taught me the basics of the field and likewise Carl Metelko, who continued to provide informed and useful feedback throughout my PhD. Andrew Carroll I would like to thank for his friendship and engaged interest in my research and, along with Gedminas Elertas, for providing considered and thorough feedback to this manuscript.

At the National Physical Laboratory, I must acknowledge Soliman Edris's efforts on the fountain system before my arrival and for his continued help throughout my time there. Sean Donnellan also for his work on the reference source for the interferometric laser system. I'd like to thank my office partners, especially Sean Mulholand and Charles Baynham, for their comradeship and keenness to discuss experimental problems and issues. Particular thanks to William Bowden and Richard Hobson for always been willing to provide both equipment and invaluable advice.

Author's Contribution

The time of my PhD was divided between an initial, approximately one-year period working on a ^{85}Rb interferometry system at the University of Liverpool, followed by a placement at the National Physical Laboratory (NPL), which lasted for a total of two years and three months. All of the data presented within this thesis is from work performed at NPL during this period, aside from the occasional data collected during a few subsequent visits. No work pertaining to the University of Liverpool system is presented.

When arriving at NPL, the fountain system had recently been reassembled and had a functioning electronic control and optical system, allowing a magneto-optical trap to be formed, although I ultimately re-built the optical system several times, for example due to the lasers utilised changing. Shortly following my arrival, I became the main person responsible for running and working on the fountain on a daily basis and was therefore involved in all aspects of the experiment from this point, personally taking all of the data and making all the calculations presented within this thesis.

When it was proving difficult to observe light-pulse-based interference on the atoms, I identified that the optical limitations imposed upon the Raman beams by the continued presence of the clock cavity, might prove a fundamental barrier to a fountain-based interferometer. It was therefore decided to break the vacuum and reconstruct the fountain without the cavity and with a few other modifications. The reconstruction and subsequent baking procedure I performed with my supervisor, Yuri Ovchinnikov, and thereafter I reassembled the optics and re-optimised the fountain's performance.

The basics of the Raman laser system, including the choice of lasers and feedback electronics, pre-dated my involvement, but I performed the actual construction, characterisation and implementation of the setup, as well as finalising the design. This involved the designing and building the free-space optics, as well as the practicalities of constructing the rest of the system to be self-contained within a rack-based drawer system. To suppress the high phase noise observed, I installed an electro-optical modulator with a separate feedback system, allowing coherent manipulation of the atoms by the Raman beams to be observed for the first time.

Finally, I have worked together with Yuri on helping to design an upgraded system, more suitable for precision gravimetry and transportation, including performing some preliminary calculations towards its likely operation and performance.

Contents

List of Figures

List of Tables

Chapter 1

Introduction

1.1 Atomic Interferometry

Atom interferometry is a high precision measurement technique based upon the ability to create and measure atomic superpositions [1, 2]. These superpositions can be either based upon the internal, electronic states, such as is the case for atomic clocks, or they can be generated such that the de Broglie wavepacket is spatially separated. The deliberate creation and detection of superpositions of internal atomic states was first performed by Ramsey in 1949 [3] and developed into an atomic clock at the National Physical Laboratory (NPL) shortly thereafter [4]. Conversely, experiments with macroscopic superpositions, where there is an appreciable spatial separation between the two interferometer arms, were first demonstrated considerably later, requiring long-lived and long-range coherence to be achieved. Such interference was first demonstrated by Bordé et al. in 1985 [5], though it took several years for this to become apparent [6], and a number of research groups provided conclusive demonstration in 1991, each using a substantially different method: diffraction gratings for an experiment analogous to Young's double slits [7]; another grating-based method analogous to a Mach-Zehnder interferometer [8]; and a Mach-Zehnder scheme based upon stimulated Raman transitions [9]. This thesis presents interference fringes for both internal and external atomic states based upon the light-pulse technique pioneered in this last experiment [9].

In addition to the fundamental interest of the experiments themselves, the motivation for performing interferometry with atoms is that it enables many exciting possibilities for probing fundamental physics and for developing new metrological technologies, due to the large sensitivity of these measurements to any asymmetry between the interferometer arms. As the atoms propagate they accrue phase based upon the space-time path upon which they travel and the final interfered state is dependent upon the phase difference between the paths. This makes interference with macroscopic superpositions extremely sensitive to accelerations. As such, any force which couples to the atoms in a spatially inhomogeneous manner across the scale of the experiment, is in principle measurable. This sensitivity has been exploited for measurements

of the fine structure constant [10, 11], searches for dark matter [11, 12], tests of the weak equivalence principle [13, 14, 15] and of Lorentz invariance [16], to give an inexhaustive overview. Atomic interferometry can also be used to test theories of dark energy [17, 18, 19] and the dark contents of the vacuum more generally [17, 20].

Furthermore, the massive and mutually identical nature of atoms make them an ideal test source for rotation and inertial sensing [21, 22, 23, 24, 25], and gravimetry applications, including absolute gravimeters [9, 24, 26], gravity gradiometers [27, 28, 29], measurements of the gravitational curvature [30], measurements of Newton's gravitational constant [28, 31], and proposed gravitational wave detectors [32, 33, 34, 35]. Such is the maturity and robustness of this technique, that practical devices based upon atomic interferometry form a major part in current global efforts to develop and commercialise a new generation of quantum technologies [36]. The remainder of this thesis discusses the theory and the experimental work towards an absolute gravimeter and gravity gradiometer package based upon a fountain of cold ^{87}Rb atoms.

1.2 Atomic Interferometry for Gravimetry: Experimental Overview

Gravimetry has many interesting applications from both a fundamental and applied viewpoint. Most generally, gravitation, through general relativity, is fundamentally different from the other three forces, operating on a vastly different scale and without a known vector boson, although some properties of any hypothetical graviton are deducible. The gravitational constant is also comparatively poorly known and improved measurements thereof is an active field. Nevertheless, general relativity is an extremely effective theory, as recently demonstrated by the first observation of gravitational waves a hundred years after their prediction [37]. These measurements also showed the power of gravimetry as a tool for probing the deep recesses of the universe [37, 38].

Using cold atoms for gravimetry provides further advantages. By utilising objects obeying quantum mechanics to probe the gravitational force, they offer an avenue which has the potential to provide new insights into the nature of the overlap between general relativity with quantum physics, one of the major mysteries in contemporary physics. For example, the gravitational curvature *across* a wavepacket has been measured [29] and, as mentioned, Einstein's equivalence principle has been tested by looking at both the universality of free fall [13, 14, 15, 39, 40], Lorentz invariance [16] and also local position invariance via the gravitational redshift [41, 42], although the interpretation of these redshift experiments remains controversial and a source of debate [43, 44, 45, 46]. Such measurements can be made so that the method of measurement is a genuine quantum mechanical phenomenon [47], but also by classical gravimeters [48, 49]. Additional areas of interest include searching for deviations from the inverse square law of gravitational attraction [50, 51] and the gravitational analogue to the Aharonov–Bohm effect [52].

Proposals have also been made to measure the decrease in visibility in atomic interferometers

caused by relativistic time dilation, which can be different for the two arms of the interferometer and therefore provides which-path information and causes a reduction in the interference signal [45, 53]. This dilation can arise either due to the fact that the separated parts of the wavepackets travel along different worldlines [54], as in the twin paradox, or due to the gravitational time dilation felt if the two arms are in different gravitational potentials [53]. Such an observation would show natural mechanisms for decoherence of a quantum system, which are important in explaining the quantum-to-classical transition, and show a direct link between the realms of quantum mechanics and general relativity [55].

From an applications perspective, precision gravimeters and gravity gradiometers open up many practical benefits for fields such as geodesy, seismology, geophysical surveys and mineral prospecting [56].

1.2.1 Classical Gravimeters & Gradiometers

For pure gravimetry, classical devices with high precision are commercially available. The most common form of classical absolute gravimeter is a light interferometer based upon a falling corner-cube retro-reflector. Laser light is directed at a beamsplitter with half of the light passing through towards a photodiode and the other half reflected up to the corner-cube retro-reflector which is undergoing free fall in vacuum. The light reflected from the falling corner-cube is directed towards a second corner-cube retro-reflector, which is housed and vibrationally isolated at the bottom of the interferometer. After retro-reflection from this second corner-cube, the light is combined with the original undeflected light from the beamsplitter, with the configuration forming either a Michelson or Mach-Zehnder interferometer. The interference pattern is dependent upon the distance between the two corner-cube reflectors, meaning that the gravitational acceleration can be deduced from the photodiode signal. These devices have an accuracy of $2\,\mu\text{Gal}$[i] and can reach sensitivities of $15\,\mu\text{Gal}\sqrt{\text{Hz}}$ and can achieve an accuracy of $2\,\mu\text{Gal}$ [57]. However, due to the mechanical nature of the device, a more typical operating sensitivity is $100\,\mu\text{Gal}\sqrt{\text{Hz}}$, as the high repetition rate required for the maximum sensitivity would greatly reduce the operating lifetime [58].

Classical relative gravimeters are also available and can be used to measure changes in the gravitational acceleration, despite severe drifts precluding their use for absolute or long term measurements. The two main relative gravimeters are based upon the force required to maintain a suspended test mass in a constant position against gravity. These devices are either based upon a spring counteracted by an electromotive force or a diamagnetic sphere held in place by magnetic field, generated by superconducting coils. The latter class of devices are capable of reaching record sensitivities of approximately 1 nGal with a minute's integration time. Stationary devices can perform with low drifts, but require a stabilisation period of at least six months [58].

[i] $1\,\text{Gal} = 10^{-2}\,\text{m/s}^2 \sim 10^{-3}\,\text{g}$.

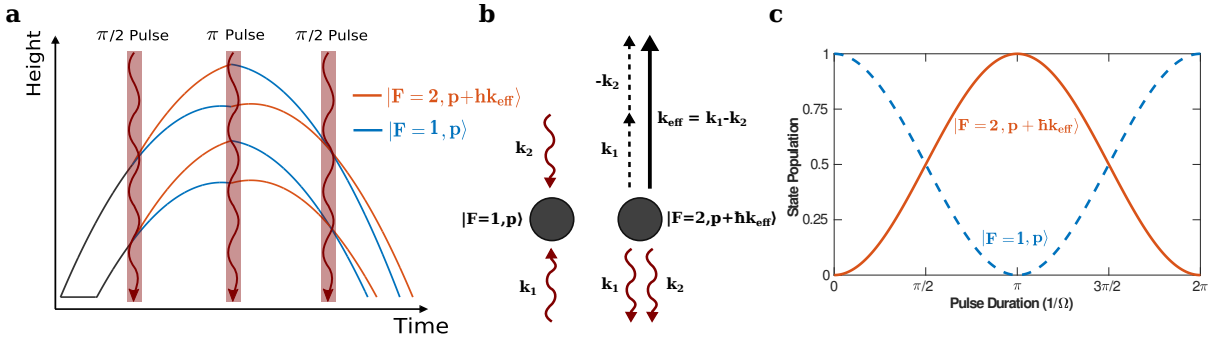

Figure 1.1: a) ^{87}Rb atoms launched in a fountain undergo a Mach-Zehnder interferometry sequence, the readout of which is proportional to the gravitational acceleration. Performing on two clouds simultaneously gives a gradient measurement. b) The sequence is controlled by counter-propagating Raman beams which impart momentum when transferring the atom between states. c) The duration of the Raman beam controls the state population, allowing beam splitters ($\pi/2$ pulses) and mirror (π pulses) analogues to be implemented.

1.2.2 A Gravimeter based on Atomic Interferometry

A typical scheme for measuring gravity via atomic interferometry is to create a Mach-Zehnder style interferometer (Figure 1.1), where an atomic population is coherently split into two different momentum states, which travel along paths which are spatially separated in the axis of gravitational acceleration. These populations are subsequently mirrored and recombined, giving rise to interference. The interferometric signal is the population of the two different atomic states and is proportional to the difference in the phase accrued by the atoms travelling along the different paths. In the case of an atomic population which is suitably isolated from the environment and shielded from other forces, e.g. electromagnetic, this phase difference is related to the local gravitational acceleration.

In general, the splitting, mirroring and recombination of the atomic population is performed optically by laser beams (see section 1.2.2.2). During these interactions, the atoms receive phase information from the laser beams. Due to their free-fall acceleration, the different paths experience different laser phases and the phase difference ($\Delta\Phi$) is, in general, non-zero. Specifically, for a population split by a momentum transfer of $\hbar\boldsymbol{k}_{\mathbf{eff}}$ and with equal times of evolution (T) between the splitting, mirroring and recombination [59]:

$$\Delta\Phi = k_{\text{eff}} g T^2 \tag{1.1}$$

It can be seen that the strength of the signal and thus the sensitivity of the measurement, is increased by increasing both the time of evolution and the momentum transfer imparted on the atoms. Practically, this implies the necessity of cooling the atoms to extremely cold effective temperatures – not just to ensure the long coherence times and an atomic sample which is spatially confined throughout the duration of the experiment, but also so that high-fidelity splitting, mirroring and recombination can be performed for the entire atomic sample, which

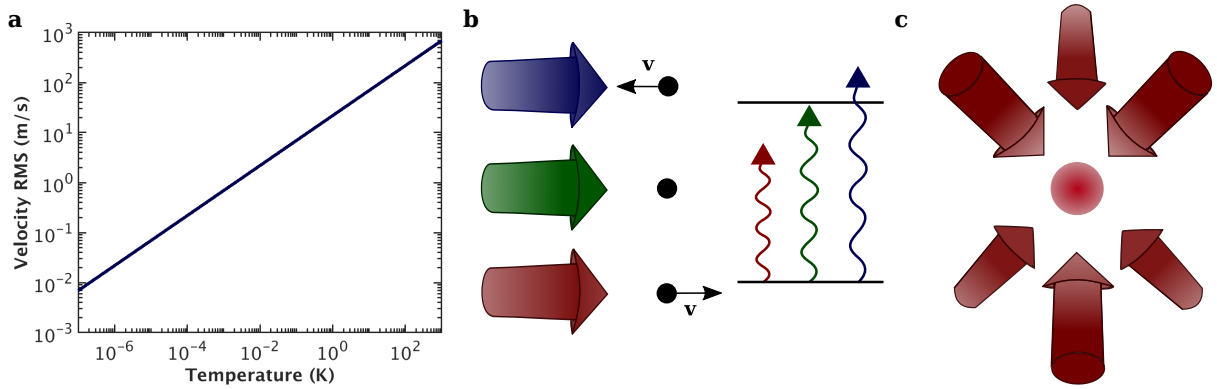

Figure 1.2: a) The root-mean-squared velocity for ^{87}Rb as a function of temperature. b) For a resonant laser beam (green), atomic motion will shift the light away from resonance. c) By illuminating the atomic sample with laser beams red-detuned from the resonance in the laboratory frame, atoms will be more likely to absorb light from a beam opposing its motion and thus be slowed (cooled).

has both spatial and velocity distributions which tend to cause dephasing and a subsequent loss of contrast and thus sensitivity.

Currently, the leading quantum gravimeters are capable of performing to a similar level or better of precision and accuracy than classical devices, with a current best reported sensitivity of $3.0 \times 10^{-11}\mathrm{g}/\sqrt{\mathrm{Hz}}$ [24]. They have the additional advantage of exhibiting a substantially reduced drift.

1.2.2.1 Laser Cooling & Trapping of Atoms

Controlled quantum mechanical manipulation of atoms, as outlined above, obviously requires special conditions, not normally available to the experimenter. For example, in a room temperature gas, atoms move at an impractically fast speed, as can be calculated from the Maxwell-Boltzmann equation (Figure 1.2). Atmospheric gas is predominately composed of N_2 which moves with a root-mean-squared velocity of 511 m/s at 293 K; for ^{87}Rb, the atom utilised in the experiments detailed in this thesis, it is 374 m/s. If nothing else, it is clear that this ballistic motion will severely limit the possible timescale of any laboratory-based experiment. Furthermore, for a fixed density and a given atom, the increased inter-atomic collisions will lead to the rapid destruction of any established quantum coherence.

Cold, localised gases in vacuum, therefore, offer many advantages for atomic interferometry. By reducing the temperature such that the atomic motion is sufficiently slow for the atoms to remain within the experimental region for appreciable times, the sample can be probed and manipulated in a controlled manner. Furthermore, by reducing the kinetic energy and inter-atomic collisions, the atomic picture is simplified with each atom acting as an effectively independent system and the deleterious effects caused by atom-atom interactions are additionally minimised.

For certain amenable atomic species, laser cooling via radiation pressure offers an excellent

avenue for reducing the temperature of the atoms from room temperature down to temperatures $\sim$100 µK, a six order of magnitude decrease. Such laser cooling occurs when the radiation pressure exerted upon a sample is such that there is a force opposing the motion of the atoms. When an atom absorbs a photon, in addition to changing the state of the atom, it also receives the momentum $\hbar\boldsymbol{k}_{\text{eff}}$ of the photon and is therefore pushed in the direction of the light. The subsequent spontaneous emission, however, occurs isotropically and so over many absorption-emission cycles will average to zero. If absorption can be made to occur preferentially against the atomic motion, cooling will therefore occur.

In Doppler cooling, laser light is detuned from an atomic transition in the laboratory frame (see Appendix A.1 for a more formal treatment). Atoms that are moving away from the laser light in the axial direction will see a further detuning and will have a further decreased probability of interacting with the light. Conversely, atoms moving opposite to the propagation of the light will see light that is shifted towards the atomic transition frequency and thus have a higher probability of absorption. By illuminating atoms so that regardless of their motion there is always an opposing detuned laser, a damping force will be provided to the atomic motion. This damping force is sufficiently strong to be able to cool a subset of warm atomic vapour (i.e. $\sim$300 K) to the $\sim$100 µK level.

A simple way of ensuring this configuration is to use three-pairs of counter-propagating beams all detuned from the resonance, which establishes sufficient cooling in the region of mutual beam overlap, producing a cold, diffusive atomic sample known as optical molasses.

1.2.2.2 Light-Pulse Atomic Interferometry for Gravimetry

Light-pulse atomic interferometry uses stimulated photon transitions to coherently impart momentum to the atomic sample. In general a two-photon scheme is employed, with either Raman beams, which impart momentum whilst transferring the atom between two different metastable internal states, or Bragg beams, which transfers atoms in a constant electronic state between different momentum states, are utilised. Bragg beams have the advantage of being more suited to large-momentum transfer techniques ($\Delta\boldsymbol{p} > 2\hbar\boldsymbol{k}$) required to maximise the device sensitivity, although the remainder of this discussion will be confined almost entirely to Raman beams, as they are the interferometric beam system used in this interferometer. Their advantage is that the different momentum states are also different internal states, meaning that the different state populations can be easily distinguished and measured by resonant fluorescence or absorption imaging, even when the momentum states aren't spatially separated.

The basic principle behind Raman-beam atomic interferometry for ^{87}Rb is shown in Figure 1.1b (see Chapter 2 for more detail). Two laser beams are set to have a frequency offset equal to the hyperfine ground state splitting, being detuned from the excited state by an amount that is sufficient to preclude to a high degree the possibility of excitation, but also prevents any non-negligible couplings to other energy levels. These laser beams transfer the atom between the two hyperfine states in a two-photon process via absorption from one beam and stimu-

lated emission into the other beam. Momentum is therefore imparted to the atom equal to the difference between the photonic momenta of the two beams. This is maximised for counter-propagating beams where the kicks from absorption and emission align, giving a total imparted momentum of $\hbar\boldsymbol{k}_{\text{eff}} = \hbar\boldsymbol{k_1} - \hbar\boldsymbol{k_2} \sim 2\hbar\boldsymbol{k_1}$. Conversely, the momentum imparted by beams which are co-propagating is effectively zero and can be ignored on practical timescales, being equal to the momentum of the microwave hyperfine transition.

Controlled creation of superpositions of the internal and momentum states of the atoms are possible due to the system mimicking a two-level atom interacting with resonant light, displaying the same dynamic behaviour of Rabi oscillations. The relative populations can therefore be controlled by simple variation of the duration for which the Raman beams are applied (Figure 1.1c). The same nomenclature is used as for Rabi oscillations: for an initial situation where all the atoms are in one of the hyperfine states, a pulse of duration such that an equal population of the states is established is called a $\pi/2$ pulse; when the state populations are inverted, it is referred to as a π pulse. A Mach-Zehnder sequence can be run by a succession of three such pulses[ii]. Atoms are first split coherently into equal populations of the two hyperfine ground states ($\pi/2$ pulse), which are simultaneously different momentum states. These states are 'mirrored' by a second pulse after a time T, which reverses the state populations and momenta (π pulse). Finally, after an equal period T, a recombination pulse ($\pi/2$) is applied and the state populations read out, with the state populations proportional to the phase difference between the two interferometer paths.

This phase difference is derived from three independent sources: the propagation phase; the recombination phase; and the laser field phase. The propagation phase is the internal atomic phase accumulated by the atom during the moments of free propagation and is equal for both interferometer arms. The recombination phase arises if the two atomic packets are not perfectly overlapped when the recombination pulse is applied and is therefore approximately zero for a symmetric pulse sequence and assuming the absence of any severe gradients across the interferometry separation[iii]. The laser field phase is the phase imparted by the Raman beams upon the atoms. Using beams resonant to the transition frequency and in the absence of AC Stark effects, this is zero except for when the atom is being transferred between states, meaning that the Raman beams consequently act as a reference for the distance fallen by the atoms between the pulses, allowing for this and therefore local gravitational acceleration to be measured with high precision.

This phase difference is good for measuring relative changes in the acceleration, but can of course only give values in the range of 0 - 2π, meaning the absolute value of the acceleration needs to be calibrated. For atoms undergoing free fall, the Doppler effect must be compensated for by a process known as chirping, where the frequency difference between the two Raman beam components is linearly altered so that they match the hyperfine splitting in the atomic

[ii] This is sometimes also referred to as a Kasevich-Chu interferometer after the first researchers to demonstrate this sequence [9].

[iii] An equivalent term also arises if instead the initial position of the atomic wavepacket is not equal.

frame. In the case of imperfect compensation, an additional phase will be imprinted upon the atoms. By finding the chirp rate which compensates for the Doppler shift due to free fall, the interferometer can be calibrated to coarsely measure the gravitational acceleration and any additional phase shifts measured provide fine information on top of this, e.g. tidal forces.

Using all of this information, equation 1.1 can be re-written in a somewhat more rigorous manner as,

$$\Delta\Phi = \Delta\phi_{path} + \Delta\phi_{sep} + \Delta\phi_{light} \tag{1.2}$$

where, $\Delta\phi_{path}$ is the phase difference between the atomic evolution along the two paths; $\Delta\phi_{sep}$ is the phase difference from any initial or recombination separation between the two wavepackets; and [60],

$$\Delta\phi_{light} = (2\pi\alpha - k_{\text{eff}} \cdot g)\, T^2 + (\phi_1 - 2\phi_2 + \phi_3), \tag{1.3}$$

where α is the frequency chirp rate and ϕ_i is the relative phase between the two Raman beam components during the i^{th} pulse. To calibrate the gravimeter and assuming $\Delta\phi_{path} = \Delta\phi_{sep} = \phi_{1,2,3} = 0$, $\Delta\phi_{light}$ is set to be zero by varying the chirp rate, giving,

$$g = \frac{2\pi\alpha}{k_{\text{eff}}}. \tag{1.4}$$

1.2.3 To a Gravity Gradiometer

Whilst a gravimeter measures the absolute value of the local gravitational force, a gradiometer measures its gradient. This can be realised by placing two gravimeters at different heights and measuring the difference in the gravitational acceleration between them. For a gravimeter based upon atomic interferometry these measurements can be performed simultaneously with the same set of interferometry beams. This provides a major advantage over classical devices as many of the noise sources will therefore be common mode for the two interferometers. This noise will therefore be cancelled when making the differential measurement.

To see this consider two independent atomic population measurements (y_A, y_B) which can be generically written as,

$$\begin{aligned} y_A &= c_{1,A}\sin(\phi_c) + c_{2,A} \\ y_B &= c_{1,B}\sin(\phi_c + \phi_d) + c_{2,B} \end{aligned} \tag{1.5}$$

where ϕ_c is the common phase between the two interferometers, ϕ_d the differential phase, and $c_{1,i}$ and $c_{2,i}$ are respectively related to the fringe contrast and offset of the i^{th} interferometer.

It is clear that when plotted parametrically that this results in an ellipse (Figure 1.3) with an ellipticity approximately equal to the desired signal of ϕ_d, allowing for extraction of information about the gravity gradient by fitting of this ellipse [61].

Current gradiometers utilising atomic interferometry are capable of achieving sensitivities

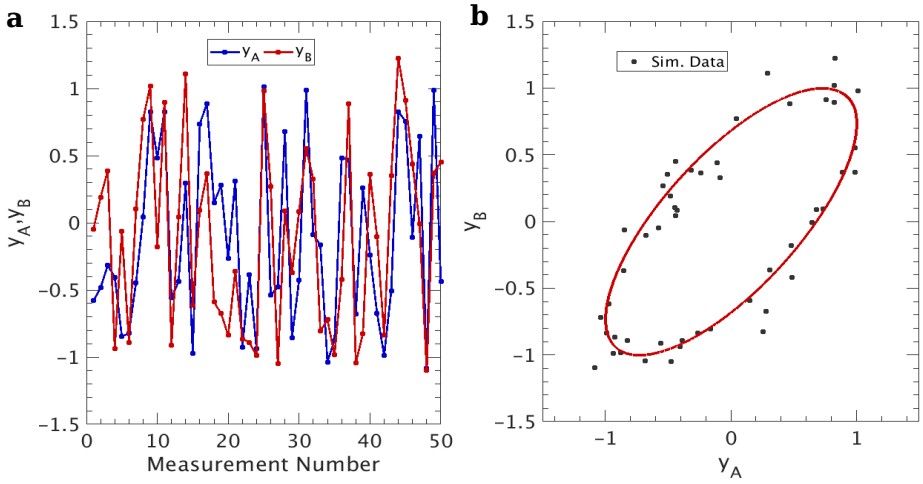

Figure 1.3: Simulated gradiometer data generated pseudorandomly plotted a) sequentially and b) parametrically. The correlation of the data is much clearer when plotted parametrically. The simulation assumed $\phi_d = 0.75 \pm 0.1$ and offsets of 0 ± 0.1. The ellipse shows the case for the underlying ϕ_d without errors.

of $15\,\mathrm{E}/\sqrt{\mathrm{Hz}}$ [29][iv], with device sensitivities limited by the quantum projection noise [62]. They are being used, for example, to measure the gravitational constant [28].

1.3 NPL Rubidium Fountain for Gravimetry

NPL has an atomic fountain for ^{87}Rb, which was operated as a frequency standard, before being decommissioned [63, 64]. This provided an attractive option for atomic interferometry due to it being convertible into a useful system with minimal vacuum modifications (see section 3.1). Furthermore, the fountain was necessarily well characterised for its operation as a frequency standard, being capable of cooling, trapping, launching, coherently manipulating and detecting a large number of atoms in a manner sufficient to achieve a performance capable of exhibiting a fractional accuracy of 2.4×10^{-16} and a daily stability of 7×10^{-16} [64]. Specifically, a fountain-based system offers a particularly attractive avenue for gravity gradiometry, as multiple clouds can be launched to different, but simultaneous apogees. The system and its operation is shown in a visual form in Figure 1.4. The operation of a gravity gradient measurement can be roughly separated into the discrete steps given below.

- **Loading:** Atoms are loaded into a magneto-optical trap (MOT) in an ultra-high vacuum of $\sim 10^{-10}$ mbar. A low-velocity injection source provides a high-flux of cold atoms, allowing for the loading of around 10^9 atoms in just 100 ms.

- **Launch:** The atoms are launched vertically upwards in a moving molasses configuration. Following the launch, the atoms undergo optimised polarisation-gradient and adiabatic

[iv] The Eötvös is the standard unit for gravity gradients: $1\,\mathrm{E} = 10^{-9}\,\mathrm{s}^{-2}$.

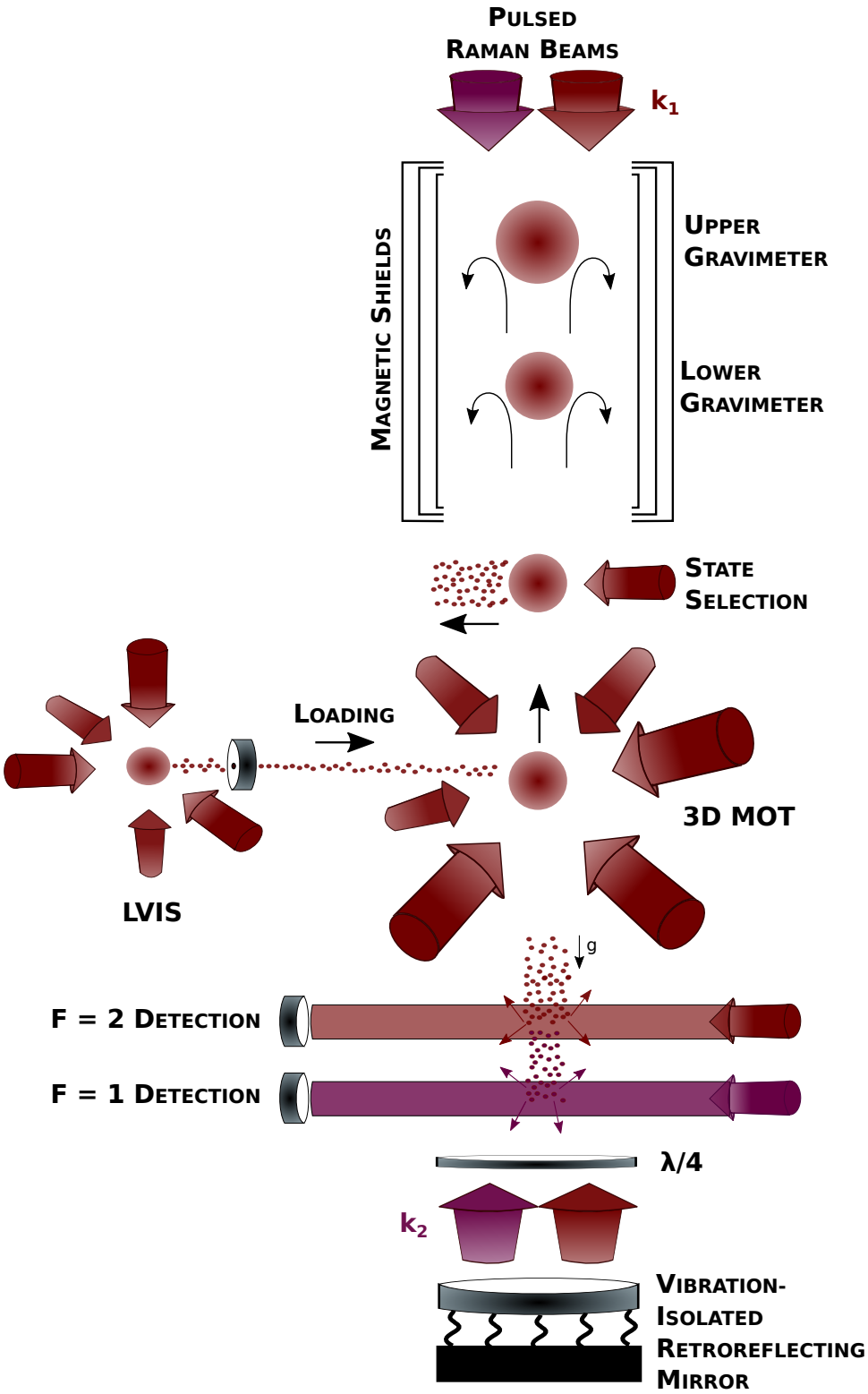

Figure 1.4: Cold atoms are loaded into a MOT from a continuous flux provided by a low-velocity intense source. These are launched in a moving molasses sequence into an interferometry region surrounded by three layers of magnetic shielding, having undergone state preparation. Vertical Raman beams, retro-reflected from a vibrationally damped mirror, perform a Mach-Zehnder sequence on the atoms. A gradiometry configuration is achieved by launching a second cloud to reach a simultaneous, but lower, apogee.

cooling to reach $\sim 5\,\mu$K temperatures.

- **State Selection:** The atoms are prepared to be in the magnetically insensitive $m_F = 0$ substate of the F = 1 state. Atoms not in the desired state are blown-away by a resonant laser beam.

- **Second Sequence:** A second MOT is loaded and undergoes the above procedure, but is launched to a different height to the first sample. Both samples will reach their apogees at the same time.

- **Interferometer Sequence:** Within the interferometry region, surrounded by three layers of magnetic shielding, a Mach-Zehnder interferometer sequence is performed using Raman beams, coherently splitting, mirroring and recombining the two clouds.

- **Detection:** The populations of the two substates are measured, giving the interferometer signal. Two vertically separated detectors are used, one for each hyperfine state. Firstly, the atoms in the F = 1 state are detected by resonant laser light which is retro-reflected to form standing wave. These atoms are then blown-away before the same standing wave scheme is implemented to detect those in the F = 2 state. This allows for normalised populations to be determined.

1.4 Outline of this Thesis

The remainder of this thesis is organised in the following manner. In Chapter 2 the scheme for measuring gravity using light-pulse atom interferometry, described qualitatively above, is presented in a more rigourous theoretical manner. Chapter 3 presents the experimental design and performance of the atomic fountain. Chapter 4 gives the design and characterisation of the Raman beam system which performs the interferometric pulses, with a design for an improved system provided in Chapter 6, along with other proposed plans and upgrades. The interferometric results are presented in Chapter 5 and Chapter 7 provides a summary of the thesis. The relevant theory of lasing cooling and trapping is presented in Appendix A and some photographs of the experimental setup and laboratory can be found in Appendix B.

Chapter 2

Gravity Gradiometry based on Light-Pulse Atom Interferometry

As discussed in the introductory chapter, the coherent manipulation of atomic states is performed via the interaction of light with the electronic states of the atom. This chapter provides the basic theory of atom-optical interactions needed to understand these processes, with specific reference to the structure of ^{87}Rb, as used in the NPL fountain. A practical interferometric signal requires the introduction of a phase shift between the different interferometry arms – the origins of this shift is also considered in detail[i].

2.1 Interactions between Light & a Two-Level Atom

2.1.1 Rubidium-87 as a Two-Level Atom

As an alkali metal, ^{87}Rb has a single valence electron, meaning that it possesses a comparatively simple electronic structure, making it an ideal candidate species for laser cooling and interferometry experiments. It has several advantages over ^{85}Rb, which is both the most abundant and technically only stable rubidium nuclide [68], including a greater hyperfine splitting in both the ground and excited states, and stronger elastic collisions across a broad range of energies, which is advantageous for Bose-Einstein condensate production [69]. In general, cooling ^{85}Rb to quantum degeneracy is considerably more challenging [69, 70], due not just to this lower elastic scattering cross section, but also because of its high inelastic scattering rate [71], a zero in its s-wave scattering cross section at low energy, and its negative scattering length, which tends to make the system unstable [72]. For the ground state of ^{87}Rb, $I = 3/2$ and $L = 0$ giving $J = 1/2$ and $F = 1$ or $F = 2$. The first excited state is for $L = 1$ and $J = 3/2$, which forms a resolvable fine-structure doublet with the $J = 1/2$ state. As the separation between this doublet is approximately 15 nm [73], they can be considered separately and only the higher energy $5^2S_{1/2} \rightarrow 5^2P_{3/2}$ transitions are considered here (the so-called D_2 line).

[i]The treatment in this chapter is based broadly on those given in various other PhD theses [58, 65, 66, 67].

The hyperfine structure of $5^2S_{1/2}$ ground state of ^{87}Rb forms an effective two-level system, assuming the interaction radiation to be considerably detuned from other transitions. This is easily achieved for light radiating close to the hyperfine resonance (∼6.835 GHz), as the next nearest transition is ∼384.2 THz (linewidth of $2\pi\cdot$6.067 MHz) – a five order of magnitude difference [73][ii].

2.1.2 Interaction Hamiltonian

The interaction of a two-level atom with electromagnetic radiation is well understood theoretically, with the full quantum treatment empirically validated by cavity quantum electrodynamic experiments. Here a semi-classical treatment is advanced – a quantised atom interacting with a classically oscillating electric field, with the magnetic field component ignored due to its weaker strength.

The unperturbed, time-independent Hamiltonian of the atom (H_0) has two orthonormal eigenstates:

$$H_0|g\rangle = E_g|g\rangle = \hbar\omega_g|g\rangle; \tag{2.1}$$

and,

$$H_0|e\rangle = E_e|e\rangle = \hbar\omega_e|e\rangle; \tag{2.2}$$

where $|g\rangle$ and $|e\rangle$ represent the ground and excited states (i.e. $\omega_g < \omega_e$), respectively. Any general state vector ($|\Psi(t)\rangle$) can therefore be written,

$$|\Psi(t)\rangle = c_g(t)\,|g\rangle e^{-i\omega_g t} + c_e(t)\,|e\rangle e^{-i\omega_e t}, \tag{2.3}$$

with the probability for the atom to be found in, for example, the ground state given by,

$$\langle g|\Psi(t)\rangle = |c_g(t)|^2. \tag{2.4}$$

To this unperturbed Hamiltonian a term ($H_I(t)$) representing the interaction with a sinusoidal electric field ($\boldsymbol{E}(t)$) oscillating with an angular frequency ω, can be added,

$$H_I(t) = -\boldsymbol{d}\cdot\boldsymbol{E}(t) = e\boldsymbol{r}\cdot\boldsymbol{E_0}\cos(\omega t), \tag{2.5}$$

where $\boldsymbol{d} = e\boldsymbol{r}$ is the dipole operator, meaning that this term represents the potential energy of a dipole in a classical electric field.

The general state vector (equation 2.3) can then be used in conjunction with the Schrödinger equation:

$$(H_0 + H_I(t))\left(c_g(t)\,|g\rangle e^{-i\omega_g t} + c_e(t)\,|e\rangle e^{-i\omega_e t}\right) = i\hbar\frac{d}{dt}\left(c_g(t)\,|g\rangle e^{-i\omega_g t} + c_e(t)\,|e\rangle e^{-i\omega_e t}\right). \tag{2.6}$$

[ii] Zeeman splitting is here and in the following sections ignored.

Following differentiation, this can be written in terms of the interaction Hamiltonian only:

$$H_I(t)\left(c_g(t)|g\rangle e^{-i\omega_g t}+c_e(t)|e\rangle e^{-i\omega_e t}\right)=i\hbar\left(\frac{d(c_g(t))}{dt}|g\rangle e^{-i\omega_g t}+\frac{d(c_e(t))}{dt}|e\rangle e^{-i\omega_e t}\right). \quad (2.7)$$

2.1.3 Rabi Oscillations

The dynamic behaviour of the atomic state populations, as dependent upon the illuminating radiation, can now be evaluated. Utilising the fact that $\langle g|H_I(t)|g\rangle = \langle e|H_I(t)|e\rangle = 0$ and taking the inner product of equation 2.7 with $|g\rangle$ yields,

$$i\frac{d}{dt}c_g(t)=\Omega\cos(\omega t)\,e^{-i\omega_0 t}c_e(t), \quad (2.8)$$

and likewise taking the inner product with $|e\rangle$:

$$i\frac{d}{dt}c_e(t)=\Omega^*\cos(\omega t)\,e^{i\omega_0 t}c_g(t); \quad (2.9)$$

where $\omega_0=\omega_e-\omega_g$ is the angular frequency difference between the two states, and Ω is the so-called Rabi frequency, being defined as,

$$\Omega=\frac{\langle g|\boldsymbol{r}\cdot\boldsymbol{E_0}|e\rangle}{\hbar}, \quad (2.10)$$

and with Ω^* its Hermitian adjoint. The above matrix elements represent the transition strength, with this being mediated via the Rabi frequency and its dependence upon the overlap between the dipole and electric field polarisation vectors.

Euler's formula can be used to re-write the trigonometric terms as exponentials, meaning that equation 2.8 becomes,

$$i\frac{d}{dt}c_g(t)=\frac{\Omega}{2}\left(e^{i(\omega-\omega_0)t}+e^{-i(\omega+\omega_0)t}\right)c_e(t). \quad (2.11)$$

For a light which is nearly resonant to the transition frequency ($\omega\sim\omega_0$), the term oscillating at approximately twice this frequency ($\omega+\omega_0$) can be ignored, as it will average to zero for integration over any timescale of practical interest. This approximation is known as the rotating-wave approximation and is commonly employed in such derivations[iii]. Application here transforms equations 2.8 and 2.9 to,

$$i\frac{d}{dt}c_g(t)=\frac{\Omega}{2}e^{i(\omega-\omega_0)t}c_e(t), \quad (2.12)$$

and,

$$i\frac{d}{dt}c_e(t)=\frac{\Omega^*}{2}e^{-i(\omega-\omega_0)t}c_g(t), \quad (2.13)$$

[iii] The rotating-wave approximation is so named due to its origins in nuclear magnetic resonance experiments, where the component of the applied magnetic field not rotating in the same direction as the particle's precession is ignored.

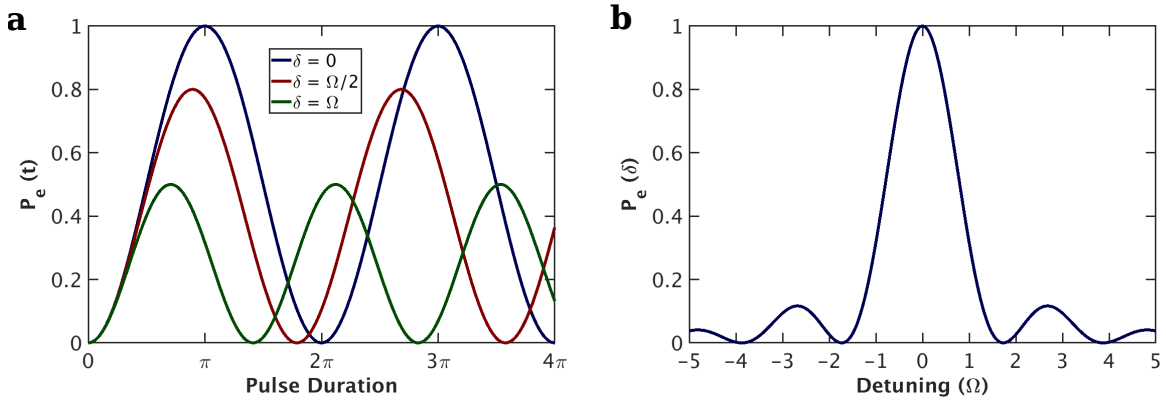

Figure 2.1: a) Rabi oscillations occur at a higher frequency but with reduced contrast for increased detuning. b) The state population following a pulse of duration π/Ω (a resonant π pulse).

respectively. These two equations can be combined to give the following second-order differential equation in terms of the excited state coefficient,

$$\frac{d^2}{dt^2}c_e(t) + i(\omega - \omega_0)\frac{d}{dt}c_e(t) + \left|\frac{\Omega}{2}\right|^2 c_e(t) = 0. \tag{2.14}$$

For the case when the atom is initially in the ground state ($c_g(0) = 1$, $c_e(0) = 0$), the solution to these equations are,

$$c_g(t) = \left[\cos\left(\frac{\Omega_D t}{2}\right) - i\frac{\delta}{\Omega_D}\sin\left(\frac{\Omega_D t}{2}\right)\right], \tag{2.15}$$

and,

$$c_e(t) = -ie^{-i\delta/2}\frac{\Omega}{\Omega_D}\sin\left(\frac{\Omega_D t}{2}\right), \tag{2.16}$$

where δ is the detuning of the interacting radiation with the atomic transition ($\delta = \omega - \omega_0$), and,

$$\Omega_D = \sqrt{\Omega^2 + \delta^2}. \tag{2.17}$$

From this the probability of finding the atom in its excited state (P_e) as a function of interaction time can be calculated,

$$P_e(t) = |c_e(t)|^2 = \frac{\Omega^2}{\Omega_D^2}\sin^2\left(\frac{\Omega_D t}{2}\right). \tag{2.18}$$

That is, the population varies sinusoidally in time, with the frequency of this oscillation increasing and the contrast decreasing as the detuning from the atomic resonance is increased (Figure 2.1). This behaviour is known as Rabi oscillations and allows for the atomic population to be controlled by varying the duration of the illumination period. Assuming light resonant to the atomic transition, two pulse durations are of particular interest: those which entirely

transfer the population to the excited state; and those which generate an equal superposition of the ground and excited state populations. The shortest pulse which achieves the former is when $t = \pi/\Omega$ and is termed a π pulse; similarly, for generating an equal superpositions the shortest pulse duration is when $t = \pi/(2\Omega)$ and these pulses are called $\pi/2$ pulses.

More generally, π pulses will invert the state population regardless of the initial conditions by causing the transition,

$$c_1|g\rangle + c_2|e\rangle \rightarrow -i\left(c_2|g\rangle + c_1|e\rangle\right). \tag{2.19}$$

This is only for radiation resonant to the atomic transition. In the case that the pulse duration is set for a π pulse on resonance, but the radiation frequency is varied, the change in population, as calculated from equations 2.17 and 2.18, is given by,

$$P_e(\delta) = \frac{\Omega^2}{\Omega^2 + \delta^2} \sin^2\left(\frac{\pi\sqrt{\Omega^2 + \delta^2}}{2\Omega}\right), \tag{2.20}$$

and displays a characteristic shape with side lobes, reminiscent of a sinc-squared function (Figure 2.1).

2.2 Three-Level Atom: Stimulated Raman Transitions

Such controlled manipulation of the state populations of an effective two-level system can also be performed by coupling to a third state via Raman beams. In this process, atoms are transferred from one state to another, via an intermediary virtual state, by the simultaneous emission and absorption from two independent electric fields. For example, an atom initially in the ground state will absorb a photon from one of the electric field components and then emit into the other component, transferring a net energy equal to the difference in the emission and absorption processes. As shown in Figure 2.2, coupling to a real atomic level is required, but it is also important that single-photon interactions with this state are suppressed in comparison to the two-photon Raman transitions. The interacting electric fields therefore need to be sufficiently detuned from the excitation frequency.

2.2.1 Dynamic Behaviour

Consider an atom as in the previous section but with an additional excited state ($|i\rangle$), far away from the states $|g\rangle$ and $|e\rangle$, and an electric field of the form,

$$\boldsymbol{E}(\boldsymbol{r}, t) = \boldsymbol{E_1}\cos\left(\omega_1 t - \boldsymbol{k_1}\cdot\boldsymbol{r} + \phi_1\right) + \boldsymbol{E_2}\cos\left(\omega_2 t - \boldsymbol{k_2}\cdot\boldsymbol{r} + \phi_2\right), \tag{2.21}$$

from which the following definitions are made,

$$\boldsymbol{k}_{\text{eff}} = \boldsymbol{k_1} - \boldsymbol{k_2}, \tag{2.22}$$

$$\omega_{\text{eff}} = \omega_1 - \omega_2. \tag{2.23}$$

$$\phi_{\text{eff}} = \phi_1 - \phi_2. \tag{2.24}$$

The two electric field components are detuned from the uppermost state ($|i\rangle$) by,

$$\Delta_1 = \omega_1 - (\omega_i - \omega_g), \tag{2.25}$$

and,

$$\Delta_2 = \omega_2 - (\omega_i - \omega_e), \tag{2.26}$$

and where it is assumed that $|\Delta_{1,2}| >> \Gamma_i$, where Γ_i is the linewidth of $|i\rangle$. The detuning of the two-photon process from resonance can also be defined,

$$\delta = (\omega_1 - \omega_2) - (\omega_e - \omega_g), \tag{2.27}$$

$$\delta = \omega_{\text{eff}} - \omega_0 = \Delta_1 - \Delta_2. \tag{2.28}$$

Considering only changes in time, the Hamiltonian for this system is,

$$H(t) = \hbar\omega_g|g\rangle\langle g| + \hbar\omega_e|e\rangle\langle e| + \hbar\omega_i|i\rangle\langle i| - \boldsymbol{r}\cdot\boldsymbol{E}(t). \tag{2.29}$$

Solving the Schrödinger equation for this Hamiltonian gives the following three equations,

$$i\frac{d}{dt}c_g(t) = \frac{\Omega_{gi}}{2}e^{i\Delta_1 t}c_i(t), \tag{2.30}$$

$$i\frac{d}{dt}c_e(t) = \frac{\Omega_{ei}}{2}e^{i\Delta_2 t}c_i(t), \tag{2.31}$$

$$i\frac{d}{dt}c_i(t) = \frac{\Omega^*_{gi}}{2}e^{-i\Delta_1 t}c_g(t) + \frac{\Omega^*_{ei}}{2}e^{-i\Delta_2 t}c_e(t), \tag{2.32}$$

where Ω_{gi} and Ω_{ei} are respectively the Rabi frequencies for the $|g\rangle \rightarrow |i\rangle$ and $|e\rangle \rightarrow |i\rangle$ transitions, and the rotating wave approximation has been applied as in the previous section.

For the case of large detunings from the intermediate state ($|\Delta_{1,2}| >> \Gamma_i$), the population of this state can be considered to be negligible and the above three-state system can be reduced to a two-state system by adiabatically eliminating the intermediate state [74, 75]. Integrating equation 2.32:

$$i\int_0^t \frac{d}{dt'}c_i(t') = \frac{1}{2}\int_0^t \left(\Omega^*_{gi}e^{-i\Delta_1 t'}c_g(t') + \Omega^*_{ei}e^{-i\Delta_2 t'}c_e(t')\right)dt'. \tag{2.33}$$

If it is assumed that the amplitude terms very much more slowly than the exponential terms, then the amplitudes can be taken to be time independent and thus removed from the integral.

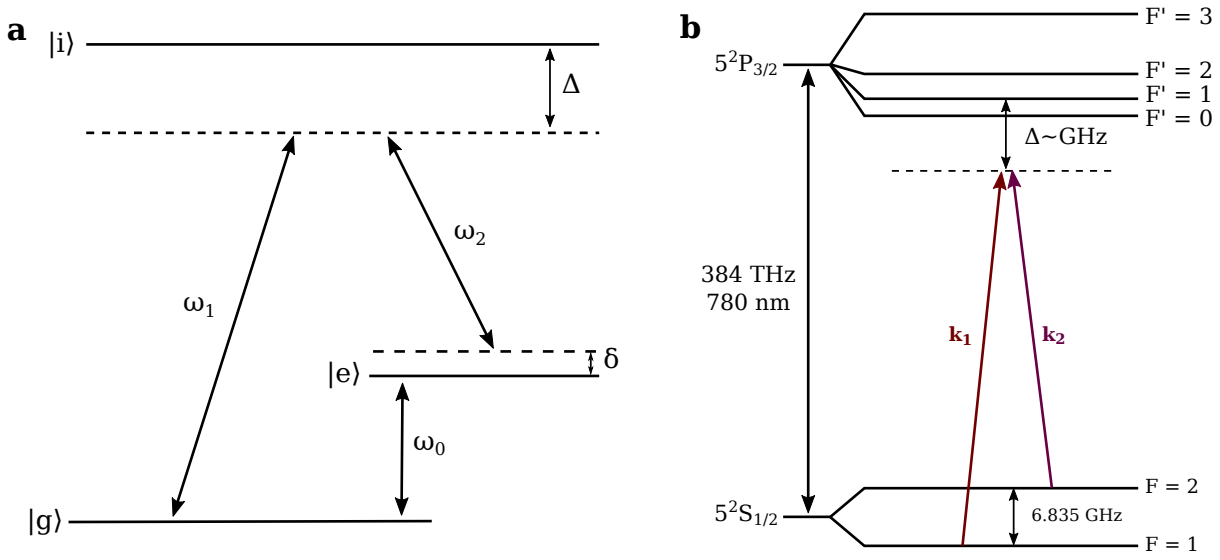

Figure 2.2: a) A three-level atom with the two lower states coupled via an intermediate state. b) The hyperfine structure and corresponding Raman beam setup for ^{87}Rb.

This means the previous equation can be rewritten as approximately,

$$i\int_0^t \frac{d}{dt'}c_i\left(t'\right) \approx \frac{1}{2}\left(\Omega_{gi}^* c_g \int_0^t e^{-i\Delta_1 t'}dt' + \Omega_{ei}^* c_e \int_0^t e^{-i\Delta_2 t'}dt'\right). \tag{2.34}$$

Solving these integrals gives the amplitude for the intermediate state:

$$c_i\left(t\right) \approx \frac{\Omega_{gi}^*}{2\Delta_1}\left(e^{-i\Delta_1 t}-1\right)c_g\left(t\right) + \frac{\Omega_{ei}^*}{2\Delta_2}\left(e^{-i\Delta_2 t}-1\right)c_e\left(t\right), \tag{2.35}$$

where the time dependence for the amplitudes has been reintroduced. This solution can now be substituted into equations 2.30 and 2.31:

$$i\hbar\begin{bmatrix}\dot{c_g}\left(t\right)\\ \dot{c_e}\left(t\right)\end{bmatrix} = \hbar\begin{bmatrix}\frac{|\Omega_{gi}|^2}{4\Delta_1}\left(1-e^{i\Delta_1 t}\right) & \frac{\Omega_{gi}\Omega_{ei}^*}{4\Delta_2}\left(e^{i\delta t}-e^{i\Delta_1 t}\right)\\ \frac{\Omega_{gi}^*\Omega_{ei}}{4\Delta_1}\left(e^{-i\delta t}-e^{i\Delta_2 t}\right) & \frac{|\Omega_{ei}|^2}{4\Delta_2}\left(1-e^{i\Delta_2 t}\right)\end{bmatrix}\begin{bmatrix}c_g\left(t\right)\\ c_e\left(t\right)\end{bmatrix}. \tag{2.36}$$

The rotating wave approximation can again be applied, here because the single-photon terms ($e^{i\Delta_{1,2}t}$) oscillate much more rapidly than their two-photon counterparts ($e^{-i\delta t}$):

$$i\hbar\begin{bmatrix}\dot{c_g}\left(t\right)\\ \dot{c_e}\left(t\right)\end{bmatrix} = \hbar\begin{bmatrix}\Omega_g^{AC} & \frac{1}{2}\Omega_{\text{eff}}e^{i\delta t}\\ \frac{1}{2}\Omega_{\text{eff}}^* e^{-i\delta t} & \Omega_e^{AC}\end{bmatrix}\begin{bmatrix}c_g\left(t\right)\\ c_e\left(t\right)\end{bmatrix}, \tag{2.37}$$

where Ω_a^{AC} is a frequency shift, known as the AC Stark or light shift, on state $|a\rangle$ due to its interaction with the illuminating radiation, and an effective Rabi frequency has been defined,

$$\Omega_{\text{eff}} = \frac{\Omega_{gi}\Omega_{ei}^*}{2\Delta}. \tag{2.38}$$

and $\Delta \approx \Delta_1 \approx \Delta_2$. As in the case for the case of a two-level atom, this Rabi frequency gives the rate at which the atom population changes between the ground and excited states, except here mediated via a two-photon rather than one-photon process. The Rabi frequency can be written in terms of the beam intensities as [76],

$$\Omega_{\text{eff}} = \frac{\Gamma^2}{4\Delta} \frac{\sqrt{I_1 I_2}}{I_{\text{sat}}}, \tag{2.39}$$

where I_i is the intensity of the i^{th} beam component, I_{sat} is the polarisation-dependent saturation intensity of the transition, and Γ is the natural linewidth of the transition.

To derive an analogous solution to the two-photon case, the Hamiltonian in equation 2.37 must be altered. First, a uniform energy shift equal to $-\hbar \left(\Omega_g^{AC} + \Omega_e^{AC}\right)/2$ is applied:

$$\hat{H} = \frac{\hbar}{2} \begin{bmatrix} \Omega_g^{AC} - \Omega_e^{AC} & \Omega_{\text{eff}} e^{i\delta t} \\ \Omega_{\text{eff}}^* e^{-i\delta t} & \Omega_e^{AC} - \Omega_g^{AC} \end{bmatrix}; \tag{2.40}$$

and, second, the Hamiltonian is transformed into a rotating frame with angular frequency equal to δ,

$$\hat{H} = \frac{\hbar}{2} \begin{bmatrix} -\left(\delta - \delta^{AC}\right) & \Omega_{\text{eff}} e^{i\delta t} \\ \Omega_{\text{eff}}^* e^{-i\delta t} & \delta - \delta^{AC} \end{bmatrix}, \tag{2.41}$$

where the AC Stark shift contribution (δ^{AC}) has been defined as,

$$\delta^{AC} = \Omega_e^{AC} - \Omega_g^{AC}. \tag{2.42}$$

The Hamiltonian in equation 2.41 can be used with the Schrödinger equation to generate the following second-order differential equation for the excited state amplitude,

$$\frac{d^2}{dt^2} c_e(t) + i\left(\delta - \delta^{AC}\right) \frac{d}{dt} c_e(t) + \frac{\Omega_{\text{eff}}^2}{4} c_e(t) = 0, \tag{2.43}$$

which can be solved to give, for an atom initially entirely in the ground state,

$$c_e(t) = -ie^{-i\left(\delta - \delta^{AC}\right)t/2} e^{-i\phi_{\text{eff}}} \frac{\Omega_{\text{eff}}}{\Omega_R} \sin\left(\frac{\Omega_R t}{2}\right), \tag{2.44}$$

where ϕ_{eff} is the phase difference between the two Raman beams ($\phi_1 - \phi_2$) and Ω_R is defined as,

$$\Omega_R = \sqrt{\Omega_{\text{eff}}^2 + \left(\delta - \delta^{AC}\right)^2}. \tag{2.45}$$

This allows the excited state population as a function of irradiation time to be calculated:

$$P_e(t) = |c_e(t)|^2 = \frac{\Omega_{\text{eff}}^2}{\Omega_R^2} \sin^2\left(\frac{\Omega_R t}{2}\right), \tag{2.46}$$

which, with the exception of the additional terms arising due to the AC Stark shift, is essentially

identical to the solution for a two-level atom (equation 2.18).

More generally, the amplitudes following the application of a pulse of duration t may be written as [58, 65],

$$c_g\left(t_0+t\right)=\left(\left[\cos\left(\frac{\Omega_R t}{2}\right)-i\frac{\delta-\delta^{AC}}{\Omega_R}\sin\left(\frac{\Omega_R t}{2}\right)\right]c_g\left(t_0\right)+ e^{i(\delta t_0+\phi_R)}\left[-i\frac{\Omega_{\text{eff}}}{\Omega_R}\sin\left(\frac{\Omega_R t}{2}\right)\right]c_e\left(t_0\right)\right)e^{-i\left(\Omega_g^{AC}+\Omega_e^{AC}-\delta\right)t/2}, \quad (2.47)$$

and,

$$c_e\left(t_0+t\right)=\left(e^{-i(\delta t_0+\phi_R)}\left[-i\frac{\Omega_{\text{eff}}}{\Omega_R}\sin\left(\frac{\Omega_R t}{2}\right)\right]c_g\left(t_0\right)+ \left[\cos\left(\frac{\Omega_R t}{2}\right)+i\frac{\delta-\delta^{AC}}{\Omega_R}\sin\left(\frac{\Omega_R t}{2}\right)\right]c_e\left(t_0\right)\right)e^{-i\left(\Omega_g^{AC}+\Omega_e^{AC}+\delta\right)t/2}, \quad (2.48)$$

where $c\left(t_0\right)$ is the amplitude at the beginning of the pulse and,

$$\phi_R=-\boldsymbol{k}_{\text{eff}}\cdot\boldsymbol{r}+\omega_{\text{eff}}t+\phi_{\text{eff}}. \quad (2.49)$$

2.2.2 Selection Rules: Permissible Raman Transitions

In the discussion so far, any structure to the atomic energy levels has been ignored. The absence of any magnetic field has been assumed and the effect of one has likewise been ignored. To properly understand the utilised Raman beam configuration, however, some understanding of the selection rules for light-mediated transitions between hyperfine levels is required. In particular, the experimental case where a magnetic field is applied parallel to the beam propagation direction must be considered: this field provides a quantisation axis and lifts the degeneracy of the magnetic substates – both of these effects determine the usable Raman beam configurations.

For an atomic transition $|F_1, m_{F_1}\rangle \rightarrow |F_2, m_{F_2}\rangle$, three types of transition can be defined: π transitions in which $(m_{F_2}-m_{F_1})=\Delta m_F=0$; σ^+ transitions in which $\Delta m_F=+1$; and σ^- transitions in which $\Delta m_F=-1$. This transitions must also satisfy the additional constraints that $\Delta L=\pm 1$ and $\Delta J=0,\pm 1$, with the caveat that $|J_1=0\rangle \rightarrow |J_2=0\rangle$ is forbidden.

These transitions are related to the field component either parallel to the quantisation direction or in the transverse plane [77]. Specifically, π transitions are driven via the dipole moment induced along the propagation axis, whilst $\sigma^{\pm}$ transitions come from the dipole moment induce in the transverse plane. Due to the transverse nature of electromagnetic radiation, π transitions therefore do not occur for the case of interaction light parallel to the quantisation axis[iv]. In this, the experimentally realised case, only $\sigma^{\pm}$ transitions are possible. In the special

[iv] $\boldsymbol{E}\cdot\boldsymbol{k}=0$ and so no dipole is induced in the direction $\hat{\boldsymbol{k}}$ and there are therefore no transitions (see equation 2.10).

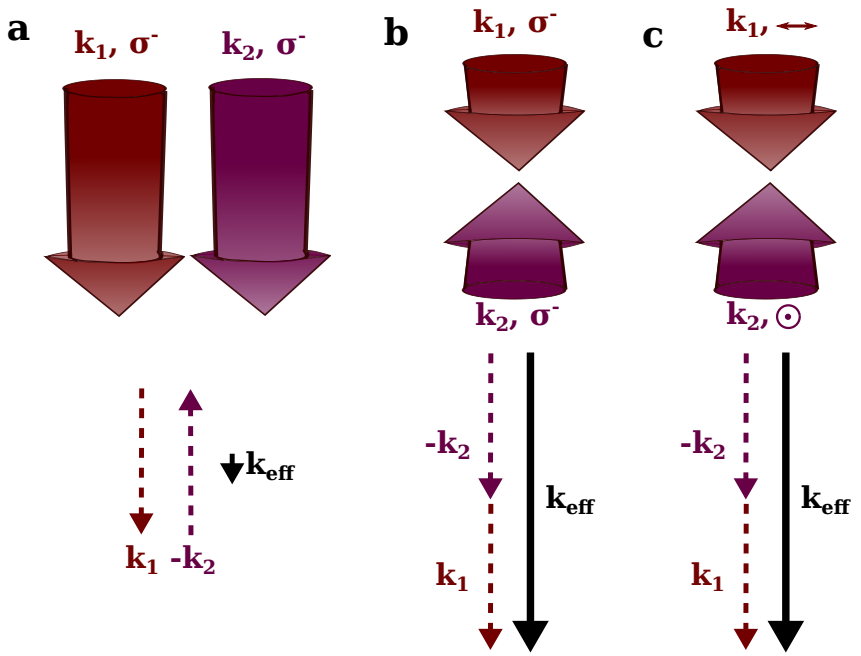

Figure 2.3: Permissible configurations for the Raman Beams: a) co-propagating and identical circular polarisation; b) counter-propagating and identical circular polarisation; c) counter-propagating and orthogonal linear polarisation.

cases of circularly polarised light, one handedness will produce σ^+ and the opposite will drive σ^- transitions. For linearly polarised light, there will be no field component transverse to the quantisation axis, precluding the possibility of $\sigma^\pm$ transitions and therefore preventing any transitions at all from occurring.

Assuming the atoms to have been prepared in the $m_F = 0$ state, only the three configurations shown in Figure 2.3 can be used [78]:

- The two field components should have identical circular polarisation and be co-propagating.

- The two field components have identical circular polarisation and are counter-propagating. In this case, to ensure they drive identical atomic transitions, the helicity of the two components is actually opposite. Incidentally, the opposite case to that in a magneto-optical trap.

- The two field components have orthogonal linear polarisation and are counter-propagating. Additionally, the atoms must have non-zero velocity in a retro-reflecting configuration as employed within this thesis.

In this thesis, the first and last configurations are utilised and their important qualities are described below.

2.2.2.1 Co-Propagating Raman Beams

The co-propagating configuration with identically circularly polarised beams has the major advantage of addressing the full velocity class of atoms, as the Doppler shift on both frequency components is identical. This means that a large signal can be extracted even for relatively hot samples, making this configuration especially useful for testing and characterising the system [78]. For example, it can be used to determine the AC Stark shift (section 5.1.1.1) or to characterise any magnetic fields (section 3.3.6).

Unfortunately, this configuration is not useful for making gravimetric measurements, due to the minimal momentum imparted for a change of internal state. This is because $\boldsymbol{k}_{\text{eff}} = \boldsymbol{k_1} - \boldsymbol{k_2} = \boldsymbol{k_{ge}}$ – that is, the wavevector for $|g\rangle \rightarrow |e\rangle$. For ^{87}Rb, this is a microwave transition and running the Raman beams in this configuration will produce interference fringes very similar to those of an atomic clock.

2.2.2.2 Counter-Propagating Raman Beams

In the counter-propagating configuration, however, $\boldsymbol{k}_{\text{eff}} \approx 2\boldsymbol{k_1} \approx 2\boldsymbol{k_2}$ and the momentum imparted is therefore considerable. However, the transition is now sensitive to the Doppler shift, as the atom is no longer moving with equal velocity relative to the two beam components. This means that the Raman beams will only interact with a certain subset of the atomic velocity class. In other words, they have become velocity selective and only atoms with the appropriate velocity (in the direction of the Raman beams) will undergo Raman transitions [79, 80]. The advantage of using velocity-selective transitions is that atoms having a known velocity travel well-defined trajectories, but the obvious disadvantage is the reduction in atom number, which decreases device sensitivity.

The velocity spread addressed by the Raman beams (Δv) is given by [80],

$$\Delta v = \Delta\omega \frac{c}{\omega_{\text{eff}}} \tag{2.50}$$

where $\Delta\omega$ is the Raman linewidth and c the speed of light. As the linewidth of the Raman beams can be very small, due to the ability to stabilise the relative frequency separation of the two Raman beam components to a very high accuracy and the long lifetimes of the two atomic states [65], this spread is dominated by the duration for which the Raman beams are applied. In this case, the limit comes from the Fourier width:

$$\Delta\omega \approx \frac{1}{\tau}. \tag{2.51}$$

The velocity spread of the selected atoms can consequently be very small. For example, for a 100 µs pulse performed on ^{87}Rb, the velocity spread is 0.62 mm/s, which has a corresponding effective temperature of 4 nK. It should be noted, however, that this is only a one-dimensional temperature – the velocity components transverse to the Raman beams are unaffected.

2.3 Interference Fringes on Internal States

2.3.1 Interference due to Phase Difference

An interferometer can be thought of as measuring the phase difference between its two arms. In the case of a light-pulse atomic interferometer, this can most easily be realised by generating an equal superposition of states with a resonant $\pi/2$ pulse, before immediately applying a second $\pi/2$ pulse with a different phase. Variation of this phase will alter the final state population and allow fringes to be observed – demonstrating how internal interference of atomic states can be performed via interaction with resonant light.

Consider the case of a two-level atom initially in the ground state and irradiated with resonant radiation for a period of time equal to a $\pi/2$ pulse ($\tau = \pi/(2\Omega)$). In this case, the excited state amplitude (equation 2.16) is simply,

$$c_e(\tau) = \frac{-i}{\sqrt{2}} e^{-i\delta\tau/2}. \tag{2.52}$$

This can be further simplified in the case of short pulse durations ($\delta\tau \ll 2\pi$):

$$c_e(\tau) = \frac{-i}{\sqrt{2}}. \tag{2.53}$$

The Hamiltonian for the second $\pi/2$ pulse needs to be modified to account for the introduced phase difference (ϕ). Specifically, the interaction Hamiltonian can now be written as (cf. equation 2.5),

$$H_I(t) = e\boldsymbol{r} \cdot \boldsymbol{E} \cos(\omega_0 + \phi). \tag{2.54}$$

From which the excited state amplitude becomes (cf. equation 2.9),

$$i\frac{d}{dt}c_e(t) = \Omega^* \cos(\omega t + \phi) e^{i\omega_0 t} c_g(t). \tag{2.55}$$

This can be simplified by using the Euler equation and then an approximation found by, as usual, ignoring the rapidly oscillating terms:

$$i\frac{d}{dt}c_e(t) = \frac{\Omega^*}{2} e^{-i\phi} \left(1 + e^{2i(\omega_0+\phi)}\right) c_g(t); \tag{2.56}$$

$$i\frac{d}{dt}c_e(t) \approx \frac{\Omega^*}{2} e^{-i\phi} c_g(t). \tag{2.57}$$

Following the procedure in section 2.1.3, this can also be done for the ground state amplitude and the two results can be combined to produce the following second-order differential equation,

$$\frac{d^2}{dt^2}c_e(t) + \left|\frac{\Omega}{2}\right|^2 c_e(t) = 0. \tag{2.58}$$

This equation can be solved for the initial conditions of a system having undergone a $\pi/2$ pulse (equation 2.53) and yields, following the application of second $\pi/2$ pulse of duration τ,

$$c_e(2\tau) = -\frac{i}{2}\left(e^{-i\phi+1}\right). \tag{2.59}$$

The excited state population following the application of two $\pi/2$ pulses is therefore, as a function of ϕ,

$$P_e(\phi) = |c_e(2\tau)|^2 = \frac{1+\cos\phi}{2}, \tag{2.60}$$

which reduces to the case of a π pulse for $\phi = 0$, as expected. It is clear, however, that the population will vary sinusoidally between the ground and excited states as a function of the phase difference between the pulses, demonstrating internal interference.

2.3.2 Ramsey Fringes

Ramsey interference fringes arise when two $\pi/2$ pulses are applied with a non-zero time interval in between. In contrast to the case above, the interference arises due to the paths accruing different phases during this interval, leading to a phase difference between these paths at the recombination stage. To observe interference fringes, either the time interval between the pulses can be varied or the frequency of the radiation can be varied and the time separation held constant. The latter is the method via which atomic clocks determine the frequency of an atomic transition with extremely high precision, whilst an intuitive method for understanding the former is presented here [77].

In the case of the first $\pi/2$ pulse, consider integrating equation 2.9 and applying the rotating wave approximation:

$$c_e(\tau) = -\frac{\Omega^*}{2}\left(\frac{1-e^{i\delta\tau}}{\delta}\right). \tag{2.61}$$

The term for a second $\pi/2$ pulse will be similar, but with an additional phase term from the free propagation time:

$$c_e(2\tau+T) \sim \frac{\Omega^*}{2}\left(\frac{1-e^{i\delta\tau}}{\delta}\right)e^{i\delta T}; \tag{2.62}$$

where T is the time between the pulses and approximations the evolution time $(\tau+T)$ for short pulses. In the case of applying only one of these pulses, the excited state population would be the same for both and be as previously calculated. However, as the atom can be transferred to the excited state by either the first or the second pulse, the excited state probability must be calculated from the summation of these two amplitude terms:

$$c_e(2\tau+T) \sim \frac{\Omega^*}{2}\left(\frac{1-e^{i\delta\tau}}{\delta} + \frac{1-e^{i\delta\tau}}{\delta}e^{i\delta T}\right). \tag{2.63}$$

The excited state probability from this combined amplitude is,

$$P_e\left(2\tau+T\right)=\left|\Omega\tau\right|^2\left[\frac{\sin\left(\delta\tau/2\right)}{\delta\tau/2}\right]^2\cos^2\left(\frac{\delta T}{2}\right), \tag{2.64}$$

which will demonstrate interference fringes when altering either δ or T. When varying δ, the sinc-squared function will have a fringe pattern superimposed from the cosine-squared term, with these fringes narrowing in frequency space for larger time separations. This is why atomic clocks seek to maximise the time between the two interrogation pulses, for example by using an atomic fountain – longer time durations lead to a a finer central fringe and hence improved spectral resolution.

A more general result for the excited state population following two identical pulses of duration τ and separated by time T can be derived and is quoted below [81],

$$P_e=4\left|\frac{\Omega}{\Omega_D}\right|^2\sin^2\left(\frac{\Omega_D\tau}{2}\right)\left[\cos\left(\frac{\delta T}{2}\right)\cos\left(\frac{\Omega_D\tau}{2}\right)-\frac{\delta}{\Omega_D}\sin\left(\frac{\delta T}{2}\right)\sin\left(\frac{\Omega_D\tau}{2}\right)\right]^2. \tag{2.65}$$

2.4 Mach-Zehnder Interferometer with Raman Transitions

Interference fringes generated with light pulses and due to the interference of internal atomic states were discussed in section 2.3, but measurements sensitive to forces, such as gravimetry, require the interference between external atomic degrees of freedom. Specifically, the superposition must be generated such that the two arms of the interferometer follow spatially separated paths, before being brought back together to achieve spatial overlap at the time of recombination. Although the interaction with resonant radiation or co-propagating Raman beams of course imparts momentum to the atom, for ^{87}Rb this is only a microwave's worth and therefore leads to unsubstantial splitting of the two states[v]. For this atom and using Raman beams, the greater momentum imparted from counter-propagating Raman beams is therefore required. This results in an interferometer analogous to a Mach-Zehnder interferometer and requires a three-pulse sequence: $\pi/2$-π-$\pi/2$ (Figure 2.4).

As discussed in Chapter 1, the total phase difference between the two paths accumulated during such an interferometer sequence ($\Delta\Phi$) can be written as three separate terms:

$$\Delta\Phi=\Delta\phi_{path}+\Delta\phi_{sep}+\Delta\phi_{light}, \tag{2.66}$$

where, $\Delta\phi_{path}$ is the phase difference between the atomic evolution along the two paths; $\Delta\phi_{sep}$ is the phase difference from any spatial separation of the wavepackets at the time of the initial or recombination pulses; and $\Delta\phi_{light}$ is the phase difference due to the phase accumulated from the interaction with the Raman beams. For atoms assumed to have a perfect initial and final

[v]Macroscopic interference from single-photon momentum recoil is possible when utilising higher frequency transitions and has been demonstrated in, for example, ^{88}Sr [60].

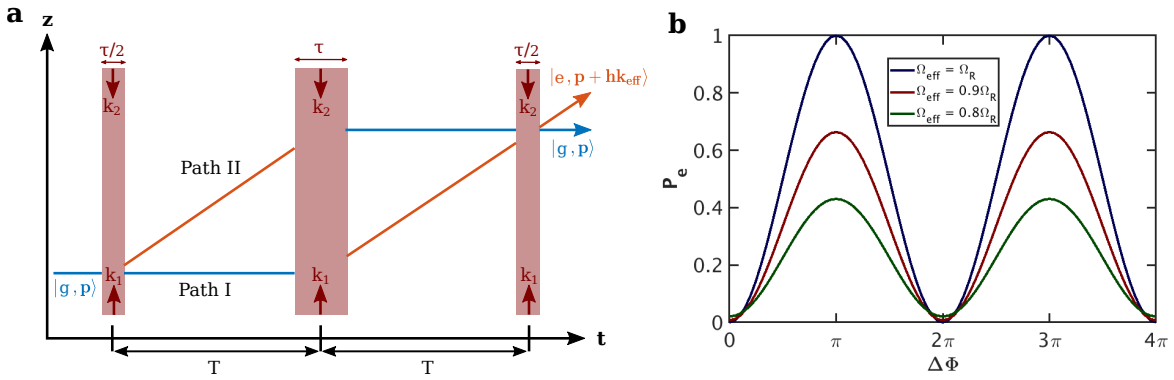

Figure 2.4: a) Diagram of the interferometer scheme in a frame which is in free fall along the atomic trajectory. b) The output of the interferometer (excited state population) as a function of the accumulated phase difference between the two paths. The populations, calculated from equation 2.83, show reduced contrast when moving the Raman beams from resonance.

overlap $\Delta\phi_{sep} = 0$. Likewise, if the gravitational field is assumed to be spatially uniform, then $\Delta\phi_{path} = 0$. This therefore leaves only the phase shift arising from the interferometer beams to be investigated[vi].

The phase difference arising from the interaction with the Raman beams is equal to the difference between the phase accumulated during the light interactions of the two paths. That is,

$$\Delta\phi_{light} = \sum_{i=1}^{3} \phi_i^I - \sum_{j=1}^{3} \phi_j^{II}, \tag{2.67}$$

where the summations are for the three interferometry pulses and ϕ_a^b is the phase imparted by the a^{th} pulse on the b^{th} path. These phase shifts are derived below and the phase shifts caused by the application of the Raman beams for different transitions are summarised for reference in Table 2.1.

Consider the general form of the amplitudes following the application of a Raman beam pulse given earlier in equations 2.47 and 2.48. In the case where a π pulse is defined as $\tau = \pi/\Omega_R$ and the Raman beam detuning is assumed to be close to resonance ($\left(\delta - \delta^{AC}\right) \ll \Omega_R$), then the amplitudes following a $\pi/2$ pulse may be written as,

$$c_g\left(t_0 + \tau/2\right) = \frac{1}{\sqrt{2}}\left[c_g\left(t_0\right) + \frac{\Omega_{\text{eff}}}{\Omega_R} e^{i(\delta t_0 + \phi_R - \pi/2)} c_e\left(t_0\right)\right] e^{-i\left(\Omega_g^{AC} + \Omega_e^{AC} - \delta\right)\tau/4}, \tag{2.68}$$

and,

$$c_e\left(t_0 + \tau/2\right) = \frac{1}{\sqrt{2}}\left[\frac{\Omega_{\text{eff}}}{\Omega_R} e^{-i(\delta t_0 + \phi_R + \pi/2)} c_g\left(t_0\right) + c_e\left(t_0\right)\right] e^{-i\left(\Omega_g^{AC} + \Omega_e^{AC} - \delta\right)\tau/4}. \tag{2.69}$$

[vi] More comprehensive treatments utilisng the Feynman path integral approach can be found in the literature [2, 59, 78, 82].

Transition	Phase Shift
$\lvert g,\boldsymbol{p}\rangle \rightarrow \lvert g,\boldsymbol{p}\rangle$	$-\left(\Omega_g^{AC}+\Omega_e^{AC}\right)\tau/2+\delta\tau/2$
$\lvert g,\boldsymbol{p}\rangle \rightarrow \lvert e,\boldsymbol{p}+\hbar\boldsymbol{k}_{\text{eff}}\rangle$	$-\left(\Omega_g^{AC}+\Omega_e^{AC}\right)\tau/2-\delta\tau/2-\delta t_0-\phi_{\text{eff}}-\pi/2$
$\lvert e,\boldsymbol{p}+\hbar\boldsymbol{k}_{\text{eff}}\rangle \rightarrow \lvert g,\boldsymbol{p}\rangle$	$-\left(\Omega_g^{AC}+\Omega_e^{AC}\right)\tau/2+\delta\tau/2+\delta t_0+\phi_{\text{eff}}-\pi/2$
$\lvert e,\boldsymbol{p}+\hbar\boldsymbol{k}_{\text{eff}}\rangle \rightarrow \lvert e,\boldsymbol{p}+\hbar\boldsymbol{k}_{\text{eff}}\rangle$	$-\left(\Omega_g^{AC}+\Omega_e^{AC}\right)\tau/2-\delta\tau/2$

Table 2.1: Phase shifts following Raman beam application for the different possible transitions, with the symbols as defined in the text.

Likewise for π pulses,

$$c_g\left(t_0+\tau\right)=\frac{\Omega_{\text{eff}}}{\Omega_R}e^{i(\delta t_0+\phi_R-\pi/2)}e^{-i\left(\Omega_g^{AC}+\Omega_e^{AC}-\delta\right)\tau/2}c_e\left(t_0\right), \tag{2.70}$$

and

$$c_e\left(t_0+\tau\right)=\frac{\Omega_{\text{eff}}}{\Omega_R}e^{-i(\delta t_0+\phi_R+\pi/2)}e^{-i\left(\Omega_g^{AC}+\Omega_e^{AC}+\delta\right)\tau/2}c_g\left(t_0\right). \tag{2.71}$$

For an interferometer run in a Mach-Zehnder configuration there are four different final state amplitudes to be considered: two for each state arising from the two different possible paths. Specifically, these paths in terms of state trajectories are,

$$c_g^I\left(t_3+\tau/2\right)\implies \lvert g,\boldsymbol{p}\rangle\rightarrow\lvert g,\boldsymbol{p}\rangle\rightarrow\lvert e,\boldsymbol{p}+\hbar\boldsymbol{k}_{\text{eff}}\rangle\rightarrow\lvert g,\boldsymbol{p}\rangle, \tag{2.72}$$

$$c_e^I\left(t_3+\tau/2\right)\implies \lvert g,\boldsymbol{p}\rangle\rightarrow\lvert g,\boldsymbol{p}\rangle\rightarrow\lvert e,\boldsymbol{p}+\hbar\boldsymbol{k}_{\text{eff}}\rangle\rightarrow\lvert e,\boldsymbol{p}+\hbar\boldsymbol{k}_{\text{eff}}\rangle, \tag{2.73}$$

$$c_g^{II}\left(t_3+\tau/2\right)\implies \lvert g,\boldsymbol{p}\rangle\rightarrow\lvert e,\boldsymbol{p}+\hbar\boldsymbol{k}_{\text{eff}}\rangle\rightarrow\lvert g,\boldsymbol{p}\rangle\rightarrow\lvert g,\boldsymbol{p}\rangle, \tag{2.74}$$

$$c_e^{II}\left(t_3+\tau/2\right)\implies \lvert g,\boldsymbol{p}\rangle\rightarrow\lvert e,\boldsymbol{p}+\hbar\boldsymbol{k}_{\text{eff}}\rangle\rightarrow\lvert g,\boldsymbol{p}\rangle\rightarrow\lvert e,\boldsymbol{p}+\hbar\boldsymbol{k}_{\text{eff}}\rangle. \tag{2.75}$$

where t_3 is the commencement time of the final pulse (Figure 2.4). These amplitudes can be calculated from application of equations 2.68 - 2.71:

$$c_g^I\left(t_3+\tau/2\right)=-\frac{1}{2}\left(\frac{\Omega_{\text{eff}}}{\Omega_R}\right)^2 e^{-i\left(\Omega_g^{AC}+\Omega_e^{AC}\right)\tau}e^{i(\delta(t_3-t_2))}e^{-i\left(\phi_R\left(z_2^I,t_2\right)-\phi_R(z_3,t_3)\right)}; \tag{2.76}$$

$$c_e^I\left(t_3+\tau/2\right)=-\frac{i}{2}\frac{\Omega_{\text{eff}}}{\Omega_R}e^{-i\left(\Omega_g^{AC}+\Omega_e^{AC}\right)\tau}e^{-i\delta t_2}e^{-i\left(\phi_R\left(z_2^I,t_2\right)+\delta\tau/2\right)}; \tag{2.77}$$

$$c_g^{II}\left(t_3+\tau/2\right)=-\frac{1}{2}\left(\frac{\Omega_{\text{eff}}}{\Omega_R}\right)^2 e^{-i\left(\Omega_g^{AC}+\Omega_e^{AC}\right)\tau}e^{i(\delta(t_2-t_1))}e^{-i\left(\phi_R(z_1,t_1)-\phi_R\left(z_2^{II},t_2\right)-\delta\tau/2\right)}; \tag{2.78}$$

$$c_e^{II}\left(t_3+\tau/2\right)=\frac{i}{2}\left(\frac{\Omega_{\text{eff}}}{\Omega_R}\right)^3 e^{-i\left(\Omega_g^{AC}+\Omega_e^{AC}\right)\tau}e^{-i(\delta(t_1-t_2+t_3))}e^{-i\left(\phi_R(z_1,t_1)-\phi_R\left(z_2^{II},t_2\right)+\phi_R(z_3,t_3)\right)}. \tag{2.79}$$

where the position and time dependence of the phase shift ϕ_R has been made explicit and, due to the symmetry of the pulses, perfect spatial overlap is assumed for the two paths for all but the second pulse. If it is further assumed that the pulses are short ($t_3-t_2\approx t_2-t_1\approx T$), the

final amplitudes for the ground and excited states can therefore be determined by summing the two relevant amplitudes:

$$c_g\left(t_3+\tau/2\right)=\frac{1}{2}\left(\frac{\Omega_{\text{eff}}}{\Omega_R}\right)^2 e^{-i\left(\Omega_g^{AC}+\Omega_e^{AC}\right)\tau}e^{i\delta\tau}e^{-i\left(\phi_R\left(z_2^I,t_2\right)-\phi_R(z_3,t_3)\right)} \left[1+e^{-i\left(\phi_R(z_1,t_1)-\phi_R\left(z_2^I,t_2\right)-\phi_R\left(z_2^{II},t_2\right)+\phi_R(z_3,t_3)-\delta\tau/2\right)}\right]; \quad (2.80)$$

$$c_e\left(t_3+\tau/2\right)=-\frac{i}{2}\frac{\Omega_{\text{eff}}}{\Omega_R}e^{-i\left(\Omega_g^{AC}+\Omega_e^{AC}\right)\tau}e^{-i\delta t_2}e^{-i\left(\phi_R\left(z_2^I,t_2\right)+\delta\tau/2\right)} \left[1-\left(\frac{\Omega_{\text{eff}}}{\Omega_R}\right)^2 e^{-i\left(\phi_R(z_1,t_1)-\phi_R\left(z_2^I,t_2\right)-\phi_R\left(z_2^{II},t_2\right)+\phi_R(z_3,t_3)-\delta\tau/2\right)}\right]. \quad (2.81)$$

From these amplitudes the final state populations of the interferometer can be determined as a function of the phase imprinted on the atoms from the Raman beams. The probability of the atom being found in the ground state is,

$$P_g=\frac{1}{2}\left|\left(\frac{\Omega_{\text{eff}}}{\Omega_R}\right)^2\right|^2\left[1+\cos\left(\phi_R\left(z_1,t_1\right)-\phi_R\left(z_2^I,t_2\right)-\phi_R\left(z_2^{II},t_2\right)+\phi_R\left(z_3,t_3\right)-\delta\tau/2\right)\right], \quad (2.82)$$

and the probability of being found in the excited state is,

$$P_e=\frac{1}{4}\left|\frac{\Omega_{\text{eff}}}{\Omega_R}\right|^2\left[1+\left|\left(\frac{\Omega_{\text{eff}}}{\Omega_R}\right)^2\right|^2-2\left(\frac{\Omega_{\text{eff}}}{\Omega_R}\right)^2 \cos\left(\phi_R\left(z_1,t_1\right)-\phi_R\left(z_2^I,t_2\right)-\phi_R\left(z_2^{II},t_2\right)+\phi_R\left(z_3,t_3\right)-\delta\tau/2\right)\right]. \quad (2.83)$$

These state populations show the importance of operating with a Raman beam frequency difference equal to the transition frequency and, moreover, the importance of cancelling the AC Stark shift. Firstly, for frequency differences not equal to the transition frequency, a reduced number of atoms participate in the interferometer as $\Omega_{\text{eff}}\leq\Omega_R$, leading to an effectively smaller contrast, as demonstrated in Figure 2.4. In the presence of an AC Stark shift, this requires the frequency difference to be offset from the unperturbed value, which means a non-zero value of δ and thus the introduction of an additional, unwanted phase shift due to the $\delta\tau/2$ term, which must therefore be properly characterised to retrieve meaningful results from the interferometer.

In the case of a properly cancelled AC Stark shift (see section 5.1.1.1) and for resonant Raman beams, equations 2.82 and 2.83 reduce to the ideal form,

$$P_g=\frac{1}{2}\left[1+\cos\left(\Delta\Phi\right)\right], \quad (2.84)$$

and,

$$P_e = \frac{1}{2}\left[1 - \cos\left(\Delta\Phi\right)\right], \tag{2.85}$$

where,

$$\Delta\Phi = \phi_R\left(z_1, t_1\right) - \phi_R\left(z_2^I, t_2\right) - \phi_R\left(z_2^{II}, t_2\right) + \phi_R\left(z_3, t_3\right). \tag{2.86}$$

The values of this remaining phase difference in the presence of a uniform gravitational field are calculated in the next section.

2.4.1 Making a Gravimetry Measurement

When using the Mach-Zehnder configuration to make a measurement of the gravitational acceleration, the atoms are prepared to be in free fall and the Raman beams are aligned with the gravitational axis. The sensitivity comes from the dependence of the imparted phase on the displacement of the atoms along the Raman beam axis – in this sense, the Raman beams act as a precision position reference for the atoms. The momentum splitting means that the two interferometer arms are spatially separated during the central, mirroring pulse and an acceleration along this axis will result in asymmetry and a measurable phase difference.

If it is assumed that the velocity components transverse to the gravitational axis ($\hat{\boldsymbol{z}}$) are zero, then the phase shift due to the Raman beams can be calculated via equation 2.49:

$$\phi_R\left(z, t\right) = -k_{\text{eff}} z + \omega_{\text{eff}} t + \phi_{\text{eff}}\left(t\right). \tag{2.87}$$

As the atoms are undergoing free fall, they follow a parabolic trajectory, which is, however, dependent upon the atomic state due to the momentum transfer from the Raman beams during a change of state. For a simple free fall, z can be calculated from the Newtonian trajectory,

$$z\left(t\right) = v_0\left(t - t_0\right) - \frac{1}{2} g \left(t - t_0\right)^2, \tag{2.88}$$

where v_0 is the velocity at time t_0, the precise value of which is irrelevant, as the phase difference is irrelevant of the initial (vertical) velocity [59]. This therefore allows the same treatment to be used for a simple drop experiment or for a fountain configuration. To determine the position at each pulse, the velocity recoil (v_R) from the Raman beams needs to be considered:

$$z_1\left(t_1\right) = 0; \tag{2.89}$$

$$z_2^I\left(t_2\right) = v_0 T - \frac{1}{2} g T^2; \tag{2.90}$$

$$z_2^{II}\left(t_2\right) = \left(v_0 + v_R\right) T - \frac{1}{2} g T^2; \tag{2.91}$$

$$z_3\left(t_3\right) = 2 v_0 T + v_R T - 2 g T^2. \tag{2.92}$$

These values can be used to determine the contribution to the phase difference from the effective

wavevector:

$$\Delta\Phi_k = -k_{\text{eff}}\left[z_1\left(t_1\right) - z_2^I\left(t_2\right) - z_2^{II}\left(t_2\right) + z_3\left(t_3\right)\right]; \tag{2.93}$$

$$\Delta\Phi_k = k_{\text{eff}} g T^2; \tag{2.94}$$

The contribution from the effective angular frequency is complicated by the requirement to chirp the Raman laser beams in order to account for the Doppler shift experienced by the freely falling atoms. The following angular frequency chirp rate is required,

$$\frac{d}{dt}\omega_{\text{eff}} = \boldsymbol{k}_{\text{eff}} \cdot \boldsymbol{g} = -k_{\text{eff}} g. \tag{2.95}$$

The value of the effective angular frequency will therefore vary with time such that,

$$\omega_{\text{eff}}\left(t\right) = \omega_{\text{eff},0} + 2\pi\alpha\left(t - t_0\right), \tag{2.96}$$

where $\omega_{\text{eff},0}$ is the value of ω_{eff} at some time t_0 and the frequency chirp rate has been defined such that,

$$\alpha = \frac{1}{2\pi}\frac{d}{dt}\omega_{\text{eff}}, \tag{2.97}$$

which is related to both local gravity and k_{eff} via equation 2.95, meaning it is around $\pm 25.1\,\text{MHz/s}$ for ^{87}Rb[vii]. The corresponding contribution to the phase difference can be calculated:

$$\Delta\Phi_\omega = \omega_{\text{eff},0}\left[t_1 - 2t_2 + t_3\right] + 2\pi\alpha\left[t_1\left(t_1 - t_0\right) - 2t_2\left(t_2 - t_0\right) + t_3\left(t_3 - t_0\right)\right]; \tag{2.98}$$

which, in the short pulse limit, reduces to,

$$\Delta\Phi_\omega = 2\pi\alpha T^2. \tag{2.99}$$

Combining this result with equation 2.94 and defining $\phi_R(t_a) = \phi_a$ gives the total phase shift,

$$\Delta\Phi = \left(2\pi\alpha + k_{\text{eff}} g\right) T^2 + \left(\phi_1 - 2\phi_2 + \phi_3\right) \tag{2.100}$$

which means that the equation quoted in the introduction (equation 1.3) has been derived, with the difference in sign of k_{eff} being arbitrary, as described in an earlier footnote.

Extraction of a value of gravity therefore requires the correct chirp rate to be determined. This can be performed by scanning the chirp rate to produce interference fringes, arising from the dependence of $\Delta\Phi$ on α. The spacing of these fringes is dependent upon the evolution time (T), but the chirp rate at which the minimum of the central fringe occurs is always unchanged,

[vii] In a retro-reflecting Raman beam configuration, the choice of a positive or negative chirp rate determines which of the two Raman beam pairs is utilised. These beams have opposite values of $\boldsymbol{k}_{\text{eff}}$, which flips the sign of $\Delta\Phi_k$, so the same gravitational value is determined.

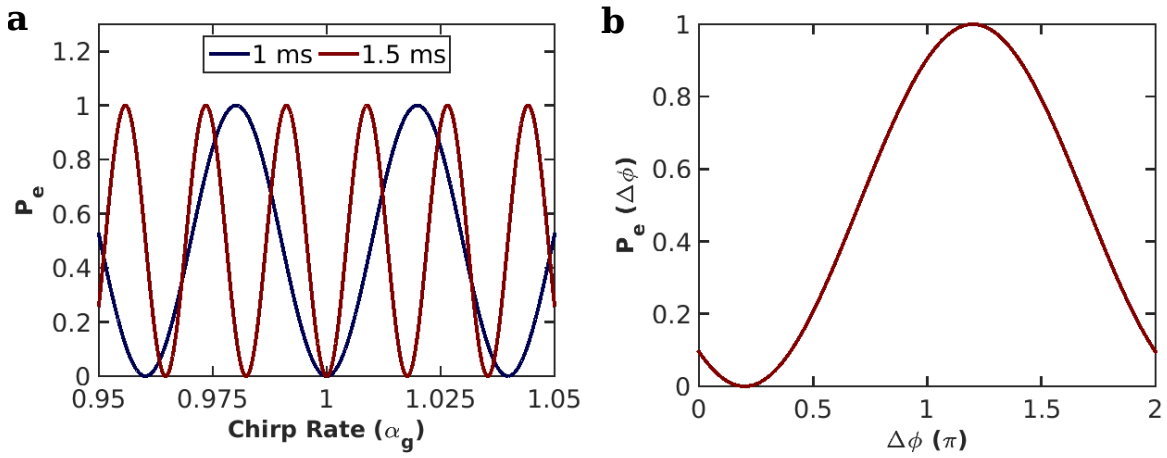

Figure 2.5: a) When producing interference fringes by scanning the chirp rate, there will always be a minimum when the chirp rate is set to match gravity (α_g), regardless of the separation time between the pulses. b) The precise position of the minimum can be found by scanning the fringe about this chirp rate.

as demonstrated in Figure 2.5. This minimum is found when,

$$\alpha = -\frac{k_{\text{eff}}}{2\pi} g, \tag{2.101}$$

meaning that the gravitational acceleration can be calculated from the chirp rate at this point. The negative sign arises due to the fact that the Doppler shift and the effective wavevector have opposite sign and here a negative chirp rate is applied (equation 2.95). This method is reminiscent of the manner in which atomic clocks determine the transition frequency, in which the central fringe position is again unchanged by the evolution time.

A finer value of gravity can then be extracted by determining the precise phase offset at the above chirp rate. This is usually performed by introducing an arbitrary phase step between two of the Raman beam pulses and varying this phase step between 0 - 2π, to scan a complete fringe (Figure 2.5). This yields the amount at which the chirp rate is offset from truly giving $\Delta\Phi = 0$ ($\Delta\phi_{\text{offset}}$) and the sensitivity of the measurement is determined by the precision at which this offset can be identified:

$$\Delta g = \frac{\Delta\phi_{\text{offset}}}{k_{\text{eff}} T^2}. \tag{2.102}$$

Finally, from inspection of equation 2.100 and the above discussion, the necessity of maintaining a constant phase difference between the two Raman beam frequency components should be clear. That is, the phase noise must be minimised, as any fluctuations in these values will be directly written on to the interferometric signal and will therefore produce spurious readings.

2.4.2 Additional Contributions to the Phase Difference

In addition to the leading-order contribution from local gravitational acceleration, there are several other effects which produce phase shifts, which have been ignored in the above analysis. Comprehensive treatments can be found elsewhere [83, 84], but a few of the most important and pertinent additional phase shifts, which must be controlled or evaluated for accurate gravimetry measurements, are discussed below and summarised in Table 2.2.

2.4.2.1 Rotation of Earth

Light-pulse Mach-Zehnder interferometers are sensitive to rotations, which is why they are employed as gyroscopes [22, 24, 85]. In this case, however, any phase differences arising from rotations is unwanted and, unfortunately, the rotation of Earth itself therefore introduces spurious shifts to the measured signal. Specifically, the contribution can be split into that arising from the centrifugal force and those from the Coriolis force.

The contribution from the centrifugal force $\Delta\phi_{\text{cent}}$ is,

$$\Delta\phi_{\text{cent}} = \boldsymbol{k}_{\text{eff}} \cdot (\boldsymbol{\Omega} \times (\boldsymbol{\Omega} \times \boldsymbol{r}))\, T^2 R_e, \tag{2.103}$$

where $\boldsymbol{\Omega}$ is the rotation rate of Earth, $R_e\boldsymbol{r}$ is the terrestrial position of the experiment, with R_e Earth's radius. The dominant term here is,

$$\Delta\phi_{\text{cent}} = k_{\text{eff}} T^2 \Omega_y^2 R_e, \tag{2.104}$$

where,

$$\Omega_y = \Omega \cos\theta_{\text{lat}}, \tag{2.105}$$

where θ_{lat} is the latitude of the experiment. This phase term is, by several orders of magnitude, the largest additional contribution to the phase difference and is estimated at 1.90×10^4 rad for this experiment. However, it is common to include this force in the definition of local gravity, meaning that it doesn't need to be cancelled or independently determined [86].

The contribution from the Coriolis force is,

$$\Delta\phi_{\text{cor}} = 2\boldsymbol{k}_{\text{eff}} \cdot (\boldsymbol{v} \times \boldsymbol{\Omega})\, T^2, \tag{2.106}$$

where $\boldsymbol{v}$ is the atomic velocity. The dominant term:

$$\Delta\phi_{\text{cor}} = 2k_{\text{eff}} v_x \Omega_y T^2; \tag{2.107}$$

where v_x is the component of the velocity in the east-west axis. Using this equation, this phase shift is estimated as 4.99 rad for this experiment.

The systematic contribution from the Coriolis force therefore arises due to the transverse

Cause	Term	Size (rad)	Relative Size
Local Gravity	$k_{\text{eff}} g T^2$	1.42×10^7	1
Centrifugal Force	$k_{\text{eff}} T^2 \Omega_y^2 R_e$	1.90×10^4	1.34×10^{-3}
Coriolis Effect	$2 k_{\text{eff}} v_x \Omega_y T^2$	4.99	3.51×10^{-7}
Gravity Gradient	$k_{\text{eff}} \Gamma_{zz} \left(v_0 + \frac{\hbar k_{\text{eff}}}{2m} \right) T^3$	4.20	2.95×10^{-7}
Gravity Gradient	$\frac{7}{12} k_{\text{eff}} \Gamma_{zz} g T^4$	2.30	1.62×10^{-7}
Quadratic Zeeman Effect	$-\frac{\hbar k_{\text{eff}}}{m} \alpha B_0 \left(\partial_z B \right) T^2$	5.23×10^{-8}	3.68×10^{-15}

Table 2.2: Expected contributions to the interferometric phase difference for some select terms. The calculations assume a launch to 1 m with 5 μK ^{87}Rb atoms: $k_{\text{eff}} = 2k_1$; $T = 300$ ms; $v_0 = 3.13$ m/s; $v_x = 38$ mm/s; $B_0 = 380$ nT; $\partial_z B = 0.36$ nT; and $\alpha = 2\pi \cdot 57.515$ GHz/T^2. Other parameters used are $g = 9.81$ m/s^2, $\Gamma_{zz} = -2g/R_e$, $R_e = 6.371 \times 10^6$ m, $\theta_{\text{lat}} = 51^\circ 25'$, and $\Omega = 7.27 \times 10^{-5}$ rad/s.

motion of the atoms, which is always present to some degree, even for very cold atomic samples, due in part to the difficulties in launching, aligning or even dropping the atoms perfectly vertically [87]. As shown in Figure 2.6, it is therefore a Sagnac effect [88]. An additional negative contribution of the Coriolis force is the imperfect overlap of the final wavepackets, which reduces interferometer contrast and therefore sensitivity [87]. This arises due to the non-inertial nature of the laboratory frame, which means that the momentum kick applied due to the interferometric beams occurs in a different direction for each pulse, as viewed from an *inertial* frame (i.e. one not rotating with Earth). In such a frame, the direction of the beams, and therefore k_{eff}, is seen to rotate between the pulses and atoms which interact with different pulses will receive differing momentum kicks (Figure 2.6c), breaking the symmetry of the interferometer and thus reducing the spatial overlap of the final states.

Fortunately, these effects can suppressed by providing a rotation at an equal but opposite rate to Earth's rotation, for example by rotating the entire apparatus [26, 88]. For a retro-reflecting Raman beam configuration, a more elegant solution is to alter the angle of the retro-reflecting mirror during the interferometry sequence [87]. In the ideal case, where the Raman beams are rotating in the opposite direction to Earth, this causes k_{eff} to rotate in the lab frame, but ensures that the atoms receive equal momentum transfer from each pulse in the inertial frame, thus suppressing the contribution of the Coriolis force[viii].

2.4.2.2 Gravity Gradient

The above derivations ignored the existence of a gravity gradient along the measurement axis, assuming a constant gravitational acceleration at all positions. In reality, however, this is not the case and a linear gravitational gradient introduces a phase shift of,

$$\Delta\phi_{gg} = k_{\text{eff}} \Gamma_{zz} T^2 \left(\frac{7}{12} g T^2 - \left(v_0 + \frac{\hbar k_{\text{eff}}}{2m} \right) T - z_0 \right), \tag{2.108}$$

[viii] It does, however, result in a change in the magnitude of k_{eff}, but thid effect is very small [89].

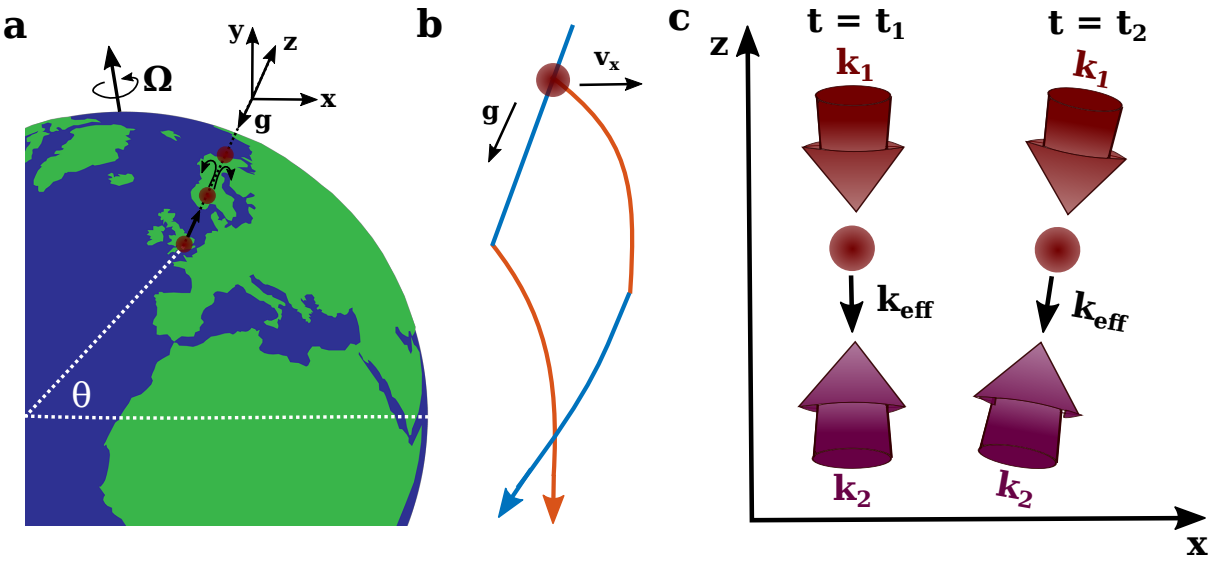

Figure 2.6: a) Showing the approximate position of the experiment relative to Earth's rotation. b) For non-zero transverse velocities, the Sagnac effect leads to a phase shift. c) In an inertial frame, take to be aligned to the initial pulse, but not rotating with Earth, the interferometry beams and therefore the momentum kick is seen to rotate with time. This prevents perfect final state overlap and reduces contrast. This can be countered by rotating the beams with the opposite direction to but with the same rate as Earth's rotation.

where Γ_{zz} is the gravity gradient component in the z direction, v_0 and z_0 are respectively the initial velocity and position, and m is the atomic mass. Taking $z_0 = 0$, then the remaining T^3 and T^4 terms can be estimated at 4.20 rad and 2.30 rad, respectively, using the values given in Table 2.2.

The gravity gradient term can form an especial difficult for high-precision measurements, such as those looking performing tests of the equivalence principle, due to its dependence on the initial position and velocity of the atoms. This requires these parameters to be extremely well known, which can be challenging, especially for a sequence involving many individual measurements. The terms depending upon position and velocity can, however, be cancelled by suitably manipulating the Raman beam phase during a pulse sequence [15, 90, 91] and the term involving k_{eff}^2 can be corrected for by running the interferometer sequentially with a reversed sign of the k_{eff} [88]. Taking the average between these two configurations will cancel out any terms with such a dependence.

Contributions from higher orders of the gravitational gradient are likely to be sixteen orders of magnitude smaller than the leading-order contribution to the phase difference and can therefore be deemed negligible [65].

2.4.2.3 Inhomogeneities of the Magnetic Field

Any inhomogeneities in the magnetic field of the experimental region will produce unwanted contributions to the phase difference. Such inhomogeneities arise from a number of sources,

including imperfections in the magnetic shielding and the field providing the quantisation axis, as well as natural variations in the ambient magnetic field, which also varies temporally. These alter the measured phase difference due to the energy dependence of the magnetic substates on the magnetic field strength via the Zeeman shift, which uncorrected for by changing the Raman beam frequency difference, resulting in variable detuning from the transition frequency[ix]. For ^{87}Rb, this effect can therefore be minimised by driving Raman transitions between the $|F = 1, m_F = 0\rangle$ and $|F = 2, m_F = 0\rangle$ states. Both these states and therefore the transition frequency are insensitive to magnetic fields to first order.

Higher-order contributions still exists, however these are small unless the magnetic field strength is high. Moreover, they will provide a constant energy shift if the field is uniform, which will provide no contribution to the final state phase difference. The second-order Zeeman contribution to the phase difference is given by,

$$\Delta\phi_{\partial_z B} = -\frac{\hbar k_{\text{eff}}}{m}\alpha B_0 \left(\partial_z B\right) T^2, \tag{2.109}$$

where B_0 is the magnetic field strength, $\partial_z B$ is the change of the magnetic field along the interferometer axis, and α is the second-order Zeeman coefficient of the atom. Using the experimental parameters (Table 2.2) yields a contribution to the phase difference of 5.23×10^{-8} rad, which is extremely small, due to the excellent magnetic field uniformity in the interferometry region (see section 3.3.6). This in combination with the use of first-order magnetically insensitive transitions, means that the contribution to the phase difference from magnetic fields can be considered negligible.

2.5 Gravity Gradiometry with Simultaneous Measurements

Measurements of the gravity gradient are made using atom interferometry by performing a differential measurement between the gravitational acceleration measured at two different heights. That is, a Mach-Zehnder interferometer is run for atoms at different heights, for example by varying the launch velocity in a fountain configuration, and the gravity gradient is extracted from the difference of the measured phase difference (equation 2.100) for these heights, which are assumed to be known. This difference can be considered as arising due to the non-cancellation of the gravity gradient's contribution to the interferometric phase (equation 2.108), which arises due to the positional dependence of this term. Equally, the atoms can be considered to be travelling in a *different mean gravitational potential* depending on their height. Regardless, it is not performed by determining the contribution of the gravity gradient to the phase difference of an individual atom interferometer.

Consider two test atom clouds which are spatially separated along the gravitational axis, such that they experience slightly different local gravitational accelerations. A *simultaneous*

[ix] Any misalignment between the magnetic field and the quantisation axis will lead to a reduction in contrast, rather than spurious phase terms.

Mach-Zehnder sequence is performed, meaning that the atoms are subjected to the same interferometric laser beam sequence and will therefore have equal contributions to their final state phase difference from the chirp rate and any laser phase fluctuations. Additionally, other terms such as the Coriolis effect and vibrational noise on the retro-reflecting mirror should also be common mode. When taking the difference between the phase difference for the two different interferometers, all of these terms will therefore cancel out with suppression being below 140 dB [92]. Subtraction therefore leaves,

$$\Delta\left(\Delta\Phi\right) = \Delta\Phi_1 - \Delta\Phi_2 = k_{\text{eff}}\left(g_1 - g_2\right)T^2 = \Delta\phi_{gg}, \tag{2.110}$$

where $\Delta\Phi_i$ and g_i are the phase difference and the mean local gravitational accelerations, respectively, for the interferometer at height h_i. If these heights are known, the gravity gradient can therefore be trivially extracted from the phase difference.

As discussed in Chapter 1, this phase difference is usually extracted by plotting the final state populations of the gradiometer parametrically and then using an ellipse fitting method [61]. The robustness of this method to common-mode noise was highlighted in Figure 1.3 and is also clearly demonstrated in actual experimental data [93]. To see this, consider the output of the interferometers in the general forms (cf. equations 2.84 and 2.85):

$$P_e^1 = A_1\left[\cos\left(\Delta\Phi_2 + \Delta\phi_{gg}\right)\right] + B_1; \tag{2.111}$$

and,

$$P_e^2 = A_2\left[\cos\left(\Delta\Phi_2\right)\right] + B_2; \tag{2.112}$$

The general form of a conic is given by,

$$f\left(x, y\right) = ax^2 + bxy + cy^2 + dx + ey + f = 0. \tag{2.113}$$

By plotting P_e^1 and P_e^2 parametrically, these parameters can be determined via a fitting procedure and the phase difference due to the gravity gradient can be extracted from the following relation [61],

$$\Delta\phi_{gg} = \arccos\left(-\frac{b}{2\sqrt{ac}}\right). \tag{2.114}$$

Alternatively, Bayesian estimation techniques can be used [94]. An advantage of this method is that it allows for the estimation of the gradient from just a single data point and allows for known information about the experiment, such as statistical fluctuations, to be accounted for [94].

Chapter 3

Rubidium Fountain: Theory, Design & Implementation

The basis for the device discussed in the remainder of this thesis is an atomic fountain, in which ^{87}Rb atoms are cooled, trapped and launched by laser light. This following chapter presents the experimental design and realisation of the atomic fountain, photographs of which can be seen in Appendix B. Familiarity with the practicalities of laser cooling and trapping are assumed, with the principles and basic theory behind Doppler cooling, optical molasses, magneto-optical traps (MOTs) and polarisation-gradient cooling instead presented in Appendix A.

3.1 Vacuum Chamber Design

The fountain has been through three design stages (Figure 3.1): operation as a frequency standard; first iteration for use as an atomic interferometer; and an improved and updated design for interferometry[i].

3.1.1 Basic Vacuum Design

The atomic interferometer is based upon re-purposing a frequency standard[ii], utilising a ^{87}Rb fountain. This system and its performance is described in detail elsewhere [63, 64], but it is worthwhile re-capping its major features and design here.

The chamber can be roughly divided into five sections: low-velocity intense source (LVIS); magneto-optical trap; state selection; interaction region; and detection. The below section will describe the vacuum chamber of these regions, with their optical design and experimental realisation discussed in section 3.3.

[i] The work presented within this thesis commenced shortly after the first iteration of the atomic interferometry vacuum had been established.

[ii] Colloquially referred to as atomic clocks, frequency standards differ by not having a counting mechanism.

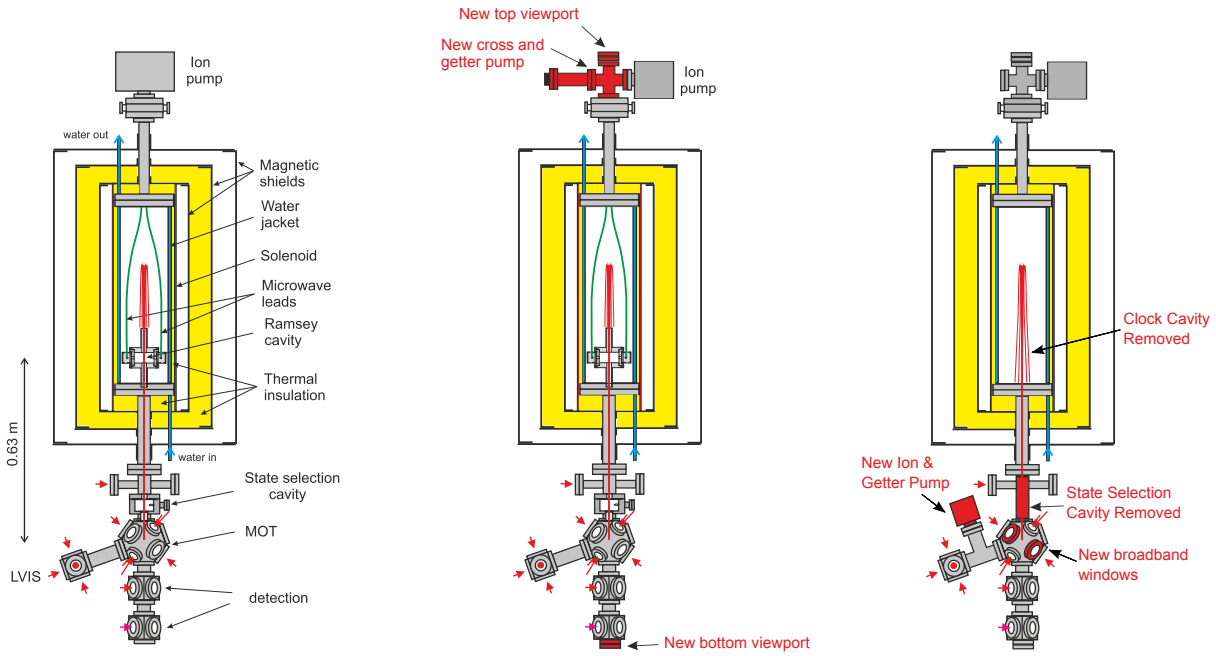

Figure 3.1: To-scale diagrams of the three iterations of the vacuum design shown from left to right: frequency standard; hybrid system; atomic interferometer. The hybrid system introduced optical access for the Raman beams, but left the clock cavity within. The final vacuum chamber removed both this and the state selection cavity, as well as introducing elements with the view towards BEC production. Changes from the previous iteration are highlighted in red and labelled.

3.1.1.1 Low-Velocity Intense Source Chamber

The LVIS region consists of a square chamber, with four of the ports filled with windows. Of the remaining two ports one is connected to a pipe with a T junction at the end. At this junction there is an additional window, but also a connection to a pipe in which a ampoule containing rubidium is stored (see later Figure 3.8). This region can be heated using heating tape to create a locally high density of rubidium vapour.

The final port contains a quarter-wave plate and a mirror combination, mounted in a copper connecting piece which centres it in the port. This port also connects the LVIS region to the MOT region via a 30 cm pipe which helps to maintain a high vacuum in the MOT region and also prevents the magnetic fields of the LVIS and the MOT from engaging in mutually damaging interaction.

3.1.1.2 Magneto-Optical Trap Chamber

The MOT chamber consists of fourteen ports: six for the cooling and trapping beams of the MOT; one for a repumper beam; one for the injection of cold atoms from the LVIS; two vertical ports that connect the chamber to the rest of the fountain; and four ports which are free to be used for miscellaneous and ad hoc purposes.

The geometry of the chamber is shown in Figure 3.2. The chamber is machined so that the six MOT windows are mutually orthogonal, with normals to their surfaces crossing in the geometric centre of the chamber. When coupled with sufficiently expanded laser beams, this allows for the optomechanics for the MOT to be mounted directly to the chamber without any need for transverse translation.

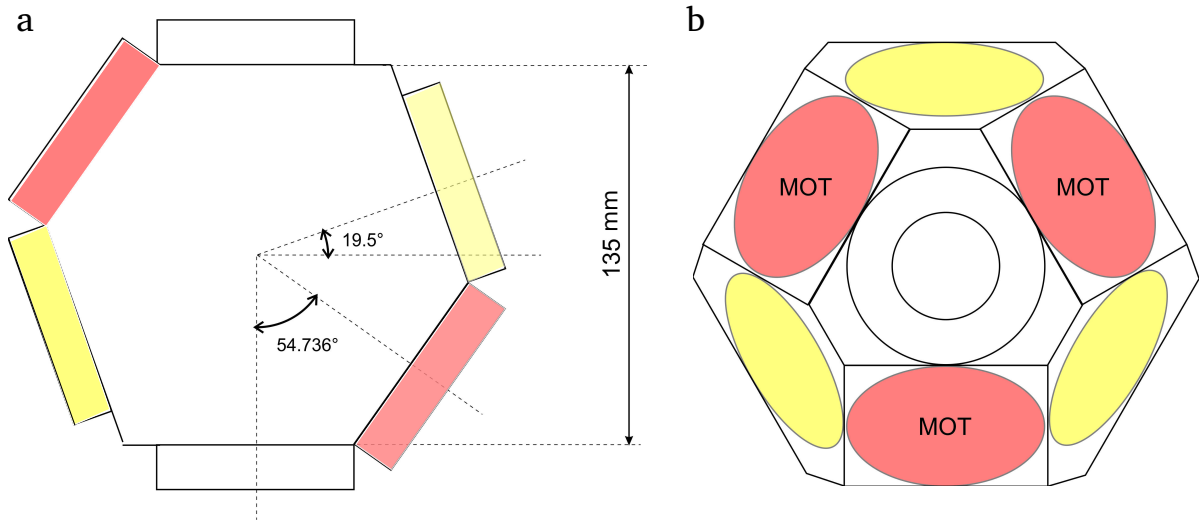

Figure 3.2: To-scale diagram of the MOT chamber shown as (a) a cross-section in the lateral plane and as viewed from above (b). The colour-coding shows which ports are used for the MOT beams, which have flexible usage (yellow), and which are connected to other vacuum components (white).

3.1.1.3 State Selection Vacuum Region

In the frequency standard, state selection was performed in a two-step process: first, the atoms interact with a resonant microwave field in a cavity, which applies a π pulse, transferring the atoms from $|F = 2, m_F = 0\rangle$ to $|F = 1, m_F = 0\rangle$; secondly, the atoms remaining in $|F = 2\rangle$ are blown away by the radiation pressure from light resonant to the $|F = 2\rangle \rightarrow |F' = 3\rangle$ transition. The state selection cavity had an opening of 22 mm and a quality factor of 800 and the beam for blowing away the residual $|F = 2\rangle$ atoms entered horizontally from a cross, with windows at each end.

The top of the cross part is split and used to attach the chamber to the large support structure. In this sense, the lower half of the chamber is suspended from this point.

3.1.1.4 Interrogation Region

The launched atoms undergo coherent interaction with electromagnetic fields in a region with a controlled, fixed magnetic field to act as a quantisation axis. This is achieved by a solenoid surrounded by three layers of mu-metal magnetic shielding. Moreover, the chamber here is

constructed with aluminium, which is significantly less magnetic than stainless steel[iii]. To connect the soft aluminium to the stainless steel portions of the chamber, aluminium transitions tubes are used, which are sealed with indium to both the steel regions and the central, aluminium interrogation tube. Similarly, all of the bolts and washers used within this region are made from aluminium or brass, the latter being used to connect the lids of the shielding to the main region. Each lid is composed of two pairs of separate, thin sheets of mu-metal, with the pairs laid perpendicular to each other to block any gaps. Likewise, the lids of the mu-metal extend upwards about the central pipe, as shown in Figure 3.1.

The three layers of magnetic shielding house inside them thermal insulation, made from aluminium oxide. Furthermore, there is the possibility to circulate water around the central region. The original purpose of the water cooling and thermal insulation was to stabilise and tune the temperature in this region, with the water cooling system sufficient to deal with the heat generated by the clock cavity, allowing the temperature to be stabilised to within $\pm 0.1\,^{\circ}\mathrm{C}$. This was important for the frequency standard, as the frequency shift caused by black body radiation is a major source of systematic noise [63, 95].

Both the triple magnetic shielding and the temperature control can be considered over-engineered for the purpose of making gravimetric measurements with atomic interferometry. However, magnetic inhomogeneities and black-body radiation do lead to systematic effects in the interferometer. For example, it has been shown that the thermal radiation field from a spatially varying local temperature induces a force via the AC Stark shift, leading to a measurable phase shift [96]. Whilst this force may prove important in, for example, searches for the gravitational Aharonov-Bohm effect [52], it is of the order of 10^{-11} m/s^2 and so likely to be of negligible importance for the current setup. Nevertheless, a controllable temperature is a potentially interesting functionality and there is no need to remove or degrade these features and thus the robustness of the fountain to these systematic effects.

3.1.1.5 State Detection Chamber Region

State detection occurs at the very bottom of the chamber, after the atoms have fallen through the MOT region. Two separate vacuum cubes are used for the detection of the $|F = 1\rangle$ (lower cube) and the $|F = 2\rangle$ states, helping to minimise cross-talk between the two detectors. The vertical ports of the cubes are occupied, leaving four remaining ports for detection purposes. Two of these ports, on opposing faces, are used to input the resonant detection light and the other two for imaging purposes (see section 3.3.7 for details).

3.1.2 Initial Vacuum Upgrade & Problems Arising

The initial design for the re-purposing of the fountain as a gravity gradiometer attempted to make as few changes to the vacuum chamber as possible. This was to allow the fountain to still

[iii] The magnetic permeability of aluminium is only $(1+2.2\times10^{-5})\mu_0$, whereas the relative increase compared to vacuum permeability for stainless steel is generally a few orders of magnitude higher.

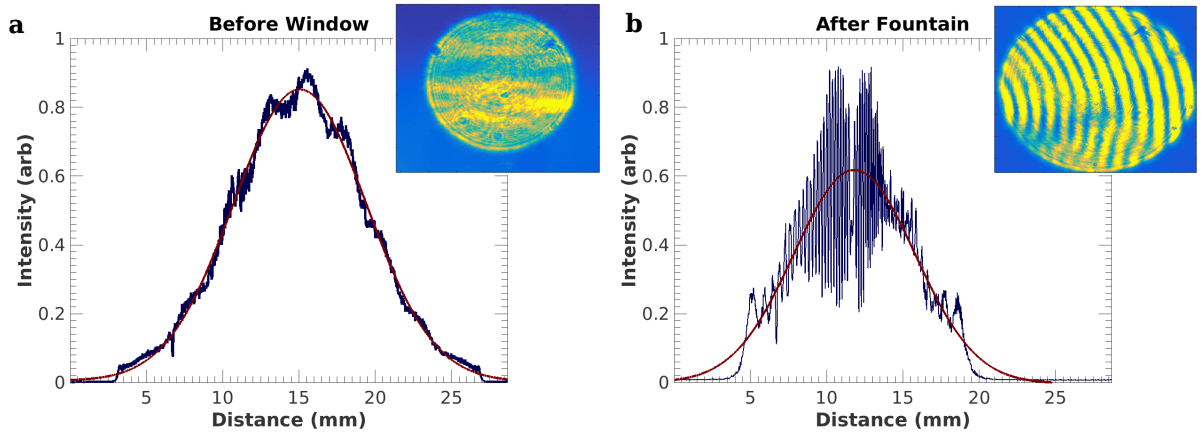

Figure 3.3: The profile of the first iteration of the Raman beams as measured with a linear CCD array (a) before and (b) after having passed through the initial configuration of the fountain, including the clock cavity. The red lines show fits to Gaussian profiles and the insets are images taken with CCD cameras, using a lens to focus down.

be run as a frequency standard, if desired. Therefore the only major changes in the vacuum chamber design were the addition of two windows at the top and the bottom of the fountain to allow optical access for the Raman beams. This change necessitated the introduction of a cross at the top of the fountain, as the ion pump had previously been mounted along the vertical axis (Figure 3.1).

To minimse the wavefront distortion across the Raman beams, the installed optical flats were selected to have specified low distortion ($< \lambda/20$). Furthermore, they were specially mounted so as to minimise mechanical stress. The conflat flange (Thorlabs, VPCH2-FL) was modified to remove the internal groove, so as to produce a smooth surface. The window was then held in place by the combination of an indium seal at the bottom and an aluminium top-plate and a teflon spacer pressing down from above.

Whilst this design did allow for all the atom cloud functionality to be implemented (i.e. cooling, trapping, launching), there were fundamental problems arising from the continued presence of the copper cavity used for resonant interaction with microwaves in the clock configuration. The problem arose from the conflict between the requirement for the clock cavity to be as close to a perfect resonator as possible ($Q_c \simeq 28500$ [63]) and the requirement for the Raman beams to be as large as possible compared to the atomic cloud. It is desirable for the Raman beams to be considerably larger than the transverse atomic cloud size so as to ensure an approximately identical wavefront and intensity distribution across the sample. The requirements of the clock cavity, however, result in an aperture of 16 mm being present in the middle of the interferometry region and therefore restricts the maximum possible size of the Raman beams to the same value. In addition, to reduce the amount of diffraction and any possible effects arising from the waveguide nature of the conducting copper, it is preferable to be smaller again than this aperture size. The severe effect on the beam profile caused by the diffraction on the clock cavity

is clearly visible in Figure 3.3, which shows the Raman beam profile as taken before and after having passed through the fountain, as measured with a linear CCD array (Thorlabs, LC100).

These problems are further exacerbated by the long times involved during an atomic fountain sequence. Despite the cold temperatures of the atoms, they can nevertheless undergo a significant thermal expansion during the launch period. Assuming a spherical Gaussian distribution, the size of the atomic cloud is governed by [97],

$$\sigma(t) = \sqrt{\sigma_0^2 + \left(\frac{k_B T}{m}\right)^2 t^2} \tag{3.1}$$

where $\sigma(t)$ is the Gaussian radius of the cloud at time t, σ_0 its initial radius, T the temperature, and k_B and m the Boltzmann constant and atomic mass, respectively. The expected size of the cloud at the apogee of different launch heights, based upon experimental values of the temperature and initial width (see section 3.3.3.2), quickly approaches and exceeds the size of the Raman beams (Figure 3.4).

The negative consequence of this conflict can be best observed by modelling the expecting dephasing that would occur from the interaction of the atomic cloud with a Gaussian beam of diameter 16 mm. This effect reduces the performance of the interferometer not by introducing any decoherence or noise terms, but by leading to a reduction in contrast. This dephasing arises in the first instance from the inhomogeneous intensity distribution leading to a variation in the effective Rabi frequency across the cloud, making the application of a perfect, for example, π pulse impossible.

Consider Raman beams of beam radius $2\sigma_{light} = r_0$ interacting with a cloud obeying equation 3.1. The Rabi frequency (Ω) across the cloud will be giving by (cf. equation 2.39),

$$\Omega(r) = \frac{\Gamma}{4} \frac{1}{(2\Delta/\Gamma)} \frac{I_0}{I_{sat}} \exp\left(-\frac{2r^2}{r_0^2}\right) \tag{3.2}$$

where r is the radial distance from the vertical axis, r_0 is the aperture radius, I_0 is the peak intensity, assumed to be equal for both Raman beam components, and the other symbols are as defined in equation 2.39. Assuming all the atoms are prepared in the same initial magnetic sub-state (e.g. $|F = 1, m_F = 0\rangle$), then the expected population transfer (P) following the application of a pulse of duration τ, is given by (see equation 2.46),

$$P(\tau, t) = \frac{1}{\sqrt{2\pi\sigma(t)}} \int_0^{r_0} \sin\left(\frac{\Omega(r)\tau}{2}\right) \exp\left(-\frac{r^2}{2\sigma(t)^2}\right) \mathrm{dr} \tag{3.3}$$

where the limits are set by the fact that the clock cavity also acts as a spatial filter for the atoms[iv]. The solution to this equation can be numerically approximated by converting to Cartesian co-ordinates and approximating the space using voxels. As shown in Figure 3.5, a

[iv] The situation is complicated by the continued thermal expansion of the atoms after the apogee. However, these effects are ignored for the purposes of this demonstration of the principle behind the dephasing.

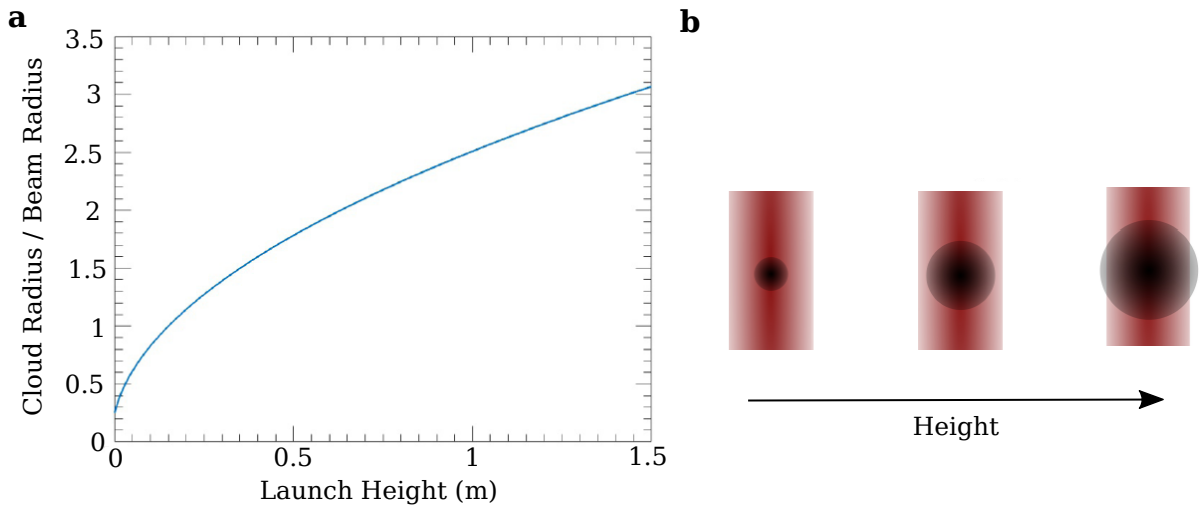

Figure 3.4: a) The expected size of the atomic cloud as a function of the launch height. It quickly exceeds the width of the Raman Beams, defined here as being of equal diameter to the clock cavity aperture. This leads to an unequal intensity distribution across the cloud, as shown in panel b.

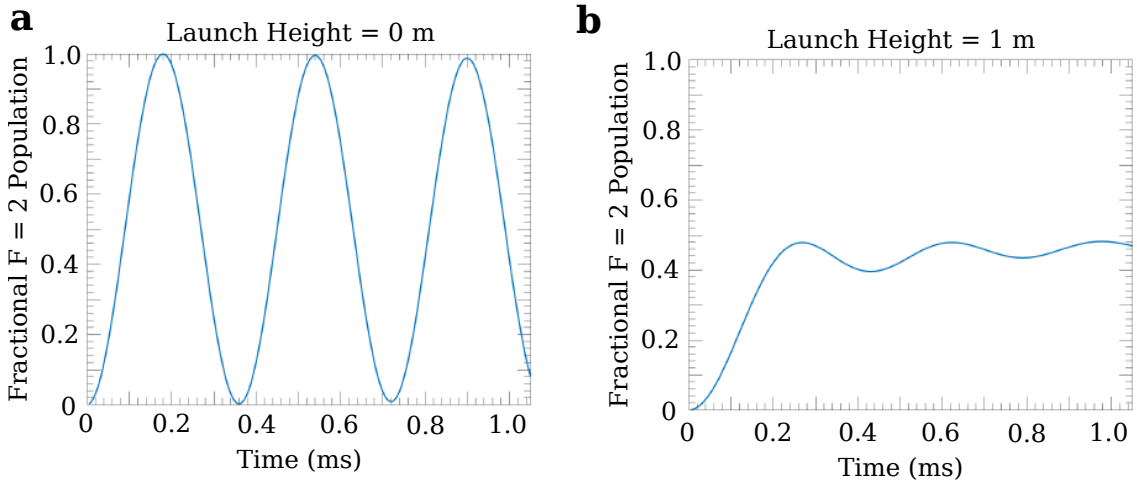

Figure 3.5: The expected state population transfer for different launch heights using experimentally realistic values for the Rabi frequency. A clear loss of contrast is expected as the launch height is increased and the cloud size is as shown in Figure 3.4. The population transfer is calculated by numerically approximating equation 3.3.

clear loss of contrast is visible for higher launch heights, with the results almost identical to a over-damped system at a height of 1 m.

For these reasons, it was decided to redesign and reconstruct the vacuum chamber as a dedicated atom interferometry system. The remainder of this chapter deals with this updated system, which is described in detail in the section below.

3.1.3 Updated Vacuum Design

The final vacuum chamber was designed so as to allow the maximum possible Raman beam diameter to be used. The major modification required was therefore the removal of the clock cavity – the 16 mm diameter aperture of which was the main limit on the usable Raman beam size. In addition the state selection cavity was also removed, which had an aperture of 22 mm. This was permissible as the state selection can be performed by either use of an external microwave horn (see section 3.3.5) or by the Raman beams themselves (section 5.2.1). Following these modifications the diameter is now limited by the diameter of the Raman Beam windows to 35 mm.

Removing the clock cavity required the top of the cavity to be opened and the cavity and its connecting RF-feedthroughs (green wires in Figure 3.1) to be lifted out. As this represented a large modification which would necessitate the chamber to be exposed for a considerable period of time and thus a long baking process, it was decided to utilise this opportunity to make some additional upgrades to the chamber design. Specifically, there is a long-term goal to use Bose-Einstein condensates (BECs) as the atomic source of the experiment. Rapid production of BECs is best achieved by optical means, as outlined in Chapter 6. Therefore, three of the access windows on the MOT section of the chamber were replaced with new windows which were coated with a broadband dielectric coating. Furthermore, a new dual getter and ion pump (SAES Getters, NEXTorr D 100-5) was attached at the bottom of the chamber. The purpose of this getter was to both prevent the establishment of a pressure gradient caused by having only one ion pump at the very top of the fountain and to further decrease the background pressure level, partially due to increased pumping capacity, but also due to the sensitivity of the getter pump to hydrogen.

A final change was the introduction of a new ampoule containing 1 g of rubidium, as the previous ampoule was found to be depleted[v].

3.1.3.1 Vacuum Baking Process

Following the completion of the stages outlined above, the vacuum chamber underwent a re-baking process. Due to the physical size of the fountain it is too cumbersome to move to a dedicated oven, so the baking process was performed in the laboratory by using heated

[v]The rubidium is released by smashing the ampoule within vacuum after the baking process has been completed. A small metal piece is dropped onto the ampoule, having previously been held aloft by a permanent magnet.

electrodes and several layers of insulation (a photograph is shown in Figure B.5). Strategically placed thermistors were used to prevent the temperature from exceeding the melting point of indium (157 °C), which would break these seals and thus the vacuum. Despite the insulation, however, a large temperature gradient existed in the fountain, with temperatures ranging from around 100 °C to 140 °C and so extending the baking process to a total of around three weeks.

During the baking process, a turbo-molecular pump was used as the main pump (Pfeiffer Vacuum, HiCube), with the magnets from the ion pumps removed, to prevent any damage from heating. The getter pump was also conditioned and then activated for several days at the end of the baking process. During baking and the subsequent further pump down by the ion pumps, the gas in the chamber was analysed by a residual gas analyser to check for possible leaks and equilibrium.

The final achieved vacuum pressure, as measured by the current through the secondary ion pump, was 4×10^{-10} mbar, compared to a previous value of around 10^{-9} mbar. This reduction is most likely due to the removal of material from within the chamber and the introduction of the getter and second ion pump. The primary goal of decreasing the vacuum pressure was to allow for an increased lifetime in any optical dipole trap, which is typically limited by collisions with background gas. As a general rule of thumb, a pressure 10^{-9} mbar allows for a 1 s lifetime and 10^{-10} mbar allows for a 10 s lifetime. The achieved background pressure should therefore be compatible with the rapid cooling towards quantum degeneracy in a such a trap (see section 6.2) [98].

3.2 Optical Circuitry

There are two main lasers used in the cold atom preparation section of the experiment: a primary laser which, after amplification, is used for cooling, trapping and launching of the atoms; and a repumper laser, to keep the atoms from falling into dark states of the primary laser. A full optical circuit for the fountain is shown in Figure 3.6 and photographs in Figure 3.7.

3.2.1 Primary Laser

The main laser of the setup is a cateye external-cavity diode laser (ECDL, MOGLabs, CEF v002), with a wavelength of 780 nm, a linewidth < 100 kHz and a maximum output power of around 80 mW. As this is an insufficient amount of power to control the whole experiment, this laser is used to seed a tapered amplifier (Toptica, BoosTA pro), which results in a maximum fibre-coupled output power of around 1.5 W. The tapered amplifier has optical fibres at both its input and its output, which acts to segment the experiment, allowing for changes to be made to the seed laser without affecting the downstream setup. All the optics before the amplification are mounted on a single 30 cm $\times$ 30 cm optical breadboard, and those after on a 60 cm $\times$ 60 cm one. This requires the use of minaturised optics and a very tight use of space, but has the advantage of being highly stable and robust, making it useful for use in conjunction with a

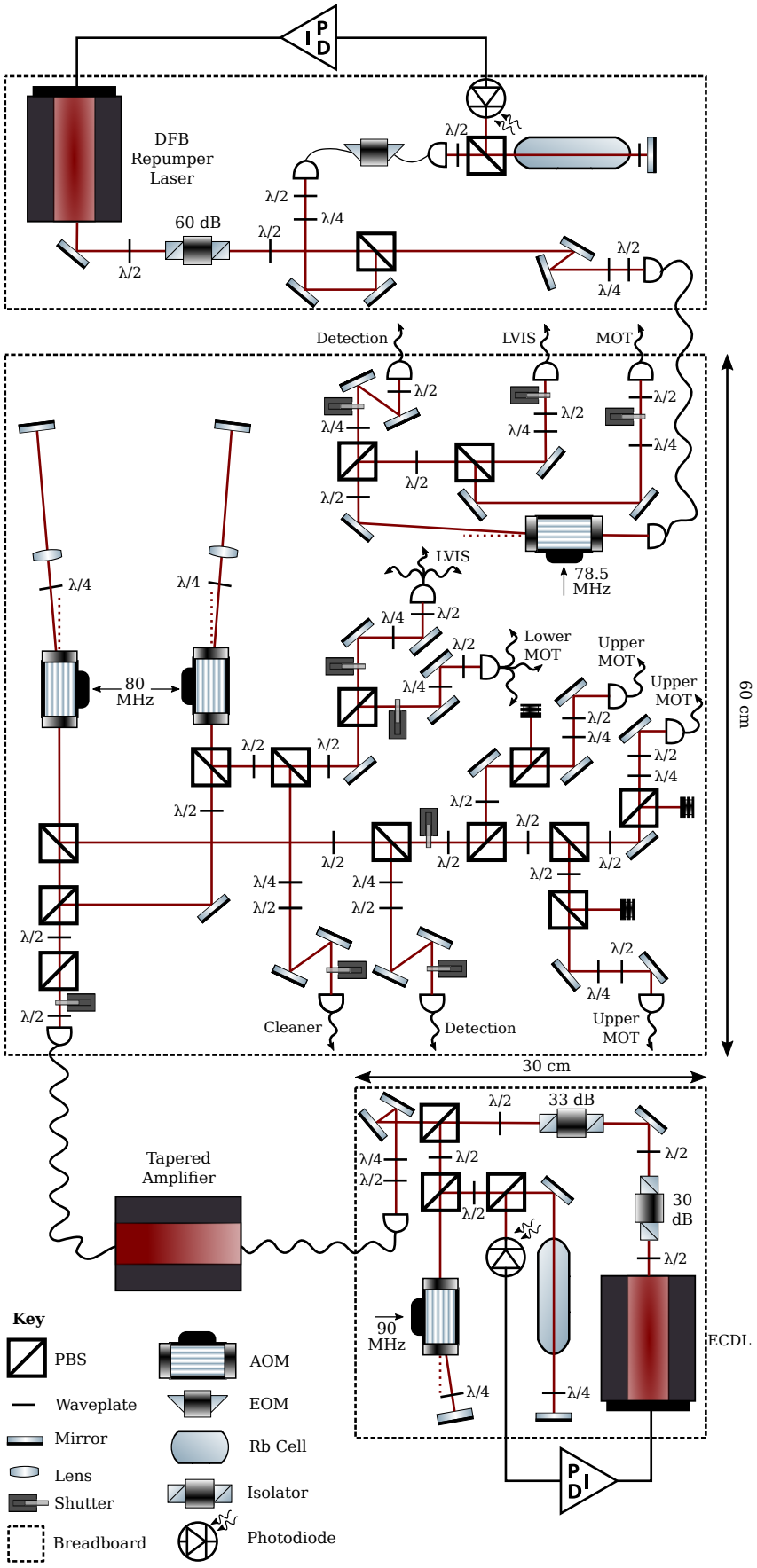

Figure 3.6: Optical circuit diagram for controlling the atomic fountain.

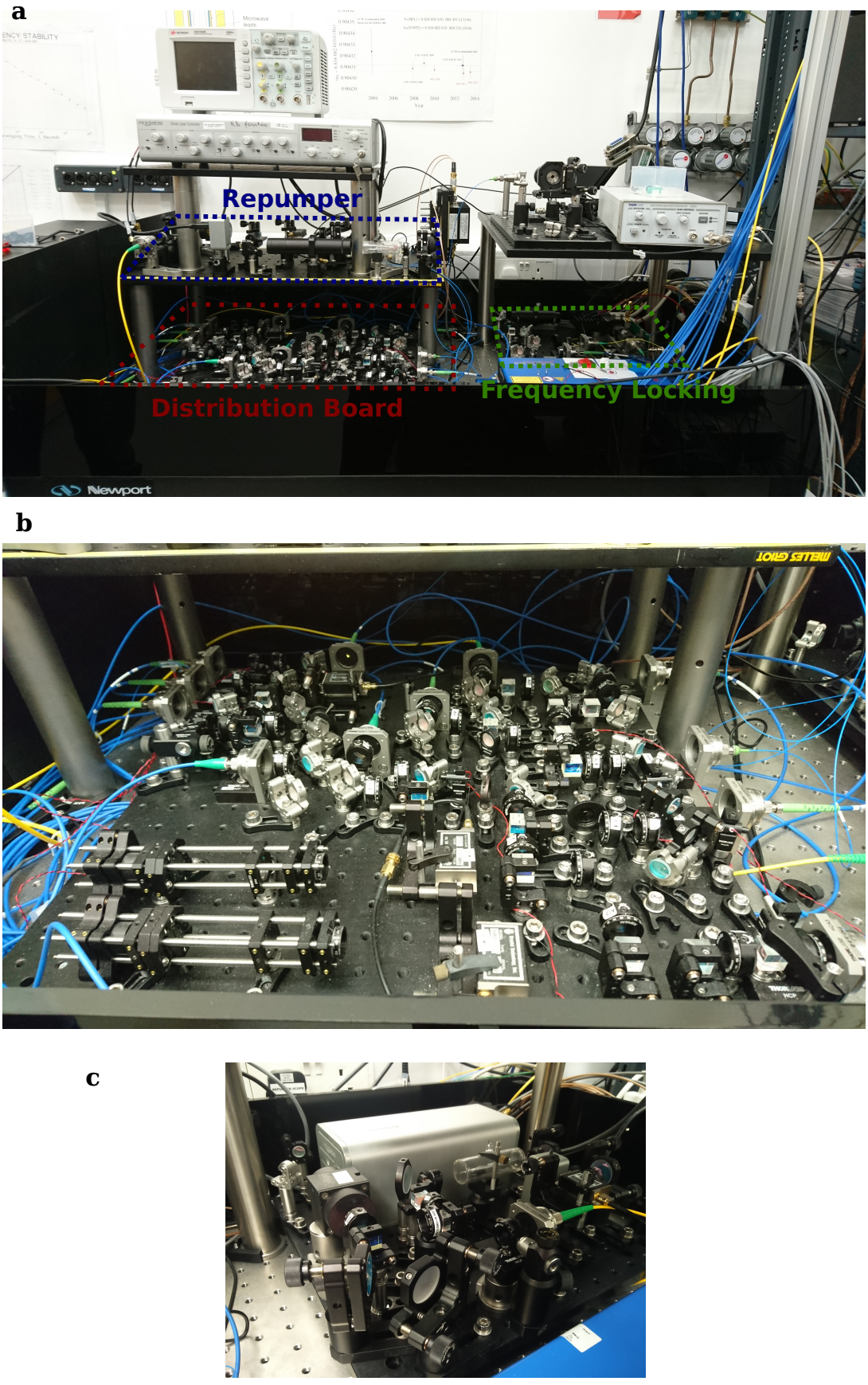

Figure 3.7: a) The optical setup to control the fountain is contained on three breadboards: one for the repumper laser locking; one for the frequency and intensity control (shown in b); and one for the locking of the primary laser (shown in c)

potential field-based device. The robustness of the setup can be highlighted by the breadboards being used on an optical table itself placed on a standard office table – that is, the usual optical table legs required for vibration isolation were not required.

Stable performance of the seed laser requires strong optical isolation to prevent back-reflections returning to the cavity. It is therefore important to minimise these by using, e.g., an angled collimator when coupling light into an optical fibre. The laser comes with an adjustable, internal optical isolator, based upon the Faraday effect, but this is in inadequate when used in conjunction with the tapered amplifier, which produces a broadband background of light in both directions, due to amplified spontaneous emission. This therefore necessitates the introduction of an additional optical isolator, providing 33 dB of isolation, for a total of 63 dB. Whilst this leads to a reduction in available seed and, hence, total amplified power, without it frequency stabilisation is impossible.

Frequency stabilisation is achieved by modulating the laser current at 250 kHz and sending a small fraction of the light to a rubidium cell (Figure 3.6). This light is first passed twice through an acousto-optical modulator (AOM), being shifted up in frequency by 90 MHz on each pass. Saturated absorption spectroscopy is then used to achieve a spectrum free of Doppler broadening and displaying the hyperfine peaks within the manifold, with the laser frequency being scanned by using a piezoelectric device to vary the external cavity at a rate of 10 Hz. A photodiode signal of this spectrum is fed to a controller (MOGLabs, DLC) which demodulates the input to produce an error signal, which allows for the frequency to be locked to a hyperfine transition. In this case the laser is locked to the ^{87}Rb $|5^2S_{1/2}, F = 2\rangle \rightarrow |5^2P_{3/2}, F = 3\rangle$ transition.

The controller allows for two forms of locking: 'slow' locking with control of the piezo; and 'fast' locking with control of the current. However, due to the fast and large frequency jump required for maximum cooling of the atoms during the optical molasses stage (see section 3.3.3), only the 'slow' lock can be used. This is an idiosyncrasy of the controller design, where the voltage generated by the external modulation is summed with the 'fast' locking voltage. The effect of this is to prevent the laser from re-locking to its original position after a frequency jump, if the fast lock is engaged. Nonetheless, a stable lock is achieved with only the feedback to the piezo engaged.

After amplification, the light is split into two paths, which are both shifted in frequency by 160 MHz from independent acousto-optical modulators (Gooch & Housego, 3080-122), bringing the total frequency detuning to -20 MHz. Two paths with independent acousto-optical modulators are used as one path is used for, amongst other things, the upper MOT beams and the other for the lower MOT beams (Figure 3.6). Having separate AOMs for these two arms, allows for their frequencies to be independently controlled, as is required for launching (see section 3.3.4). The frequencies for the AOMs are provided by direct-digital synthesisers (DDSs, Novatech, DDS8m), with their output controlled by directly altering the DDS output power and frequency, but also with a tunable solid-state RF attenuator (Mini-Circuits, ZMAS-3). Following this they are amplified to the experimental level.

The light for the LVIS and the lower MOT beams is coupled into single-mode polarisation-maintaining fibres, which are then split by a fibre-based splitter into three approximately equal outputs. The upper MOT beams each have a separate coupler and an additional half-wave plate and polarising beamsplitter combination. This allows the power of the upper beams to be manually tuned so as to achieve equal power in each of the beams of each opposing pair. There are two additional couplers from which light is delivered to the detection region and for state selection, respectively.

Shutters are installed at various key positions so as to ensure the complete darkness of the chamber when required. This is necessary because, although the RF is controlled before the amplifier, some power tends to leak through which is then amplified and results in some light being coupled to the experiment, even when the AOMs are nominally in their off-state. Additionally, any leaking light can have potentially fatal consequence as it is near resonance and therefore liable to interact with the atoms and break any established coherence. Shutters must be used in combination with the AOMs because their closing time is both considerably slower (order 100 µs) and subject to jitter (∼1 ms).

3.2.2 Repumper Laser

A second laser is required to repump any atoms which are returned to the $|F = 1\rangle$, rather than $|F = 2\rangle$ ground state (see Appendix A.1.2). The laser is consequently set to be resonant with the $|5^2S_{1/2}, F = 1\rangle \rightarrow |5^2P_{3/2}, F = 2\rangle$ transition.

A butterfly-package, distributed feedback (DFB) laser with an output power of 80 mW and a linewidth of 2 MHz is used for this purpose (Eagleyard, DFB-0780-00080). The package is mounted in a laser diode mount (Thorlabs, LM14S2) with in-built thermoelectric coolers (TECs) for controlling the case temperature. Temperature stabilisation (Thorlabs, TED200C) and current control (Thorlabs, LDC202C) are provided by off-the-shelf components. The PID feedback settings for the temperature controller were set using the Ziegler-Nichols method [99].

Whilst such lasers are very stable due to a lack of moving parts, they are very susceptible to optical feedback, so a 60 dB optical isolator is installed immediately after the output (Thorlabs, IOT-5-780-MP). Following this, the light is split on a polarising beamsplitter with the majority of the light being coupled into a fibre for use in the experiment. The remainder is coupled into a fibre-based electro-optical modulator (EOM), which provides modulation, preventing the need to directly modulate the laser current itself, and then passed through a rubidium fluorescence cell. An in-house board supplies the modulating signal as well as performing the demodulation to produce an error signal. The error signal is sent to a servo (Vescent, D2-125) which feeds back to a voltage modulation port on the main current controller. Due to the smaller signal size of the repumper manifold, the laser is actually locked to the cross-over peak between the $|F = 1\rangle \rightarrow |F' = 1\rangle$ and the $|F = 1\rangle \rightarrow |F' = 2\rangle$ transitions, which is larger and therefore provides a more stable lock.

The light to be used in the experiment is carried by polarisation-maintaining single-mode

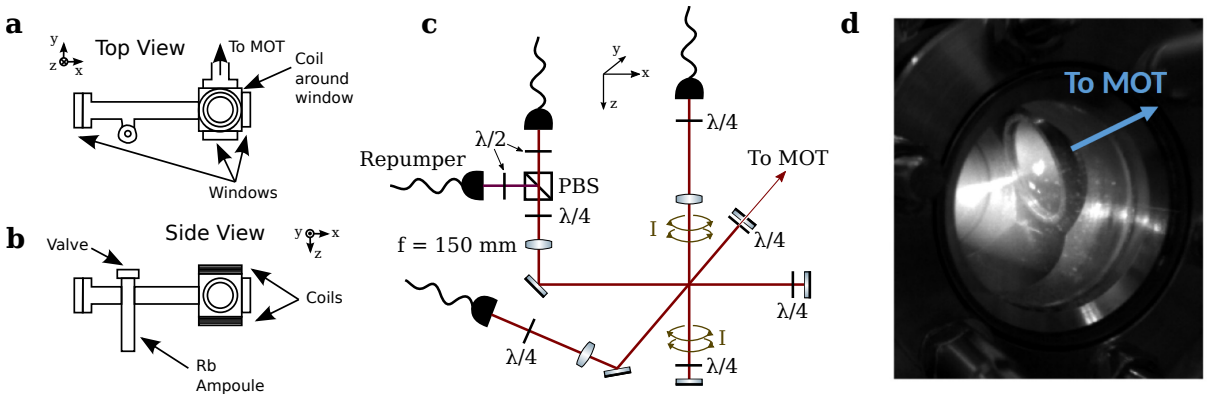

Figure 3.8: The chamber design for the low-velocity intensity source of atom viewed from the top (a) and from the side (b). c) The optical design: a retro-reflected MOT is formed by collimating the output beams with 150 mm lenses and overlapping them in the centre of the chamber. The repumper beam is overlapped on a polarising beamsplitter (PBS) with one of the cooling beams. One of the quarter-wave plate ($\lambda/4$) and mirror combinations has a hole through their centres pushing a continuous beam of atoms in the direction of the main MOT. d) An image of the LVIS in operation.

fibre to the main breadboard also used for the primary laser circuit (Figure 3.6). The light is first passed through an AOM which has the dual function of controlling the intensity of the light going to the experiment and of shifting the frequency up by 78.5 MHz, to bring it on resonance to the repumper transition. Following the AOM, the light is split into three parts and coupled into three separate fibres: one for the MOT; one for the LVIS; and one for the detection system. Each coupler is preceded by a shutter to provide total darkness when required, but also to allow some of these beams to be off, whilst others are on.

3.3 Experimental Sub-System Performance & Design

3.3.1 Low-Velocity Intense Source

The low-velocity intense source is effectively a standard magneto-optical trap, but with a central push beam [100, 101]. This is achieved by using a retro-reflecting configuration, but with the quarter-wave plate and mirror along the axis pointing towards the MOT chamber, having a small hole (1 mm diameter) drilled through the centre of them. This results in an imbalance of radiation pressure, which gives the atoms a longitudinal velocity, whilst remaining transversely cooled.

The three input optical fibres, each containing around 30 mW of power, are terminated and the light is allowed to expand in free-space before being collimated by a 150 mm lens and passing through a quarter-wave plate to produce circularly polarised light. These beams enter on three mutually orthogonal ports, before passing through the chamber and being retro-reflected by a mirror and passing, twice, through a second quarter-wave plate. The repumper light (~ 5 mW) is overlapped on a polarising beamsplitter with one of the cooling beams (Figure 3.8). The

requisite magnetic field is provided by two coils of 1 mm diameter copper wire, mounted upon the chamber and arranged to have currents of 2.5 A propagating in opposite directions (i.e. an approximate anti-Helmholtz configuration). Water cooling is provided by passing the same water used for the MOT coils through copper pipes mounted between the chamber and the coils, with an added layer of thermal paste.

As the purpose of the LVIS is to provide a cold flux of atoms for the MOT, the final alignment of the laser beams is achieved by experimentally tilting the retro-reflecting mirrors to achieve the maximum possible loading rate of the MOT [101]. The loading rate is measured by estimating the atom number of the magneto-optical trap as a function of time after turn on. The atom number is estimated by imaging the MOT onto a photodiode. To ensure, good alignment, a CCD camera is first used to bring a focussed image of the MOT onto an area smaller than the active region of the photodiode. The photodiode's voltage output is calibrated by making similar measurements with a power meter (which lacks the bandwidth to be used for the final measurement). This output can then be converted into an atom number (N) according to [73]:

$$N = \frac{8\pi \left[1 + 4\pi \left(\Delta/\Gamma\right)^2 + \left(6I_0/I_{sat}\right)\right]}{\Gamma \left(6I_0/I_{sat}\right) \delta\Omega} \eta V \tag{3.4}$$

where Δ is the angular frequency detuning of the MOT beams, Γ is the transition linewidth, I_0 the intensity of an individual MOT beam (assumed all equal), I_{sat} is the saturation intensity (isotropic pump field), $\delta\Omega$ the solid angle of the light collected by the photodiode, V the photodiode voltage, and η is the conversion factor between the photodiode signal and the optical power.

In conjunction with the LVIS, the loading rate of the MOT is observed to be around 10^9 atoms/s (Figure 3.9), over a broad range of experimental parameters (e.g. repumper intensity).

3.3.2 Magneto-Optical Trap

The MOT acts as the main source for the cold atoms in the experiment by combining the ability to simultaneously cool and trap the atomic sample (see Appendix A.3). It is made up of three mutually orthogonal pairs of counter-propagating beams with Gaussian radii of approximately 12.5 mm and intensities of $\sim$12 mW/cm^2 ($\sim 7I_{sat}$)[vi]. The magnetic field is provided by passing 7 A through copper wire coils, which are mounted directly around the conflat flanges and cooled by cycling 18 °C water. The two coils are connected in series, but with current circulating with opposing helicities. Although the two coils are identical, they do not produce a perfect spherical quadrupole magnetic field, as the radius of the coils is not equal to the separation between them (i.e. they are not ideal anti-Helmholtz coils). Nevertheless, the magnetic field, as calculated

[vi] For $\sigma^{\pm}$ transitions. Beams above saturation intensity are required to generate a sufficient number of transitions to cool the atoms whilst they remain within the beam overlap region. They are also less sensitive to misalignment.

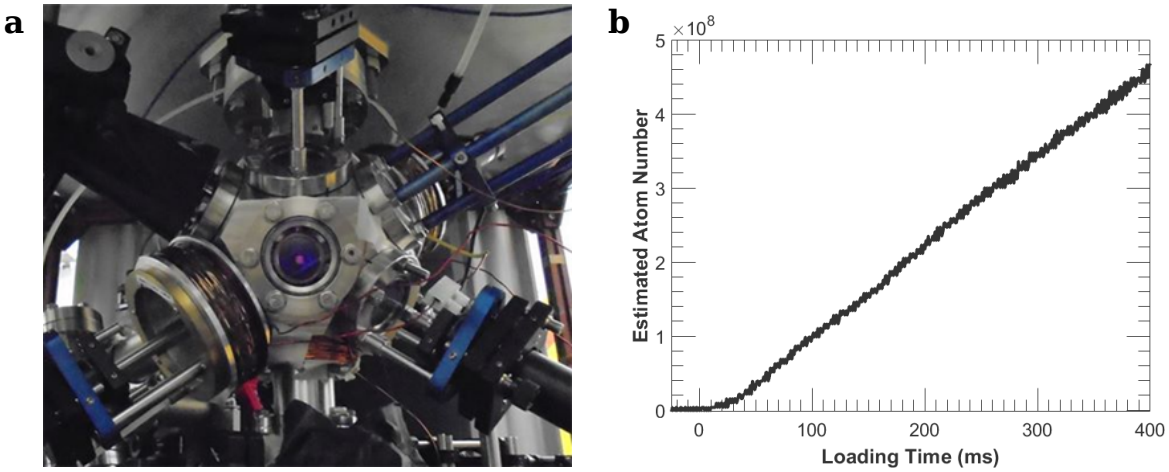

Figure 3.9: a) The magneto-optical trap as imaged with a commercial, digital camera (red dot in the centre of the chamber). b) The loading rate of the MOT as function of mutual turn on time of the MOT and LVIS – around 10^8 atoms are loaded per 100 ms. The atom number is calculated according to equation 3.4.

from the Biot-Savart law, is seen to produce the required gradients and trapping is achieved.

To achieve the outlined beam parameters, the MOT beams are constructed in a lens-tubing housing. Firstly, the optical fibres are terminated into fixed-length collimators (Thorlabs, F280APC-780), before passing through quarter-wave plates to produce circular polarisation. Finally, they pass through a Gallelian telescope, which expands them to their full size. Collimation is checked using a shearing interferometer (Thorlabs, SI500), with the second lens of the telescope being adjustable, which also ensures the approximate equality of the various beam radii in the MOT region. These collimation packages are mounted onto the chamber, but maintain tip and tilt degrees of freedom, allowing their overlap to be optimised (see section 3.3.3 for more detail).

When fully loaded the MOT is large and sufficiently bright to be clearly visible with the naked eye (Figure 3.9), containing approximately 10^{10} atoms. In the case of an experimental cycle, however, the loading time is limited to around 50-200 ms, giving closer to 10^8 atoms (Figure 3.9).

3.3.3 Optical Molasses

Following the MOT stage the atoms undergo a period of optical molasses – that is, the same laser configuration as the MOT, but without the applied magnetic field. During this process the atoms undergo further cooling via the Sisyphus and motion-induced orientation cooling mechanisms of polarisation-gradient cooling [102, 103]. These mechanisms take the atoms beneath the Doppler limit and towards the recoil limit (see Appendix A.4 for more information). The optical molasses stage is used to perfect the alignment of the beams, with slow, spherical growth of the molasses indicating good alignment. It should be noted that the optimal alignment isn't necessarily

perfect overlap of the beams, as this can lead to a standing wave being established. Such a standing wave pattern can be readily observed, as it induces an observable fringe pattern across the molasses, as seen in Figure 3.10. The origins of these interference effects isn't perfectly understood, but there will be contributions from the interference of the two beams (which are derived from the same, coherent source), but each beam will also interfere with back-reflections from the various surfaces it passes through. These will be exacerbated for very good beam overlap, as reflections from the other beam's optics will now return close to exactly along the beam path, and also because good alignment is likely to require the beams entering normal to the windows.

The key experimental detail, however, is the attainment of a stable and cold sample of atoms in the central region of the chamber. A good alignment strategy is therefore to observe this fringe pattern, before tilting both the beams away in the same direction, maintaining a strong region of overlap over the atomic population.

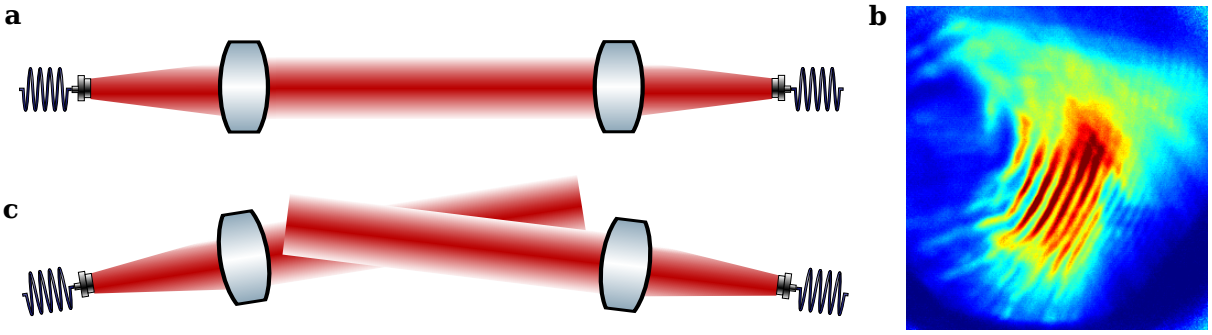

Figure 3.10: a) When the counter-propagating beams for the molasses are perfectly overlapped, interference effects lead to instabilities and a pattern reminiscent of a standing wave, as shown in b). c) The solution is to tip both the beams in the same direction, so that they maintain good overlap in the important central region, but the interference effects are avoided. The amount the beams are misaligned from perfect overlap is greatly exaggerated.

3.3.3.1 Ambient Magnetic Field Minimisation

Good optical molasses, attaining the lowest possible temperatures, requires the absence of any magnetic fields, to allow for maximum state degeneracy and optical pumping during the polarisation-gradient cooling stage. Consequently, some experiments therefore place permanent passive magnetic shielding around the MOT region, allowing temperatures approaching 2 μK to be observed [104]. Here the ambient magnetic field is minimised by a set of three mutually perpendicular quasi-Helmholtz coils. These provide an approximately homogeneous, static magnetic field, which is tuned by independently altering the current running through the different coils. Due to the imperfections of the applied field and the inhomogeneity of the Earth's field, it is only possible to cancel the field at one particular point. This is achieved by performing magnetic spectroscopy on the molasses, which ensures that the coils are setup to minimise the magnetic field at the point of the molasses.

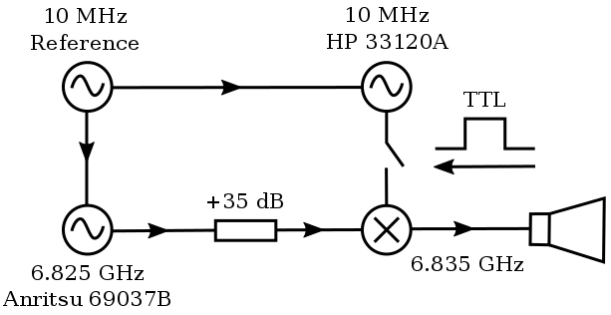

Figure 3.11: Schematic of the RF source for the microwave horn. An RF generator (Anritsu, 69037B) produces 6.824 GHz which is amplified and then mixed with an additional 10 MHz when a TTL pulse is applied, bringing the microwaves to the atomic resonance on demand. Both sources are referenced to the 10 MHz reference (see section 4.1.3 for details)

Magnetic spectroscopy is performed by illuminating the molasses with a pulse of microwaves from a microwave horn[vii], with the duration and power of the pulse selected to drive an approximate π pulse. The microwaves are sourced from an RF generator (Anritsu, 69037B) and amplified (Mini-Circuits, ZVE-3W-83), with the pulse duration being controlled by mixing in a 10 dBm, 10 MHz signal from a second frequency source (Hewlett-Packard, 33120A) when a TTL pulse is applied (Mini-Circuits, ZYSW-2-50DR). That is, the horn is continually emitting microwaves, but this is held 10 MHz from resonance, except when desired (Figure 3.11). Both frequency sources are clocked with the 10 MHz source from the maser (see section 4.1.3) for frequency reference details).

Spectroscopy is performed by scanning the frequency of the applied pulse and observing the change in hyperfine ground state population. The molasses are initially prepared to be almost entirely in the $|F = 2\rangle$ state, by leaving the repumper laser on for around a millisecond after the main beams have been turned off (the precise timing depends upon the shutter jitter). The atoms are prepared equally, however, in all the different magnetic sub-states, so the scan reveals the Zeeman splitting (-0.70 MHz/G [73]) caused by the residual, ambient magnetic field (Figure 3.12). This splitting is measured for different current settings and the field minimised, until the different hyperfine peaks become degenerate, as shown in Figure 3.12. This peak is noticeably wider in frequency than the case for a $|F = 2, m_F = 0\rangle \rightarrow |F = 1, m_F = 0\rangle$ transition, highlighting that the field cancellation is not perfect: there is both a small residual field, but moreover, as the ambient field is not uniform, there are inhomogeneities in the field across the molasses.

It should be noted that this process is repeated occasionally, as the ambient field changes and drifts with time, due to differences in the Earth's field and the laboratory environment (e.g. electrical components)[viii].

[vii] It is standard in the field of atomic physics to refer to these wavelengths as microwaves, though they are more generally regarded as belonging to the radio-frequency band in other fields.

[viii] For example, in the case shown in Figure 3.12, the non-degenerate spectrum is using the previous current settings for producing the minimum magnetic field, based upon data taken six weeks previously.

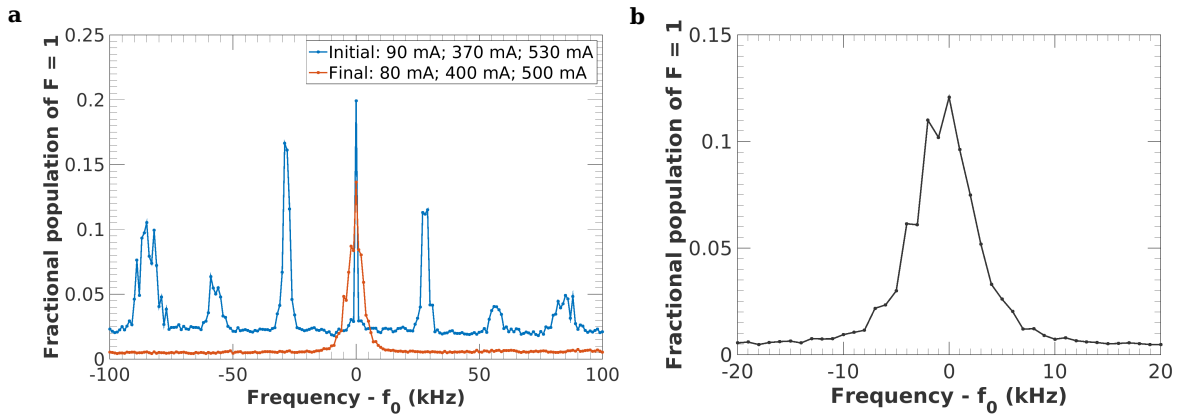

Figure 3.12: (**a**) Spectra taken with the microwave horn from before (blue) and after ambient magnetic field has been minimised at the point of the molasses. The currents in the legend refer to the east/west, north/south and vertical components, respectively. (**b**) A zoom of the final, central peak – it is broadened compared to the $|F = 2, m_F = 0\rangle \rightarrow |F = 1, m_F = 0\rangle$ transition due to there being some residual magnetic field and inhomogeneities in the field across the molasses.

3.3.3.2 Temperature Measurements

Following magnetic field minimisation the lowest temperatures achievable by polarisation-gradient cooling can be reached. In this configuration of the fountain, the lowest achieved repeatable temperatures were typically in the region of 5 µK, though 3 µK was previously achieved in the frequency standard [63].

The main method of measuring the temperature of the atoms was to image the ballistic expansion of the cloud following release from the molasses stage, which can be used to deduce a temperature from equation 3.1 (Figure 3.13). The cloud is imaged onto a CCD camera (Photo Lines, pco.pixelfly usb) via a telescope and the time between release and a measurement is varied, with a TTL pulse triggering the camera to ensure good timing accuracy. The collected images are analysed by fitting Gaussian distributions to the summation of the horizontal and vertical directions. The σ values of two different directions are independently fit to equation 3.1, giving an idea of the uniformity of the expansion rate (temperature).

Each temporal data point requires a separate experimental sequence to be run, as the image of the atomic cloud is captured via fluorescence imaging which destroys the cloud. However, due to the fast loading enabled by the LVIS, all the data can be gathered and the analysis performed in less than a minute, allowing parameters to be systematically varied to achieve the lowest temperature. For example, the additional frequency detuning selected for the molasses sequence was determined empirically by temperature minimisation, with a final detuning of around -140 MHz being used for the polarisation-gradient cooling stage.

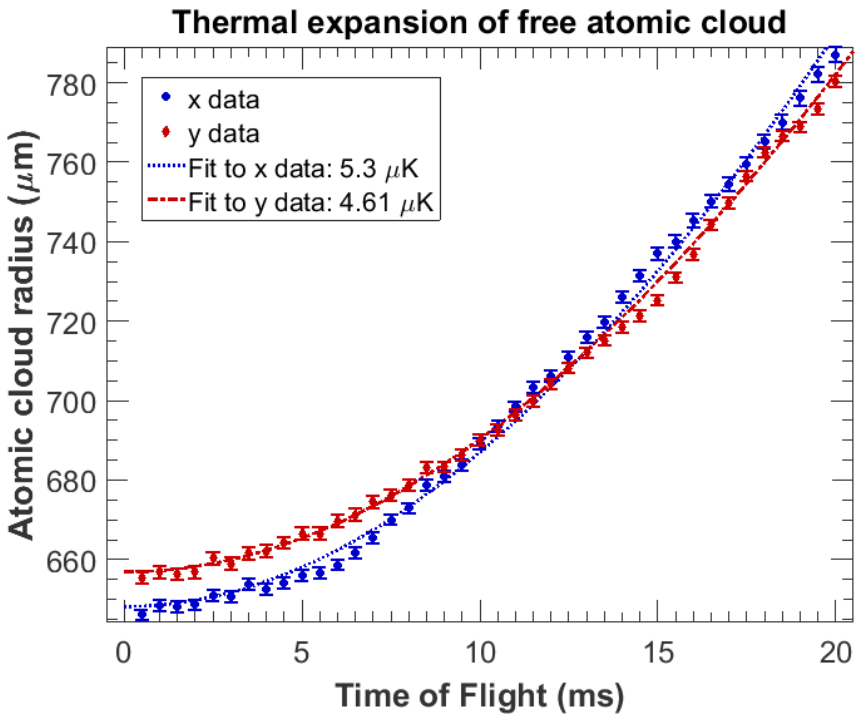

Figure 3.13: The temperature as measured from fitting the ballistic expansion to equation 3.1. Each point represents a different run of the experiment and the error bars are 90% confidence limits on the Gaussian fits to the cloud size.

3.3.4 Launching

The atoms are launched in a moving molasses configuration [105], allowing the atoms to be launched without the low temperatures from the polarisation-gradient cooling being lost. An imbalance in the radiation pressure between the upper and lower MOT beams is established by independently changing the frequency detuning of the two beams. The frequency sent to the AOM controlling the upper beams is decreased, increasing the absolute detuning from the base 20 MHz in the MOT. Conversely, the frequency going to the AOM controlling the lower beams is increased. These frequency changes occur linearly in equal steps 100 μs apart, so as to make the acceleration as adiabatic as possible. After this, the atoms undergo the polarisation-gradient cooling procedure described above, with care taken to make this process sufficiently short, so that the atoms haven't left the influence of the beams.

The precise settings for the launch parameters is found by varying the settings in a heuristic manner, until the largest number of cold atoms is determined to return. The final settings were for the frequencies to be linearly ramped over 2 ms, 1 ms of further expansion in far-detuned beams, and for adiabatic ramping of the power over a final 1 ms (Figure 3.14).

The fractional number of returning atoms is estimated by a simple model of the the detection system (see section 3.3.7 and Figure 3.20), which calculates the expected number of scatters for an expanding and accelerating cloud, using the measured experimental parameters. For large

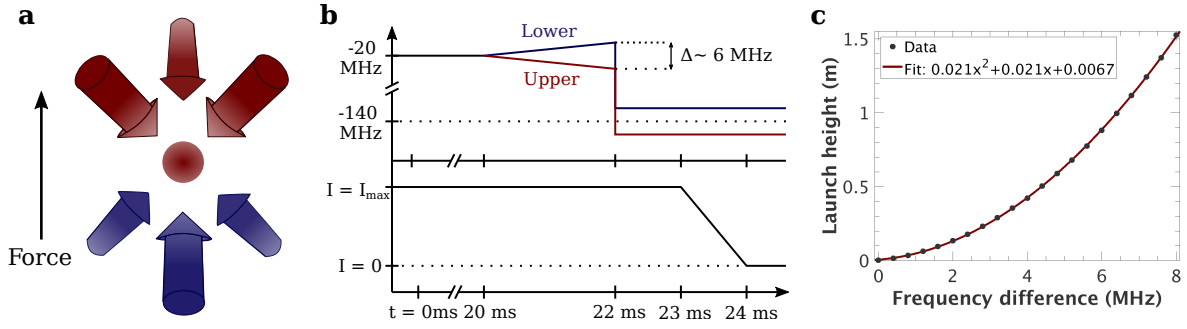

Figure 3.14: a) A moving molasses configuration launches the atom by moving the frequency of the lower beams closer to resonance and the opposite for the upper beams. b) The frequency (top half) and intensity control during the launch sequence. The 20 ms is for the eddy currents to die down. c) The launched height as a function of the frequency difference between the upper and lower beams.

launch heights, it is estimated at approximately 50 %, which compares reasonably with other systems [65].

Once the optimum settings have been established, it is possible to calibrate the launch by measuring the time taken for the atoms to arrive at the detection system. The launch height is controlled by the size of the frequency difference between the upper and lower beams. As the final interferometer will use velocity-selective pulses for state selection (see section 5.2.1) – which will precisely determine the vertical velocity and thus the launch height – the launching of the cloud here needs simply to be of sufficient accuracy to allow as many atoms as possible to be selected.

A functioning launch can be used as a coarse means of aligning the fountain to the vertical direction. For a vertical launch, the number of atoms returning to the detection system is maximised when the fountain is aligned along the vertical axis. Alignment can therefore be performed by systematically tipping and tilting the whole fountain to maximise the detection system. To track the angular position of the fountain, a small amount of laser light was fired from the top of the fountain across the longest axis of the laboratory, giving a travel distance of around 8 m and providing a reference tip and tilt position for each detection measurement. This method allowed the fountain to be vertically aligned to the milliradian level, with precision vertical alignment of the Raman beams performed using a different method (section 4.3.3).

3.3.5 State Selection with a Microwave Horn

The microwave horn used for ambient magnetic field spectroscopy (section 3.3.3.1, Figure 3.12) can also be used for preparing the atoms in an initial magnetic sub-state. This is especially useful when originally establishing and characterising the Raman beams and can be used in any case with co-propagating Raman beams, which like the microwaves, address the whole atomic velocity class (see section 5.1).

Specifically, the interferometer operates on the two $m_F = 0$ hyperfine ground states, which

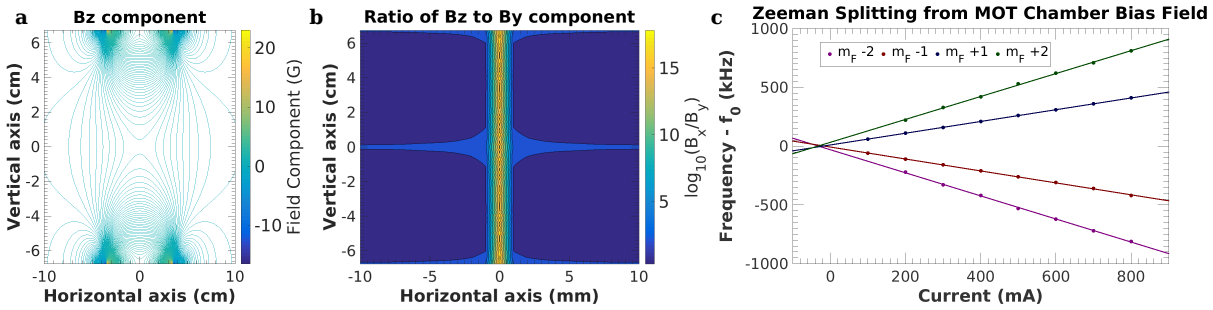

Figure 3.15: a) The vertical component of the magnetic field for the MOT-region bias coils calculated from the Biot-Savart law. b) The calculated ratio of the vertical to horizontal components for the bias field, showing a strong quantisation axis in over several millimetres. c) The bias field as measured using magnetic field spectroscopy.

are insensitive to the magnetic field strength to first order. As the ambient magnetic field has been approximately cancelled, an external magnetic field is applied after the launch to both lift the sub-state degeneracy and provide a known quantisation axis (Figure 3.15), which is otherwise not well defined (see discussion in section 3.3.5.1 below). The magnetic field is produced by using a solid-state switch to temporarily run 400 mA of current through two sets of 0.8 mm diameter copper wire wrapped in 25 loops directly around the top and bottom of the MOT chamber and held in place by glass tape. The field as modelled by the Biot-Savart law is in reasonable agreement with the field as determined from the observed Zeeman splitting, despite the inelegance of the method (Figure 3.15). The calculated magnetic field exhibits a strong vertical directionality across the region of the molasses.

A pulse of microwaves is applied for 800 µs, as controlled by a TTL pulse (Figure 3.11), with the power and frequency of the microwave selected so as to achieve the maximum possible transfer of atoms (a π pulse), which is 20 % due to the five different initial magnetic sub-states (Figure 3.16) and with a frequency shifted around 37 Hz from the unperturbed value mainly due to the second-order Zeeman shift. Following this, the population is cleaned by the application light resonant to the $|F = 2\rangle \rightarrow |F' = 3\rangle$ transition. This light enters horizontally approximately 20 cm above the MOT position (section 3.1.1.3), with the radiation pressure meaning only those atoms transferred to the $|F = 1, m_F = 0\rangle$ state and a small amount of background $|F = 1\rangle$ from inefficient repumping remaining[ix]. The laser is frequency shifted to resonance by either jumping the laser current or by switching the DDS frequency. The latter is more stable, but leads to a reduction in usable power, though both methods are suitable for this purpose (cf. section 3.3.7).

This method of state selection gives a fidelity of approximately 95 % or greater.

[ix] For experiments in which the atoms or either dropped or launched beneath the dedicated ports for the state selection beams, a pulse of 800 µs duration is applied through one of the spare ports on the MOT chamber, 100 µs after the end of the microwave pulse.

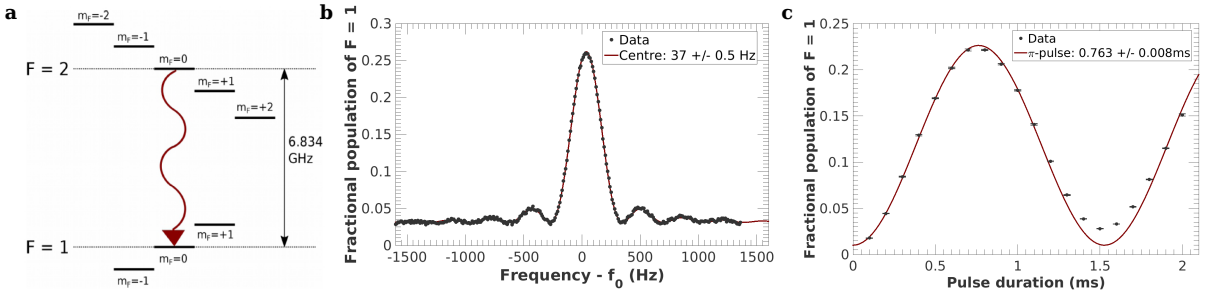

Figure 3.16: a) State selection is performed by lifting the degeneracy between the states and applying a π pulse resonant to the $|F = 2, m_F = 0\rangle \rightarrow |F = 1, m_F = 0\rangle$ transition. High-fidelity state selection is ensured by removing the remaining $F = 2\rangle$ atoms. b) The result of scanning the frequency a π pulse across the resonance – the offset is due to the second-order Zeeman shift (fit to equation 2.20). c) Varying the pulse duration to observe Rabi oscillations, allowing the precise π pulse duration to be found (fit to equation 2.18).

3.3.5.1 Establishing & Maintaining a Quantisation Axis

As mentioned, state selection requires a quantisation axis to be provided, but it is equally important to maintain this axis following state selection until and throughout the interferometry measurements. In particular, for an axis provided by a magnetic field, it is particularly important to prevent any crossing points and inversions in the magnetic field, which would lead to Majorana spin flips and the consequent degradation of the fidelity of the prepared state [106, 107]. It is therefore necessary to provide a continuous magnetic field along the vertical axis of the fountain whilst the atoms are in flight. Clearly, this is provided by the solenoid in the interferometry region, but it is necessary to provide additional coils along the axis. Moreover, the three layers of magnetic shielding provides an additional complication as the solenoid is entirely contained within the innermost layer. Without any additional coils, the quantisation axis would be completely lost every time the atoms entered the next level of shielding and the state preparation rendered worthless by spin flips. This is countered by placing three sets of coils, connected in series, at the entrance point of each shielding layer. These coils run a small, permanent current of around 10 mA.

There are therefore sets of current coils to be aligned: the solenoid; the additional coils at each magnetic shielding entrance; and the coils on the main chamber, which consist of, all connected in series, the aforementioned state selection coils for lifting the Zeeman degeneracy and similar coils around the state cleaning beam cross. Alignment is performed by using the Raman beams to transfer the atoms which have been prepared into the $|F = 1, m_F = 0\rangle$ state to the $|F = 2, m_F = 0\rangle$ state. In the case of good alignment, something approaching 100 % transfer should be achievable, whilst for improperly aligned coils, the atoms will be distributed across all the available sub-states and only 33 % of the atoms are transferred. This allows the various quantisation coils to be rapidly synchronised.

3.3.6 Magnetic Shielding & Solenoid

It is desirable to provide an equal magnetic field throughout the whole interferometry region to reduce the deleterious effects of a variable frequency shift caused by the second-order Zeeman effect. This is particularly true when making gravity gradient measurements, which necessitate making simultaneous measurements on atoms at different heights in the chamber. It should be emphasised, however, that these effects are predicted to be small (section 2.4.2). Nevertheless, the current for the solenoid is therefore provided by a stable current supply (Keithley, 6220), which is run at 100 μA, producing a magnetic field of around 280 nT.

The uniformity of the magnetic field inside the chamber is most easily probed by measuring the Zeeman splitting at different heights within the interferometry region. Although, this was previously measured with high accuracy for the frequency standard [63], it was important to reproduce these results as the mu-metal shielding was repeatedly knocked during the vacuum reconstruction and baking processes, which can have the adverse effect of realigning the local ferromagnetic structure.

Mapping of the Zeeman splitting was performed by illuminating the atoms with co-propagating Raman beams at different times during a launch sequence (see Chapter 4 and section 5.1 for details of the Raman beams). The atoms were initially prepared in the $|F = 2\rangle$ state, but without any particular magnetic sub-states being selected, and launched to a height slightly above 1 m. As co-propagating Raman beams drive transitions where $|\Delta m_F| = 0$, a scan of the Raman beam frequency difference produces three resonance peaks. These three resonance peaks were simultaneously fit using a linear superposition of equation 2.20 with three separate resonant values, as shown in Figure 3.17. From this fit, the Zeeman splitting can be determined and the magnetic field strength approximated. As is clear from Figure 3.17, the magnetic shielding is functioning well and the magnetic field produced by the solenoid is extremely uniform, being previously measured at 0.36 nT across the interferometry region [63]. Furthermore, for these test experiments, the current through the solenoid was increased from its standard experimental value to 400 μA, so that the Zeeman splitting became sufficiently large for three individual peaks to be observed. This will tend to increase the absolute size of any inhomogeneities caused by the solenoid, as such inhomogenities tend to scale with field strength (i.e. $\delta B \propto B$).

3.3.7 State Detection

In an atom interferometer based upon pulsed Raman beams, the signal is the relative population of the two hyperfine states to which the beams are coupled. In ^{87}Rb, this requires the normalised populations of the $|F = 1\rangle$ and $|F = 2\rangle$ states to be measured. Here, this state detection is performed by measuring the relative fluorescence of the atoms as they pass through two flat beams of resonant light at the bottom of the chamber. The upper beam is used for detecting and blowing away atoms in the $|F = 2\rangle$ state, whilst the lower beam then detects the remaining atoms, which are in the $|F = 1\rangle$ state for a properly setup system. The fluores-

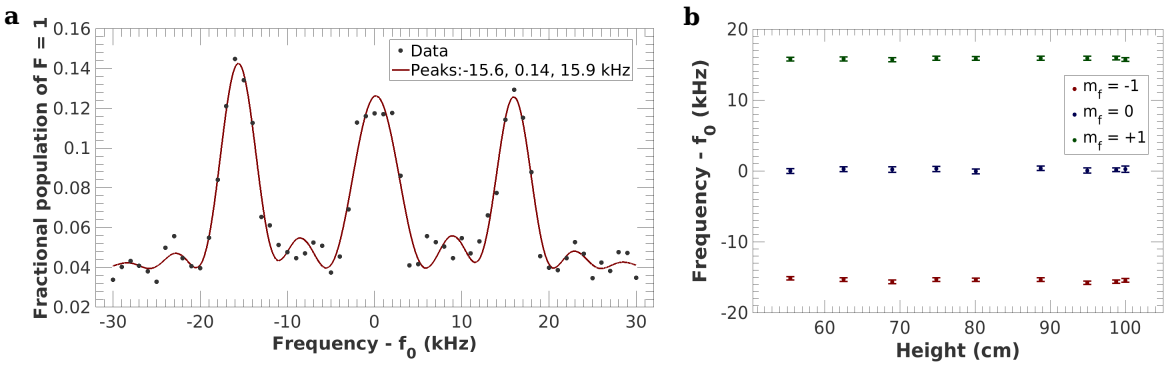

Figure 3.17: The magnetic field in the interferometry region as measured by Zeeman splitting by using co-propagating Raman beams. a) Three peaks, representing the $\Delta m_F = 0$ transitions, are simultaneously fit and b) the Zeeman splitting plotted by using the centre of these resonances (error bars 90 % fit confidence limits). The splitting and thus the magnetic field is very constant along the vertical axis, showing good shielding and solenoid performance.

cence from each beam, which is proportional to the number of atoms in each state, is imaged onto a photodiode (Hamamatsu Photonics, S3590-08) allowing normalised populations to be determined. A schematic of the detection system is shown in Figure 3.18.

The detection light for both states is sourced from the same polarisation-maintaining fibre, which is, after collimation, first cleaned in polarisation using a polarising beamsplitter. After this, 1 % of the beam intensity is reflected by a beamsplitter onto a variable gain photodiode, the signal of which is used for stabilising the power via a commercial PID system (Stanford Research Systems, SIM960) which modulates the voltage going to the controlling AOM, reaching a stability level of around 4 parts in 10^3 (Figure 3.18). This combination produces a beam of fixed polarisation and intensity, allowing reliable and repeatable population measurements both during a single experiment and from shot to shot. Good polarisation stability is important because the splitting between the two detection beams is also performed using a polarising beamsplitter, meaning any variations in polarisation will be translated as variations in intensity and therefore affect the measured state populations.

Additionally, it is important for the frequency to be stabilised, as the scattering rate is a function of the frequency detuning from the resonance. As described above, changing the laser frequency by jumping its current leads to a drift during its unlocked state (i.e. during a detection period) and the precise frequency shift will also depend upon the ambient conditions. It is therefore preferable to alter the laser frequency by shifting the AOM frequency, which can be precisely controlled. The disadvantage of this method is the diffraction efficiency of the AOM decreases away from 80 MHz and this problem is exacerbated by the light undergoing a double pass through the AOM. The optimum frequency is therefore determined by empirically tuning the AOM frequency to find the maximum possible scattering rate. This resulting in a frequency of -1 MHz detuning being used. It should be noted that experiments often use detection light with frequencies negatively detuned from the resonance, as the cooling force provided by such

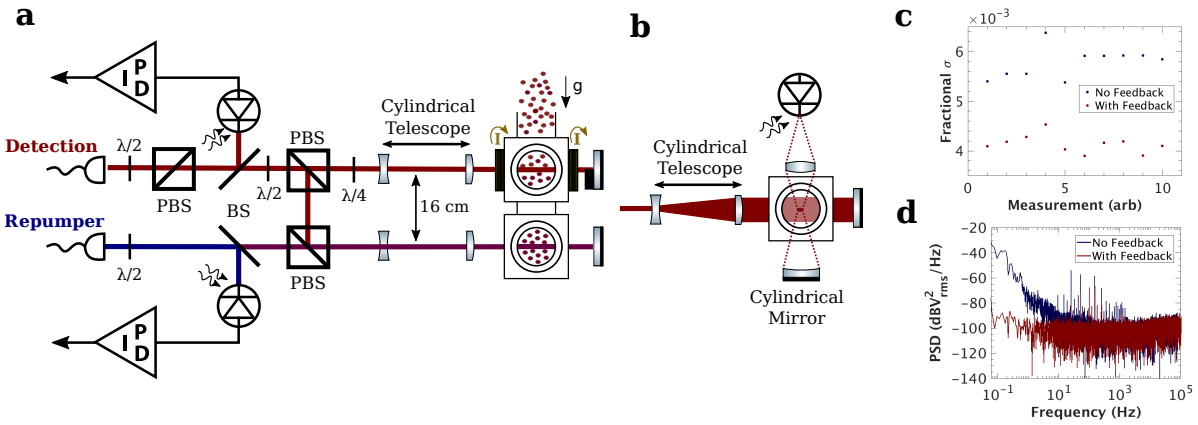

Figure 3.18: Detection setup as viewed (a) side-on and (b) from above. Detection light is cleaned in polarisation before being split into two channels. Both channels are expanded into horizontal beams with one each for $|F = 1\rangle$ and $|F = 2\rangle$ detection. For $|F = 1\rangle$ a small amount of repumper light is overlapped with the detection light. A radiation pressure imbalance and 16 cm separation, ensures low cross-talk between the two channels. A small fraction of light from both beams is picked-off for power stabilisation, which leads to an approximate one-third reduction of the standard deviation of the intensity during a detection pulse (c). The main improvement, however, is preventing drift (d), which ensures the intensity is constant for every shot.

a setup can increase the total yield of light collected.

After the stabilisation optics, the light is, as mentioned, split into two separate beams by a polarising beamsplitter, with the relative splitting set by a half-wave plate. The splitting ratio is set so that equal signals are produced by the same number of atoms in each detector. To achieve this, only atoms in the $|F = 2\rangle$ state are detected – first, in the upper detector, and then in the lower detector, with the upper beam blocked. The waveplate is adjusted until these two signals are equal in magnitude. Repumper light, power stabilised at the μW level in the same manner as for the main detection light, is overlapped with the lower detection beam to pump the $|F = 1\rangle$ atoms to the $|F = 2\rangle$ state.

Hitherto cylindrically symmetric, the beams pass through Galilean cylindrical telescopes which expands their horizontal component by a factor of five to a Gaussian diameter of 30 mm, with irises used to prevent any clipping on the windows, which would lead to irreducible background. As each detection beam contains around 5 mW of power, this results in the beams operating above saturation intensity. This results in the beam undergoing power broadening, resulting in an effectively flatter beam as viewed by the atoms (Figure 3.20). Whilst this ensures good spatial coverage of the detection light across the atom cloud, using a higher intensity increases the background irrepressible background fluctuations, which scale linearly with intensity. However, as the thermal expansion of the atom cloud and atom number are major limitations of the current experiment (see section 5.2.3), operating above saturation intensity to maximise the number of collected photons is the preferred method.

These cylindrical beams are retro-reflected to both double the expected scattering and to

prevent the atoms being prematurely pushed from the detection region by radiation pressure. The bottom section of the upper retro-reflecting mirror is blocked to create an imbalance that pushes the $|F = 2\rangle$ atoms away and prevents their being detected in the second detector. This configuration results in considerably less than 1 % of $|F = 2\rangle$ atoms being detected again in the $|F = 1\rangle$ channel.

The upper beam operates on a closed transition to prevent atoms falling into the $|F = 1\rangle$ state and being erroneously detected in the lower detector, but also to increase the total number of possible scatters (as atoms which fall into the $|F = 1\rangle$ state become dark). For this reason, prior to the cylindrical telescope, the upper beam is passed through a quarter-wave plate to rotate its polarisation to be circular, meaning that it will only drive σ transitions, for which $|\Delta m_F| = 1$. In the case of σ^+ polarisation, only transitions which alter m_F by $+1$ are allowed, so the atoms will be pumped into the $|F = 2, m_F = 2\rangle$ state. As the $|F = 2, m_F = 2\rangle \rightarrow |F' = 3, m_F = 3\rangle$ transition is truly closed, this has the desired effect of increasing the size of the detection signal and of reducing spurious $|F = 1\rangle$ detections[x]. A quantisation axis is provided by using a set of Helmholtz-like coils, attached around the windows of the upper region of the detection chamber, to produce a magnetic field along the beam axis. The quarter-wave plate angle and quantisation coil current are both set by experimentally maximising the detected signal.

The florescence is imaged using a commercial objective (Zeiss, Distagon 2.8/25 ZF IR), with adjustable focal length and back-focal aperture, and by a concave mirror positioned at the opposite window, which increases the effective solid angle of the detected light. Good alignment of both the objective system and the mirror is ensured by first imaging the falling cloud onto a CCD camera, before replacing the camera with the photodiodes. Frequency filters and adjustable apertures are placed between the objective and the photodiodes to reduce the effects of background light. Low-noise amplifiers amplify the signals by 20 dB prior to read-out, which suppresses the relative effect of any additive read-out noise.

These signal are converted into normalised hyperfine state populations, as required for interferometry, by one of two means. The primary method employed is to define two regions for each detection channel: a signal region; and a background region (Figure 3.19a). The signal region encompasses the region at which the atoms pass through the detection beam and the background region a subsequent period, and the signal size is determined by simply subtracting the mean of the background region from the mean of the signal region. The durations of both regions are chosen so that any 50 Hz noise will be averaged to zero across the whole period, with 80 ms for the signal and 40 ms for the detection employed in general.

Alternatively, the signal can be fit to a skewed Gaussian. This provides a better fit to the observed signal than a standard Gaussian distribution, which fails to adequately account for the observed signal distribution's tails, as shown in Figure 3.19b. This method is especially useful

[x]The same logic applies to σ^- polarisation but with the relevant transition being $|F = 2, m_F = -2\rangle \rightarrow |F' = 3, m_F = -3\rangle$.

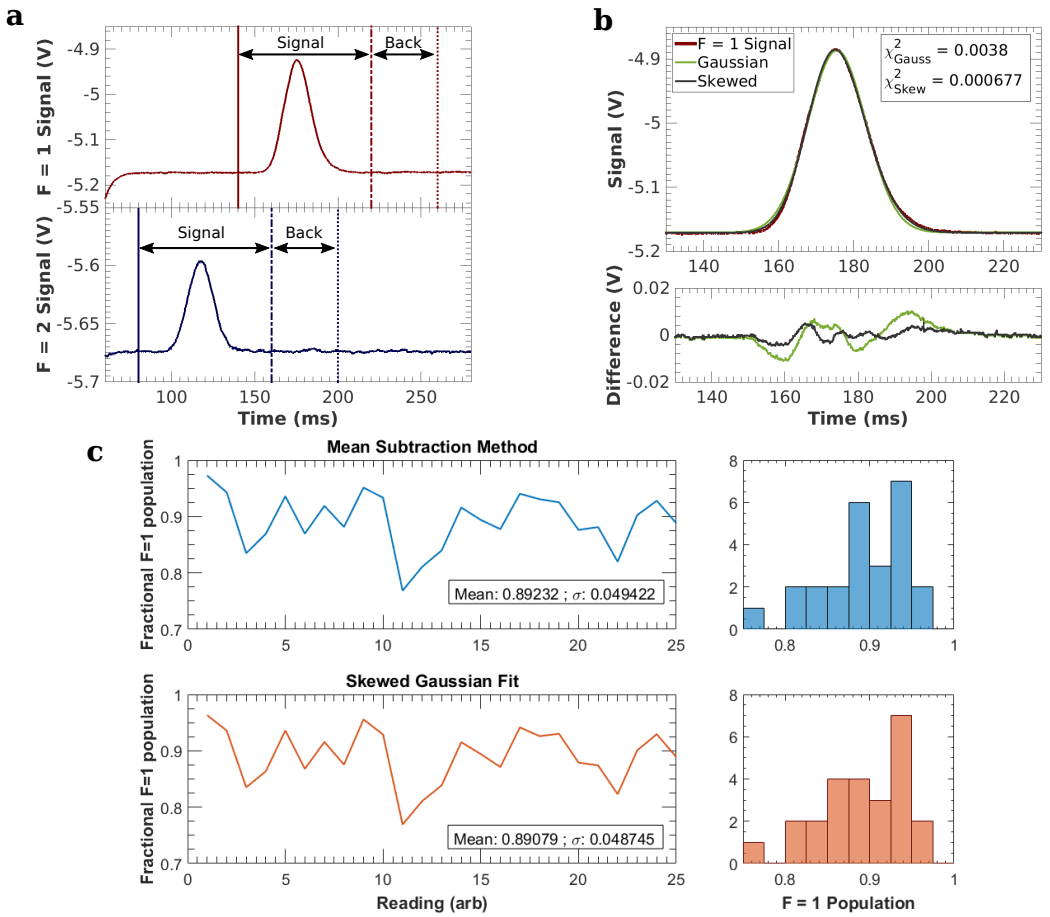

Figure 3.19: a) The detection signal can be converted into state populations by a simple background-subtraction method, or (b) by fitting to a skewed Gaussian. c) For a high number of atoms, they give very similar results as shown, so the simpler background-subtraction method is preferred. For small signals, the fitting method is more robust.

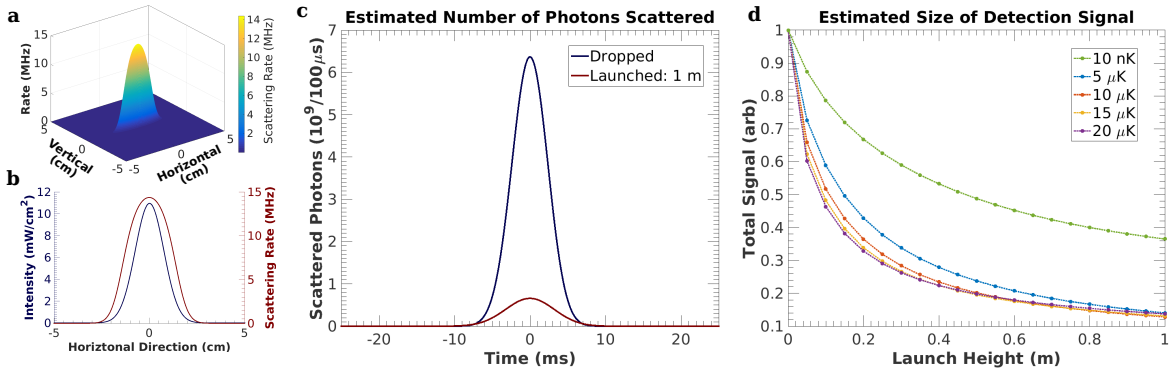

Figure 3.20: a) A simple model of the detection system can be performed by calculating the scattering rate of the beam. b) As the beam is above saturation intensity, there is significant power broadening and the scattering rate (right line, right axis) is more homogeneous across the beam than the Gaussian intensity profile (blue line, left axis). c) The detected signal is seen to significantly decrease with launching, as estimated here with 10^7 atoms at 5 μK integrated in 100 μs sections. d) This is mainly due to the thermal expansion – even at a very low temperatures (10 nK), the signal is more than halved.

for low-intensity signals as a linear (or higher-order) offset can be set to account for any drift in the observed background, which can result in results which aren't physical in the background-subtraction case. For cases with large signals, the improvement in using the fitting method is only minimal (Figure 3.19c), but is computationally far more intensive, currently requiring significant post-processing time, whereas the method of taking the mean and subtracting the background gives results effectively immediately.

To better understand the behaviour of the detection system, a simple model was devised (Figure 3.20). Here the scattering rate expected was calculated for the experimental parameters, taking into account not just the detection beam parameters, but also the fountain geometry, the launch height and the atom temperature. The expected signal was taken to be proportional to the integrated number of scattered events, with all effects of the detection photodiode, subsequent electronics and read-out ignored. Nevertheless, the results are still instructive for evaluating performance, being used to estimate the efficiency of the detection launch (section 3.3.4 by comparing the experimental decrease in signal for atoms which launched rather than for those which dropped, to the calculated decrease in scattering rate (Figure 3.20c). The model also shows that this decrease in signal is dominated by the increased velocity with which the atoms pass through the detection region, rather than by thermal expansion, at least within the region of experimentally attainable temperatures. Even at the very low temperatures attained by gases at quantum degeneracy, which observe minimal thermal expansion, the expected detection signal is more than halved (Figure 3.20d). A potential future upgrade could therefore to be to place the detection system above the MOT chamber reducing the atomic speed at the time of detection and thus increasing signal.

3.4 Launching Multiple Clouds

The gravity gradiometer which is the ultimate aim of the current incarnation of this atomic fountain, requires interferometry to be performed at two different heights simultaneously within the same system, if it is to utilise its potential advantages over classical systems. Whilst there are multiple ways to achieve this, such as loading two clouds at two independent heights [27], or by splitting a single launched population [29], here the intention is to launch two clouds in an independent manner. Again, this can either be achieved by juggling the clouds to maximise the loading time [104], or by loading and launching the second cloud whilst the first cloud is on the rise. The difference between these two schemes is highlighted in Figure 3.21.

The second scheme is favoured, as it reduces the total experimental time and thus increases device sensitivity, and is the one pursued and demonstrated in this thesis. It is only possible due to the rapid loading enabled by well-optimised cold atom sources, such as the LVIS (section 3.3.1). Nevertheless and as discussed below, it presents considerable challenges, which have yet to be fully resolved for this experiment.

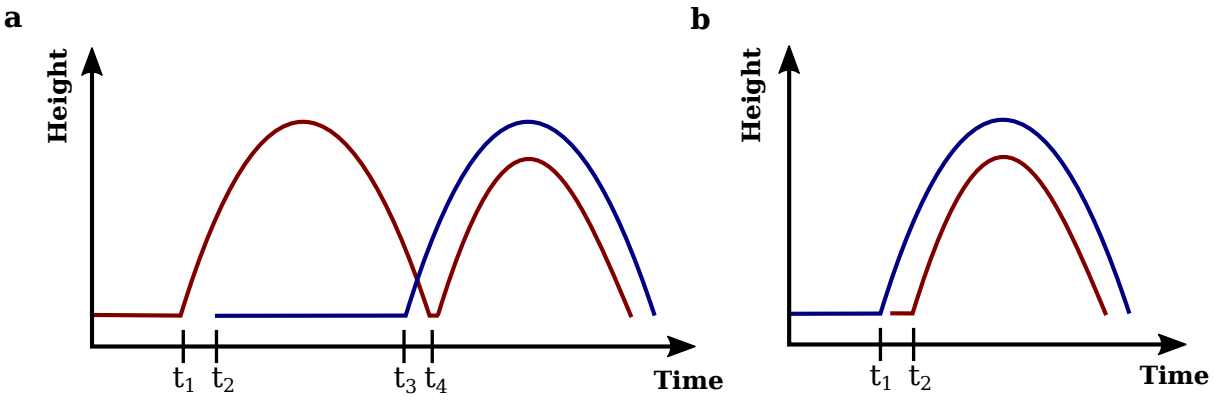

Figure 3.21: a) In a juggling configuration, a cloud is first loaded in the MOT before being launched at time t_1. Loading of a second cloud can then begin at time t_2, whilst the first cloud is following its launch trajectory. The second cloud is then launched to its experimental height at time t_3, before the original cloud is recaptured in the MOT at time t_4 and launched to the second, lower height. b) In the configuration utilised in this thesis, the second cloud is instead loaded in the short interval between the required launch times of the higher (t_1) and lower (t_2) clouds. This places more stringent requirements on the performance of the MOT loading, but with the gain of increasing the repetition rate and therefore the potential sensitivity of the device.

3.4.1 Multi-Cloud Launching Sequence

Simultaneous interferometry with Raman beams requires the velocity of the atomic populations to be matched, so that the Doppler shifts of the different Raman beam components are observed to be identical for all interacting clouds. Ultimately, this is ensured by the velocity-selective state selection process (see section 5.2.1), but the various atomic clouds still need to be launched with basically the correct velocities and at the correct time intervals. Ignoring the effect of any gravity gradients, this criterion is equivalent to stating that the different clouds need to reach their respective apogees simultaneously. For atoms launched to fixed heights, this criterion therefore establishes the time interval between the launches – for example, to achieve the proposed specifications, a cloud which is to be launched to 70 cm must do so 74 ms after one launched to 1 m, if they are to follow the required spatially offset, but otherwise identical arcs, greatly limiting the amount of time available to trap the necessary cold atoms.

Excepting this limitation, the sequence remains essentially identical to that detailed in section 3.3. Atoms are loaded in the MOT and then launched and cooled in a moving molasses sequence. Whilst this cloud is travelling upwards a second cloud is loaded, cooled and launched, with the timing between the two launches is controlled to within 100 µs by the data acquisition board.

Difficulties arise, however, in making the two launch sequences independent. For example, it is clear that re-initiating the MOT too soon will result in the previous cloud being recaptured or blown away by scattering interactions with the beams. In fact, it was observed that even with long wait times (up to 50 ms), when the first cloud should be far from the MOT chamber

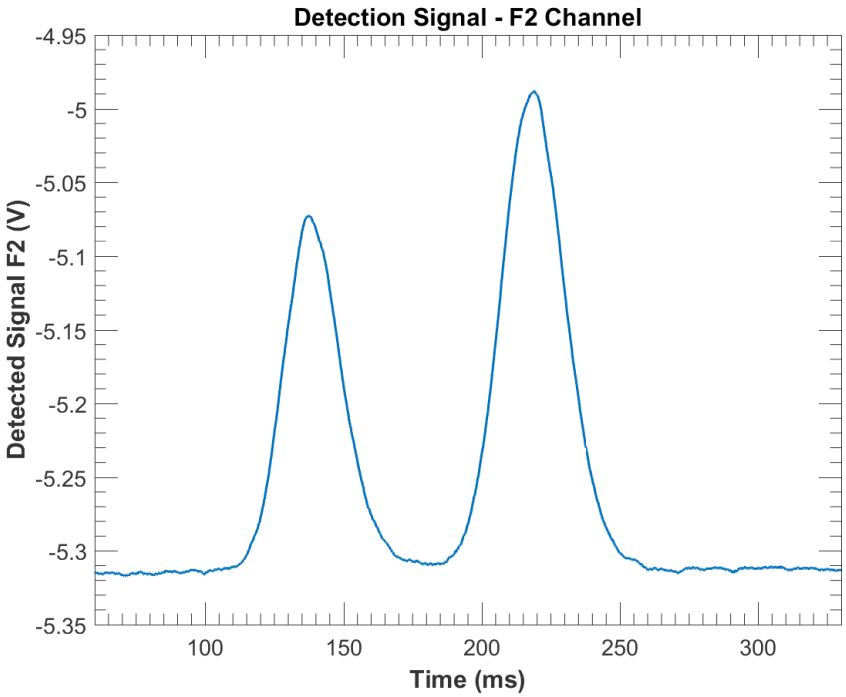

Figure 3.22: The detection signal in the $|F = 2\rangle$ channel from two clouds launched to simultaneous apogees at heights of 0.7 m and 1 m.

region, the returning temperature and atom number of the first cloud was adversely affected. Likewise it is not possible to use the microwave horn to perform state selection on the atoms as, in the case of the first cloud, scattered light from the second cloud is observed to interact with the already launched cloud and thus damage the state selection, and, in the case of applying microwaves to the second cloud, they are again seen to interact with the first cloud. It is probable that the atoms being lost are primarily from the spatially lower region of the cloud and would therefore not pass the velocity-dependent state selection process anyway – rendering their loss immaterial[xi]. Regardless, both the above effects serve to limit the amount of time available to load the second cloud and thus the number of atoms and the interferometer's sensitivity.

Loading time is further limited by the necessity to wait for the eddy currents to dissipate in the optical molasses (section 3.3.3). This waiting period is currently 20 ms, though it may be possible to reduce this by approximately 5-10 ms, gaining more atoms at a cost of a slightly higher temperature.

Nevertheless, it was possible to launch two clouds in this manner to heights of 70 cm and 1 m, without any catastrophic heating or atom loss. Two peaks of comparable height are clearly visible and distinguishable in the detection region (Figure 3.22), paving the way for simultaneous interferometric measurements to be made, as presented in section 5.1.4.

[xi] This suggested by the fact that the mean time it takes the unaffected atoms to arrive at the detection signal is increased by the earlier loading of a second cloud.

3.4.2 Outstanding Issues

Despite the success of launching and detecting the two clouds, there remain issues pertaining to the optimisation of this part of the experiment. Primarily, the precise means of performing the state selection is unclear. Ideally a single state selection pulse would be used on both beams, ensuring that atoms with identical velocity distributions are selected. The main issue is that the first cloud is at a height of 30 cm above the MOT region and it is therefore not possible to use the horizontal port normally used to clean the state populations. One possibility would seem to be to perform the state selection on the first cloud in the normal way, before the second cloud begins the loading process. The state selection pulse on the second cloud would then also transfer the first cloud back to the $|F = 2, m_F = 0\rangle$ state, or preferably back to the $|F = 1, m_F = 0\rangle$ state, if a second intermediate π pulse had previously been applied. This scheme, however, is clearly reliant on high fidelity π pulses with transfer probabilities very close to unity to be effective, which is experimentally challenging (cf. Figure 5.3). Otherwise, background atoms will reduce the contrast of the interferometer. It is also not at all certain that the light and the magnetic fields used for loading the second cloud wouldn't affect the states of the prepared atoms.

A more promising solution, therefore, would be one in which the scheme for cleaning the atomic population after the state selection pulse is revised. Based upon the vacuum geometry, the only conceivable option is for the cleaning beams to enter via the Raman beam window ports. Whilst getting such a beam to enter approximately vertically is spatially challenging, it is the current preferred option, though as yet unimplemented. Alternatives would be to either mix the beam on some kind of beamsplitter with the Raman beams after their fibre output, which would necessarily degrade both the wavefront of the Raman beams and decrease their intensity, or to deliver the cleaning beam via the same optics as the Raman beam. The latter option is a possibility though it would be important to ensure that this light is effectively shuttered during the interferometry sequence and it is also unclear of how effective such a scheme would be at applying sufficient radiation pressure to the $|F = 2\rangle$ atoms, due to the retro-reflecting nature of the Raman beams.

There remain other less crucial issues, such as increasing the atom number. As will be discussed in section 5.2.3, the number of atoms from a single launch is already potentially too low for the current iteration of the Raman beams. One option is to load the initial cloud for a longer period of time – allowing the loading of the second cloud to begin slightly earlier for an unchanged number of atoms in the first cloud – although this would reduce the experimental cycling time and hence the sensitivity of the gradiometer.

Chapter 4

Interferometric Laser Beam Design and Implementation

As discussed in Chapter 2, an atom interferometric gravity gradiometery sequence is to be performed by the controlled manipulation of the momentum states of the atomic sample by Raman beams. These beams additionally result in a synchronous change in the ground hyperfine state of the atom, aiding in the detection process. This chapter outlines the fundamental requirements, design and implementation of the Raman beams used in the interferometry experiments presented in the next chapter.

4.1 Raman Laser Beam Design

There are two major components to the Raman beam design: the lasers and associated optical components; and the reference frequency source. A schematic of the Raman laser system, incorporating both these elements and described in detail below, can be seen in Figure 4.1, with photographs in Figure 4.2.

4.1.1 Design Overview

The Raman lasers are constructed from two amplified, narrow-linewidth 1560-nm lasers, which undergo second-harmonic generation in temperature-stabilised periodically-poled lithium niobate crystals to produce light at 780 nm. One of the lasers is frequency locked via saturation absorption spectroscopy, whilst the other laser is then phase-locked to this laser at a variable frequency offset approximately equal to the ^{87}Rb ground state hyperfine splitting ($\sim$6.835 GHz). The phase-lock is achieved by current feedback to the laser from an off-the-shelf offset servo (Vescent, D2-135), with further phase noise suppression coming from the introduction of an electro-optical modulator (EOM) prior to frequency doubling.

The phase lock is achieved by comparing the divided-down beat note, taken at 1560 nm with a high-bandwidth, fast photodiode (Newport,1544-B-50), with a reference frequency source. The

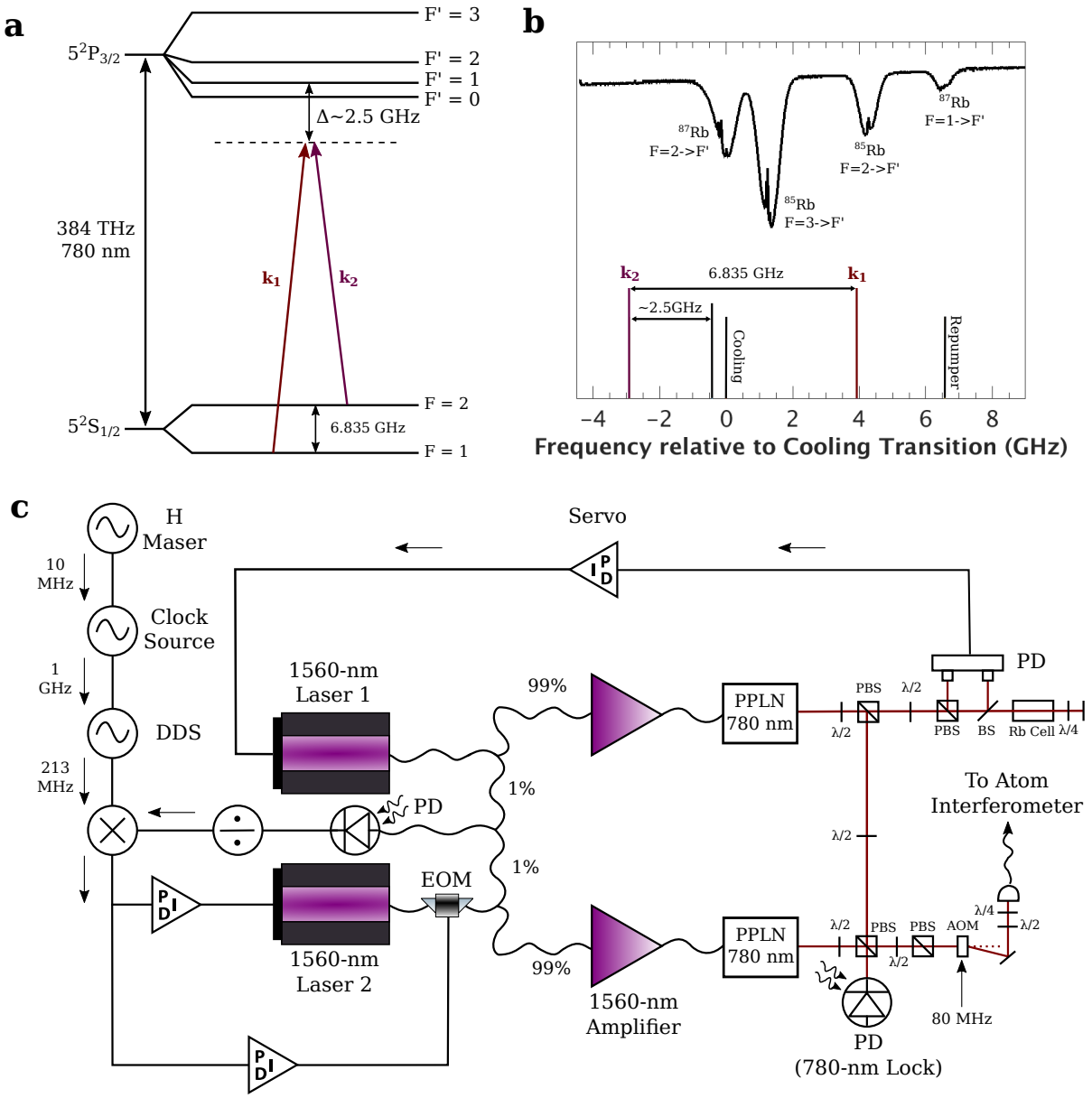

Figure 4.1: Schematic of the key features of the Raman laser beam design. a) Raman beam frequency diagram. b) Comparison of frequencies to other Rb D_2 frequencies. c) Design: two 1560-nm lasers are independently amplified and frequency doubled. One of the lasers (Laser 1) is frequency locked via spectroscopy in a Rb cell and the other (Laser 2) is phase-locked at a frequency offset to this laser. The beat note for this offset lock is collected by combining the two lasers in fibre at the 1560-nm regime and sending this signal to a fast photodiode. The fibre-based section is contained within a standard rack draw and the free-space section uses minaturised optics to be fully contained on a 30 cm by 30 cm breadboard.

reference frequency is derived from a direct digital synthesiser (DDS) based on a chip with high resolution (Analog Devices, AD9912 IC). An approximate 213 MHz signal produced by the DDS is compared with the beat note which has been amplified and divided down by a factor of sixteen. The DDS is clocked by a 1 GHz source, which is also a miniaturised component based upon phase locking a voltage-controlled oscillator to a 10 MHz source (IGY-Systems, 0271GY).

The entire system, including all of the necessary control electronics and computing, is contained within a 24-inch rack system. Furthermore, the lasers and amplifiers etc. are self-contained within a single rack draw, which helps to shield it from the environment and enhance stability. The design is therefore highly compact and suitable for transportation (Figure 4.2).

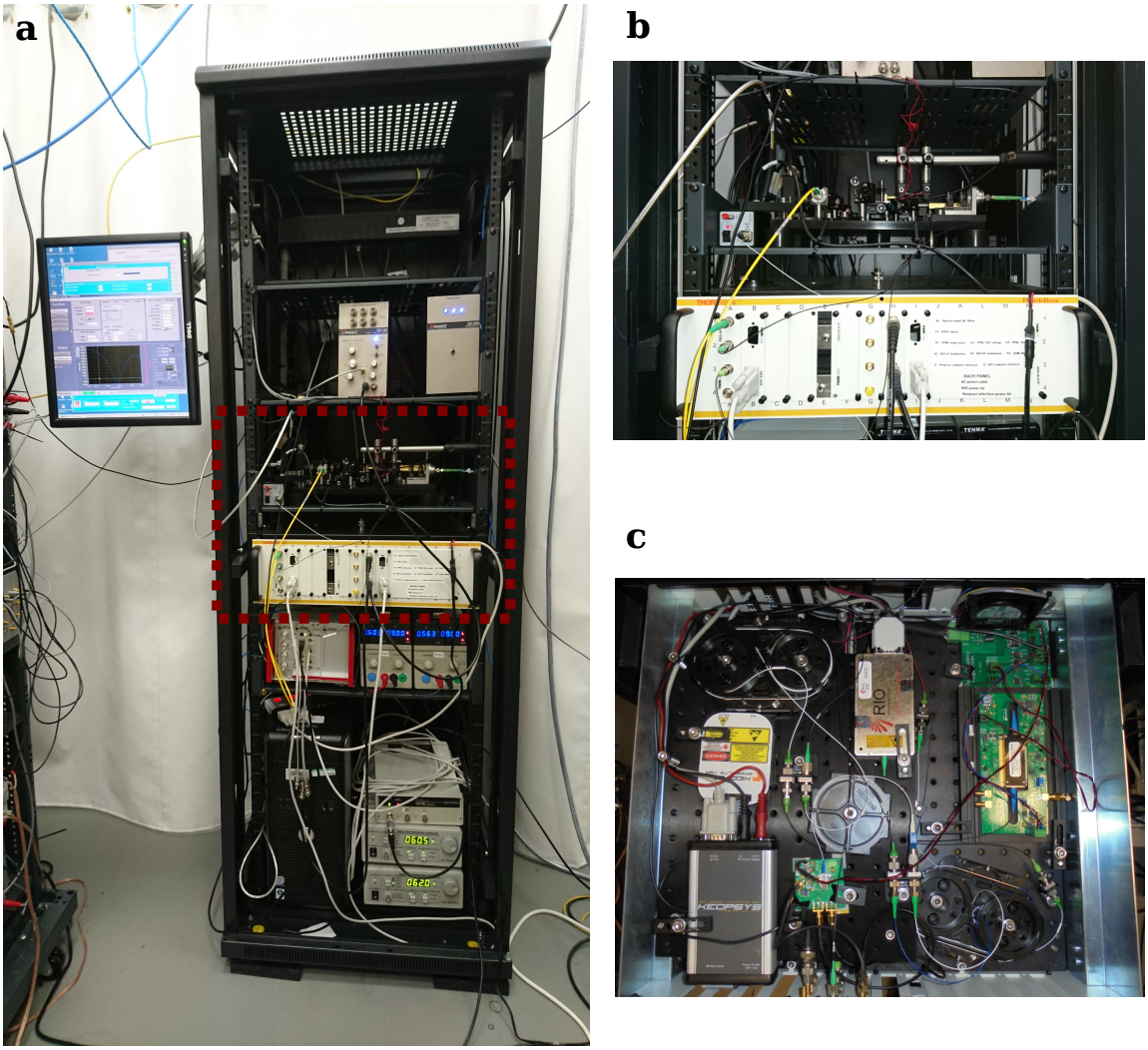

Figure 4.2: a) The Raman beam design is mounted in a single standard 19-inch rack system, with the Raman beam lasers and optics contained with the area marked by the red box. b) The Raman beam lasers and amplifiers are contained in a single draw of approximate 3 U height. The free-space optics are mounted above on a 30 cm by 30 cm optical breadboard, also suitable for mounting in a draw. c) Inside the draw, the optics are mounted in two layers – hidden in this photo is a second laser and amplifier combination. (These photographs were taken before full completion so some components are not shown.)

4.1.2 Laser & Optical Design

The Raman laser beam system is based upon phase locking two independent, fibre-based lasers at 1560 nm (RIO Orion), with linewidths of ∼1 kHz (Lorentzian FWHM), phase noise of $2\,\mu\text{rad}/\sqrt{\text{Hz}}$ at a 200 Hz offset and approximately 10 mW of output power. Working with 1560 nm lasers has multiple advantages, mainly due to the technological advantages of the telecommunications industry, which operates around this wavelength. The importance here is that stable, compact and reliable lasers are readily available and affordable at this wavelength, with the robustness coming from the solid-state nature of the laser design (i.e. there are no moving parts).

Following independent amplification to 350 mW (Keopsys, CEFA-C-BO-H), these lasers undergo frequency doubling to the required experimental wavelengths via second harmonic generation in a periodically-poled lithium niobate crystal (PPLN)[i] (NTT Electronics, WH-0780-000-A-B-C), which are temperature stabilised (Newport, 350B) at around 60 °C, with the precise temperature to produce a maximum output power of around 100 mW being found experimentally. The 780-nm output from the two PPLNs are overlapped in free space and coupled into the same polarisation-maintaining single-mode fibre for delivery to the experiment. The beams are combined on a polarising beamsplitter (PBS), before being passed through a second half-wave plate and PBS combination, which ensures they have identical polarisation, at the cost of an approximate halving of the optical power. An AOM is used to control whether the beams are coupled into the fibre, as detailed in section 4.3.1, and two mechanical shutters are used to prevent any light being coupled, when required.

The lasers need to be both locked in frequency and relative phase, with the latter being especially demanding. To achieve this one of the lasers is frequency locked to the ^{85}Rb repumper manifold. This transition is separated from the ^{87}Rb repumper manifold by around 2.5 GHz and so produces Raman beams with a large single-photon detuning. The lock is performed by locking to the side of a fringe from a Doppler-free absorption spectrum. Side-of-fringe locking is sufficient in this case as a precise frequency is not required and small changes in frequency will produce only small effects in the interferometer due to the large single-photon detuning. Locking in this way has the additional advantage of not requiring the laser to be directly modulated[ii].

The second laser is then phase-locked to the other via feedback from a beat note. The beat note is generated by combining the two lasers in a fibre at 1560 nm and feeding this signal

[i] PPLN is a material with a large optical non-linearity, making it amenable for frequency mixing purposes. The periodic inversion of the crystal structure allows for the production of light throughout the crystal which is at least partially in phase. The phase matching conditions and therefore the efficiency of the second harmonic generation, are set on a coarse level by the distance between the inverted crystal regions and can be controlled to a fine level by adjustments to the temperature.

[ii] It is possible to lock to the peak of a signal without directly modulating the laser by using techniques such as DAVLL [108], Zeeman modulation [109] or polarisation-spectroscopy locking [110]. The first two, however, requires the introduction of external (varying) magnetic fields, which are not in general desirable. Polarisation-spectroscopy locking was tried, but was found to be less stable in the long-term than side-of-fringe locking, for this particular setup.

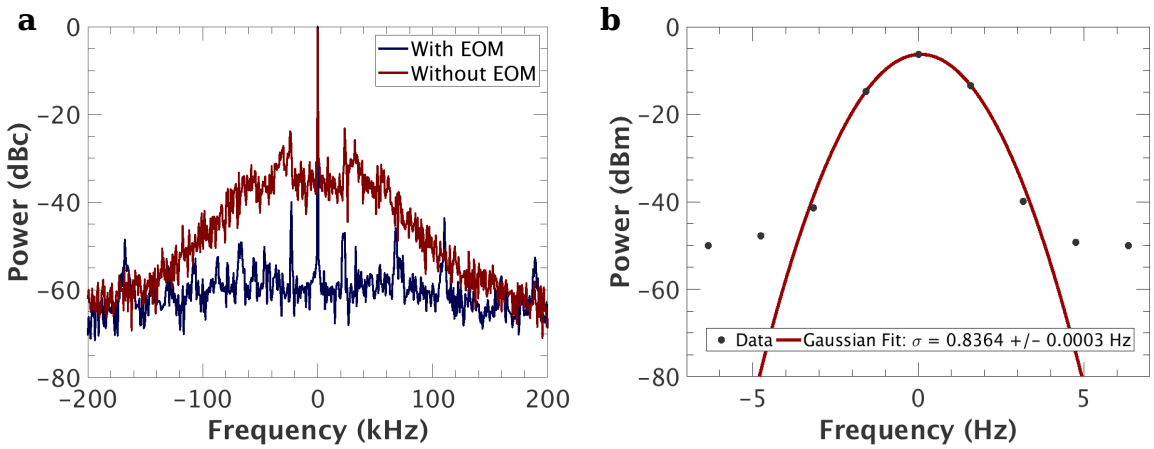

Figure 4.3: a) The beat note for the lasers with and without the use of an EOM. b) A Gaussian fit to the central peak of the beat note (with EOM), showing a width ∼Hz, though with only a small number of data points, due to the limited bandwidth of the spectrum analyser.

to a DC-coupled fast photodiode (Newport, 1544-B-50)[iii], with sufficient bandwidth to accept the 3.4 GHz signal (half the ground state hyperfine splitting of ^{87}Rb). This signal is sent to a locking servo (Vescent Electronics, D2-135) where it is divided down and compared on a phase-frequency comparator to the reference signal. After some filtering, the servo uses the output of the phase-frequency detector as an error signal for feedback to the offset laser. This is output to a modulation port of the laser current with a bandwidth of 100 kHz.

Phase locking can also be established using a beat note collected at 780 nm, by fibre coupling the light discarded on the second PBS. Using feedback from this point is preferable as it will account for all of the phase noise accrued from the different optical paths of the two beam components [111, 112]. Even for a stable setup, this noise can be considerable as only differences comparable to the wavelength are required to produce sizeable phase noise (see section 4.2.1). The disadvantage is the decreased sensitivity of the indium gallium arsenide photodiode at 780 nm, requiring significantly greater amplification of the beat note than for the 1560-nm case. All of the interferometric experiments detailed in Chapter 5 used the 1560-nm lock, though the long-term plan is to switch permanently to a 780-nm based phase lock. Plans for an improved Raman beam system are shown in section 6.1.1.

The servo allows different possible divisions to be selected, but the bandwidth of the internal electronics limit the reference to a maximum of 240 MHz. As the tightest achievable phase lock is attained with the lowest possible divider setting, this means that a reference signal of around 213 MHz and a divider setting of sixteen were used. For a phase lock using the beat note derived at 780 nm, the reference signal is kept the same but the divider value doubled.

It was found that this current control was insufficient to produce a suitable phase lock. Al-

[iii]The fast photodiode also has an AC-coupled option, which should help to produce a symmetric beat note of constant amplitude, by removing low-frequency and DC asymmetries in the coupled power. The DC-coupling setting, however, was found experimentally to reduce phase noise at low frequencies and was therefore preferred.

though an offset frequency lock and apparently some phase locking could be achieved, the Raman system was incapable of manipulating the atoms in a coherent and reliable manner. This was possibly caused by the voltage modulation inducing frequency-dependent phase modulations. An electro-optical modulator (EOM), with a bandwidth of 12 GHz (Photoline, MPZ-LN-10), was therefore added into the arm of the second laser before the fibre-combination for the beat note. The error signal from the servo was then fed to a PID controller (Stanford Research Systems, SIM960) which controlled the output of the EOM, although the bandwidth of this controller is again limited to 100 kHz. As can be seen in Figure 4.3a, this significantly reduced the frequency noise across the spectrum, as well as increasing the power in the central, phase-locked region, leading to a central beat note width of approximately 1 Hz. The increase in cost is modest as EOMs for 1560 nm are readily available – although they are significantly more expensive if 780 nm is required.

The main disadvantage of using the EOM is a decrease in the power stability, with intensity fluctuations on the order of a few per cent being induced (Figure 4.4a). Spectrally, the fluctuations are within the approximate range of 200 kHz to 1 MHz (Figure 4.4b), with the intensity spectra being otherwise effectively identical[iv]. Intensity fluctuations can lead to degrading effects on the interferometer, both by varying the effect Rabi frequency and by introducing spurious phase shits due to a variable AC Stark shift. The effect of these intensity fluctuations can be characterised by the following equation [113, 114],

$$\sigma_I^2(t) = \frac{T_c}{t}\int_0^\infty S_I(f)\,|H_I(f)|^2\,df, \tag{4.1}$$

where $\sigma_I^2(t)$ is the Allan variance, T_c the experimental cycle time, $S_I(f)$ the spectral density of the Raman beam intensity, and the sensitivity function $H_I(f)$ is given by,

$$|H_I(f)|^2 = \frac{\pi\sqrt{3}}{C}\frac{\sin^4(2\pi fT)}{(2\pi fT)^2}, \tag{4.2}$$

with T the time between interferometer pulses and C the interferometer contrast. Equation 4.2 clearly shows that the contribution to the phase error is dominated by low frequencies, meaning that the intensity fluctuations induced by the EOM are unlikely to affect the device sensitivity. Indeed, the contribution to the phase error from a single measurement ($T_c = t$) can be estimated by comparing the value of equation 4.1 for the cases of with and without the EOM. Assuming $T = 10$ ms and integrating over the frequency range of interest, results in the EOM producing a phase error ($\delta\Phi = \sqrt{\sigma_I^2}$) of 1.3 µrad which, whilst being over an order of magnitude higher than without the EOM, is nevertheless small. Taking the difference between the two cases, the resultant increase in the phase error caused by using the EOM is only 1.1 µrad, which is small enough to be considered negligible (cf. section 4.2.2).

Regardless, the EOM is crucial to this Raman system, allowing the coherent manipulation

[iv] Measured from 1 Hz to 10 MHz (not shown).

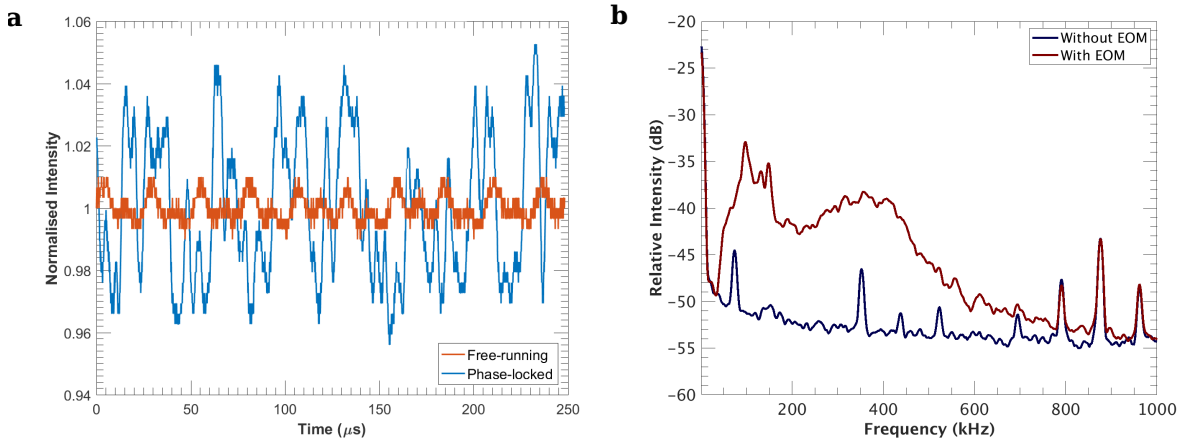

Figure 4.4: a) Whilst the use of the EOM improves the phase lock, it introduces fast intensity fluctuations in the phase-locked laser output of a few per cent. b) These fluctuations are within the range of approximately 200 kHz - 1 MHz and consequently do not add much error to the interferometry signal.

of the atomic samples, which were otherwise unachievable (Chapter 5).

4.1.3 Reference Frequency Source Design

As mentioned, a reference frequency source of around 213 MHz is used for phase-locking the Raman beams. In combination with the 1/16 divider, this results in two laser frequency components offset by 3.4 GHz, which is then matched to the hyperfine splitting of 6.8 GHz after frequency doubling. In addition to producing a reliable single-tone frequency with a stable phase, the reference frequency also needs to be chirped to account for the Doppler shift experienced by the atoms during free fall.

The final design of the Raman beams utilises a custom-built direct digital synthesiser (DDS) module based on a chip with high resolution (Analog Devices, AD9912 IC), locked to a 1 GHz reference [115]. This source outputs a fixed 13 dBm of a programmable frequency of up to around 500 MHz (limited by Nyquist sampling), with a precision of 4 μHz. The DDS is controlled by a field-programmable gate array (FPGA) and implemented on a bespoke printed circuit board. The use of an FPGA to control the DDS output means that the output signal can be modulated, ramped and stepped in a very flexible manner, and forms an area of growing interest in the atomic, molecular and optical physics community [116, 117, 118].

The dynamic frequency control necessary for a Mach-Zehnder interferometry experiment on free-falling atoms is outlined in Figure 4.5. There are two defined frequencies: one for the velocity and state selection; and one for the beginning of the chirp period. The chirp rate is controlled by additionally defining a constant frequency step, which is updated every 8 μs, and the chirp duration is determined by setting the number of frequency steps. The time between steps is limited by the communication from the FPGA to the DDS chip, which is performed via an SPI cable, which is incapable of performing reliably at faster times. To prevent any large,

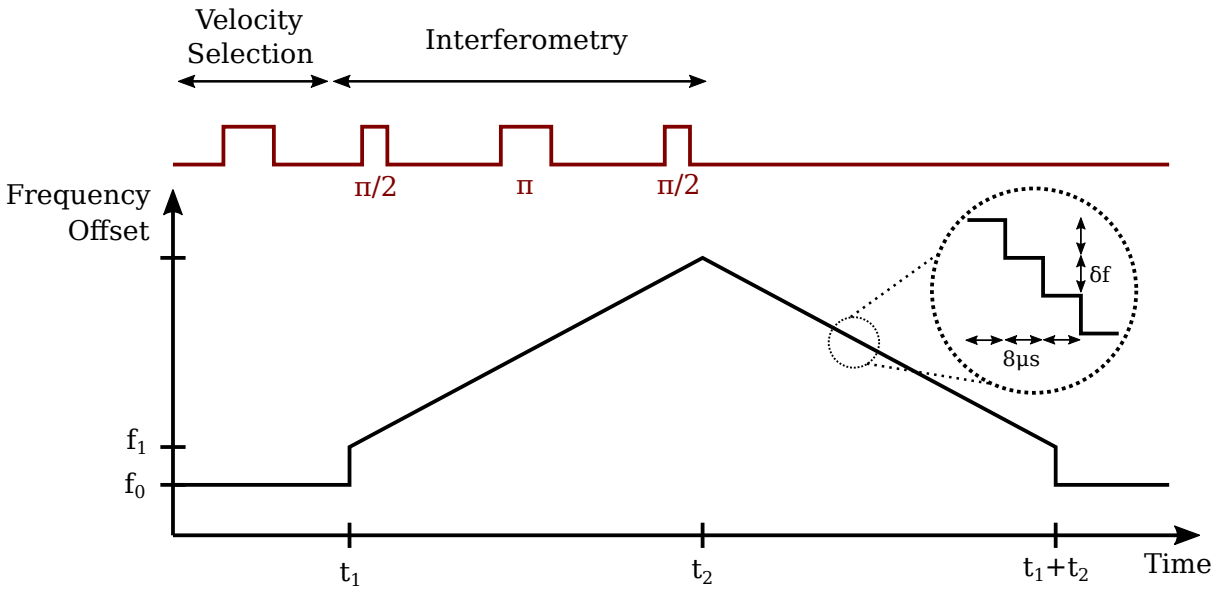

Figure 4.5: Schematic of the dynamic frequency control for the Raman beams. The DDS operates at a base frequency (f_0) suitable for the velocity selection procedure. The chirp for the interferometry sequence is controlled by a second frequency (f_1) and a frequency step (δf) which is performed every 8 μs and for a specified number of times.

abrupt shifts in frequency, which were observed to have the tendency to break the phase lock, the chirp is performed in a triangular manner. This doesn't critically influence the achievable repetition rate as there is time for the DDS to return to its base frequency during the time taken to detect the atoms and reload the atoms for the next experiment.

The DDS is referenced to a 1 GHz signal provided by a voltage-controlled oscillator (IGY-Systems, 0271GY) which is itself referenced to an ultra-low phase noise 10 MHz reference source. This source was previously used as a reference for the local oscillators (microwave source) in NPL's rubidium and caesium fountain frequency standards [63, 119]. This ultra-low phase noise reference is based upon phase-locking a 10 MHz maser signal to two temperature-stabilised quartz oscillators. These consist of a BVA crystal oscillator at 5 MHz (Oscilloquartz) and a low-noise crystal 100 MHz oscillator (Wenzel Associates Inc.). The 10 MHz output achieves optimal performance by replicating the phase noise of the different oscillators in the frequency

Offset Frequency	Phase Noise (dBc/Hz)			
	DDS Reference (213 MHz)	1 GHz Reference	10 MHz Reference	Maser (10 MHz)
1 kHz	-99	-83	-131	-128
10 kHz	-119	-118	-138	-131
100 kHz	-121	-120	-137	-132
1 MHz	-	-136	-139	-128

Table 4.1: The measured phase noise at various offset frequencies for the references used for the phase lock of the Raman beams. See text for source details.

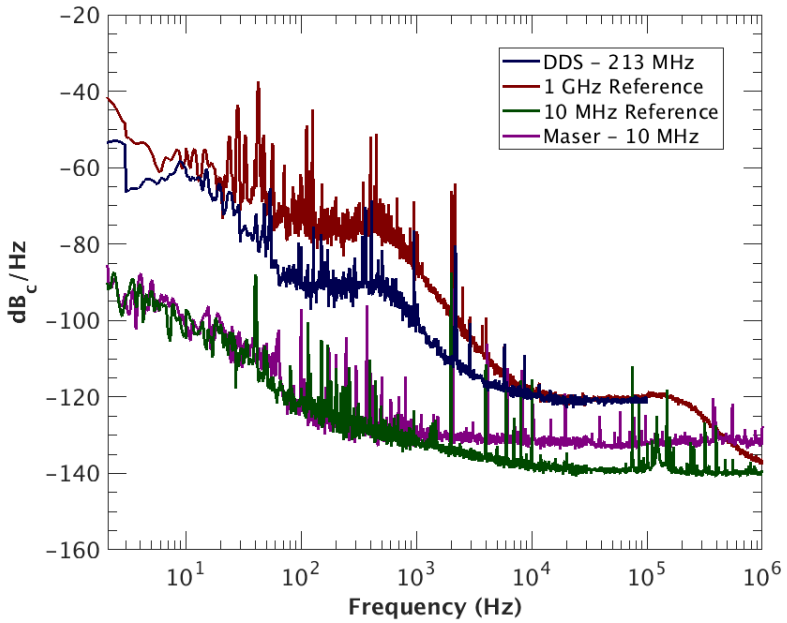

Figure 4.6: The phase noise of the DDS, the 1 GHz source, the 10 MHz ultra-low phase noise source and the 10 MHz derived from the Maser, which used as references for the Raman beam phase lock.

regime at which each oscillator performs best [119].

The use of these quartz oscillators is essentially necessary as a means to improve the short-term stability of the maser output. On long timescales, however, the maser provides an extremely stable reference, being disciplined by NPL's Cs fountain frequency standard – one of the atomic clocks which contributes to the official definition of the second and to the dissemination of global Coordinated Universal Time [119, 120]. The output of this 10 MHz source is used to clock all the important RF sources in the experiment, meaning that reliable frequencies should be assured, as demonstrated by the phase noise measurements shown in Figure 4.6 and summarised in Table 4.1.

4.1.4 Compact Construction for Transportability

As a long-term goal of the project is to produce a transportable gravimetry package, the Raman beam system was designed to be as compact and robust as possible and amenable to potential remote operation. Consequently, the entire Raman system is housed within a single, standard 19-inch rack ensemble. All of the fibre-optic components (both 1560-nm lasers, amplifiers, the fast photodiode and power supplies) are contained within a single draw (height ∼3U). The free-space optics are mounted on a single, square 900 cm^2 breadboard, which can easily be placed within a similar rack-mountable draw. This would have the advantage of isolating the setup from the environment and reducing the effect of, for example, thermal currents upon the fibre coupling.

The electronics are also contained with the rack, with the use of the DDS board and the compact voltage-controlled oscillator 1 GHz reference source greatly aiding the small scale of the setup. Currently, the main impediment to a transportable device is the use of the maser signal as the primary 10 MHz reference. Fortunately, as outlined in section 4.2.2, the interferometer is only sensitive to a certain frequency range, meaning low and high frequency noise below and above certain thresholds, respectively, can largely be ignored. The other main requirement for the reference frequency source is to provide accurate timing for the pulse separation, with the Mach-Zehnder sequence required to be symmetric in time to a high degree of accuracy. For a transportable device, sufficient accuracy can be provided by miniature commercial systems, such as chip-scale atomic clocks based on caesium, or by using a reference based upon GPS.

4.2 Phase Noise Characterisation

The minimisation of the phase noise of the Raman beams is crucial because the phase of the Raman lasers are directly imprinted upon the atoms. Any noise in the relative phase between the Raman beams will therefore translate into noise on the interferometric readout, although in the case of a gradiometer, this should be common mode to both arms. Nevertheless, it is consequently clear that the phase noise of the Raman beams needs to be minimised and characterised for an accurate interferometer [62, 121].

In addition to simply minimising the total phase noise, it is also important to consider the frequency components of this noise. The precise frequencies of importance depends upon the interferometry sequence being performed and its specific experimental values [122], but the frequency range will be approximately bounded by the inverse of the $\pi/2$ pulse duration and total sequence time. Phase fluctuations slower than the latter will result in negligible noise during the experimental cycle, whilst those higher than the former will tend to average out. This means that the key frequency range of interest is of the order Hz up to 10s of kHz.

4.2.1 Phase Noise Measurement

The phase noise on the Raman beams were characterised by sending the beat note signal to a phase noise analyser (Rohde & Schwarz, FSVA13). This measures the phase noise from the signal, however it is important to clarify that when multiplying and dividing the signals that the phase noise itself is changed by a related factor [123]:

$$\Delta\phi\left(f\right) = \Delta\phi_0\left(f\right) + 20\log_{10}\left(N\right) \tag{4.3}$$

where $\Delta\phi_0\left(f\right)$ is the phase noise of the unmultiplied signal (in dB units) at frequency f, and N is the multiplication factor. That is, multiplying the frequency by a factor of thirty-two, as the phase lock effectively is to get to the 780-nm regime, increases the phase noise by a factor of 30 dB. As the phase noise on the Raman beams is the important value, all of the phase noise

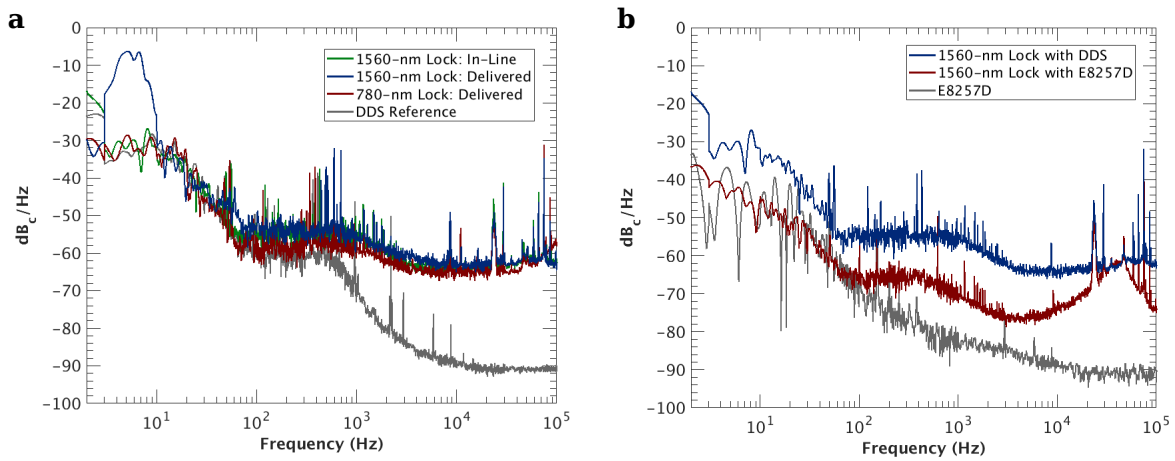

Figure 4.7: a) The phase noise spectrum of the Raman beams compared to the reference DDS. The phase noise tracks the reference signal at low frequencies before flattening out. The additional, uncancelled phase noise from the free-space optics is clearly visible in the blue line. b) The phase noise of the in-line Raman beam beat note using a second, low-noise synthesiser (Keysight, E8257D), with the spectrum from the equivalent measurement with the DDS repeated for ease of comparison. The phase noise again tracks the reference frequency at low frequencies, but the 'servo bumps' from the limited bandwidth of the laser and PID controller are now more clearly visible. All spectra are scaled to the 780-nm regime.

should be scaled to this regime.

The phase noise was measured in three configurations: the in-line beat note for the 1560-nm lock; after the fibre delivering the Raman beams for the 1560-nm lock; and after the fibre for a phase lock at 780 nm. To make the measurements after the delivery fibre, a second fast photodiode was used (Newport, 818-BB-45).

As is shown in Figure 4.7a, the laser system is limited by the reference source at low frequencies (<1 kHz) and is broadly flat at around 60 dBc/Hz at higher frequencies, with a 'servo bump' at 23 kHz from the limited laser bandwidth frequency. The increase in phase noise caused by not cancelling the noise accrued during the different optical paths is clearly observed, with a prominent peak in low frequencies (∼3-10 Hz), but also a general increase of around 5 dB across a broad frequency range, highlighting the importance of switching to the 780-nm lock in the future. Although it should be noted that a deliberately bad spectrum has been here selected to demonstrate the problem and to evaluate the worst case scenario. The various spikes in the spectrum are attributable to electronic noise.

To investigate whether the phase noise is limited by the reference or by the feedback mechanisms, a low-noise RF synthesiser was employed in place of the DDS (Figure 4.7b). Similar behaviour was observed, though the spectrum, having begun at lower level due to the lower reference frequency noise, also flattened out at a lower level (∼70 dBc/Hz). The combined data appears to suggest that the phase noise will approximately flatten out at its value at 100 Hz, with the level at this frequency and below dictated by the reference source. With the phase

noise pushed lower the full 'servo bump' is now clearly visible and this will provide the limit to the phase noise in this regime for the current laser and electronic setup.

Although this laser system is capable of performing coherent manipulations on the atoms (Chapter 5), this noise compares poorly with other interferometric laser beam systems [111, 112, 124], even when using the synthesiser with lower phase noise. The primary reason for this seems to be the limitations imposed by using a multiplied reference signal (equation 4.3), which is increasing the baseline phase noise too high for the very-low-phase-noise interferometric applications being pursued here. To overcome this limitation, a new design of the Raman beams using a mixed-down, rather than divided, beat note is presented in section 6.1.1, along with some preliminary measurements and results.

4.2.2 Phase Noise Limits to Gravimetry

Whilst such a phase noise spectral density plot as shown in Figure 4.7 is an important characterisation in and of itself, it is necessary to determine how this noise will translate to any gravity measurements. Comparison of this noise value to other, independent sources of noise and the desired sensitivity, provides a fundamental measure of the suitability of the constructed Raman beams.

As mentioned above, the precise range of the important frequencies in the phase noise depends upon the specific measurement being performed via the transfer function [122]:

$$\Delta\Phi^2 = \int_0^\infty S_\phi(f)\,|H_\phi(2\pi f)|^2\,df; \tag{4.4}$$

where $S_\phi(f)$ is the phase spectral density of the Raman lasers, $H_\phi(2\pi f) = H_\phi(\omega)$ is the transfer function, and $\Delta\Phi^2$ is the contribution from the Raman beams to the variance of the interferometric phase difference. In the case of a $\pi/2$-π-$\pi/2$ sequence, such as in a gravimeter, the transfer function is given by [122],

$$|H_\phi(\omega)|^2 = \left|\frac{4\Omega\omega}{\Omega^2\omega^2}\sin\left(\omega\frac{T+2\tau}{2}\right)\left[\cos\left(\omega\frac{T+2\tau}{2}\right)+\frac{\Omega}{\omega}\sin\left(\omega\frac{T}{2}\right)\right]\right|^2, \tag{4.5}$$

where τ is the duration of the $\pi/2$ pulses, T is the time interval between pulses, and Ω is the Rabi frequency. For this function, a general estimate of the important frequency range can be given as between $1/(\pi T)$ and $1/(4\tau)$ [125]. The high-frequency cut-off represents the point at which the averaged line has fallen by 3 dB from the plateau region [122]. A plot of this function for the measured phase noise spectral density and realistic values of τ and T is shown in Figure 4.8a.

The phase noise spectral density weight by the transfer function is shown in Figure 4.8b, for the two different lock configurations and for the reference source. The low-frequency noise of the 1560-nm lock is prominent and provides an obvious impediment to performing high-precision gravimetry with these Raman beams, giving an integrated phase error of 392 mrad ($T = 10$ ms,

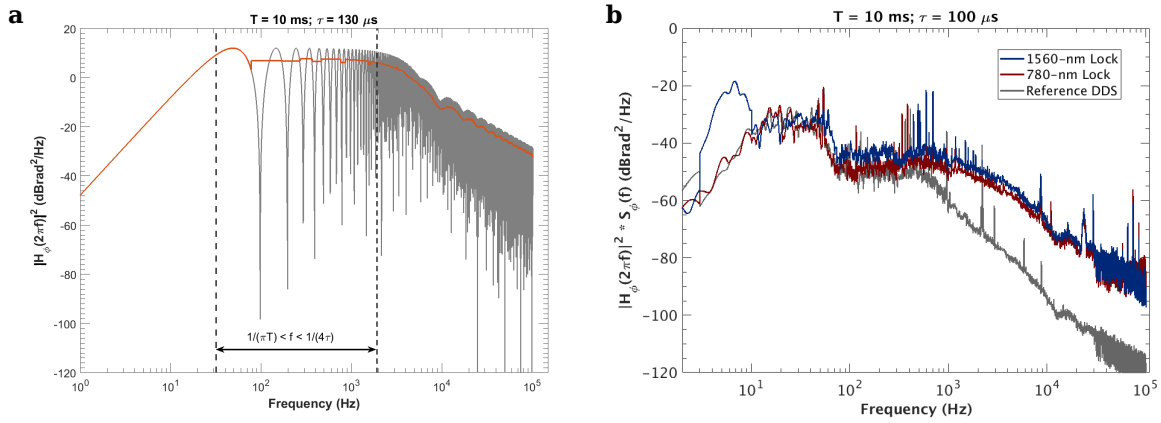

Figure 4.8: a) The calculated transfer function for a measurement of the acceleration due to local gravity, with T=10 ms and τ=130 μs. The grey line shows the calculated line, whilst the orange shows the average over the period of an oscillation to make the trend clearer. The approximate range of crucial frequencies is highlighted. b) The phase noise spectral density weighted by the transfer function (averaged), shown for both the 1560-nm and 780-nm lock, as well as the reference DDS, to show the best obtainable for this setup. They correspond to an integrated phase error of 392 mrad, 288 mrad and 240 mrad, respectively. In these calculations, T=10 ms and τ=130 μs.

$\tau = 130\,\mu$s). Even when using the noise of the reference DDS, which would represent the best achievable noise using this method, the phase error is 240 mrad.

A good benchmark for characterising the noise is the quantum projection noise [126], as this provides a fundamental limit on the precision of a single measurement[v]. Moreover, this limit is attainable, being the leading noise term in other, similar experiments [62], although here the Raman beam phase noise is highly suppressed due to operating in a gradiometer configuration. Assuming 10^6 atoms in the interferometer, the expected error from the quantum projection noise is 1.6 mrad, meaning that the Raman system has, even in principle, two orders of magnitude more noise than desired.

The integrated phase noise is useful for deciding upon the best experimental parameters for T and τ, as the periodic nature of the transfer function and its limited region of interest mean that the values of T and τ can be selected so as to suppress parts of the phase noise spectrum, which is particularly useful for avoiding noisey features, such as 'servo bumps'. Figure 4.9 shows the calculated phase error for both the 1560-nm and 780-nm phase locks, as well as the error on the determination of the corresponding gravitational acceleration. The phase error is seen to rise for longer pulse separation times, due to the high low-frequency noise of both the reference source and, especially, the uncancelled phase noise from the different optical paths for the 1560-nm lock. Nevertheless, longer pulse separations still tend to lead to an improved gravity

[v]The quantum projection noise can be circumvented somewhat by using squeezing techniques, similar to the squeezed states of light used in, for example, gravitational wave detection [127]. Spin squeezing techniques [128] have been used to lower the noise below the quantum limit in an atomic clock by 10.5 dB [129] and a technique for squeezing the momentum has been proposed for atomic interferometer gravimeters based upon strontium [130].

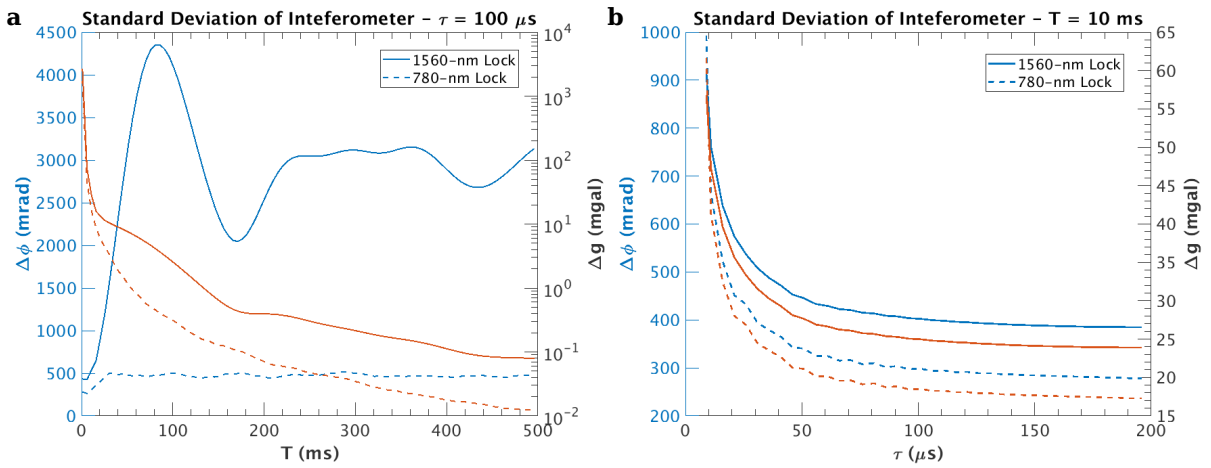

Figure 4.9: a) The calculated phase error (left axis, blue lines) and the subsequent error on a gravitational measurement (right axis, orange lines) for varying pulse separation ($\tau = 100\,\mu s$). For the 1560-nm lock (solid lines), the phase error increases dramatically for short times, but Δg continues to decrease. The effect is less pronounced in the 780-nm lock (dashed lines). b) Varying instead pulse duration ($T = 10\,ms$), gives approximately constant values after around $70\,\mu s$.

measurement, due to the increased sensitivity that comes with the interferometer enclosing a larger spacetime envelope. For pulse durations, it appears clear that longer interrogation times tend to give reduced phase error and more precise single-shot gravity measurements. However, increasing the pulse duration leads to more a more stringent criterion for the velocity selection, reducing the total number of usable atoms and therefore increasing quantum projection noise. A trade-off therefore needs to be found and it would appear around $50\,\mu s$ would be a good value for this Raman beam system (Figure 4.9b).

4.3 Experimental Implementation of the Raman Beams

4.3.1 Pulse Generation

A single-pass 80 MHz AOM (Gooch & Housego, 3080-122) is used as a fast switch to control the delivery of the beams to the experiment. The RF to the AOM is controlled by the combination of a fast RF switch (Mini-Circuits, ZFSWHA-1-20B) and an arbitrary function generator (AIM TTi, TG2511A). This is used to generate reliable pulses (it is clocked to the ultra-stable 10 MHz source), with approximately nanosecond precision. When multiple pulses of different durations need to applied, such as during a $\pi/2 - \pi - \pi/2$ sequence (see sections 5.2.2 and 5.2.3), a second, identical RF switch is used and a second arbitrary function generator (AIM TTi, TGP3151) was used. In this configuration, one of the pulse trains acts as a gate for the other, allowing for variable pulse durations to be applied.

4.3.2 Raman Beam Output

The coupled Raman beam light is output using a simple collimator alignment, where the number of the components is minimised to give maximum beam quality. The collimator is therefore an angled fibre connector after which the light propagates and expands freely over 200 mm until being collimated by an achromatic doublet (Thorlabs, AC508-200-B). For maximum possible beam quality, it is desirable to be able to translate the output position laterally and tip and tilt it relative to the collimating lens (or vice versa), which is not possible in the current configuration. However, the use of lens tubing should ensure internal alignment to a reasonable level. Likewise, there is no lateral translation of the entire collimator, which is attached via 6 mm diameter cage rods to the fountain. This ensures that the collimator of the beam is approximately centred on the top window. The collimator does, however, have the freedom to be tipped and tilted to allow the alignment of the Raman beams with the axis of local gravitational acceleration. For a coarse alignment, the beams can be centred on the bottom window, which due to the comparable beam size, is equivalent to it being output uncropped. The precision alignment method is discussed below in Section 4.3.3.

The polarisation optics come after the collimation to ensure that the whole beam passes through the same thickness of the waveplate. A linear polariser (Thorlabs, LPNIRE200-B) is screwed into the lens tubing and rotated for maximum transition. This ensures a constant polarisation axis of the beams at the expense of intensity fluctuations, in the case of variable polarisation from the fibre output. This is followed by a rotatable quarter-wave plate (Thorlabs, WPH20ME-780) for co-propagating beams, which is moved to the bottom of the fountain for the counter-propagating case.

The quality of the optics after the achromatic doublet are not of the highest standard. For example, the retardance accuracy of the quarter-wave plate is only specified to be less than $\lambda/100$, its wavefront distortion to $\lambda/4$, and a surface quality of 60-40 Scratch-Dig. The limitation is due to the ready availability of affordable optics at $2''$ diameter. These imperfections will lead to a reduced performance due to induced wavefront errors and impurities and variations in the polarisation across the beam. The ultimate effect will be the loss of contrast and, worse, the introduction of spurious phase shifts into the interferometer. Most likely, it will be necessary to have the requisite optical components custom produced for optimal performance. However, these effects are small enough to not prevent the observation of coherent behaviour.

This result of this setup is the production a high-quality beam of approximate diameter 33 mm, which is however compared to a window with a clear aperture of 28.7 mm, meaning there will be considerable resultant diffraction [131, 132]. The diffraction pattern calculated for these experimental parameters in the radial and axial direction is shown in Figure 4.10, clearly demonstrating large fringes in both the axial and, especially, radial directions. Furthermore, even weak diffraction from a circular aperture alters the characteristics of the Gaussian beam – including the alteration of the divergence [133], which results in a curvature of the wavefront

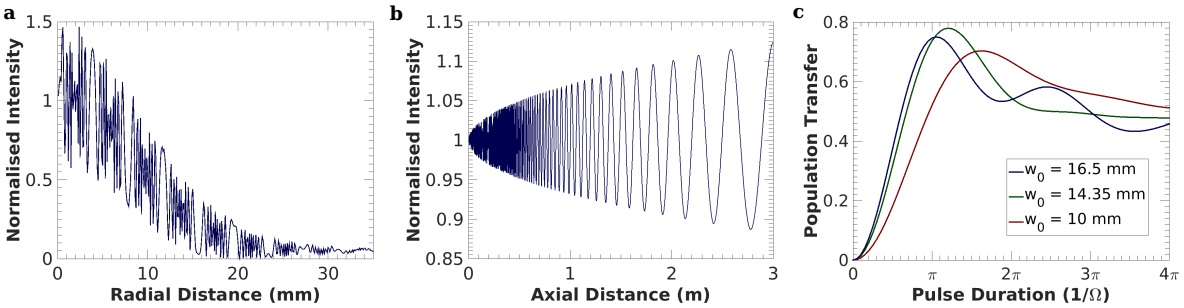

Figure 4.10: The calculated diffraction pattern caused by the window on the Raman beam in the (a) radial and (b) axial direction. For the axial calculation, the pattern is taken along an axis 1 mm from the beam centre. c) The effect on the Rabi oscillations of the diffraction caused by different input beam radii: the experimental value (blue); the clear aperture (green); and a 1 cm radius (red). Making the beam smaller reduces diffraction, but the atom cloud is now comparatively too large (cf. Figures 3.4 and 3.5).

and thus an error on any atom interferometer. In order to achieve intensity variations at the 1 % level, the beam diameter must be approximately 2.5 times smaller than the aperture diameter, which would be infeasibly small for the current setup.

To characterise the effect of this diffraction on the expected interferometer performance, a simple modelling was employed, similar to that presented in section 3.1.2. The difference being that instead of using a Gaussian profile to determine the expected population transfer, the diffraction pattern resulting from the input Gaussian upon the window, calculated analytically [132], is used (Figure 4.10a-b). The second difference to the previous calculations, is the introduction of the finite size of the detection beam, meaning that only atoms calculated to return to the detection region are used, as only these atoms will contribute to any measured signal. Computationally, this is approximated by only integrating over a section of the atomic cloud, with this size estimated from the cloud expansion rate (temperature) and the time between the Raman pulse application and the atoms reaching the detection region.

As the diffraction occurs both radially and axially, a three-dimensional numerical calculation for the population transfer is performed, with the results as shown in Figure 4.10 for atoms of 5 µK launched to a height of 1 m and with a pulse applied at their apogee. Reductions in both contrast and visibility is evident for the experimental parameters, which will tend to degrade the interferometer performance, although oscillations are clearly visible and the contrast is still reasonable. However, switching to a smaller beam, and thus reducing the diffraction, does not necessarily produce preferable results, as can be seen by the worse performance for a beam of 10 mm radius in the calculations – the contrast is lower and the visibility is almost entirely zero. This is due to the same dephasing mechanism discussed in section 3.1.2, where the size of the atomic cloud exceeds or is comparable to the interferometric beam size. Although this setup is therefore far from ideal, it is still the preferred delivery method for this experiment, although longer term it will be necessary to increase the size of the windows for the interferometry beams and the diameter of all on-axis vacuum chamber components, or to reduce the temperature by

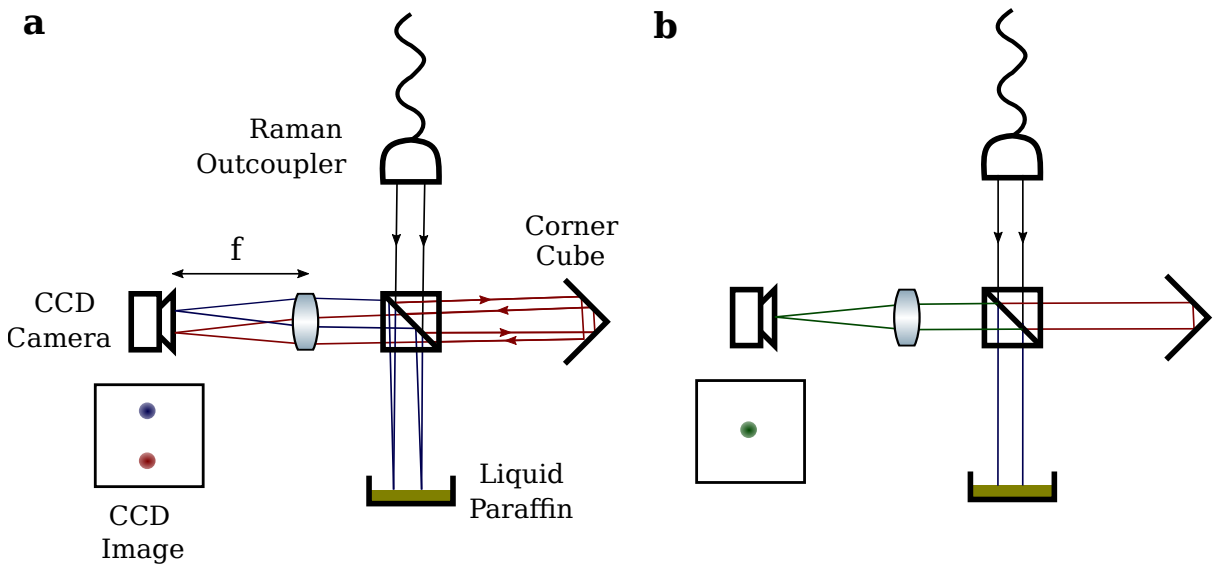

Figure 4.11: Raman beam alignment procedure showing cases of (a) misaligned beams and (b) aligned beams. The incoming beam is split on a beamsplitter with some of the light (red lines) sent towards a corner-cube retro-reflector and the rest transmitted to a liquid paraffin mirror (blue lines). When the beams are travelling normal to the paraffin surface, the beams will overlap and produce a single focal spot on the CCD.

several orders of magnitude to allow smaller beams to be utilised (see section 6.2).

4.3.3 Raman Beam Retro-Reflecting Mirror

The interferometer measures the acceleration along the axis of the Raman beams. Therefore to measure the acceleration due to local gravitation, the beams must be aligned along this axis. In other words, the surface of the retro-reflecting mirror must be both normal to the Raman beams and the axis of gravity. Furthermore, this mirror must be stable, as any vibrations will be directly transferred onto the interferometric phase difference, irreparably so in the case of an absolute gravimetry measurement. Vibrations are therefore reduced by mounting the mirror on a vibration isolation platform (Minus-L, 100BM-4) to provide passive isolation from ambient noise.

The simplest method to align the beams to the axis of gravity is to use a reflecting, viscous medium as a mirror. One possible medium is liquid paraffin, which is suitably reflective at 780 nm, yet also a liquid at standard conditions, meaning its surface will be normal to the axis of gravity.

To align the Raman beams normal to this surface a device as shown in Figure 4.11 was constructed. The light is partially reflected and partially transmitted at a PBS, with a corner-cube retro-reflector employed to send the reflected beam back towards a CCD camera, positioned at the focal length of a 75 mm plano-convex lens. The transmitted light is then reflected from the liquid paraffin and, following a double-pass through a quarter-wave plate at 45° to the polarisation axis, reflected towards the camera. The two beams will overlap to form a single

spot on the camera when they enter the lens parallel. That is, they will overlap when the incoming beam is aligned to the axis of gravity.

Alignment is therefore performed by adjusting the input angle of the Raman beam until a single spot is formed. The liquid paraffin is then removed and the retro-reflecting mirror inserted. The mirror is then itself adjusted to align with the now well-aligned Raman beams. Such a method gives an alignment good to around 0.1 mrad [134], which is sufficient for a fractional accuracy of around 10^{-9} g. Finer alignment can be performed when the system is in full operation, by utilising the parabolic dependence of the measured value of local gravity on the Raman beam angle [78].

Chapter 5

Demonstration of Atomic Interferometry

5.1 Interferometry with Co-propagating Raman Beams

Initially, the Raman beams are applied in a co-propagating configuration, where both the frequency components have the same σ^+ or σ^- polarisation. Whilst the momentum transfer in this configuration is equivalent only to the momentum from the microwave hyperfine ground state transition, it offers numerous advantages for calibration and testing purposes [78]. Having the beams co-propagate through the same optical system ensures that their spatial profiles are almost identical and their polarisations are known to be equal. Moreover, the Doppler shift for both components is likewise effectively identical, meaning that the whole velocity class of the atomic population is addressed and that Raman transitions will occur unshifted from the hyperfine transition frequency, allowing systematic shifts, such as the AC Stark shift (section 5.1.1.1) or inhomogeneities in the magnetic field (section 3.3.6), to be measured and cancelled where possible. As the resonant Rabi frequency depends only upon the intensity of the beams and the frequency detuning from the upper state (equation 2.39), these transitions can also be used to inform experiments with counter-propagating beams, for which these values are only different due to the reduction in intensity arising from the retro-reflection.

5.1.1 Two-photon Resonances

As previously described, the Raman beams are used to transfer atoms between the two ^{87}Rb ground hyperfine states, by approximately matching the frequency difference between the two Raman beam components to the hyperfine resonance. One of the first tasks is therefore to observe such two-photon transitions and also to find the experimental resonant frequency (f_0), which will be shifted from the unperturbed resonance by various effects, e.g. the AC Stark shift.

The precise dependence of the state transfer probability is given in equation 2.46. For long pulse durations (considerably longer than a π pulse), the peak transfer will tend to one half,

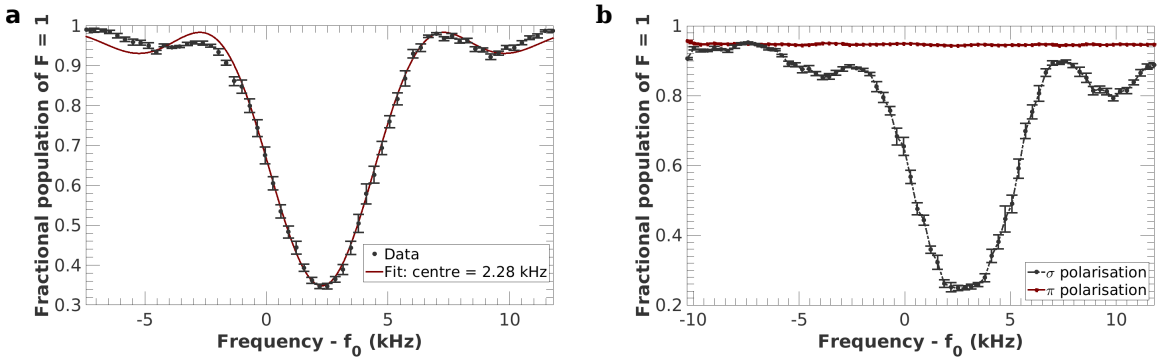

Figure 5.1: a) Two-photon transition resonance for co-propagating Raman beams applied for 200 μs at the apogee of a 1 m launch sequence. The abscissa shows the frequency difference between the Raman beam components relative to the unperturbed hyperfine resonance (f_0). The fit is to equation 2.20. b) Effect of Raman beam polarisation on the two-photon transitions. Co-propagating Raman beams require the two components to have equal circular polarisation. In both plots, error bars are standard error of the mean from repeated measurements.

regardless of any slight shifts, due to decoherence and dephasing effects. The initial scans in two-photon frequency difference were therefore taken for longer pulse durations (~ 1 ms), until the resonance could be located and the π pulse time experimentally determined (see section 5.1.2). Figure 5.1a shows such an observed two-photon resonance, for atoms launched to 1 m and initially prepared in $|F = 1, m_F = 0\rangle$ by the microwave horn[i] (section 3.3.5), fit with equation 2.20, but with an added scalar term to account for the reduced contrast and another term to account for the resonant frequency offset. The data and these fits demonstrate the characteristic side-lobes of coherent population transfer. The Raman beams' behaviour can be verified by rotating the quarter-wave plate to produce either linear polarisation or circular polarisation – as expected, only the latter produces two-photon transitions (Figure 5.1b).

5.1.1.1 AC-Stark Shift Cancellation

A noticeable shift in the frequency from the unperturbed value is clear in Figure 5.1, the origin of which is chiefly due to the AC Stark shift. Whilst not technically required for interferometry of this nature, as demonstrated in sections 5.1.3.1 and 5.2.3, any AC Stark shift introduces an unwanted additional term into the interferometric phase difference (equations 2.82 and 2.83).

There are several possible schemes for cancelling the AC Stark, often involving an introduction of additional beams to apply equal and opposite shifts [76]. The method used here is in many regards the simplest and involves the adjusting of the relative intensities of the two Raman components. The advantages of this method are its simplicity and easy adjustability, but it is sensitive to intensity fluctuations, which as explained earlier are an issue with the use of the EOM in the Raman beam generation (see section 4.1.2).

[i] In the remainder of this section, atoms have been prepared in this way, except when explicitly mentioned.

Nevertheless, it is possible to approximately cancel the AC Stark shift via this method as shown in Figure 5.2. Here the resonant frequency for different intensity ratios was measured, with the atoms not undergoing any state selection and being simply dropped. As the shift is linearly dependent on the ratio of the intensity between the two beams, a straight-line fit is used to find the ratio which will cancel the shift (Figure 5.2a), which can then easily be set (Figure 5.2b).

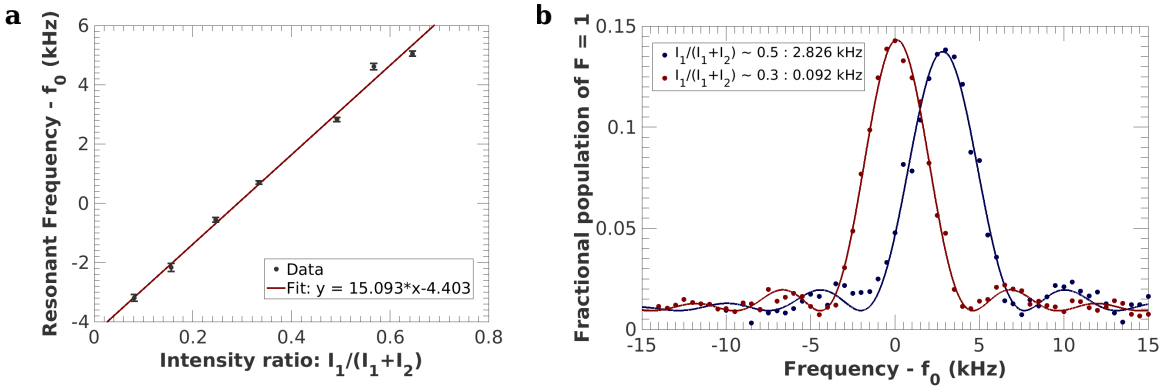

Figure 5.2: a) Frequency of two-photon resonance relative to the unperturbed frequency for different ratios of the intensities of the two Raman beam components. The linear fit is to the resonant frequency as determined from a fit to equation 2.20, as shown in panel b (error bars are 90 % confidence limits from these fits). b) Single-shot measurements for the two-photon resonance, with fits to equation 2.20, for equal intensities in each beam (blue) and for a ratio approximately cancelling the AC Stark shift.

5.1.2 Rabi Oscillations

Light-pulse atom interferometry requires the atomic states to be manipulated in a controlled way into superpositions of different momentum states. Experimentally this is performed by applying the Raman beams for different durations of time, with the pulse duration determining the established superposition. Whilst co-propagating beams don't generate this momentum splitting, they can be used to characterise the oscillation parameters, which in this case is purely between the two hyperfine states. For these measurements the frequency offset between the two Raman beam components is set to be on the previously determined resonance (e.g. Figure 5.1).

Such a Rabi oscillation sequence is shown in Figure 5.3, clearly demonstrating the predicted oscillatory behaviour. There is, however, a clear decay in the contrast with increasing pulse duration, suggesting the presence of decoherence or dephasing effects. Furthermore, it also appears that the oscillation period increases with increased pulse duration, implying a dephasing effect and explaining why the function fails to accurately fit the data, although if the data is limited to a period of less than around 2π, the fit performs very well (cf. Figure 5.10). The pulse fidelity is also limited, with a maximum transfer of atoms of only 70 - 80 %, despite the

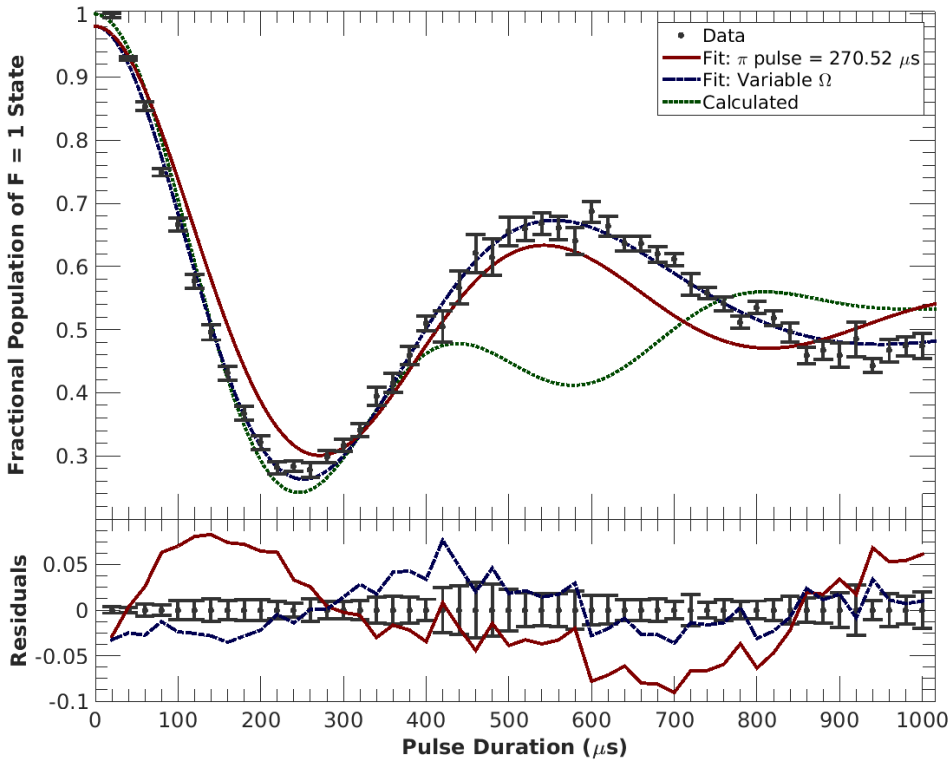

Figure 5.3: Rabi oscillations as observed for co-propagating Raman beams applied with resonant frequency difference and at the apogee of a 1 m launch. The oscillations are fit to damped Rabi oscillations (red line), which nevertheless fails to accurately capture the behaviour, due to an apparent increase in the oscillation period with pulse duration. A fit using a linearly increasing Rabi frequency is also shown (dash-dotted blue line) and the residuals to these fits are shown in the lower section of the plot. The dotted green line shows a calculation for the expected population transfer for the experimental conditions, which predicts the contrast but not subsequent behaviour.

state selection process.

The data can be accurately fit by making the Rabi frequency a linear function of pulse duration; that is, $\Omega \rightarrow \Omega(\tau) = \Omega_0 + a\tau$, where a is a constant. This fit is shown in Figure 5.3 and clearly outperforms the fit using a standard, non-varying Rabi frequency. In this case the initial Rabi frequency is given as 13.4±0.2 kHz and the constant as -3.8±0.4 kHz/ms, where the quoted errors are the 90 % confidence limit on the fit, exhibiting the observed decrease in Rabi frequency as a function of pulse duration. This is in comparison to a value of 11.6±0.4 kHz for the fit using a constant Rabi frequency.

A number of factors serve to limit the efficiency of the Rabi transfer process [135, 136], many of which have already been discussed and some can be discounted. For example, the single-photon scattering rate can be estimated for the experimental parameters at around 30 Hz, which translates as only a 3 % probability of an atom scattering during the maximum pulse duration

shown in Figure 5.3 and is therefore clearly incapable of causing the observed decay. This small change in population was confirmed by measuring the population change when the Raman beams were phase-locked but with a frequency offset far away from resonance. To prevent light leaking into the system when the Raman beams are ostensibly turned off, two shutters were installed to operate in tandem and only provide a few ms window for the application of the pulse. Any light leaking when both shutters were open and the AOM controlling the Raman beams nominally off, was measured to be of the order nW and thus negligible.

The thermal expansion of the cloud in comparison to the beam size can also be ruled out as the principle cause of the imperfect pulse transfer as the same limit of 70 - 80 % was achieved regardless of the launch height. Indeed, this was observed even when the atoms were dropped, for which the atom cloud is only around 1 mm in radius and therefore considerably smaller than the Raman beams. This suggests the possibility that it is the imperfect beam profile, caused by diffraction, that is limiting the observed contrast, as this is approximately equivalent for atoms launched to any height in the interferometry region. The expected oscillations for the calculated diffraction profile is shown in Figure 5.3, where the only free parameter was the Rabi frequency, which was set to the observed experimental value. Despite the simplicity of the calculations (see section 4.3.2), the initial behaviour is well estimated, with the calculated and observed contrasts being very similar. However, the calculated patently fails to account for the subsequent data, predicting neither the elongated oscillation period or the full oscillation visibility, suggesting that further effects are occurring which are currently unaccounted for.

Regardless, such observed oscillations are enough to establish the approximate durations needed for $\pi/2$ ($\sim 130\,\mu s$) and π pulses and show the ability to coherently transfer atoms between the two hyperfine ground states of ^{87}Rb.

5.1.3 Ramsey Sequence Experiments

With the duration of a $\pi/2$ pulse thus established, a Ramsey sequence can be performed. A Ramsey sequence consists of two $\pi/2$ pulses applied with a separation period in between the two applications. Therefore, although the total application time equals a single π pulse, the final state population will be dependent upon any phase accrued by the atoms during this period of free evolution (see section 2.3.2 for a more detailed description). There are two basic modes: varying the frequency of the $\pi/2$ pulses; and varying the time delay between the pulses.

5.1.3.1 Varied Frequency Pulses

Ramsey fringes produced when varying the frequency of the applied pulses are the foundational experimental technique behind atomic clocks [4]. The basic idea is that when the two frequency components are entirely on resonance no phase is accrued during the free evolution period and the atoms are transferred as if a single π pulse had been applied. When the frequency of the two pulses is detuned from resonance, however, the atoms will precess around the Bloch sphere

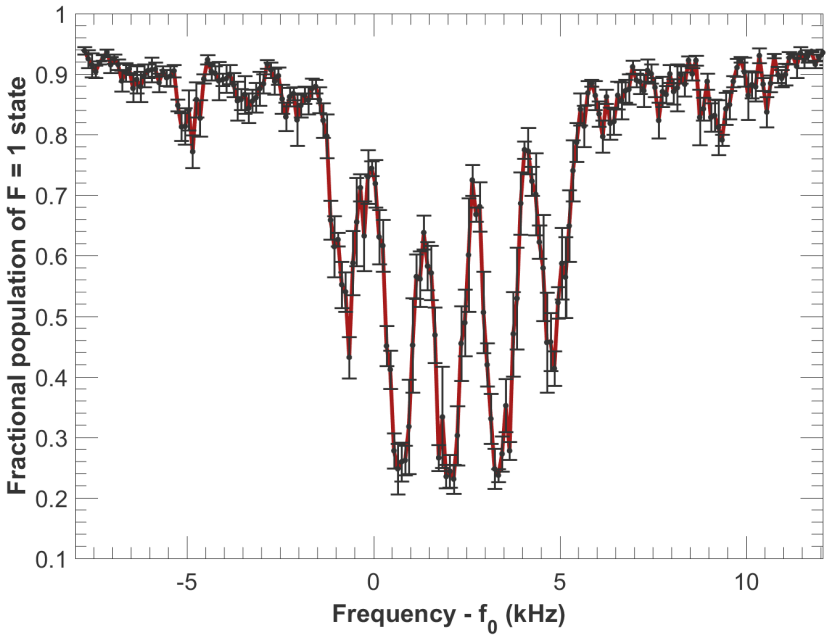

Figure 5.4: Ramsey fringes generated by varying the applied two-photon frequency difference of the two $\pi/2$ pulses, separated by 500 µs. The error bars are standard error of the mean for repeated measurements and the red line is an aid for the eye.

at a rate proportional to the frequency detuning, resulting in a final state population which is frequency dependent. Interference fringes can therefore be observed in frequency space, with the contrast decaying as the applied frequency moves away from resonance, as the transfer efficiency decreases with increased detuning (see equation 2.65).

Ramsey fringes were observed for variable frequency of the applied pulses as shown in Figure 5.4, giving an unambiguous signal of atomic coherence. The behaviour is in agreement with that predicted from theory, although there is an obvious reduction in visibility and contrast compared to the ideal case, and the offset is due to the AC Stark shift being uncompensated for in these measurements. Interestingly, it appears that using two $\pi/2$ pulses produces a greater contrast than observed in the Rabi oscillations, suggesting the decay in contrast in Figure 5.3 to be coming from the beams themselves, e.g. through Raman beam phase noise and intensity fluctuations.

5.1.3.2 Temporally Varied Pulses

Alternatively, it is possible to generate interference fringes in the time domain by holding the frequency of the Raman beams constant and varying the time between their application. This method, also known as Ramsey's method of separated fields, is particularly useful for probing the coherence time of the system, as interference is predicated on the ability to sustain coherence. As the sensitivity of the interferometer scales with the square of the time between the pulses in the Mach-Zehnder sequence, being able to maintain long coherence times is a key requirement

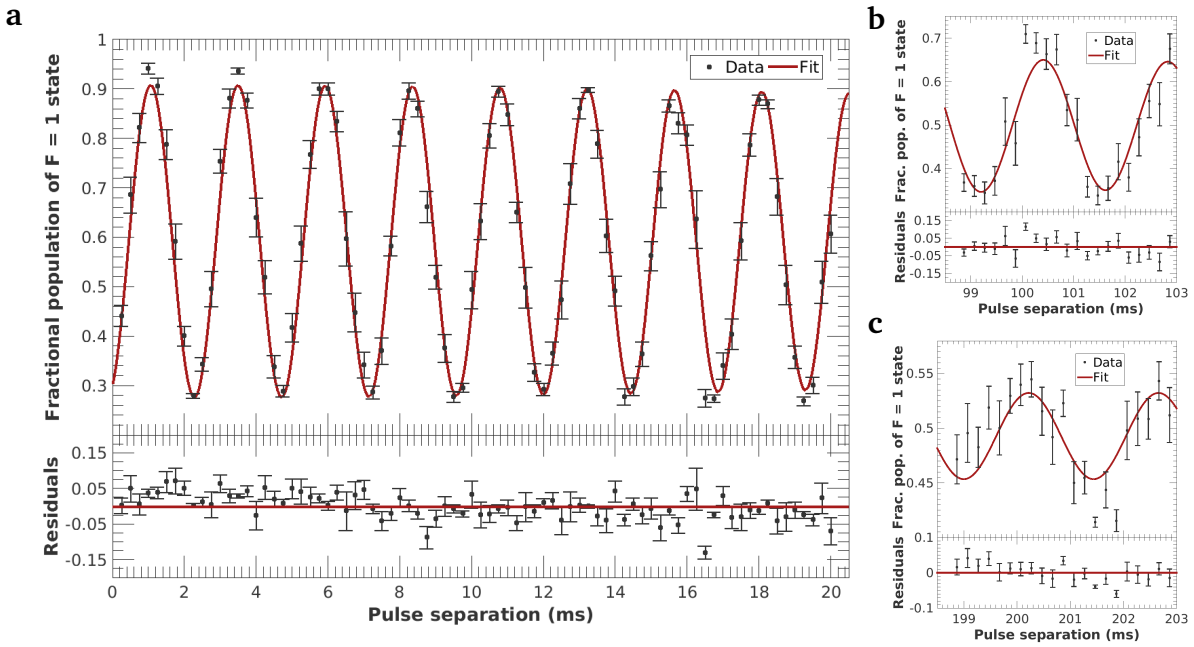

Figure 5.5: Ramsey fringes generated by varying the time delay between the two applied $\pi/2$ pulses, with frequency detuning of 1 kHz. The error bars are standard error of the mean for repeated measurements and the red line is a fit to equation 29 from reference [135]. Panels a-c show the data for increasing separations, which whilst maintaining clear oscillations, do show a reduction in contrast. The lower sections of each panel show the residuals from the fit.

and the target is for separations of order 100 ms.

To observe interference fringes, as is clear from Figure 5.4, the frequency must be detuned from the resonance, with faster oscillations with a reduced contrast for larger detunings. Here a frequency detuning of 1 kHz was used ($\sim 0.08\,\Omega_{\text{eff}}$) allowing for multiple, high-contrast interference fringes over the period of interest. Figure 5.5 shows the results of these experiments fit with a theoretical dephasing model [135], showing the ability to maintain coherence over long time periods, with interference still evident after 200 ms, albeit at a reduced contrast.

These results provide useful evidence about the suitability of the fountain for performing gravimetry based upon atomic interferometry. Although the fountain was previously used as a frequency standard which naturally also required the ability to maintain long-time coherence, there have been substantial modifications in the interim, including two vacuum baking processes. Verifying the continued capability of the fountain was therefore an important check – that is, checking that the vacuum pressure within the interferometry region remains sufficiently low, the magnetic shielding of a sufficiently high fidelity etc. Moreover, it serves as a necessary demonstration of the ability of Raman beams to drive such transitions and demonstrates that whatever noise is added to the system after the beat note detection is non-fatal. However, they do add credence to the hypothesis that the dominant noise source comes from the laser beams themselves, as the decay in contrast is over a considerably longer time period than for Rabi oscillations.

5.1.4 Interferometry on Multiple Clouds

The previous section demonstrated the capability of the apparatus to perform controlled coherent manipulations on launched atomic samples. However, to utilise all the advantages atomic interferometer provides for a gravity gradiometer, such experiments need to be performed on two clouds launched to different heights, but travelling with the same velocity at any given time.

Two-photon resonances (Figure 5.6a), Rabi oscillations (Figure 5.6b) and Ramsey fringes in frequency space (Figure 5.6c) have all been demonstrated for atomic clouds launched to simultaneous apogees at 0.7 m and 1 m. For the reasons outlined in section 3.4.2, no state selection could be performed for these sequences. Nevertheless, clear coherent behaviour can be observed – demonstrating the ability of this experiment to interact with two clouds simultaneously and to be able to measure the effects of these interactions.

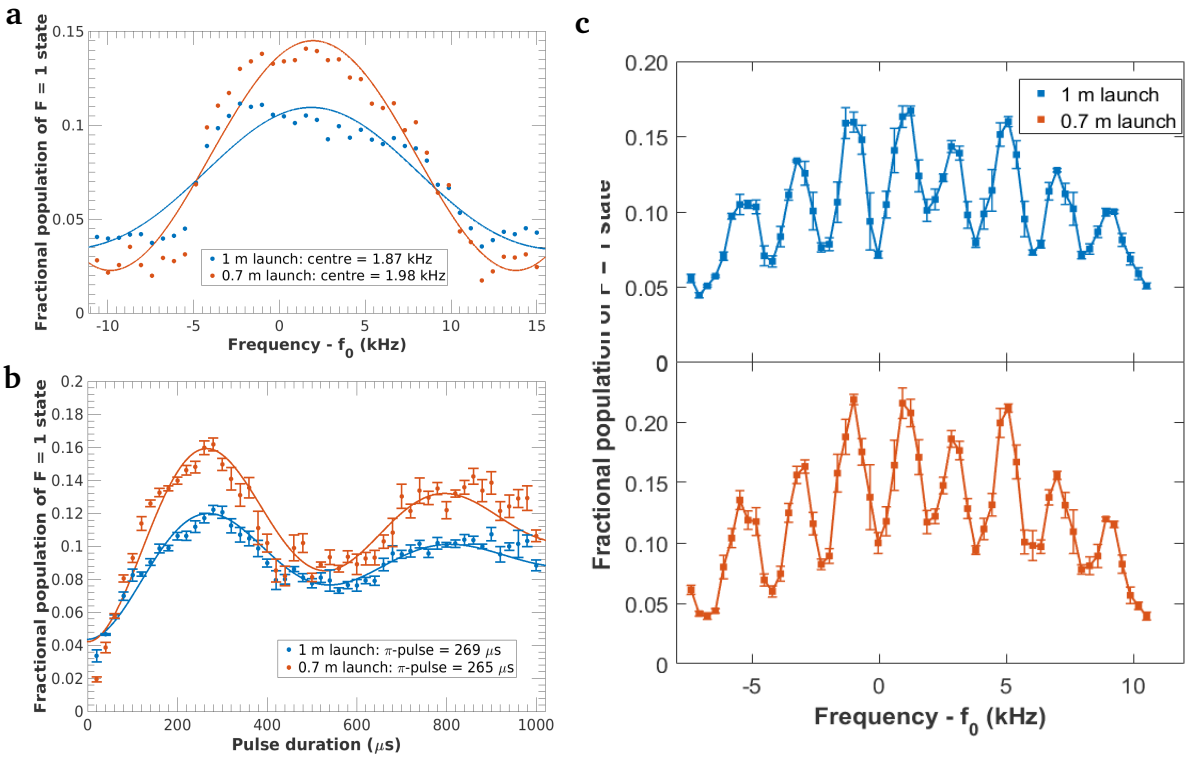

Figure 5.6: a) The two-photon resonances and (b) Rabi oscillations measured on two clouds launched to reach simultaneous apogees at 70 cm (orange line) and 1 m (blue line). c) Simultaneous Ramsey fringes generated by varying the frequency of the applied $\pi/2$ pulses on these two clouds. The reduced contrast compared to Figure 5.4 is due to a lack of state selection. On all plots, the error bars are standard error of the mean for repeated measurements.

5.2 Interferometry with Counter-propagating Raman Beams

Gravimetric measurements require the wavepacket to be split along the axis of gravity during free fall, requiring the Raman beams to impart a significant amount of momentum. This is achieved here by having the Raman beams in a counter-propagating, retro-reflecting configuration with orthogonal linear polarisations. In this setup, the emission and absorption occur in beams travelling in opposite directions, allowing the momentum recoil to be positively summed, rather than effectively cancelled as in the case of co-propagating beams. This spatial separation of the wavepacket requires a different pulse sequence ($\pi/2$-π-$\pi/2$ rather than $\pi/2$-$\pi/2$) and the interference comes from a different source; namely, it derives predominately from the laser phase imprinted upon the atoms during the interactions, which is not equal for the two interferometer arms during the π pulse for accelerating atoms, even when the Raman beams are resonant with the transition (see section 2.4 for details).

5.2.1 Velocity-Selective Pulses

It was mentioned early that one of the advantages of co-propagating beams is that they interact with the full velocity class of the atoms. This is no longer the case for counter-propagating beams, which only interact with a sub-set of the atomic population for any given Raman beam frequency offset [79]. This is due to the differing Doppler shifts experienced by the atoms for the two laser beam components and the number of atoms which are addressed by the Raman beams is inversely proportional to the pulse duration (see section 2.2.2.2). Conversely, velocity selection is important for ensuring a localised and repeatable launch height, especially if the same velocity selection can be applied to both atom clouds in the gradiometer. The velocity-selective nature of the counter-propagating Raman beams is therefore a double-edged sword – a well-defined vertical velocity is preferable, but so is maximising the number of atoms.

For an interferometry sequence, a velocity-selective π pulse is used to prepare the atoms into the $|F = 1, m_F = 0\rangle$ sub-state. This process is demonstrated in Figure 5.7. Initially there are multiple peaks arising from the various possible $\Delta m_F = 0$ transitions, which are further split from interactions with the two different available Raman beam pairs[ii] and broadened comparative to those shown in Figure 5.1 by the Doppler effect. Tuning the frequency of this pulse to be centred upon one of the two $|F = 2, m_F = 0\rangle \rightarrow |F = 1, m_F = 0\rangle$ transitions, allows the maximum available proportion of the atoms to be transferred to the desired $|F = 1, m_F = 0\rangle$ state (here around 1 %). After this initial π pulse, the residual $|F = 2\rangle$ atoms are removed by the radiation pressure caused by the application of light resonant to the $|F = 2\rangle \rightarrow |F' = 3\rangle$ transition. As a check, a second Raman beam pulse is then applied, this time showing only narrow $|F = 1, m_F = 0\rangle \rightarrow |F = 2, m_F = 0\rangle$ transitions, demonstrating that these velocity and

[ii] The atom can interact with k_1 from above and k_2 from below, and vice versa. The thin central peaks show the interaction with both pairs – i.e. when the Doppler shift is equal – and is reminiscent of saturated absorption spectroscopy.

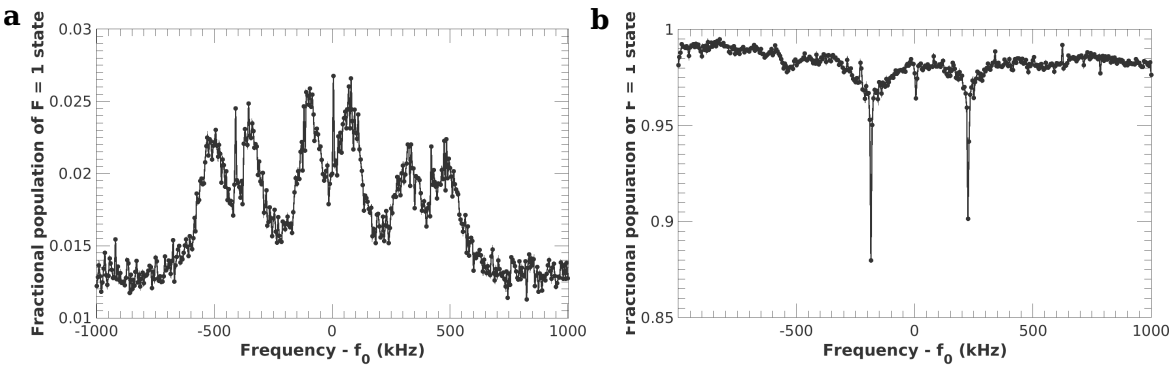

Figure 5.7: a) Atoms transferred from a single π-like, counter-propagating pulse (200 µs), with three resolvable $\Delta m_F = 0$ transitions, each split into two. b) Atoms transferred by a second pulse, with the atoms not transferred by an initial $|F = 2, m_F = 0\rangle \rightarrow |F = 1, m_F = 0\rangle$ pulse previously blown away. This second pulse was performed to check the state selection and is not required in the normal interferometry sequence.

state selecting processes are working (Figure 5.7b).

5.2.2 Mach-Zehnder Interferometry on Dropped Atoms

Following state selection, a $\pi/2$-π-$\pi/2$ sequence can be performed. To do this the frequency of the Raman laser beams must be chirped so as to remain resonant with the hyperfine transition. That is, the dynamic Doppler shifts caused by the acceleration of the free falling atoms must be compensated for, which is achieved by a linear chirp. For ^{87}Rb the necessary chirp rate is approximately 25 MHz/s and this can be verified by finding the two-photon resonance as a function of time. Whether the chirp needs to be positive or negative depends upon which of the two resonances is selected (see Figure 5.7).

Interference fringes can be generated in a similar way to Ramsey fringes by varying the chirp rate during a sequence, with the first $\pi/2$ pulse initially being resonant. This will introduce additional phase terms due to the changing effective angular frequency of the Raman beams between pulses and therefore lead to interference fringes as a function of the chirp rate (detailed in section 2.4.1). Such interference fringes are shown in Figure 5.8 taken for dropped atoms with various different times between pulses. These interference fringes show the expected sinusoidal behaviour with varying chirp rate, as demonstrated in Figure 5.9, where the central region of each scan is fit to a sine wave.

Moreover, these fringes are more noteworthy than those shown previously for the co-propagating configuration because they are dependent upon generating a macroscopic (from the atomic perspective) superposition. Consider that the de Broglie wavelength of a 5 µK atom is approximately 20 nm and that the separation of the two portions of the matter-wave following the original $\pi/2$ pulse and after 1 ms of free evolution is around 12 µm[iii] – the two atomic states are

[iii]The de Broglie wavelength is calculated from using the mean velocity given by the Maxwell-Boltzmann distribution of ^{87}Rb at 5 µK.

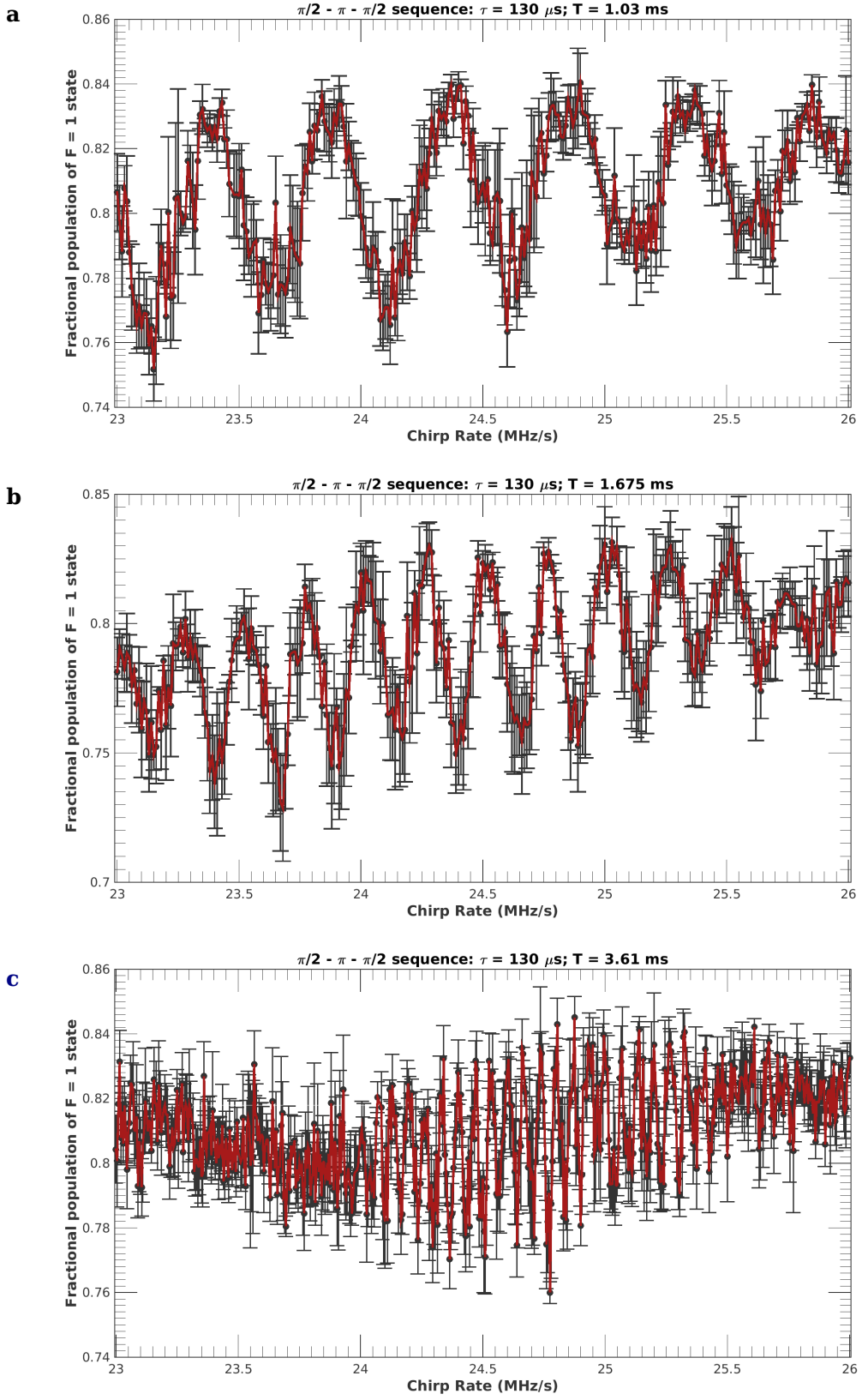

Figure 5.8: Dropped atoms undergoing a Mach-Zehnder interferometry sequence ($\pi/2$-π-$\pi/2$; $\pi/2 = 130\,\mu s$). The separation times between the pulses is increased from 1.030 ms (a) to 1.675 ms (b) to 3.61 ms (c). The error bars are standard error of the mean and the red line is an aid to the eye.

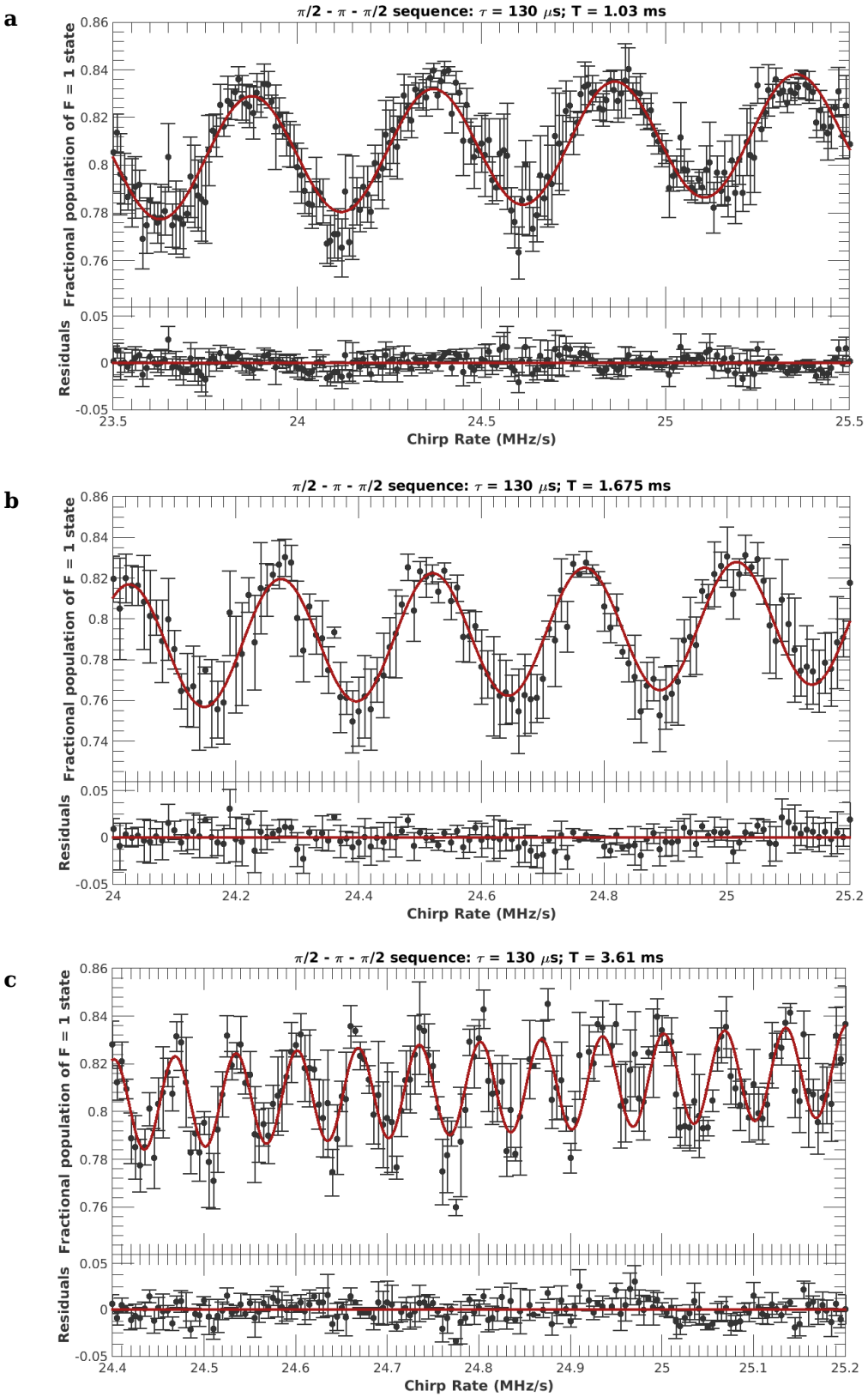

Figure 5.9: The central regions of the data shown in Figure 5.8 fit to a sine wave with a linear background (red lines, top sections). The bottom section of each panel shows the residuals between the data and the fitted function. The plots are shown in the same ordering as in Figure 5.8.

therefore separated by over 500 de Broglie wavelengths, explaining the necessity of the mirroring π pulse in the counter-propagating case, even at small separation times. For the co-propagating case, however, the momentum transferred by the Raman beams to the atoms is five orders of magnitude smaller, so the spatial separation is minimal, even in comparison to the de Broglie wavelength.

These fringes can also be used to estimate the phase error on the measurement in a coarse manner. As multiple data points are taken at each chirp rate (between 3 to 5), the standard deviation can be calculated. The root-mean-square standard deviation for the whole data set can then be converted into a phase noise by using the expected deviation for a sinusoid of known contrast and with a phase which is normally distributed. An estimate to the phase noise extracted from the data in this manner showed approximate agreement with the measured phase noise from the Raman beams, determined for the experimental parameters via equation 4.4. For example, for pulses separated by 1.03 ms (Figure 5.8a), the phase noise estimated from the fringes was 0.36 rad and from the measured Raman beam phase noise it was 0.39 rad[iv]. This approximate agreement shows that the Raman beam phase noise is indeed most likely the dominant noise source on the interferometer, making an reduction of this phase noise a priority for future experimental iterations (see section 6.1.1).

5.2.3 Mach-Zehnder Interferometry on Launched Atoms

Although the Mach-Zehnder fringes observed on dropped atoms could be used in principle to make a measurement of local gravity (see section 5.2.4), dropped atoms are not suitable for making measurements of the gradient of gravity in this system. This is because, in order to have common-mode noise rejection, which is the principle advantage of gradiometers based upon atomic interferometry, there needs to be two vertically separated clouds simultaneously falling with identical velocity, which is only possible for two independent MOT systems, which is prohibited by the chamber geometry. Furthermore, switching to a launch topology allows for longer interferometry times and utilises a well-defined and stable quantisation axis (section 3.3.5.1), which is ill-defined for the drop region, leading to potential systematic uncertainties.

Performing interference experiments with counter-propagating Raman beams on a launched sample, however, proved to be difficult for a variety of reasons, but principally due to a lack of detectable signal (Figure 5.10). The signal is suppressed for launched atoms, compared to dropped atoms, due to the increased velocity of the atoms as they pass through the detection region reducing the interaction time and therefore the signal size. What is a detectable number of atoms when dropping, is therefore not necessarily so when launching and the detection signal was found to be too noisy to make any reliable measurements of the state population, with the measured signal being comparable to the noise in the background arising from probe intensity

[iv] For separation of 1.675 ms, the estimates were 0.44 rad and 0.33 rad, and for 3.61 ms they were 0.33 rad and 0.40 rad. In both cases, the phase noise estimated from the fringes is listed first and that from the Raman beams second.

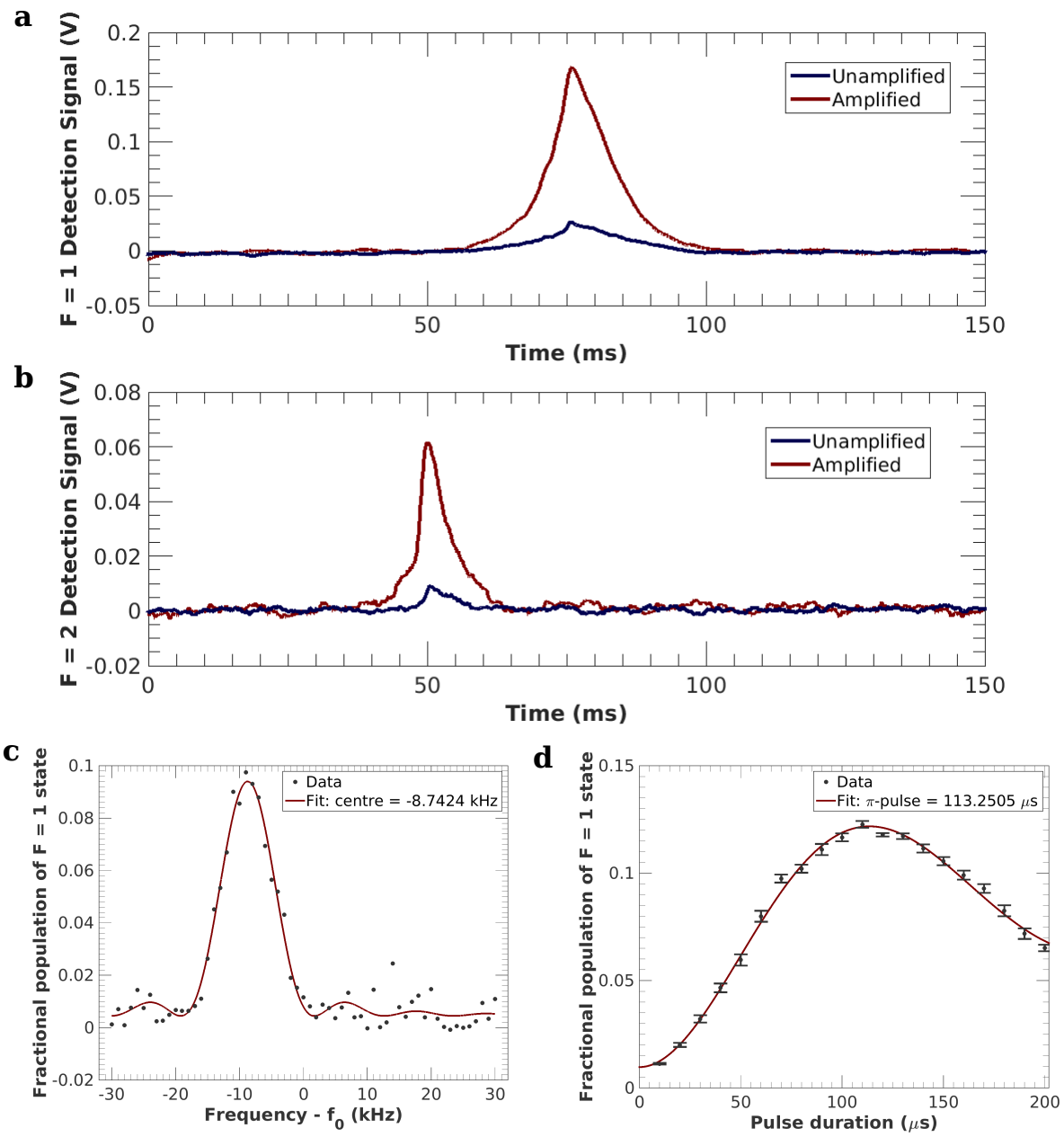

Figure 5.10: Amplifying one of the Raman beam components led to a large increase in the detection signal in both (a) the F = 1 channel and (b) the F = 2 channel, as shown in these sample detection signals. This is especially important for the latter, where the signal was previously comparable to the intensity fluctuations preventing reliable measurements being performed. c) The two-photon resonance for the amplified Raman beam configuration, showing a large AC Stark shift, and (d) Rabi oscillations at this resonance, using co-propagating beams. Error bars are standard error of the mean from repeated measurements.

fluctuations.

The loading rate of the MOT already being experimentally optimised and longer loading times leading to only small increases in the number of returning atoms. The density of the MOT being fixed, more loading leads to a larger cloud which will expand to larger than the detection beams and so doesn't increase the detected signal. In any case, it will also lead to significant dephasing as the loaded MOT size begins to approach the Raman beam diameter (Figure 3.5). The main way to increase the number of launched atoms, therefore, is a reduction in the Raman beam π pulse duration – relaxing the velocity-selective window and leading to more atoms than 1 % being selected (Figure 5.7). An increase in the Rabi frequency can be achieved by increasing the intensity of the Raman beams, which can most readily be implemented by increasing the amplification of the current Raman beams.

5.2.3.1 Amplifying the Raman Beams

Raman beam amplification was therefore performed by using an amplifier and frequency doubler combination (Quantel, EYLSA) to increase the power of one of the beam components[v]. 1560-nm light from the frequency-offset component was sent to this system from the current 1560-nm amplifier, with the independent frequency doubling crystal bypassed. Following this amplification, around 800 mW of usable light at 780 nm is produced, compared to around 100 mW in the usual configuration. Due to the necessity of beam overlap and preventing too large of an asymmetry between the two beams, a final configuration of 10 mW for the frequency-locked component and 90 mW for the frequency-offset component was selected. This increased the Rabi frequency to 28 kHz (Figure 5.10d), but with the disadvantage of introducing an AC Stark shift of -8.7 kHz (Figure 5.10c).

Using these amplified beams, it was then possible to observe interference fringes on launched atoms, due to the large increase in signal (Figure 5.10). There was still a problem with a low number of atoms, but fringes were visible for atoms launched to just inside the interferometry region (46 cm) and at a further height of 60 cm (Figure 5.11). Furthermore, the frequency of these fringes was observed to increase when increasing the interferometer time for 1 ms to 1.5 ms and by approximately the expected amount of 1.5^2. Clearly the fringes are still noisy, with a major contribution coming from the low atom number, in addition to the Raman beam noise which was the dominant noise source for the case of dropped atoms. The data presented is largely single-shot, with repeat measurements only for some obvious anomalies, and the detection signals were fit to skewed Gaussians to extract the most reliable population numbers (see section 3.3.7).

One problem which was identified was for the tendency for the phase lock to come undone when making large jumps in the frequency offset – this is phenomenon is visible in the occasional large spikes in the data, most prominently in Figure 5.8b. To counteract this a longer chirp period was introduced, beginning almost immediately after the state selection, with a small step

[v] Amplification of only a single beam could be performed due to time and equipment limitations.

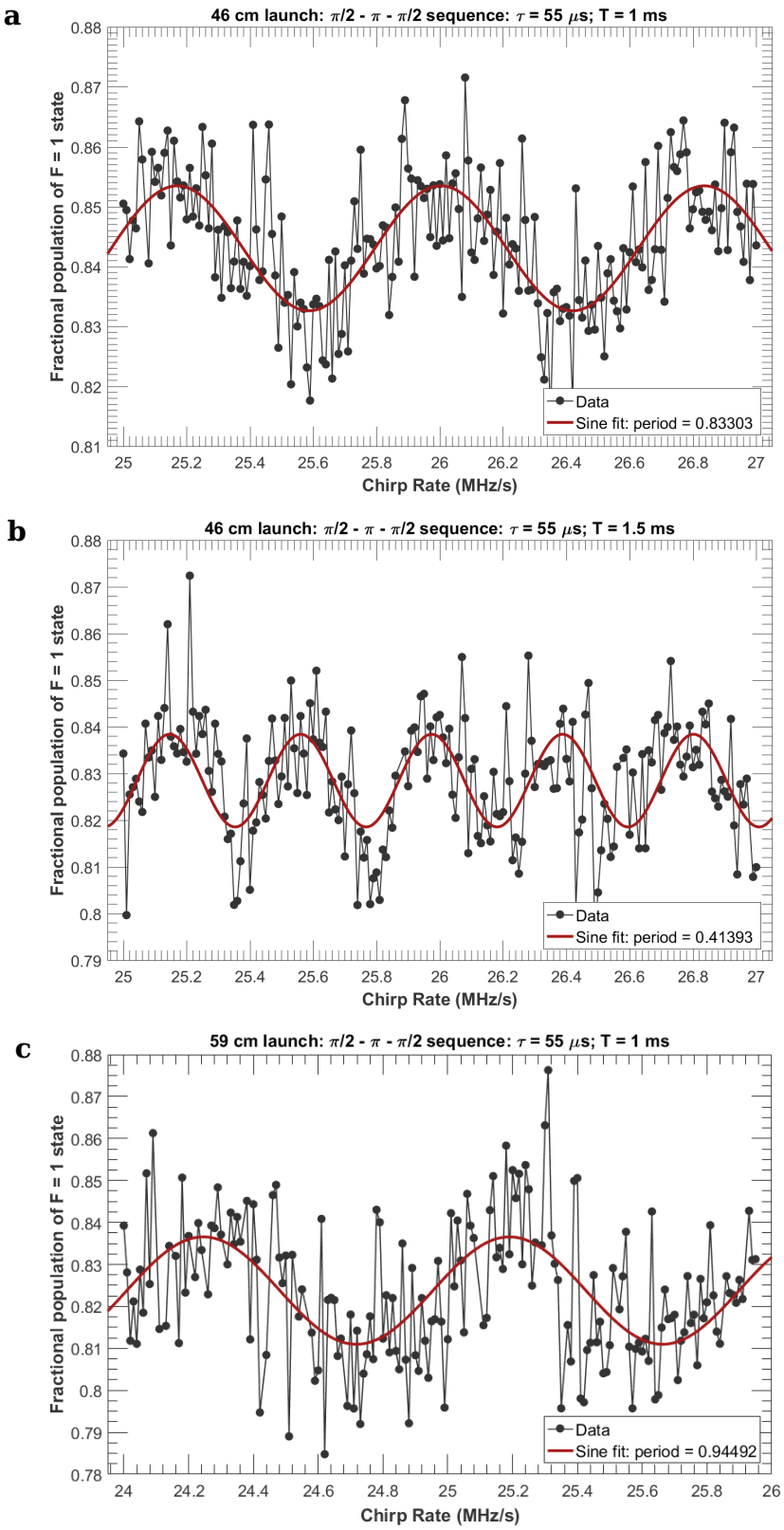

Figure 5.11: Using the amplified Raman beams and switching to a counter-propagating configuration, interference fringes from a Mach-Zehnder sequence with variable chirp rate for atoms launched to (a-b) 46 cm and (d) 59 cm were observed, shown fit with sine waves. Increasing the time between pulses for 46-cm launch (b), shows the expected decrease in fringe period.

in reference frequency adjusted so that the first interferometry pulse would always begin with the same frequency, regardless of the chirp rate. Nevertheless, it is clear that the noise sources will have to be reduced for a high-quality gravity measurement to be made.

5.2.4 To a Gravity Measurement

In order to use the achievable interference fringes to make a gravity measurement, they need to be calibrated. As previously discussed in section 2.4.1, the chirp rate provides the coarse measurement of the local acceleration by identifying which of the degenerate interference fringes is being measured and the population changes about this point according to $\Delta\Phi = k_{\text{eff}} g T^2$ give the ultimate precision. As shown in Figure 2.5, this calibration is a two-stage process: first, the central interference fringe, as a function of chirp rate, needs to be identified; second, the fringe itself needs to be calibrated at this chirp rate, by introducing a controlled phase difference between the pulses.

Identification of the central interference fringe is performed by varying the time between the pulses. As the peak position of central fringe alone is unaffected by changes in the temporal separation of the pulses, it can clearly be identified by comparing across multiple interference patterns. The experiment is in a position to perform this step immediately, it being necessary only to gather sufficient data for an unambiguous identification, by repeating the experiments shown in Figures 5.8 and 5.11 on a finer time scale.

Calibration of the central fringe is performed by introducing a controlled phase step to the Raman beams during the sequence – generally between the second and third pulses. Varying this phase shift between 0 and 2π gives information for a full fringe, which can be fit with a sinusoid to determine the phase offset. This phase offset in conjunction with the chirp rate, gives a reading for the local gravitational acceleration. When operating as a gravimeter, it is usual to toggle the phase difference by the same amount either side of the central point (i.e. the chirp rate matching gravitational acceleration), and to use the difference in the population to refine the current estimate for gravity. This is essentially the same method as used in atomic clocks to identify the transition frequency.

Device sensitivity can be gauged from the fit to such a generated fringe, its uncertainty and the time taken to collect the data. The ability to introduce such a controlled phase offset is not currently implemented, requiring the re-programming of the FPGAs which control the DDS. However, DDS boards are ideal for this purpose as they function by providing a fixed phase increment at each clock step, so by stepping this at one point, the desired phase offset will be achieved.

Chapter 6

Future Plans

6.1 Improvements to the Current Fountain Setup

6.1.1 Reduction in the Phase Noise of the Raman Beams

The Raman beam noise needs to be reduced if the target device sensitivity – of being limited by the quantum projection noise – is to be reached. Currently, there are two major contributions to the phase noise in this region: the introduction of phase noise from the separate optical paths; and the phase noise contribution of the reference source. As previously discussed, the former can be effectively suppressed by switching to a lock with a beat note taken at 780 nm (Figure 4.7), but the latter is largely an issue of the method of performing the phase lock comparing different frequencies via multiplication. That is, the use of the divider to compare the 6.835 GHz beat note to the DDS signal at 213 MHz, inherently degrades the phase noise spectrum by three orders of magnitude. A different method for comparing the reference source to the beat note is therefore required.

One such method is to first mix down the beat note signal to, for example, 213 MHz, allowing it to be directly compared to the DDS signal, as outlined in Figure 6.1. Assuming a relatively lower noise profile for the 6.835 GHz reference, this would maintain the phase noise profile of the DDS itself, allowing for a phase error of 7.5 mrad to potentially be reached, which is a factor of fifty lower than the phase noise of the beams used in the experiments shown in Chapter 5 and approaching the quantum projection noise ($\sim$1 mrad). While it is not necessarily clear that the reference level could be trivially reached, this possibility is suggested by Figure 4.7 and other systems show this behaviour over similar frequency ranges. Lower reference signals than 213 MHz could be used – it being dependent only upon the difference between the target beat note frequency and the mixing reference – which could again reduce the phase noise.

Mixing the beat note signal down requires a frequency synthesiser capable of reaching near the hyperfine splitting value, a role which could be performed by the frequency synthesiser previously used for irradiating the atoms with resonant microwaves (Anritsu, 69037B). Similarly the RF mixer used to add 10 MHz to this signal (Figure 3.11) could also be repurposed. Un-

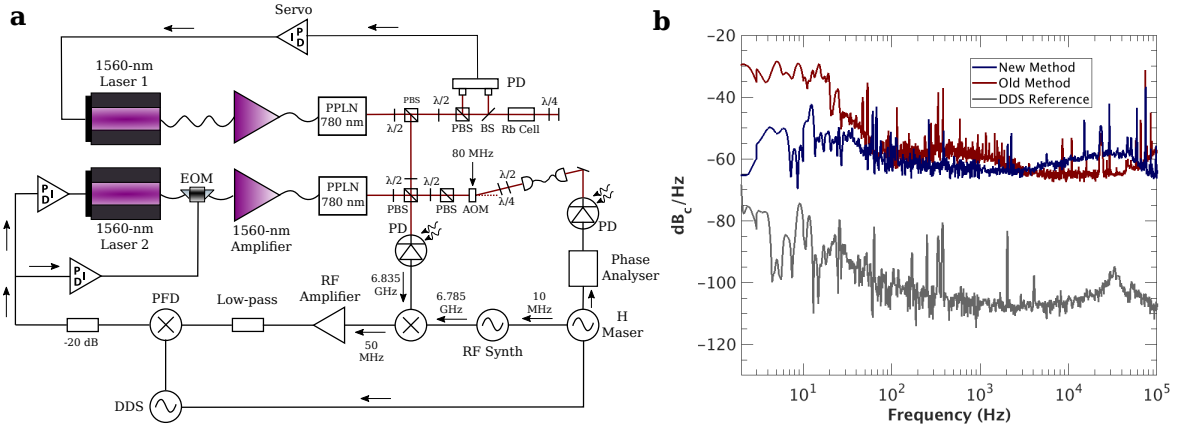

Figure 6.1: a) New design for the Raman beams. The signal from a beat note taken at 780 nm is mixed down to 50 MHz, with this signal then being compared to a reference source on phase frequency detector (PFD). b) This method achieves considerably better performance at low frequencies, but remains well above the noise floor. The equivalent plot using the earlier phase-locking method is shown for comparison. Note that a different DDS is used (see text for details).

fortunately, using the mixer prevents the current servo system (Vescent, D2-135) being used, however, this can then be replaced by a phase-frequency detector and PID controller, such as used for controlling the voltage sent to the EOM in the current setup. Alternatively, if the current feedback system is maintained, a minimum division factor of eight is required, leading to a potential reduction in Raman beam phase noise of 12 dB compared to the current setup.

To demonstrate the feasibility of this method, a test was performed using the setup shown in Figure 6.1. The beat note, measured at 780 nm, was mixed down with a signal 50 MHz below the hyperfine splitting, before being amplified to 0 dBm (Mini-Circuits, ZFL-1000LN) and having the resultant sidebands suppressed with a low-pass filter (Mini-Circuits, BLP-90). This signal is then compared with a 50 MHz signal from a DDS (Novatech, DDS8m) on a phase frequency detector (Analogue Devices, HMC3716LP4E) to produce a signal which can be used as an error signal for phase locking. This error signal is attenuated and sent to a laser servo (Vescent, D2-125) which provides active feedback to one of the Raman lasers. The other Raman laser is frequency locked as previously and the error signal is likewise again also used to control an EOM to further suppress the phase noise.

Such a setup was able to achieve a stable phase lock, whose spectrum compared well to those achieved previously (Figure 6.1), achieving substantially reduced phase noise in the low-frequency spectrum (∼20 dB reduction below 10 Hz). However, performance above these frequencies is broadly comparable and considerably above the phase noise of the reference DDS, suggesting that the limiting factor in this frequency range is not the reference source, as also seemed to be the case with the previous phase-locking method (Figure 4.7). Furthermore, although the phase-frequency detector is specified to work better with square, rather than sine waves, no difference in the phase noise was appreciable when running the DDS between these

two settings, again highlighting that the limiting factor is not the reference phase noise. Most likely, therefore, it is the feedback to the laser and EOM that needs to be optimised, for example, by further tuning the PID parameters and bandwidths.

Nevertheless, this proof-of-principle experiment shows obvious improvement over the previous method. The integrated interferometric phase noise, as calculated via equation 4.4 and using $T = 10\,\text{ms}$ and $\tau = 130\,\mu\text{s}$, is 163 mrad, which whilst still considerably larger than desired, is less than the 288 mrad from the equivalent lock using the divided down beat note. In fact, this noise is lower than best achievable noise of the previous system of 240 mrad (Figure 4.8). It is therefore clear that there are gains to be made by switching to this new method and improvements should be achievable with further experimental efforts.

6.1.2 Miscellaneous Improvements

In addition to the phase noise of the Raman beams, the other major experimental limitation was the lack of the detection signal. The easiest way to increase the detection signal is to increase the number of atoms, an improvement which will also have the advantage of reducing the quantum projection noise. More atoms can be achieved via amplifying the Raman beams in order to reduce the effective Rabi frequency and thus loosen the velocity selection criterion, as demonstrated in section 5.2.3.1. Indeed the situation is suitably critical, that no interference fringes for the Mach-Zehnder configuration were visible without this amplification. Amplification of the beams would require either new 1560-nm amplifiers and frequency doublers, or amplifiers for 780 nm, preferably one for each of the two beam components. Aside from these technical upgrades, no change in design is here required.

There are many additional experimental improvements that could be introduced to the interferometer, the most pressing experimental challenge is the introduction of state selection for the case of launching multiple atoms, as discussed in section 3.4.2. One potential solution would be the re-designing of the vacuum chamber to move the state selection port to a higher position. In the current configuration, this would be troublesome due to the three layers of magnetic shielding limiting available space (see Figure 3.1). However, due to the small effect of the quadratic Zeeman shift, the shielding is not as critical as for the clock, so some layers could potentially be removed – such a change may also allow for the detection chambers to be moved above the MOT region, potentially increasing the detection signal due to the decreased velocity of the atoms as they pass through the detection beams.

Work on vibrationally isolating the retro-reflecting mirror has so far been minimal and the device would benefit from the introduction of active feedback to the vibration isolation platform and a full calibration of the vibrational noise by use of a seismometer. The frequency locking of the Raman beams could be improved from the simple side-of-fringe setup by, for example, introducing modulation with an EOM on the light used for locking, as is the case for the locking of the repumper laser (section 3.2.2). An improved microwave reference source could also help to further lower the phase noise of the Raman beams. Finally, a proposed scheme to reduce the

effect of dephasing and move to large momentum transfer by cooling to quantum degeneracy is outlined in the following section.

6.2 Interferometry with launched BECs

One of the major improvements to the experimental design would be the reduction of the temperature of the sample significantly below the current experimental limit. This provides multiple advantages, mainly due to the reduced spatial spread of the atomic cloud during the launch. This reduces systematic effects, but moreover allows for an increase in the efficiency of the applied interferometry pulses, especially over long time periods. This is especially important for large-momentum transfer experiments, in which significantly more than $2\,\hbar k_{\text{eff}}$ is applied to the atoms, leading to an effective increase in k_{eff} and thus the sensitivity of the interferometer for the same physical size (i.e. for a constant inter-pulse time). Experiments transferring momenta of over $100\,\hbar k$ have been demonstrated [29, 137], giving a potential factor fifty increase in sensitivity. Large-momentum transfer is typically achieved by a succession of π pulses, often with Bragg beams [137, 138], but is also achievable with Raman beams [139, 140, 141]. Due to the multiplicative effect of losses, high-fidelity π pulses are therefore crucial for large-momentum transfer experiments. For example, if the pulse fidelity is 99 %, only 60 % of the atoms will be remaining in the correct state after fifty π pulses.

There are multiple methods for pushing the temperature below the µK limit typically achieved by polarisation-gradient cooling, including Raman sideband cooling and various evaporative cooling techniques. One such evaporative cooling technique is to use an all-optical method to trap the atoms in an optical dipole trap, before ramping down the trap potential to evaporatively cool the sample. Although such a technique does not reach the absolute lowest temperatures achieved by magnetic lensing [24], it does allow for the rapid production ($\sim 1\,\text{s}$) of an ultracold sample – sufficiently cold for BEC formation to occur [98]. A proposed gravity gradiometer using optical dipole trapping to produce multiple BECs is outlined in the following two sections.

6.2.1 Experimental Overview

The initial stages of the experiment would be identical to the current setup with atoms loaded into a MOT and further cooled in optical molasses by polarisation-gradient cooling. To increase the phase-space density of the atoms prior to loading into the dipole trap, a dark molasses configuration can be used [142, 143]. A crossed dipole trap will then be loaded and its optical intensity ramped down exponentially, evaporatively cooling the atoms to quantum degeneracy and an effective temperature of $\sim$10 nK.

To perform gradiometry, there needs to be at least two atomic samples at different heights in the interferometer. Whilst it is possible to rapidly produce multiple BECs in parallel [144] or in rapid sequence [145], it is simpler to begin with a single sample, which can then be split into

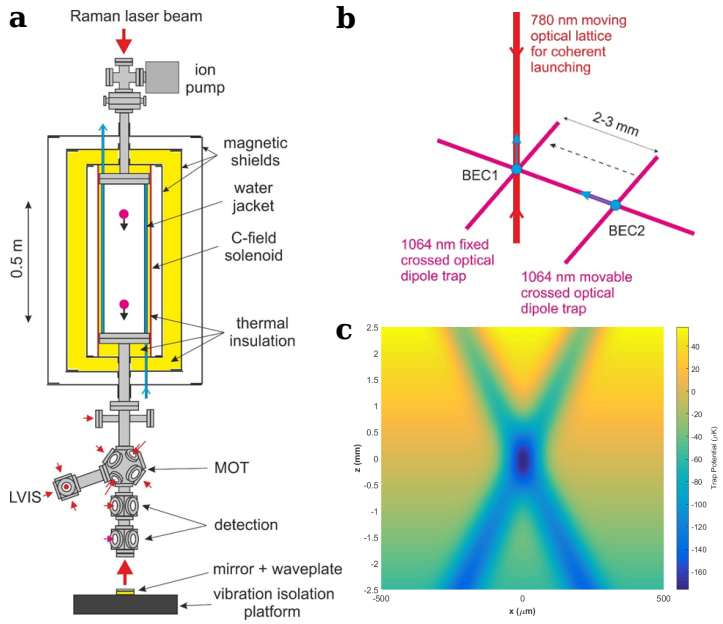

Figure 6.2: The same vacuum chamber (a) will be used to produce a BEC all optically, (b) which will be split and launched sequentially by an optical lattice. c) Cross-section of a sample calculated potential for a crossed dipole trap using 16 W of 1064-nm light focussed down to a waist of 60 μm. The beams are propagating along the z-axis at an inclination of 19.5° – the gradient introduced by gravity is clearly seen.

different samples. This can be performed by using large-momentum transfer techniques [29], by launching only a portion of the atoms each time [60], or using for example a dimple beam controlled by an AOM to generate a movable potential, allowing the BEC to be split in two horizontally [146], from which the two independent samples could then be launched sequentially to different heights (Figure 6.2). The latter scheme has the potential to allow for multiple such clouds to be produced simultaneously, by introducing multiple, controllable beams. The launch would be controlled by a moving optical lattice, the frequency of which will be detuned far from the transition.

By using such a rapid BEC production method, the repetition rate of the device is greatly increased in comparison to the current leading atomic interferometry gravity gradiometer [29]. This means that with only a modest momentum transfer of 10 $\hbar k$ on 3×10^5 atoms, performed at a repetition rate of 3 s, such a 1 m device as outlined above, could produce sensitivities of 1×10^{-9} g/$\sqrt{\text{Hz}}$ and 32 E/$\sqrt{\text{Hz}}$, assuming the quantum projection noise can be reached [62]. This is only a factor two worse than the current record gradiometry sensitivity, despite the device being an order of magnitude smaller [29].

6.2.2 Dipole Trap Configuration

As discussed in section 3.1.3, broadband-coated windows – suitable for light at both 780 nm and 1064 nm – have been installed on the vacuum chamber. This is to allow a dipole trap using

1064-nm light to be established [147], using a similar design to that in reference [98]. Around 16 W of power would be used to make a crossed dipole trap, with the same beam being recycled to form both arms of the cross to maximise the intensity, with both beams focussed down to the same point. The crossing angle is limited by the practicality of using the same window for the input of the two beams and the focussed diameter by the practicalities of the available lenses and establishing good alignment of the beams. The optimal values for these parameters can be determined by calculating the optical dipole potential, which should be as deep and as wide as possible.

The optical dipole potential ($U(\boldsymbol{r})$) is given by [147],

$$U(\boldsymbol{r}) = -\frac{3\pi c^2}{2\omega_0^3}\left(\frac{\Gamma}{\omega_0-\omega}+\frac{\Gamma}{\omega_0+\omega}\right) I(\boldsymbol{r}) \sim -\frac{3\pi c^2}{2\omega_0^3}\left(\frac{\Gamma}{\omega_0-\omega}\right) I(\boldsymbol{r}), \tag{6.1}$$

where Γ and ω_0 are respectively the natural linewidth and angular frequency of the transition, and ω and $I(\boldsymbol{r})$ are the angular frequency and intensity of the illuminating electromagnetic radiation, respectively. The counter-rotating term has been ignored following the application of the rotating wave approximation.

Equation 6.1, however, is for the case of a two-level and is therefore only accurate to the order of 10 % for ^{87}Rb, systematically increasing the depth of the potential well. For more accurate treatments the fine splitting of the ground state needs to be considered, i.e. the previously ignored D_1 line must also be included. For linearly polarised light [147]:

$$U(\boldsymbol{r}) = -\frac{\pi c^2}{2}\left[\frac{\Gamma_1}{\omega_1^3}\left(\frac{1}{\omega_1-\omega}+\frac{1}{\omega_1+\omega}\right)+\frac{2\Gamma_2}{\omega_2^3}\left(\frac{1}{\omega_2-\omega}+\frac{1}{\omega_2+\omega}\right)\right] I(\boldsymbol{r}); \tag{6.2}$$

where the subscript refers to the properties for the D_i line and there is a g-factor of two for the D_2 line.

Ideally, the dipole trap beams would enter horizontally so as to support the atoms against

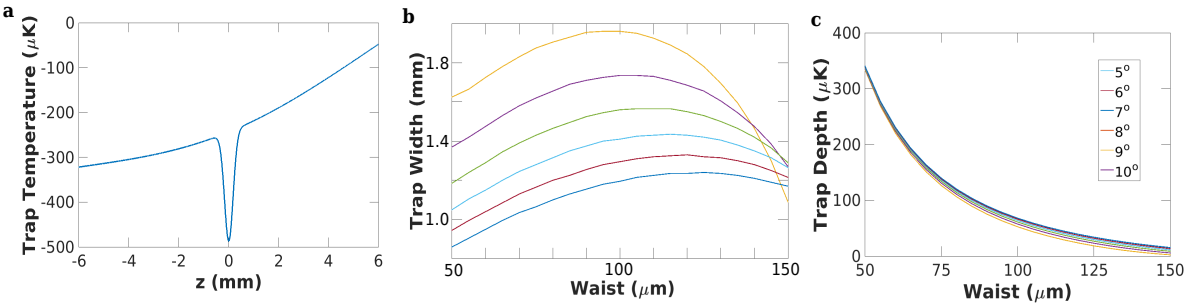

Figure 6.3: a) The projection of the optical dipole trap potential in the plane of the beam propagation and along the axis making an equal angle with the two beams (60 μm waist). The trap depth and trap width are defined by the potential difference between the turning point of the lower edge and the minimum of the well. b) The calculated trap width and c) the trap depth for different beam crossing angles and waists. For the key to both, see panel c.

gravity. Any vertical slope to the beams will introduce a gradient to the potential, which will tend to diminish the trap volume, as more energetic atoms escape and fall down the gravitationally induced gradient (Figure 6.3). Due to the geometry of the vacuum chamber, however, it is not possible to have the dipole trap beams enter horizontally, and they instead being limited to an inclination of 19.5° (Figure 3.1).

The total potential is therefore calculated from the summation of two potentials from the dipole trap beams calculated from equation 6.1 and the gravitational potential. Following conversion to temperature via the equipartition theorem, the trap depth is determined by the potential difference between the minimum of the well and the turning point of its lower edge, whilst the trap width is defined as the diametric distance from this turning point to the equipotential point on the other side of the waist (Figure 6.3). Using these models, approximately optimal values for crossing angle and focal spot size can be determined, being 7° and 80 μm, respectively.

Chapter 7

Summary

The work presented in this thesis represents the progress towards a ^{87}Rb atom interferometer capable of being operated simultaneously as an absolute gravimeter and gravity gradiometer. To this end, an atomic fountain and complimentary Raman beam system have been designed, constructed, implemented and tested. This system is capable of observing atomic interference on two independent atomic samples simultaneously and of generating macroscopic superpositions, demonstrating their coherence by observing interference fringes. However, the conversion of these interference fringes into gravimetric data has yet to be performed, although a clear pathway for such measurements exists.

The atomic fountain system was originally leveraged from a decommissioned atomic frequency standard, with only minor modifications to the vacuum system undertaken. Later investigations suggested the unsuitability of this setup for performing interferometry, due to the limiting effects of the clock cavity, the opening aperture of which would reduce both the experimental number of atoms and the possible contrast. The vacuum chamber was therefore reconstructed with the cavity removed and additional improvements were made allowing for the vacuum pressure to be halved and the optical access changed to allow for increased spectral flexibility.

Using a miniaturised optical distribution setup to allow for good long-term stability and potential transportability, the system was capable of loading 10^8 atoms in 100 ms into a magneto-optical trap. These atoms could then be launched in a moving optical molasses configuration at a temperature of 5 μK, before being detected in a stabilised detection system at the bottom of the fountain. Launching was performed so that two clouds were launched sequentially to simultaneous apogees, reaching heights of 70 cm and 1 m. This configuration keeps the repetition rate of the experiment equal to that of a single launch, reducing experimental dead time and increasing sensitivity, in comparison to a juggling setup.

A Raman beam system for performing the interferometric light-pulse sequence was designed and constructed, also with stability and miniaturisation for potential transportability being considered. The design utilised two amplified solid-state 1560-nm lasers which underwent second-

harmonic generation to the required frequency. One of the lasers was phase locked to the other via the comparison of their divided-down beat note to a reference frequency, with the lock controlled by both current feedback and with independent feedback to an electro-optical modulator. With this setup, interference fringes on launched atoms were observed, initially using a velocity-insensitive, co-propagating configuration to generate Ramsey fringes. These fringes were observed on timescales of 100s ms and on two independent clouds simultaneously, with a contrast possibly limited by the diffraction on the Raman beams. This configuration was also used to observe and cancel the AC Stark shift. Switching to a velocity-selective, counter-propagating configuration, interference fringes from a Mach-Zehnder interferometer were additionally observed on both dropped and launched atoms, with the primary limitation here being the lack of atoms passing the velocity selection stage. This configuration is that required for gravimetric measurements to be made.

Currently, this Raman beam system is the main source of noise for the interferometer, which in addition to a low number of atoms caused by the comparatively slow Rabi oscillations, is precluding the possibility of using the device for gravimetry. The latter is especially severe for launched atoms and will affect the gradiometer in particular, which has fewer atoms than for a single-launch configuration, but a substantially reduced dependence on Raman beam phase noise. The primary contribution to the noise arises from the noise on the phase lock of the Raman beams, which is limited by the method of using a divided-down beat note signal, which leads to an unavoidable effective increase in the reference source noise level.

To overcome these issues, it is proposed to amplify the Raman laser beams to allow for shorter pulses and therefore more atoms to pass the velocity selection procedure. Less trivially, a new Raman laser beam system has been designed and constructed, exhibiting reduced phase noise and the potential for further reductions down towards the quantum projection noise limit. Longer term, a launched Bose-Einstein condensate system, utilising the improvements in the new vacuum chamber, has been preliminarily designed with the higher phase space density and lower temperature allowing for higher fidelity π pulses for large-momentum transfer sequences and increased contrast due to decreased dephasing.

Appendix A

Laser Cooling & Trapping Theory

Atomic fountains were made possible by the rapid advances in laser cooling and trapping, discussed qualitatively in Chapter 1, being used for atomic timekeeping and interferometry from an early stage [9, 105, 148, 149]. To better understand the design and operation of the fountain, a more quantitative introduction to these mechanisms is presented in this appendix[i].

A.1 Doppler Cooling: Origin of Damping Force

The scattering rate (R) for a two-level atom is given by [81],

$$R = \frac{\Gamma}{2} \frac{I/I_{sat}}{1 + I/I_{sat} + 4\Delta^2/\Gamma^2} \tag{A.1}$$

where Γ is the linewidth of the transition, I is the intensity of the beam, I_{sat} is the saturation intensity of the transition, and Δ is the angular frequency detuning of the radiation from the transition angular frequency. For constant and low optical intensity, the scattering rate is therefore strongly dependent upon the detuning from the transition (Figure A.1a).

Consider the one-dimensional case of an atom moving along with a velocity v in the laboratory frame along the axis of a laser beam with wavevector k. Due to the Doppler effect the scattering rate will be a function of the atom's velocity:

$$R(\boldsymbol{v}) = \frac{\Gamma}{2} \frac{I/I_{sat}}{1 + I/I_{sat} + 4(\Delta - \boldsymbol{k} \cdot \boldsymbol{v})^2/\Gamma^2}. \tag{A.2}$$

In the case of two beams, counter-propagating and assumed to be acting independently, the scattering rate will obviously be unequal from the two beams due to the Doppler shift, for all velocities not equal to zero (Figure A.1b). Moreover, for red-detuned beams, the scattering rate will be larger for the beam opposing the motion of the atom, leading to a net damping force. To see this, consider that each photon emission or absorption imparts momentum $\hbar\boldsymbol{k}$ onto the

[i] Fuller descriptions are available in many of the early publications in this field and textbooks [77, 81, 150].

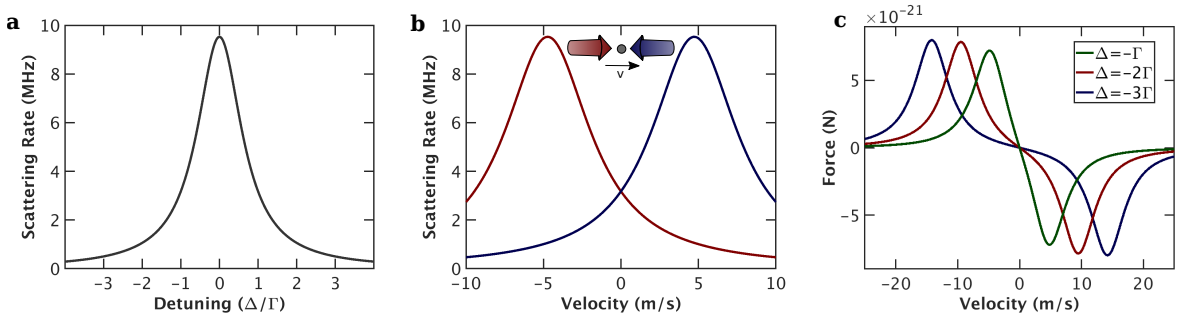

Figure A.1: a) The scattering rate for ^{87}Rb as a function of angular frequency detuning. b) The scattering rate from two counter-propagating beams with identical detuning ($\Delta = -\Gamma$) as a function of atomic velocity. c) The resultant force from the situation in c) and for multiple different detunings – note the linear capture region for $\Delta = -\Gamma$. All plots assume illumination by isotropically polarised light at the saturation intensity.

atom. Combining this with equation A.2, gives the velocity-dependent force from a single beam:

$$\boldsymbol{F}(\boldsymbol{v}) = \hbar\boldsymbol{k}\frac{\Gamma}{2}\frac{I/I_{sat}}{1 + I/I_{sat} + 4\left(\Delta - \boldsymbol{k}\cdot\boldsymbol{v}\right)^2/\Gamma^2} = \hbar\boldsymbol{k}R(\boldsymbol{v})\,; \tag{A.3}$$

and for two counter-propagating beams ($\boldsymbol{k_1} = -\boldsymbol{k_2} = \boldsymbol{k}$) of,

$$\boldsymbol{F}(\boldsymbol{v}) = \hbar\boldsymbol{k}\frac{\Gamma}{2}\left[\frac{I/I_{sat}}{1 + I/I_{sat} + 4\left(\Delta - \boldsymbol{k}\cdot\boldsymbol{v}\right)^2/\Gamma^2} - \frac{I/I_{sat}}{1 + I/I_{sat} + 4\left(\Delta + \boldsymbol{k}\cdot\boldsymbol{v}\right)^2/\Gamma^2}\right]. \tag{A.4}$$

In the case of low velocities ($v \ll \Gamma$) the higher-order terms can be neglected:

$$\boldsymbol{F}(\boldsymbol{v}) = 8\hbar k^2\frac{I}{I_{sat}}\frac{\Delta/\Gamma}{\left[1 + I/I_{sat} + 4\left(\Delta^2/\Gamma^2\right)\right]^2}\boldsymbol{v} = -\beta\boldsymbol{v} \tag{A.5}$$

where β is the damping coefficient and is positive for negative (red) detunings, as expected. This force is shown for the one-dimensional case in Figure A.1c and displays an approximately linear (pure) damping force in the central region around zero velocity. This central, linear region is used to define a capture velocity, the magnitude of which is approximately Γ/k, for low optical intensities and moderate detunings. For ^{87}Rb, the capture velocity is therefore 4.73 ms^{-1} compared to a room temperature (root-mean-squared) velocity of 290 ms^{-1}, meaning a fraction of just 6×10^{-6} atoms from the Maxwell-Boltzmann distribution is contained within this capture velocity. Therefore to cool a large number of atoms in the main experimental region, the background vapour should be maximised (without excessively increasing the collision or absorption rates) or the atoms should be pre-cooled. The latter approach is used in the fountain, as detailed in section 3.3.1.

A.1.1 Limits to Doppler Cooling: Heating Mechanisms

The expression in equation A.5 would appear to be able to damp the atomic motion to 0 K, in obvious contradiction to the third law of thermodynamics. In reality, of course, there will be numerous heating mechanisms preventing this, but one comes from the fluctuations in the Doppler cooling force itself and provides a limit to achievable cooling generally in the 100 μK regime [150] and is called the Doppler (cooling) limit [151].

The Doppler cooling process requires the preferential absorption of light, resulting in a transfer of momentum along the beam axis of $\hbar k$ to the atom, which is naturally followed by a spontaneous emission, which dissipates the energy from the system, at a time approximately $1/\Gamma$ later. This spontaneous emission also provides a momentum $\hbar k$, but isotropically[ii], meaning that while $\langle v \rangle = 0$, $\langle v^2 \rangle \neq 0$. The atom can therefore be considered to be undergoing a random walk in momentum space in discrete steps of $\hbar k$ at a rate of 2R (for two non-interfering beams). In a steady state system, the temperature will therefore be determined by the balance between this diffusive motion and the damping force and be related to the natural linewidth of the transition.

More formally, the rate of change of the mean velocity-squared can be considered:

$$\frac{\mathrm{d}}{\mathrm{dt}}\langle v^2 \rangle = \frac{2}{m}\langle \boldsymbol{F} \cdot \boldsymbol{v} \rangle \tag{A.6}$$

where m is the atomic mass. For the Doppler cooling force of equation A.5, this becomes,

$$\frac{\mathrm{d}}{\mathrm{dt}}\langle v^2 \rangle = \frac{16\hbar k^2}{m}\frac{I}{I_{sat}}\frac{\Delta/\Gamma}{\left[1 + I/I_{sat} + 4\left(\Delta^2/\Gamma^2\right)\right]^2}\langle v^2 \rangle. \tag{A.7}$$

For the momentum imparted by the absorption and the emission:

$$\langle v^2 \rangle = 2\left(\frac{\hbar k}{m}\right)^2; \tag{A.8}$$

and thus,

$$\frac{\mathrm{d}}{\mathrm{dt}}\langle v^2 \rangle = 2R\langle v^2 \rangle = 2\Gamma\frac{I/I_{sat}}{1 + I/I_{sat} + 4\Delta^2/\Gamma^2}\frac{\hbar^2 k^2}{m^2}; \tag{A.9}$$

where the factor two in equation A.8 is due to the fact emission and absorption is a two-step process and in equation A.9 due to the fact that scattering occurs from two beams.

When the sample is at thermal equilibrium, equations A.7 and A.9 must be equal and opposite, meaning,

$$\langle v^2 \rangle = \frac{\hbar\Gamma}{4m}\left(\frac{1 + I/I_{sat} + 4\Delta^2/\Gamma^2}{-2\Delta/\Gamma}\right). \tag{A.10}$$

From the equipartition theorem, this can be related to a temperature. In the case of low intensity

[ii] Assuming an isotropic polarisation of the light, as is approximately the case for six-beam three-dimensional optical molasses (Appendix A.2).

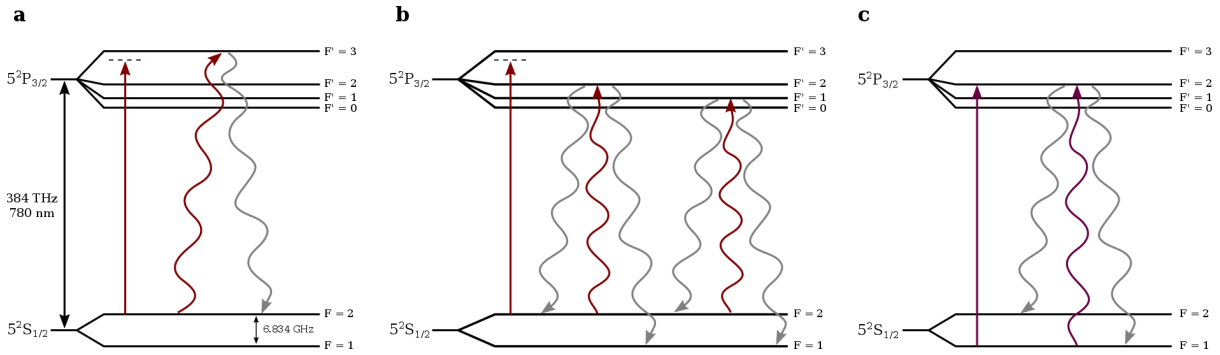

Figure A.2: a) The cooling light predominately excites atoms from the $F = 2$ to $F' = 3$ state, which is a closed transition, as $|\Delta F| \leq 1$. b) However, transitions to the $F' = 2$ or $F' = 3$ states are also possible, from which the atoms can decay to the $F = 1$ state and be lost to the cooling process. Although the process in a) dominates, the scattering rate is sufficiently high that the processes in b) prevent atoms being cooled or trapped on an experimentally useful timescale. c) Light resonant to the $|F = 1\rangle \rightarrow |F' = 2\rangle$ transition is therefore used to repump the atoms into the $F = 2$ state via spontaneous emission from $F' = 2$. Diagrams are not to scale.

beams, the I/I_{sat} term can be ignored, yielding a function for the steady state temperature of,

$$T = \frac{\hbar\Gamma}{4k_B}\left(\frac{1 + 4\Delta^2/\Gamma^2}{-2\Delta/\Gamma}\right) \tag{A.11}$$

where k_B is the Boltzmann constant. The minimum of this function is the Doppler cooling limit (T_D) [151] and is found when $\Delta = -\Gamma/2$:

$$T_D = \frac{\hbar\Gamma}{2} \tag{A.12}$$

For the low-intensity limit, this temperature is surprisingly dependent only on the linewidth of the transition, not on the frequency of the transition, nor the optical intensity or atomic mass. This result is general, including when using a full three-dimensional treatment, and can also be derived by, for example, consideration of the Fokker-Planck equation [81, 150]

For ^{87}Rb the Doppler cooling limit is 147 μK, but temperatures smaller than this are readily achieved in optical molasses (Appendix A.2) due to additional cooling mechanisms dependent upon the magnetic substructure of the atom (see Appendix A.4).

A.1.2 Doppler Cooling ^{87}Rb: Repumping Transitions

It is clear that Doppler cooling only works for atoms undergoing absorption and spontaneous emission between two specific energy levels and that in order to suitably lower the temperature, many such absorptions and re-emissions must occur. Doppler cooling therefore requires a closed transition. The typical cooling transition for ^{87}Rb, between the $|F = 2\rangle$ and $|F' = 3\rangle$ states, is such a closed transition, due to selection rules (Figure A.2). However, it is also possible

that off-resonant excitations to the $|F' = 1\rangle$ and $|F' = 2\rangle$ states can occur[iii]. Following such an excitation, the atom can decay to the $|F = 1\rangle$ state and so be lost to the cooling process. Uncompensated for, this effect leads to a rapid decay of all the atoms to the $|F = 1\rangle$ state and cooling can no longer occur and nor can the atoms be trapped (see Appendix A.3).

The solution is to introduce a small quantity of light which is resonant with the $|F = 1\rangle \rightarrow |F' = 2\rangle$ transition, which allows the $|F = 2\rangle$ state to be repopulated and for the cooling process to proceed. This process is referred to as repumping and explains the need for the second laser in the setup (section 3.2.2).

A.2 Optical Molasses

Using Doppler cooling to generate three-dimensional cooling upon an atomic sample, requires a configuration of laser beams such that there is a velocity-dependent, motion-opposing force irrespective of the precise direction of the atom. That is, regardless of the atomic motion, there must always be red-detuned light opposing it. This can be achieved by a minimum of four such laser beams[iv], though it is generally performed with a three pairs of counter-propagating beams. When cooled in such a field atoms are observed to move and diffuse slowly outwards, leading the original researchers to name the phenomenon optical molasses [152, 153].

The cooling observed in optical molasses was actually observed to be considerably below the Doppler cooling limit [153, 154], for reasons discussed in Appendix A.4, though the atoms are not actually trapped by the molasses. In fact, it is impossible to trap atoms using the scattering force alone [155], leading to the necessity of combining optical molasses with other methods for trapping, usually via a magneto-optical trap (MOT).

A.3 Magneto-Optical Traps

Achieving a trap from an optical molasses setup requires the introduction of a position-dependent damping force to return the diffusing atoms towards the centre of the beam overlap region. In a MOT, such a force is generated by introducing a magnetic field gradient and suitably chosen beam polarisations [156]. In the quintessential MOT, anti-Helmholtz coils[v], are used to generate a spherical quadrupole magnetic field:

$$\boldsymbol{B} = B_0 \left(-\frac{1}{2} x\hat{\boldsymbol{x}} - \frac{1}{2} y\hat{\boldsymbol{y}} + z\hat{\boldsymbol{z}} \right) \tag{A.13}$$

[iii] Using equation A.1, the ratio of the scattering rate for F=2 to F'=1,2,3 is 0.0026:0.0069:1 for illuminating light of saturation intensity and detuned 20 MHz below the $|F = 2\rangle \rightarrow |F' = 3\rangle$ transition. Whilst the cooling transition clearly dominates, the scattering rates for the other two transitions are here still $\sim$ kHz. For light resonant to the $|F = 2\rangle \rightarrow |F' = 3\rangle$ transition, the ratio is 0.0001:0.0002:1.

[iv] In general, n-dimensional Doppler cooling requires a minimum of $n + 1$ laser beams.

[v] Anti-Helmholtz coils are the same as Helmholtz coils, but with the current of the two coils running in opposite directions (helicities). That is, the coils of radius r are separated by axial distance r, with equal current running clockwise through one coil, and anti-clockwise through the other.

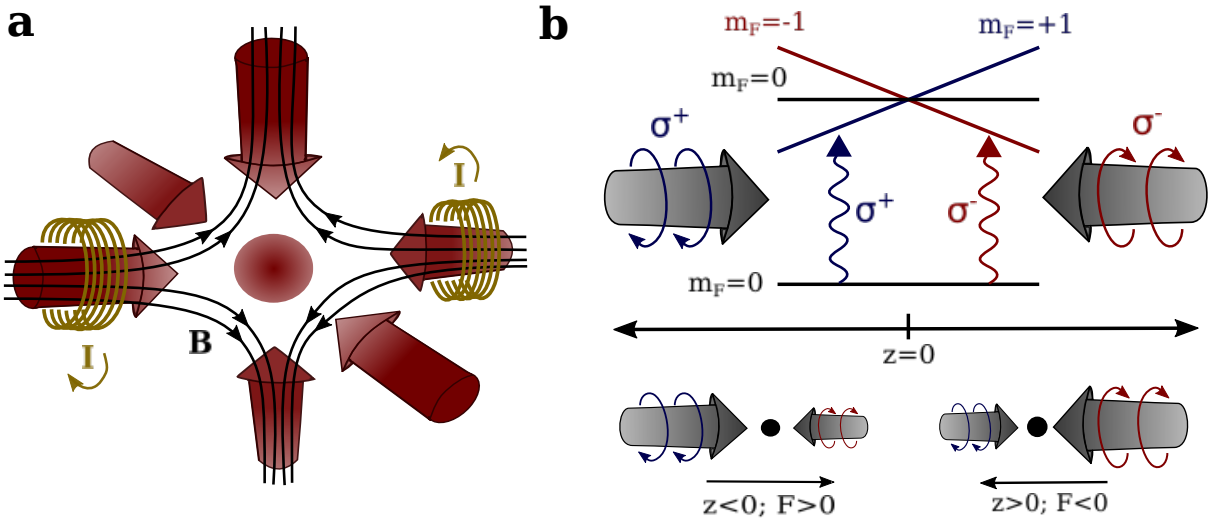

Figure A.3: a) In a standard magneto-optical trap, the atoms are illuminated by three pairs of mutually orthogonal counter-propagating beams, overlapped with a spherical quadrupole magnetic field. Each beam drives opposite σ transitions to its partner beam. b) This generates a position-dependent restoring force due to the Zeeman splitting of the energy levels shifting the transitions driven by the beam opposing the motion of the atom closer to resonance as the atom moves away from the centre. This force is complimentary to the Doppler cooling mechanism, allowing for simultaneous cooling and trapping. The atomic levels have been simplified for demonstration purposes.

with B_0 the magnetic field gradient at the centre of the trap and with one the counter-propagating beam pairs along the z-axis. This field causes a Zeeman shift of the magnetically sensitive ground and excited state sub-levels, the strength of which increases radially from the centre, and so varying the atomic resonance frequencies. Each pair of counter-propagating beams are set to have opposite circular polarisation ($\sigma^{\pm}$), which drive transitions that alter the magnetic sub-level by $\Delta m_F = \pm 1$. As the energy of the magnetic sub-levels depends upon the position of the atom, the probability of $\Delta m_F = \pm 1$ transitions is also position dependent. Specifically, due to the red-detuned cooling light, σ^+ and σ^- transitions become closer to resonance as the atom moves into the negative and positive magnetic field regions, respectively. As each absorption pushes the atom in the direction of the laser propagation, correct setting of the polarisation generates a restoring force. This is most easily visualised for the one-dimensional case and assuming all atoms to be in a magnetically-insensitive ground state (Figure A.3). Therefore, by giving the cooling beams the suitable circular polarisation, the atoms can be both cooled and trapped in this configuration.

Specifically, the probability of $\sigma^{\pm}$ transitions will now vary with position, as illustrated in Figure A.3. In the illustrated configuration and taking the z-axis, the frequency of $\Delta m_F = +1$ transitions varies linearly and positively with axial position, whilst for $\Delta m_F = -1$ transitions, it is the same but negatively. That is, for negatively-detuned beams and in comparison to the zero-field case, σ^+ transitions are shifted closer to resonance in the negative region and further

from resonance in the positive region, with the converse true for σ^- transitions. Therefore, by setting the beam propagating in the positive z-direction (from left to right in Figure A.3) to have σ^+ polarisation and the beam in the negative direction to have σ^-, a position-dependent scattering force can be established. As each absorption pushes the atom in the direction of the laser propagation, suitable setting of the polarisation has therefore generated a restoring force, without effecting the Doppler cooling mechanism, allowing the atoms to be both cooled and trapped in a MOT.

The argument outlined above is also applicable to the x and y axes, but with the polarisations reversed, in line with equation A.13. To establish a MOT, each counter-propagating beam pair must have circular polarisations with the same helicity[vi], with this helicity the same for the x and y directions and opposite for the z. In general when establishing a MOT, these polarisations are first set and then the current through the magnets flipped if the initial configuration is incorrect.

A.4 Polarisation-Gradient Cooling

Cooling below the Doppler limit occurs naturally in a MOT and, much more prominently, optical molasses configuration for coherent cooling beams, a condition usually satisfied as beams are typically derived from the same laser. This cooling mechanism depends upon the establishment of polarisation gradients across the atomic population which generate forces which oppose the atomic motion [102, 103]. When analysing this problem in one dimension, there are two quantitatively different mechanisms depending on whether these polarisation gradients are established from two perpendicularly linearly polarised beams, or, as in a MOT, by two opposing σ^+ and σ^- beams. These two cooling mechanisms are called Sisyphus cooling (Figure A.4) and motion-induced orientation cooling (Figure A.5), respectively, and have been experimentally tested in one-dimensional cases [157, 158]. In a standard experimental situation, however, both cooling mechanisms will occur and contribute to the final state temperature, due to the complicated nature of the composite electric field and its polarisation gradients formed by the six laser beams overlapped in three-dimensional space [77, 102, 150].

A.4.1 Sisyphus Cooling

In the case of two counter-propagating beams with perpendicular linear polarisations ($\boldsymbol{\epsilon_x}$ and $\boldsymbol{\epsilon_y}$) and equal amplitudes ($\mathcal{E}_0$), a gradient of ellipticity is established[vii]:

$$\mathcal{E}(z) = \mathcal{E}_0 \boldsymbol{\epsilon_x} e^{ikz} + \mathcal{E}_0 \boldsymbol{\epsilon_y} e^{-ikz} \tag{A.14}$$

[vi] They drive opposite σ transitions due to their different propagation directions.

[vii] The derivations and descriptions in this and the following section on motion-induced orientation cooling is based upon that in Jean Dalibard and Claude Cohen-Tannoudji's 1989 paper [102].

$$\mathcal{E}(z) = \mathcal{E}_0\sqrt{2}\left[\cos(kz)\left(\frac{\boldsymbol{\epsilon_y}+\boldsymbol{\epsilon_x}}{\sqrt{2}}\right) - i\sin(kz)\left(\frac{\boldsymbol{\epsilon_y}-\boldsymbol{\epsilon_x}}{\sqrt{2}}\right)\right] \tag{A.15}$$

where the beams are travelling along the z axis and the time component has been ignored. From equation A.15 the ellipticity can be seen to rotate along the axial direction of the beams (Figure A.4b). For example, the beam is seen to be linearly polarised in the $(\boldsymbol{\epsilon_x}+\boldsymbol{\epsilon_y})/\sqrt{2}$ direction at $z=0$, but circularly polarised (σ^-) at $z=\lambda/8$, before being linearly polarised in the perpendicular $(\boldsymbol{\epsilon_y}-\boldsymbol{\epsilon_x})/\sqrt{2}$ direction at $z=3\lambda/8$, and circular again (but σ^+) at $z=\lambda/2$. Such a rotating pattern repeats along the axis with a total periodicity equal to the wavelength[viii].

To understand how such a gradient of elliptical polarisation can lead to cooling, consider a two-level atom, whose ground state has two Zeeman sub-levels ($|g, J=1/2\rangle$) and whose excited state has four ($|e, J=3/2\rangle$). Assuming that the laser light establishing these gradients is red-detuned from the transition, as is the case for Doppler cooling, then the AC Stark shifts experienced by the two ground sub-states is such as to shift the energy of these states downwards. However, due to the unequal nature of the Clebsch-Gordan coefficients for the $|g, J=1\rangle \rightarrow |e, J=2\rangle$ transitions, these light shifts are not in general equal for the two sub-states and depend upon the polarisation of the light. For example, for σ^+ polarisation, the Clebsch-Gordan coefficient for $|J=1/2, m_J=+1/2\rangle \rightarrow |J'=3/2, m_{J'}=+3/2\rangle$ transitions is 1 and the coefficient for $|J=1/2, m_J=-1/2\rangle \rightarrow |J'=1/2, m_{J'}=+1/2\rangle$ is $1/\sqrt{3}$, meaning the shift is three times stronger (more negative) for the $|g, m_J=+1\rangle$ than the $|g, m_J=-1\rangle$ sub-state. The situation is reversed for σ^- polarisation and the light shift is equal for linear polarisations. Therefore it is clear that the relative energy of the ground sub-states changes along the axial direction of the laser beams (Figure A.4c). Furthermore, it should also be clear that such a situation leads to optical pumping. That is, in regions of σ^+ polarisation, the atom will tend to be pumped to the lower energy $|g, m_J=+1/2\rangle$ sub-state as the $|g, m_J=+1/2\rangle \rightarrow |e, m_J=+3/2\rangle$ is closed, whereas following an absorption from the $|g, m_J=-1/2\rangle$ sub-state, it is possible for the atom to undergo spontaneous emission to the $|g, m_J=+1/2\rangle$ sub-state (Figure A.4d).

Consider, finally, an atom in the $|g, m_J=-1/2\rangle$ sub-state moving in the positive z direction and with an initial position of $z=\lambda/8$ (Figure A.4c). The atom will convert kinetic energy into potential energy as it moves, in a conservative manner, with this exchange of energy mediated via a corresponding change in the momentum of the laser field, by a process of stimulated emission and absorption between the two laser beams. However, when the atom reaches the top of the potential hill at $z=3\lambda/8$, there is also a high probability, due to the optical pumping process, for it to absorb a photon to the excited state, only to emit down to the other sub-state state ($|g, m_J=+1/2\rangle$), which is now the lower in energy. This *spontaneously emitted* photon breaks the symmetry of emission and absorption processes, carrying away an excess equal to

[viii] It should be noted that such gradients of ellipticity occur for all configurations of non-identical polarisation, with the exception of σ^+-σ^- (the motion-induced cooling configuration), and that identical amplitude is not strictly required [102].

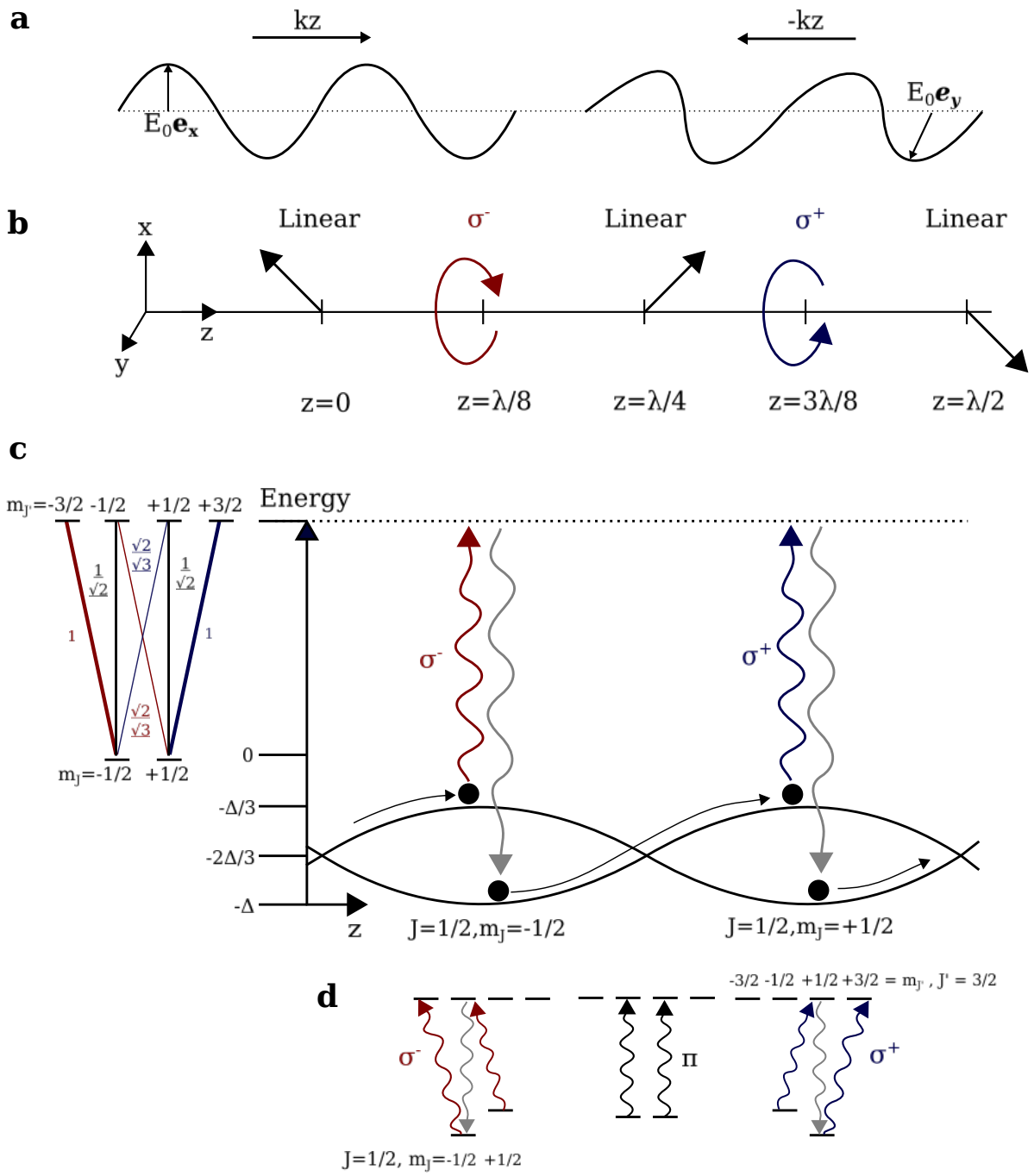

Figure A.4: An explanation of the 1-D sub-Doppler polarisation-gradient Sisyphus cooling mechanism. a) Two coherent laser beams of perpendicular linear polarisation are counter-propagating and (b) their superposition establishes a polarisation gradient of rotating ellipticity. c) For the case of a two-level atom with $J = 1/2$ and $J' = 3/2$, a combination of the Clebsch-Gordon coefficients and the AC Stark shift produce a variation in the energy of the two ground sub-states along the beam axis, causing an moving atom to climb potential hills. d) Optical pumping preferentially populates the lower energy state and allows energy to be removed from the system via spontaneous emission (grey lines).

the light shift between the two states. Averaging over many such events, which can add as well as remove energy, there is seen to be a net removal of energy from the atoms, leading to a reduction in temperature.

The atom can therefore be considered to be constantly in the process of climbing potential hills, only to fall down via a process of spontaneous emission, explaining the name of Sisyphus cooling[ix]. Such a class of cooling was originally used to explain the behaviour of atoms in high-intensity stimulated optical molasses [159, 160] and similar mechanisms are exploited for cooling atoms in other entirely unrelated ways [161, 162, 163].

A.4.2 Motion-Induced Orientation Cooling

Consider, in contrast, the situation in Figure A.5a where the two equal amplitude, counter-propagating beams are orthogonally circularly polarised:

$$\mathcal{E}(z) = -\frac{\mathcal{E}_0}{\sqrt{2}}\left(\boldsymbol{\epsilon_x} + i\boldsymbol{\epsilon_y}\right)e^{ikz} + \frac{\mathcal{E}_0}{\sqrt{2}}\left(\boldsymbol{\epsilon_x} - i\boldsymbol{\epsilon_y}\right)e^{-ikz} \tag{A.16}$$

$$\mathcal{E}(z) = -\frac{2i\mathcal{E}_0}{\sqrt{2}}\left[\boldsymbol{\epsilon_x}\sin(kz) + \boldsymbol{\epsilon_y}\cos(kz)\right]. \tag{A.17}$$

That is, the composite field is linearly polarised, but the axis of polarisation rotates as one moves along the beam axis, forming a helix with a pitch equal to the wavelength (Figure A.5a). This is more easily seen by defining the polarisation axis:

$$\boldsymbol{\epsilon_Y} = \boldsymbol{\epsilon_x}\sin(kz) + \boldsymbol{\epsilon_y}\cos(kz). \tag{A.18}$$

From which equation A.17 becomes,

$$\mathcal{E}(z) = -\frac{2i\mathcal{E}_0}{\sqrt{2}}\boldsymbol{\epsilon_Y}. \tag{A.19}$$

Such a phenomenon of a pure, but rotating polarisation only occurs for this σ^+-σ^- configuration[x], all other combinations produce the elliptical gradients described in the previous section.

The cooling mechanism associating with this type of polarisation gradient can be elucidated by again considering a two-level atom, but this time with a ground state of $|g, J = 1\rangle$ and an excited state of $|e, J' = 2\rangle$. As the light is linearly polarised only π excitations are possible, which will tend to preferentially pump the atoms into the $|m_J = 0\rangle$ sub-state of the *projection parallel to the polarisation axis*, Y. The situation is shown in Figure A.5b, with the ground

[ix] The name Sisyphus cooling is, of course, derived from the mythical ancient Greek king who was condemned to roll a boulder up a hill for perpetuity, as punishment for his various schemes to cheat death. The analogy isn't perfect as Sisyphus receives no respite, whereas for sufficient cooling the atoms can cease to have the energy to climb their hills.

[x] For the case of unequal amplitudes, the same phenomena is observed but the rotating polarisation is elliptical rather than linear.

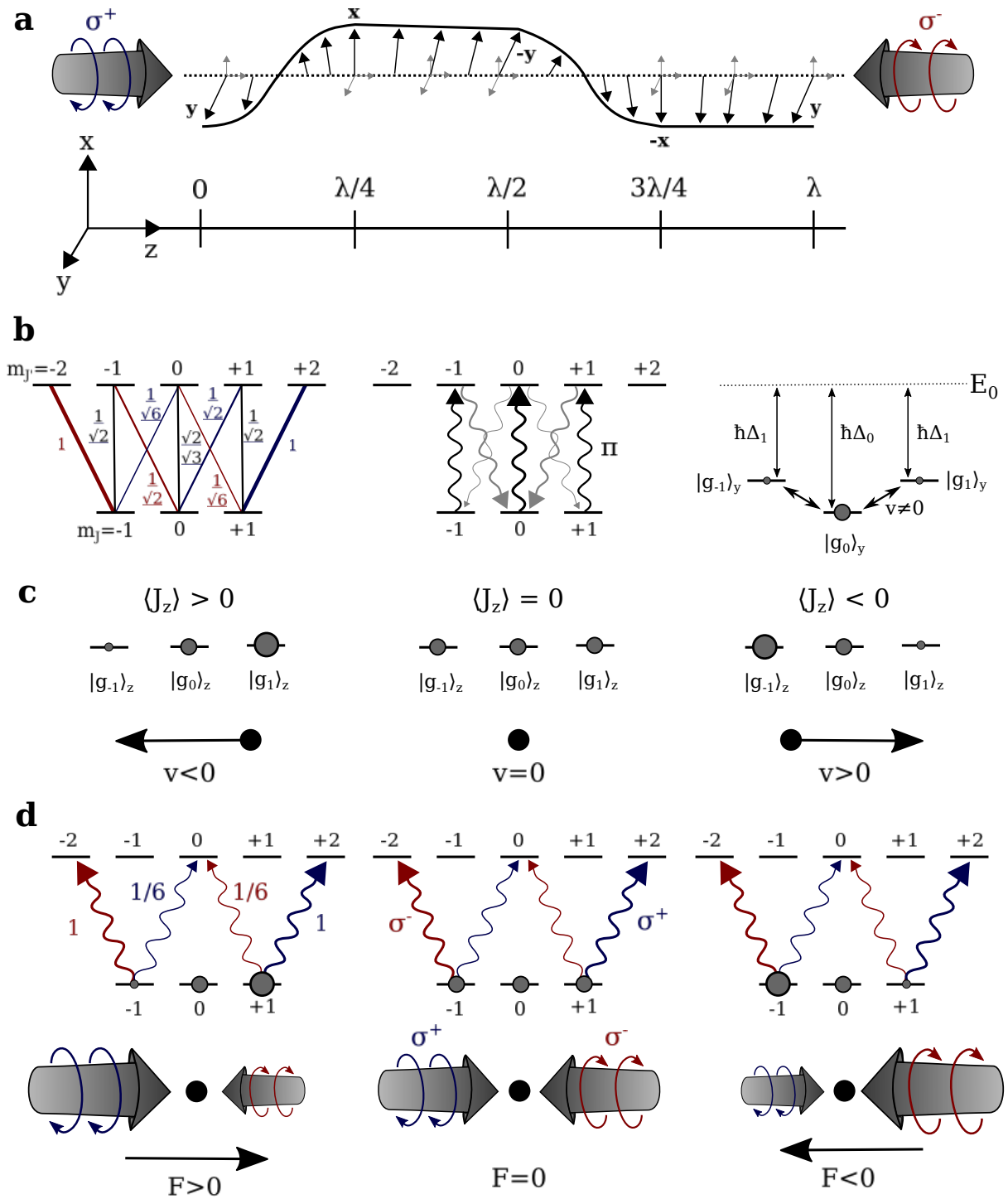

Figure A.5: Motion-induced orientation cooling. a) Two coherent laser beams of orthogonal circular polarisation are counter-propagating and their superposition establishes a helix of pure linear polarisation, with pitch λ. b) The Clebsch-Gordon coefficients for a two-level atom with $J = 1$ and $J' = 2$ lead to the $m_J = 0$ state being preferentially populated via optical pumping. Couplings between the different sub-states are established for a moving atom, leading (c) to a motion-dependent orientation being established. d) As the different $m_J = \pm 1$ sub-states (in the z-projection) scatter at different rates from the two input laser beams, this orientation leads to a motion-opposing scattering imbalance, i.e. a cooling force.

sub-states, as calculated from the relevant Clebsch-Gordon coefficients, having populations in the ratio of 4/17, 9/17 and 4/17, in order of ascending m_J values. The sub-states also observe different light shifts, again due to differences in the values of the Clebsch-Gordon coefficients, which can be labelled Δ_0 for the $m_J = 0$ sub-state and Δ_1 for the $m_J = \pm 1$ states, and with $\Delta_0 = 4/3\Delta_1$. Again, in the case of red-detuned light, these shifts are negative.

This situation is the same along all parts of the axis, as long as the projection is rotated to remain parallel to the polarisation axis. When considering an atom moving with speed v along the positive axial beam direction, it therefore makes sense to move to a frame which is both *co-moving* with the atom and *rotating* with the polarisation. Introduction of a rotating frame, however, leads to an inertial term being added into the Hamiltonian, equivalent to a magnetic field parallel to the rotation axis and with a Larmor frequency equal to that of the rotation. The effect of this term is the introduction of an additional potential of $V = kvJ_z$. Due to the non-commuting nature of J_y and J_z, this introduces couplings proportional to the velocity between the ground sub-states in the y projection, which are the eigenstates of the light-shifted Zeeman sub-levels at $z = 0$. Alternatively, the couplings can be understood as arising from the fact that these eigenstates are for angular momentum components parallel to the polarisation, the direction of which is constantly changing for a moving atom.

These couplings, which are therefore dependent upon the motion of the atom, lead to an atomic orientation. To see this, consider the three uncoupled ground states for the case of $z = 0$: $|g, m_J = 0\rangle = |g_0\rangle_y$ and $|g, m_J = \pm 1\rangle = |g_{\pm 1}\rangle_y$. The couplings can be considered as perturbations:

$$|g_0\rangle'_y = |g_0\rangle_y + \frac{kv}{\sqrt{2}\,(\Delta_0 - \Delta_1)}|g_{+1}\rangle_y + \frac{kv}{\sqrt{2}\,(\Delta_0 - \Delta_1)}|g_{-1}\rangle_y \tag{A.20}$$

$$|g_{\pm 1}\rangle'_y = |g_{\pm 1}\rangle_y + \frac{kv}{\sqrt{2}\,(\Delta_1 - \Delta_0)}|g_0\rangle_y \tag{A.21}$$

The crucial fact leading to an atomic orientation is that the populations of the equivalent $|g_{-1}\rangle_z$ and $|g_{+1}\rangle_z$ eigenstates are not equal in these new perturbed states. An equivalent way of stating this is to say that the expectation value of the angular momentum projection along the beam axis (J_z) is no longer zero:

$$'_y\langle g_0|J_z|g_0\rangle'_y = \frac{2\hbar kv}{\Delta_0 - \Delta_1} \tag{A.22}$$

$$'_y\langle g_{\pm 1}|J_z|g_{\pm 1}\rangle'_y = \frac{\hbar kv}{\Delta_1 - \Delta_0} \tag{A.23}$$

The expectation value of J_z can be calculated by weighting these values by the relative populations of the ground sub-states[xi]:

[xi] It can be shown that the expected population values for the perturbed states are the same as for the unperturbed states calculated above [102].

$$\langle J_z \rangle = \frac{2\hbar k v}{\Delta_0 - \Delta_1} \left(\frac{9}{17} - \frac{2}{17} - \frac{2}{17} \right) \tag{A.24}$$

$$\langle J_z \rangle = \frac{40}{17} \frac{\hbar k v}{\Delta_0} \tag{A.25}$$

This orientation is clearly induced by the motion as demonstrated by its vanishing as $v \to 0$ and is negative for $v > 0$, due to the negative value of Δ for red-detuned beams. To reiterate, this non-zero value means that there is an imbalance in the $|g_{\pm 1}\rangle_z$ populations, with $|g_{-1}\rangle_z$ more populated for an atom moving in the positive axial direction, and $|g_{+1}\rangle_z$ is more populated for an atom moving in the negative direction (Figure A.5c).

With this imbalance in the ground sub-states established, the cooling mechanism can be elucidated. In a very similar way to Doppler cooling, there is preferential scatter from the beam opposing the motion of the atom. The source of disparity in the scattering rates comes not, however, from the relative Doppler shift between the two beams, but instead from the Clebsch-Gordon coefficients: an atom in the $|g_{-1}\rangle_z$ is six times more likely to scatter from a σ^- beam than a σ^+ one. As the atomic population is weighted towards $|g_{-1}\rangle_z$ for atoms moving in the positive direction, it will preferentially scatter from the σ^- which is opposing its motion. Clearly the reverse is also true for the $|g_{+1}\rangle_z$ state, meaning that there is always a force opposing the motion regardless of its direction (Figure A.5d). The cooling mechanism is therefore superficially similar to the trapping force of a magneto-optical trap and operates in tandem and conjunction with the Doppler cooling mechanism, with the energy dissipated in the same manner by the isotropically orientated spontaneous emissions. Crucially, however, it works for much lower velocities.

A.4.3 Limits to Polarisation-Gradient Cooling

The ultimate physical limit to polarisation-gradient cooling is the single-photon recoil limit, which for rubidium is 370 nK [164]. This limit arises from the manner of the energy dissipation, which is spontaneous emission. Therefore, regardless of the situation, the atom will always have at least the momentum imparted in recoil from the emitted photon.

In reality, however, there are additional heating mechanisms which serve to prevent the attainment of this temperature and temperatures an order of magnitude higher than the recoil limit are typically achievable. For example, when the atom changes between m_J sub-states in the molasses, there is an abrupt change in the dipole force, equivalent to a heating mechanism [165]. Practical imperfections in the experimental conditions are also important in preventing the recoil limit being reached. Most pertinently, the above analysis assumed the absence of any magnetic fields which would perturb the Zeeman sub-levels. If the Zeeman shift caused by any stray magnetic fields begins to approach the magnitude of the AC Stark shifts, the Sisyphus cooling mechanism will be strongly adversely affected. Likewise it is clear that motion-induced orientation cooling also relies on there being only low-level ambient magnetic fields. For this

reason, minimisation of the background magnetic field is a key experimental factor in attaining the lowest atomic temperatures (see section 3.3.3.1).

Appendix B

Photographs of the Experiment

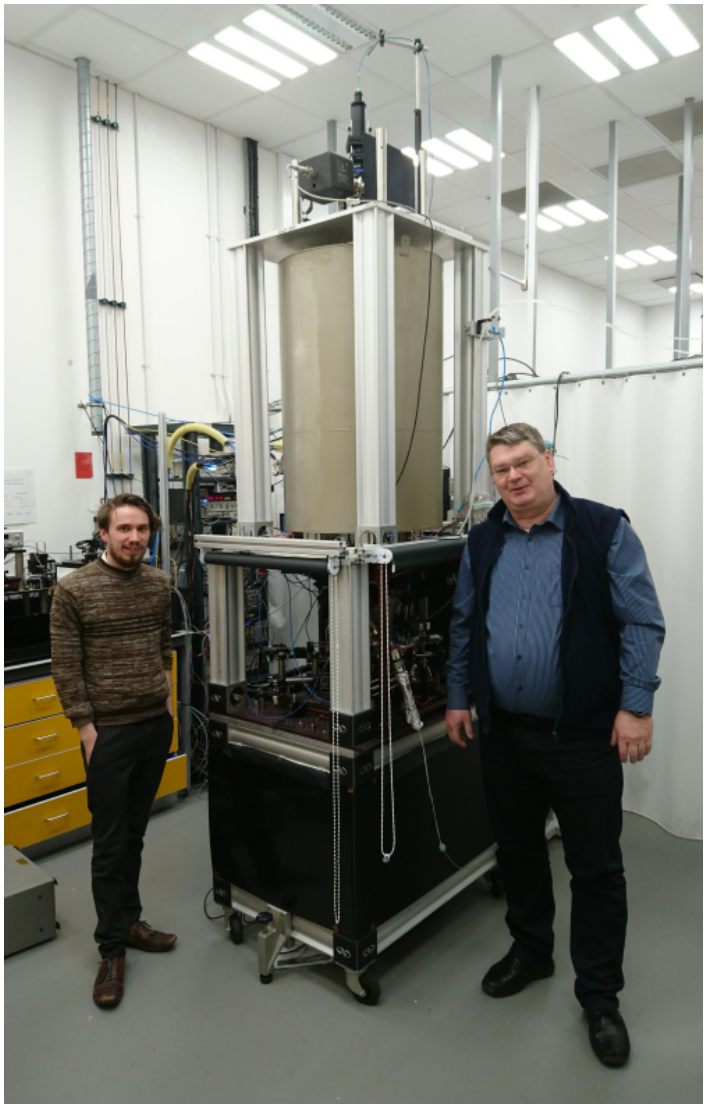

Figure B.1: Photograph taken in November 2017 of the author (left), the fountain (centre), and Yuri B. Ovchinnikov (right).

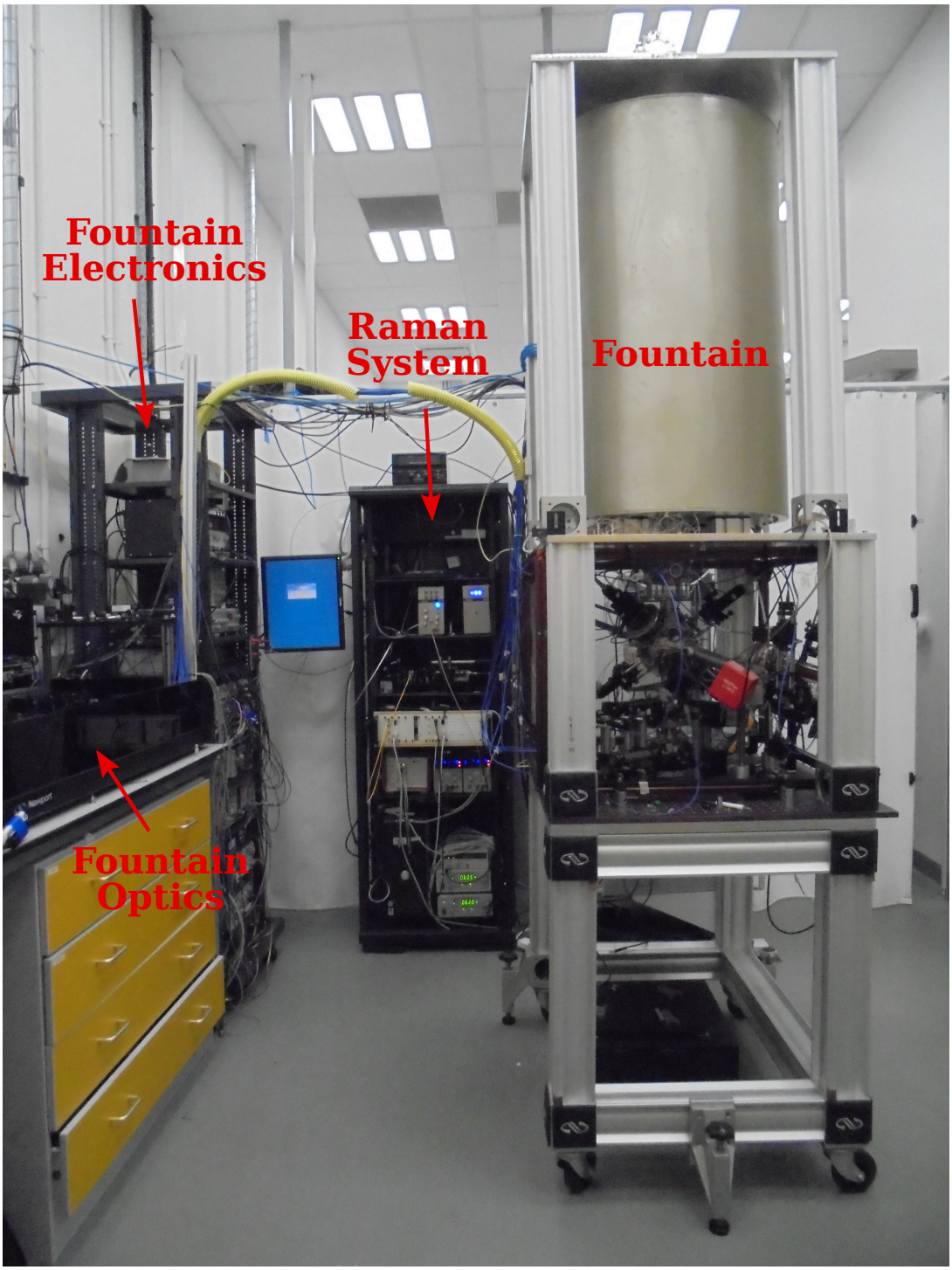

Figure B.2: Photograph of the laboratory showing the fountain, the Raman system rack, the bench for the optical circuity, and the rack used for control electronics. An additional rack, hidden from view behind the fountain, was used also used.

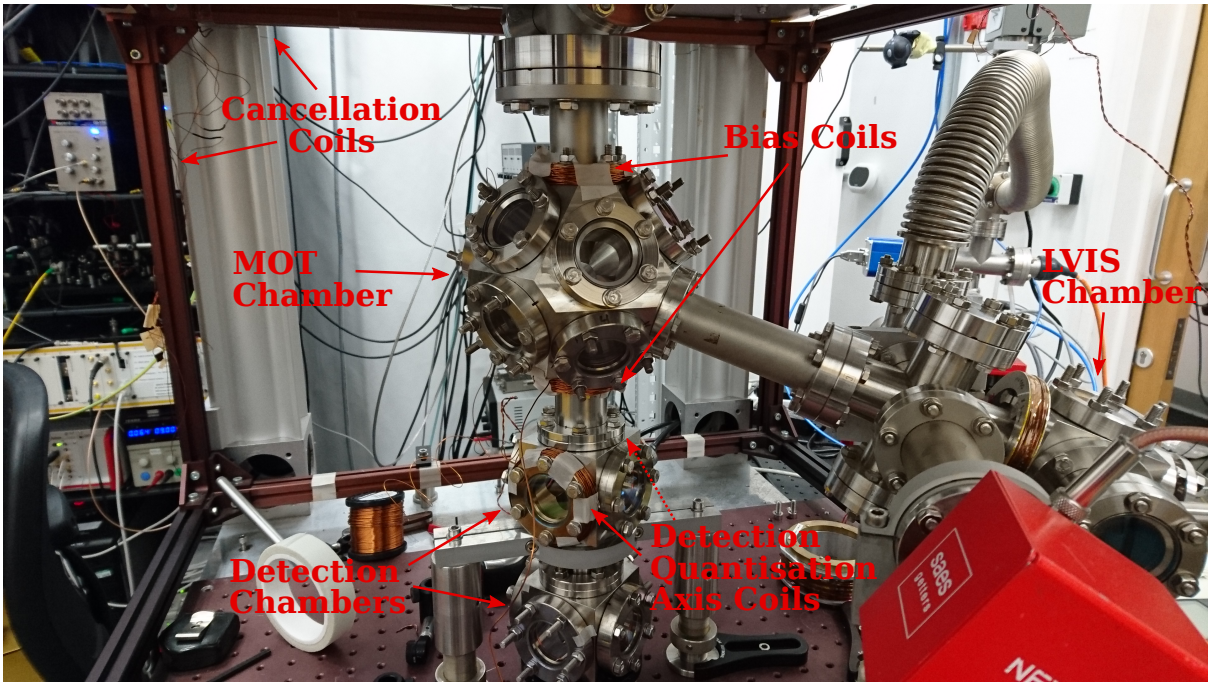

Figure B.3: Photograph of the chamber without the attached optics. The tube on the right is to temporarily connect to the turbomolecular pump as this photograph was taken immediately following the end of a baking process (see Figure B.5).

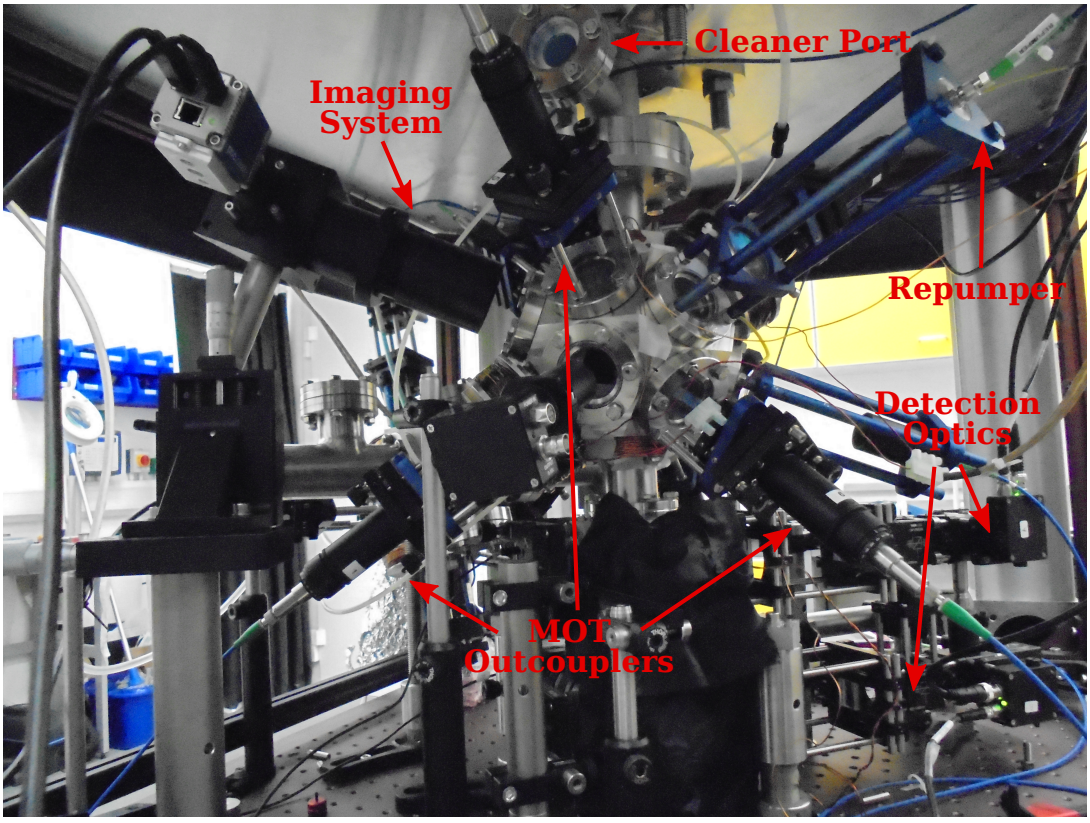

Figure B.4: Photograph of the chamber with some of the attached optics.

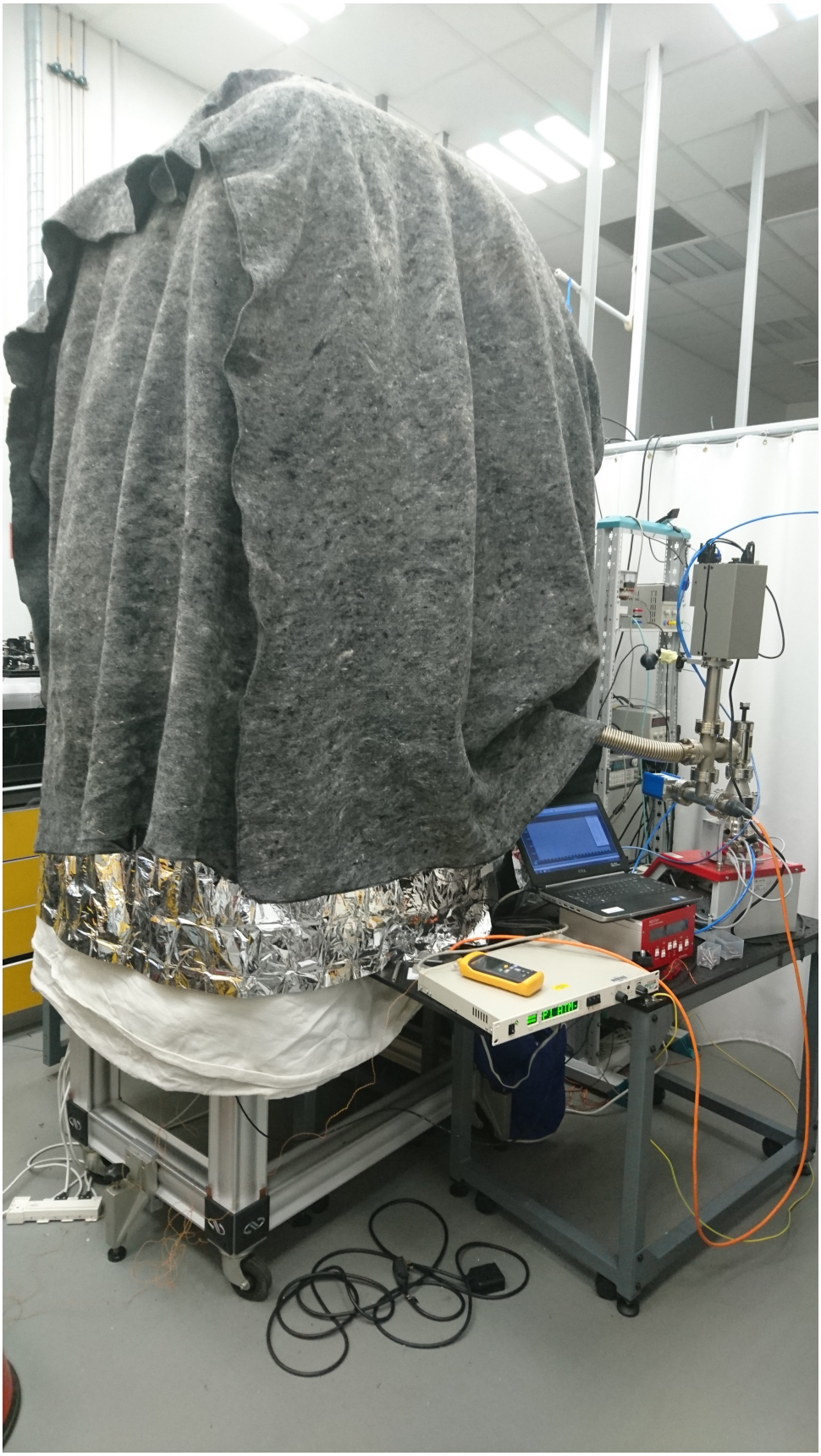

Figure B.5: Photograph of the chamber during the baking process.

Bibliography

[1] A. D. Cronin, J. Schmiedmayer, and D. E. Pritchard, "Optics and interferometry with atoms and molecules," *Rev. Mod. Phys.*, vol. 81, pp. 1051–1129, July 2009.

[2] G. M. Tino and M. A. Kasevich, eds., *Atom Interferometry: Proceedings of the International School of Physics "Enrico Fermi"*. IOS Press, 2014.

[3] N. F. Ramsey, "A Molecular Beam Resonance Method with Separated Oscillating Fields," *Phys. Rev.*, vol. 78, pp. 695–699, June 1950.

[4] L. Essen and J. V. L. Parry, "An Atomic Standard of Frequency and Time Interval: A Caesium Resonator," *Nature*, vol. 176, August 1955.

[5] C. J. Bordé, C. Salomon, S. Avrillier, A. van Lerberghe, C. Bréant, D. Bassi, and G. Scoles, "Optical Ramsey fringes with traveling waves," *Phys. Rev. A*, vol. 30, pp. 1836–1848, October 1984.

[6] C. Bordé, "Atomic interferometry with internal state labelling," *Physics Letters A*, vol. 140, no. 1, pp. 10 – 12, 1989.

[7] O. Carnal and J. Mlynek, "Young's Double-Slit Experiment with Atoms: A Simple Atom Interferometer," *Phys. Rev. Lett.*, vol. 66, pp. 2689–2692, May 1991.

[8] D. W. Keith, C. R. Ekstrom, Q. A. Turchette, and D. E. Pritchard, "An interferometer for atoms," *Phys. Rev. Lett.*, vol. 66, pp. 2693–2696, May 1991.

[9] M. Kasevich and S. Chu, "Atomic interferometry using stimulated Raman transitions," *Phys. Rev. Lett.*, vol. 67, pp. 181–184, July 1991.

[10] M. Cadoret, E. de Mirandes, P. Cladé, S. Guellati-Khélifa, C. Schwob, F. m. c. Nez, L. Julien, and F. m. c. Biraben, "Combination of Bloch Oscillations with a Ramsey-Bordé Interferometer: New Determination of the Fine Structure Constant," *Phys. Rev. Lett.*, vol. 101, p. 230801, December 2008.

[11] R. H. Parker, C. Yu, W. Zhong, B. Estey, and H. Müller, "Measurement of the fine-structure constant as a test of the standard model," *Science*, vol. 360, no. 6385, pp. 191–195, 2018.

[12] P. W. Graham, D. E. Kaplan, J. Mardon, S. Rajendran, and W. A. Terrano, "Dark matter direct detection with accelerometers," *Phys. Rev. D*, vol. 93, p. 075029, April 2016.

[13] S. Fray, C. A. Diez, T. W. Hänsch, and M. Weitz, "Atomic Interferometer with Amplitude Gratings of Light and Its Applications to Atom Based Tests of the Equivalence Principle," *Phys. Rev. Lett.*, vol. 93, p. 240404, December 2004.

[14] L. Zhou, S. Long, B. Tang, X. Chen, F. Gao, W. Peng, W. Duan, J. Zhong, Z. Xiong, J. Wang, Y. Zhang, and M. Zhan, "Test of Equivalence Principle at 10^{-8} Level by a Dual-Species Double-Diffraction Raman Atom Interferometer," *Phys. Rev. Lett.*, vol. 115, p. 013004, July 2015.

[15] C. Overstreet, P. Asenbaum, T. Kovachy, R. Notermans, J. M. Hogan, and M. A. Kasevich, "Effective Inertial Frame in an Atom Interferometric Test of the Equivalence Principle," *Phys. Rev. Lett.*, vol. 120, p. 183604, May 2018.

[16] K.-Y. Chung, S.-w. Chiow, S. Herrmann, S. Chu, and H. Müller, "Atom interferometry tests of local Lorentz invariance in gravity and electrodynamics," *Phys. Rev. D*, vol. 80, p. 016002, July 2009.

[17] R. J. Adler, H. Müller, and M. L. Perl, "A terrestrial search for dark contents of the vacuum, such as dark energy, using atom interferometry," *International Journal of Modern Physics A*, vol. 26, no. 29, pp. 4959–4979, 2011.

[18] C. Burrage, E. J. Copeland, and E. Hinds, "Probing dark energy with atom interferometry," *Journal of Cosmology and Astroparticle Physics*, vol. 2015, no. 03, p. 042, 2015.

[19] P. Hamilton, M. Jaffe, P. Haslinger, Q. Simmons, H. Müller, and J. Khoury, "Atom-interferometry constraints on dark energy," *Science*, vol. 349, no. 6250, pp. 849–851, 2015.

[20] O. Burrow, A. Carroll, S. Chattopadhyay, J. Coleman, G. Elertas, J. Heffer, C. Metelko, R. Moore, D. Morris, M. Perl, J. Ralph, and J. Tinsley, "Atom Interferometry for Dark Contents of the Vacuum Searches," *arXiv:1705.09376*, May 2017.

[21] A. Lenef, T. D. Hammond, E. T. Smith, M. S. Chapman, R. A. Rubenstein, and D. E. Pritchard, "Rotation Sensing with an Atom Interferometer," *Phys. Rev. Lett.*, vol. 78, pp. 760–763, February 1997.

[22] T. L. Gustavson, P. Bouyer, and M. A. Kasevich, "Precision Rotation Measurements with an Atom Interferometer Gyroscope," *Phys. Rev. Lett.*, vol. 78, pp. 2046–2049, March 1997.

[23] B. Canuel, F. Leduc, D. Holleville, A. Gauguet, J. Fils, A. Virdis, A. Clairon, N. Dimarcq, C. J. Bordé, A. Landragin, and P. Bouyer, "Six-Axis Inertial Sensor Using Cold-Atom Interferometry," *Phys. Rev. Lett.*, vol. 97, p. 010402, July 2006.

[24] S. M. Dickerson, J. M. Hogan, A. Sugarbaker, D. M. S. Johnson, and M. A. Kasevich, "Multiaxis inertial sensing with long-time point source atom interferometry," *Phys. Rev. Lett.*, vol. 111, p. 083001, August 2013.

[25] B. Barrett, P. Cheiney, B. Battelier, F. Napolitano, and P. Bouyer, "Multidimensional Atom Optics and Interferometry," *Phys. Rev. Lett.*, vol. 122, p. 043604, February 2019.

[26] A. Peters, K. Y. Chung, and S. Chu, "Measurement of gravitational acceleration by dropping atoms," *Nature*, vol. 400, August 1999.

[27] M. J. Snadden, J. M. McGuirk, P. Bouyer, K. G. Haritos, and M. A. Kasevich, "Measurement of the Earth's Gravity Gradient with an Atom Interferometer-Based Gravity Gradiometer," *Phys. Rev. Lett.*, vol. 81, pp. 971–974, August 1998.

[28] G. Rosi, L. Sorrentino, F. Cacciapuoti, M. Prevedelli, and G. M. Tino, "Precision measurement of the Newtonian gravitational constant using cold atoms," *Nature*, vol. 510, no. 7506, 2014.

[29] P. Asenbaum, C. Overstreet, T. Kovachy, D. D. Brown, J. M. Hogan, and M. A. Kasevich, "Phase shift in an atom interferometer due to spacetime curvature across its wave function," *Phys. Rev. Lett.*, vol. 118, p. 183602, May 2017.

[30] G. Rosi, L. Cacciapuoti, F. Sorrentino, M. Menchetti, M. Prevedelli, and G. M. Tino, "Measurement of the Gravity-Field Curvature by Atom Interferometry," *Phys. Rev. Lett.*, vol. 114, p. 013001, January 2015.

[31] J. B. Fixler, G. T. Foster, J. M. McGuirk, and M. A. Kasevich, "Atom Interferometer Measurement of the Newtonian Constant of Gravity," *Science*, vol. 315, no. 5808, pp. 74–77, 2007.

[32] S. Dimopoulos, P. W. Graham, J. M. Hogan, and M. A. Kasevich, "Testing General Relativity with Atom Interferometry," *Phys. Rev. Lett.*, vol. 98, p. 111102, March 2007.

[33] S. Dimopoulos, P. W. Graham, J. M. Hogan, M. A. Kasevich, and S. Rajendran, "Atomic gravitational wave interferometric sensor," *Phys. Rev. D*, vol. 78, p. 122002, December 2008.

[34] N. Yu and M. Tinto, "Gravitational wave detection with single-laser atom interferometers," *General Relativity and Gravitation*, vol. 43, pp. 1943–1952, July 2011.

[35] P. W. Graham, J. M. Hogan, M. A. Kasevich, and S. Rajendran, "New Method for Gravitational Wave Detection with Atomic Sensors," *Phys. Rev. Lett.*, vol. 110, p. 171102, April 2013.

[36] A. Acin, I. Bloch, H. Buhrman, T. Calarco, C. Eichler, J. Eisert, D. Esteve, N. Gisin, S. J. Glaser, F. Jelezko, S. Kuhr, M. Lewenstein, M. F. Riedel, P. O. Schmidt, R. Thew, A. Wallraff, I. Walmsley, and F. K. Wilhelm, "The quantum technologies roadmap: a European community view," *New Journal of Physics*, vol. 20, no. 8, p. 080201, 2018.

[37] LIGO Scientific Collaboration and Virgo Collaboration, "Observation of Gravitational Waves from a Binary Black Hole Merger," *Phys. Rev. Lett.*, vol. 116, p. 061102, February 2016.

[38] LIGO Scientific Collaboration and Virgo Collaboration, "GW151226: Observation of Gravitational Waves from a 22-Solar-Mass Binary Black Hole Coalescence," *Phys. Rev. Lett.*, vol. 116, p. 241103, June 2016.

[39] D. Schlippert, J. Hartwig, H. Albers, L. L. Richardson, C. Schubert, A. Roura, W. P. Schleich, W. Ertmer, and E. M. Rasel, "Quantum Test of the Universality of Free Fall," *Phys. Rev. Lett.*, vol. 112, p. 203002, May 2014.

[40] J. Williams, S. wey Chiow, N. Yu, and H. Müller, "Quantum test of the equivalence principle and space-time aboard the International Space Station," *New Journal of Physics*, vol. 18, no. 2, p. 025018, 2016.

[41] H. Müller, A. Peters, and S. Chu, "A precision measurement of the gravitational redshift by the interference of matter waves," *Nature*, vol. 463, February 2010.

[42] J. Guéna, M. Abgrall, D. Rovera, P. Rosenbusch, M. E. Tobar, P. Laurent, A. Clairon, and S. Bize, "Improved Tests of Local Position Invariance Using ^{87}Rb and ^{133}Cs Fountains," *Phys. Rev. Lett.*, vol. 109, p. 080801, August 2012.

[43] P. Wolf, L. Blanchet, C. J. Bordé, S. Reynaud, C. Salomon, and C. Cohen-Tannoudji, "Atom gravimeters and gravitational redshift," *Nature*, vol. 467, September 2010.

[44] P. Wolf, L. Blanchet, C. J. Bordé, S. Reynaud, C. Salomon, and C. Cohen-Tannoudji, "Does an atom interferometer test the gravitational redshift at the Compton frequency?," *Classical and Quantum Gravity*, vol. 28, p. 145017, June 2011.

[45] S. Sinha and J. Samuel, "Atom interferometry and the gravitational redshift," *Classical and Quantum Gravity*, vol. 28, p. 145018, June 2011.

[46] E. Giese, A. Friedrich, F. Di Pumpo, A. Roura, W. P. Schleich, D. M. Greenberger, and E. M. Rasel, "Proper time in atom interferometers: Diffractive versus specular mirrors," *Phys. Rev. A*, vol. 99, p. 013627, January 2019.

[47] M. G. Tarallo, T. Mazzoni, N. Poli, D. V. Sutyrin, X. Zhang, and G. M. Tino, "Test of Einstein Equivalence Principle for 0-Spin and Half-Integer-Spin Atoms: Search for Spin-Gravity Coupling Effects," *Phys. Rev. Lett.*, vol. 113, p. 023005, July 2014.

[48] V. A. Kostelecký, "Gravity, lorentz violation, and the standard model," *Phys. Rev. D*, vol. 69, p. 105009, May 2004.

[49] C.-G. Shao, Y.-F. Chen, R. Sun, L.-S. Cao, M.-K. Zhou, Z.-K. Hu, C. Yu, and H. Müller, "Limits on Lorentz violation in gravity from worldwide superconducting gravimeters," *Phys. Rev. D*, vol. 97, p. 024019, January 2018.

[50] G. Ferrari, N. Poli, F. Sorrentino, and G. M. Tino, "Long-Lived Bloch Oscillations with Bosonic Sr Atoms and Application to Gravity Measurement at the Micrometer Scale," *Phys. Rev. Lett.*, vol. 97, p. 060402, August 2006.

[51] G. W. Biedermann, X. Wu, L. Deslauriers, S. Roy, C. Mahadeswaraswamy, and M. A. Kasevich, "Testing gravity with cold-atom interferometers," *Phys. Rev. A*, vol. 91, p. 033629, March 2015.

[52] M. A. Hohensee, B. Estey, P. Hamilton, A. Zeilinger, and H. Müller, "Force-Free Gravitational Redshift: Proposed Gravitational Aharonov-Bohm Experiment," *Phys. Rev. Lett.*, vol. 108, p. 230404, June 2012.

[53] M. Zych, F. Costa, I. Pikovski, and Č. Brukner, "Quantum interferometric visibility as a witness of general relativistic proper time," *Nature Communications*, vol. 2, October 2011.

[54] S. Loriani, A. Friedrich, C. Ufrecht, F. Di Pumpo, S. Kleinert, S. Abend, N. Gaaloul, C. Meiners, C. Schubert, D. Tell, É. Wodey, M. Zych, W. Ertmer, A. Roura, D. Schlippert, W. P. Schleich, E. M. Rasel, and E. Giese, "Interference of Clocks: A Quantum Twin Paradox," *arXiv e-prints*, p. arXiv:1905.09102, May 2019.

[55] I. Pikovski, M. Zych, F. Costa, and Č. Brukner, "Time dilation in quantum systems and decoherence," *New Journal of Physics*, vol. 19, p. 025011, February 2017.

[56] M. de Angelis, A. Bertoldi, L. Cacciapuoti, A. Giorgini, G. Lamporesi, M. Prevedelli, G. Saccorotti, F. Sorrentino, and G. M. Tino, "Precision gravimetry with atomic sensors," *Measurement Science and Technology*, vol. 20, no. 2, p. 022001, 2009.

[57] T. M. Niebauer, G. S. Sasagawa, J. E. Faller, R. Hilt, and F. Klopping, "A new generation of absolute gravimeters," *Metrologia*, vol. 32, pp. 159–180, January 1995.

[58] M. Schmidt, "A mobile high-precision gravimeter based on atom interferometry," *PhD Thesis*, November 2011. Humboldt-Universität zu Berlin.

[59] M. Kasevich and S. Chu, "Measurement of the gravitational acceleration of an atom with a light-pulse atom interferometer," *Applied Physics B*, vol. 54, pp. 321–332, May 1992.

[60] L. Hu, N. Poli, L. Salvi, and G. M. Tino, "Atom Interferometry with the Sr Optical Clock Transition," *Phys. Rev. Lett.*, vol. 119, p. 263601, December 2017.

[61] G. T. Foster, J. B. Fixler, J. M. McGuirk, and M. A. Kasevich, "Method of phase extraction between coupled atom interferometers using ellipse-specific fitting," *Opt. Lett.*, vol. 27, pp. 951–953, June 2002.

[62] F. Sorrentino, Q. Bodart, L. Cacciapuoti, Y.-H. Lien, M. Prevedelli, G. Rosi, L. Salvi, and G. M. Tino, "Sensitivity limits of a Raman atom interferometer as a gravity gradiometer," *Phys. Rev. A*, vol. 89, p. 023607, February 2014.

[63] Y. Ovchinnikov and G. Marra, "Accurate rubidium atomic fountain frequency standard," *Metrologia*, vol. 48, no. 3, p. 87, 2011.

[64] Y. B. Ovchinnikov, K. Szymaniec, and S. Edris, "Measurement of rubidium ground-state hyperfine transition frequency using atomic fountains," *Metrologia*, vol. 52, no. 4, p. 595, 2015.

[65] T. Petelski, "Atom Interferometery for Precision Gravity Measurements," *PhD Thesis*, February 2005. Universite Paris 6 and Università degli Studi di Firenze.

[66] J. S. T. Heffer, "Towards precision gravimetry with light-pulse atom interferometry," *PhD Thesis*, August 2017. University of Liverpool.

[67] A. E. Carroll, "Atom Interferometry in ^{85}Rb," *PhD Thesis*, September 2018. University of Liverpool.

[68] D. A. Steck, "Rubidium 85 D Line Data," September 2013.

[69] A. L. Marchant, S. Händel, S. A. Hopkins, T. P. Wiles, and S. L. Cornish, "Bose-Einstein condensation of ^{85}Rb by direct evaporation in an optical dipole trap," *Phys. Rev. A*, vol. 85, p. 053647, May 2012.

[70] S. L. Cornish, N. R. Claussen, J. L. Roberts, E. A. Cornell, and C. E. Wieman, "Stable ^{85}Rb Bose-Einstein Condensates with Widely Tunable Interactions," *Phys. Rev. Lett.*, vol. 85, pp. 1795–1798, August 2000.

[71] J. L. Roberts, N. R. Claussen, S. L. Cornish, and C. E. Wieman, "Magnetic Field Dependence of Ultracold Inelastic Collisions near a Feshbach Resonance," *Phys. Rev. Lett.*, vol. 85, pp. 728–731, July 2000.

[72] J. P. Burke, J. L. Bohn, B. D. Esry, and C. H. Greene, "Prospects for Mixed-Isotope Bose-Einstein Condensates in Rubidium," *Phys. Rev. Lett.*, vol. 80, pp. 2097–2100, March 1998.

[73] D. A. Steck, "Rubidium 87 D Line Data," January 2015.

[74] E. Brion, L. J. Pedersen, and K. Molmer, "Adiabatic elimination in a lambda system," *Journal of Physics A: Mathematical and Theoretical*, vol. 40, no. 5, p. 1033, 2007.

[75] R. Han, H. Khoon Ng, and B.-G. Englert, "Raman transitions without adiabatic elimination: a simple and accurate treatment," *Journal of Modern Optics*, vol. 60, no. 4, pp. 255–265, 2013.

[76] A. Sugarbaker, "Atom Interferometery in a 10 m Fountain," *PhD Thesis*, August 2014. Stanford University.

[77] C. J. Foot, *Atomic Physics*. Oxford University Press, 2005.

[78] A. Peters, K. Y. Chung, and S. Chu, "High-precision gravity measurements using atom interferometry," *Metrologia*, vol. 38, no. 1, p. 25, 2001.

[79] M. Kasevich, D. S. Weiss, E. Riis, K. Moler, S. Kasapi, and S. Chu, "Atomic velocity selection using stimulated Raman transitions," *Phys. Rev. Lett.*, vol. 66, pp. 2297–2300, May 1991.

[80] K. Moler, D. S. Weiss, M. Kasevich, and S. Chu, "Theoretical analysis of velocity-selective Raman transitions," *Phys. Rev. A*, vol. 45, pp. 342–348, January 1992.

[81] D. A. Steck, *Quantum and Atom Optics*. http://steck.us/teaching, revision 0.11.0, 2016 ed., 2007.

[82] Pippa Storey and Claude Cohen-Tannoudji, "The Feynman path integral approach to atomic interferometry. A tutorial," *J. Phys. II France*, vol. 4, no. 11, pp. 1999–2027, 1994.

[83] K. Bongs, R. Launay, and M. Kasevich, "High-order inertial phase shifts for time-domain atom interferometers," *Applied Physics B*, vol. 84, pp. 599–602, September 2006.

[84] J. Hogan, "Atom Interferometery in a 10 m Fountain," *PhD Thesis*, June 2010. Stanford University.

[85] T. L. Gustavson, A. Landragin, and M. A. Kasevich, "Rotation sensing with a dual atom-interferometer Sagnac gyroscope," *Classical and Quantum Gravity*, vol. 17, no. 12, p. 2385, 2000.

[86] M. Hauth, C. Freier, V. Schkolnik, A. Senger, M. Schmidt, and A. Peters, "First gravity measurements using the mobile atom interferometer gain," *Applied Physics B*, vol. 113, no. 1, pp. 49–55, 2013.

[87] S.-Y. Lan, P.-C. Kuan, B. Estey, P. Haslinger, and H. Müller, "Influence of the Coriolis Force in Atom Interferometry," *Phys. Rev. Lett.*, vol. 108, p. 090402, February 2012.

[88] A. Louchet-Chauvet, T. Farah, Q. Bodart, A. Clairon, A. Landragin, S. Merlet, and F. Pereira Dos Santos, "The influence of transverse motion within an atomic gravimeter," *New Journal of Physics*, vol. 13, no. 6, p. 065025, 2011.

[89] B. V. Estey, "Precision Measurement in Atom Interferometery Using Bragg Diffraction," *PhD Thesis*, 2016. University of California, Berkeley.

[90] A. Roura, "Circumventing Heisenberg's Uncertainty Principle in Atom Interferometry Tests of the Equivalence Principle," *Phys. Rev. Lett.*, vol. 118, p. 160401, April 2017.

[91] G. D'Amico, G. Rosi, S. Zhan, L. Cacciapuoti, M. Fattori, and G. M. Tino, "Canceling the Gravity Gradient Phase Shift in Atom Interferometry," *Phys. Rev. Lett.*, vol. 119, p. 253201, December 2017.

[92] J. M. McGuirk, G. T. Foster, J. B. Fixler, M. J. Snadden, and M. A. Kasevich, "Sensitive absolute-gravity gradiometry using atom interferometry," *Phys. Rev. A*, vol. 65, p. 033608, February 2002.

[93] F. Sorrentino, "Sensitivity limits of atom interferometry gravity gradiometers and strainmeters," *Conference Presentation*, May 2016.

[94] J. K. Stockton, X. Wu, and M. A. Kasevich, "Bayesian estimation of differential interferometer phase," *Phys. Rev. A*, vol. 76, p. 033613, September 2007.

[95] M. S. Safronova, D. Jiang, B. Arora, C. W. Clark, M. G. Kozlov, U. I. Safronova, and W. R. Johnson, "Black-body radiation shifts and theoretical contributions to atomic clock research," *IEEE Transactions on Ultrasonics, Ferroelectrics, and Frequency Control*, vol. 57, pp. 94–105, Jan 2010.

[96] P. Haslinger, M. Jaffe, V. Xu, O. Schwartz, M. Sonnleitner, M. Ritsch-Marte, H. Ritsch, and H. Müller, "Attractive force on atoms due to blackbody radiation," *Nature Physics*, vol. 14, March 2018.

[97] T. M. Brzozowski, M. Maczynska, M. Zawada, J. Zachorowski, and W. Gawlik, "Time-of-flight measurement of the temperature of cold atoms for short trap-probe beam distances," *Journal of Optics B: Quantum and Semiclassical Optics*, vol. 4, no. 1, p. 62, 2002.

[98] V. Guarrera, R. Moore, A. Bunting, T. Vanderbruggen, and Y. B. Ovchinnikov, "Distributed quasi-Bragg beam splitter in crossed atomic waveguides," *Scientific Reports*, vol. 7, July 2017.

[99] J. G. Ziegler and N. B. Nichols, "Optimum settings for automatic controllers," *Transactions of the ASM*, vol. 64, November 1942.

[100] Z. T. Lu, K. L. Corwin, M. J. Renn, M. H. Anderson, E. A. Cornell, and C. E. Wieman, "Low-velocity intense source of atoms from a magneto-optical trap," *Phys. Rev. Lett.*, vol. 77, pp. 3331–3334, October 1996.

[101] Y. B. Ovchinnikov, "Compact magneto-optical sources of slow atoms," *Optics Communications*, vol. 249, no. 4–6, pp. 473 – 481, 2005.

[102] J. Dalibard and C. Cohen-Tannoudji, "Laser cooling below the Doppler limit by polarization gradients: simple theoretical models," *J. Opt. Soc. Am. B*, vol. 6, pp. 2023–2045, November 1989.

[103] P. J. Ungar, D. S. Weiss, E. Riis, and S. Chu, "Optical molasses and multilevel atoms: theory," *J. Opt. Soc. Am. B*, vol. 6, pp. 2058–2071, November 1989.

[104] Q. Hu, J. Yang, Y. Luo, A. Jia, F. Xu, C. Wei, and Q. Li, "Towards a juggling 87Rb atomic dual fountain," *AIP Advances*, vol. 8, no. 3, p. 035316, 2018.

[105] A. Clairon, C. Salomon, S. Guellati, and W. D. Phillips, "Ramsey Resonance in a Zacharias Fountain," *EPL (Europhysics Letters)*, vol. 16, no. 2, p. 165, 1991.

[106] E. Majorana, "Atomi orientati in campo magnetico variabile," *Il Nuovo Cimento (1924-1942)*, vol. 9, pp. 43–50, Feb 1932.

[107] R. T. Robiscoe, "A Spin Flip Problem," *American Journal of Physics*, vol. 39, no. 2, pp. 146–150, 1971.

[108] K. L. Corwin, Z.-T. Lu, C. F. Hand, R. J. Epstein, and C. E. Wieman, "Frequency-stabilized diode laser with the Zeeman shift in an atomic vapor," *Appl. Opt.*, vol. 37, pp. 3295–3298, May 1998.

[109] S. Lecomte, E. Fretel, G. Mileti, and P. Thomann, "Self-aligned extended-cavity diode laser stabilized by the Zeeman effect on the cesium D2 line," *Appl. Opt.*, vol. 39, pp. 1426–1429, March 2000.

[110] C. P. Pearman, C. S. Adams, S. G. Cox, P. F. Griffin, D. A. Smith, and I. G. Hughes, "Polarization spectroscopy of a closed atomic transition: applications to laser frequency locking," *Journal of Physics B: Atomic, Molecular and Optical Physics*, vol. 35, no. 24, p. 5141, 2002.

[111] F. Sorrentino, Y.-H. Lien, G. Rosi, L. Cacciapuoti, M. Prevedelli, and G. M. Tino, "Sensitive gravity-gradiometry with atom interferometry: progress towards an improved determination of the gravitational constant," *New Journal of Physics*, vol. 12, no. 9, p. 095009, 2010.

[112] K. Wang, Z. Yao, R. Li, S. Lu, X. Chen, J. Wang, and M. Zhan, "Hybrid wide-band, low-phase-noise scheme for Raman lasers in atom interferometry by integrating an acousto-optic modulator and a feedback loop," *Appl. Opt.*, vol. 55, pp. 989–992, February 2016.

[113] A. Peters, "High Precision Gravity Measurements using Atom Interferometry," *PhD Thesis*, May 1998. Stanford University.

[114] T. Mazzoni, X. Zhang, R. Del Aguila, L. Salvi, N. Poli, and G. M. Tino, "Large-momentum-transfer Bragg interferometer with strontium atoms," *Phys. Rev. A*, vol. 92, p. 053619, November 2015.

[115] S. Donnellan, I. R. Hill, W. Bowden, and R. Hobson, "A scalable arbitrary waveform generator for atomic physics experiments based on field-programmable gate array technology," *Review of Scientific Instruments*, vol. 90, no. 4, p. 043101, 2019.

[116] M. T. Baig, M. Johanning, A. Wiese, S. Heidbrink, M. Ziolkowski, and C. Wunderlich, "A scalable, fast, and multichannel arbitrary waveform generator," *Review of Scientific Instruments*, vol. 84, no. 12, p. 124701, 2013.

[117] T. Pruttivarasin and H. Katori, "Compact field programmable gate array-based pulse-sequencer and radio-frequency generator for experiments with trapped atoms," *Review of Scientific Instruments*, vol. 86, no. 11, p. 115106, 2015.

[118] E. Perego, M. Pomponio, A. Detti, L. Duca, C. Sias, and C. E. Calosso, "A scalable hardware and software control apparatus for experiments with hybrid quantum systems," *Review of Scientific Instruments*, vol. 89, no. 11, p. 113116, 2018.

[119] K. Szymaniec, S. E. Park, G. Marra, and W. Chałupczak, "First accuracy evaluation of the NPL-CsF2 primary frequency standard," *Metrologia*, vol. 47, no. 4, p. 363, 2010.

[120] K. Szymaniec, W. Chalupczak, P. B. Whibberley, S. N. Lea, and D. Henderson, "Evaluation of the primary frequency standard NPL-CsF1," *Metrologia*, vol. 42, no. 1, p. 49, 2005.

[121] J. Le Gouët, T. Mehlstäubler, J. Kim, S. Merlet, A. Clairon, A. Landragin, and F. Pereira Dos Santos, "Limits to the sensitivity of a low noise compact atomic gravimeter," *Applied Physics B*, vol. 92, pp. 133–144, Aug 2008.

[122] P. Cheinet, B. Canuel, F. P. D. Santos, A. Gauguet, F. Yver-Leduc, and A. Landragin, "Measurement of the sensitivity function in a time-domain atomic interferometer," *IEEE Transactions on Instrumentation and Measurement*, vol. 57, pp. 1141–1148, June 2008.

[123] F. L. Walls and A. Demarchi, "RF Spectrum of a Signal after Frequency Multiplication; Measurement and Comparison with a Simple Calculation," *IEEE Transactions on Instrumentation and Measurement*, vol. 24, pp. 210–217, September 1975.

[124] Y. Cheng, K. Zhang, L.-L. Chen, W.-J. Xu, Q. Luo, M.-K. Zhou, and Z.-K. Hu, "Low-phase noise and high-power laser for Bragg atom interferometer," *AIP Advances*, vol. 7, no. 9, p. 095211, 2017.

[125] G. Lamporesi, "Determination of the gravitational constant by atom interferometry," *PhD Thesis*, December 2006. Università degli Studi di Firenze.

[126] W. M. Itano, J. C. Bergquist, J. J. Bollinger, J. M. Gilligan, D. J. Heinzen, F. L. Moore, M. G. Raizen, and D. J. Wineland, "Quantum projection noise: Population fluctuations in two-level systems," *Phys. Rev. A*, vol. 47, pp. 3554–3570, May 1993.

[127] The LIGO Scientific Collaboration, "A gravitational wave observatory operating beyond the quantum shot-noise limit," *Nature Physics*, vol. 7, December 2011.

[128] M. Kitagawa and M. Ueda, "Squeezed spin states," *Phys. Rev. A*, vol. 47, pp. 5138–5143, June 1993.

[129] O. Hosten, N. J. Engelsen, R. Krishnakumar, and M. A. Kasevich, "Measurement noise 100 times lower than the quantum-projection limit using entangled atoms," *Nature*, vol. 529, January 2016.

[130] L. Salvi, N. Poli, V. Vuletić, and G. M. Tino, "Squeezing on Momentum States for Atom Interferometry," *Phys. Rev. Lett.*, vol. 120, p. 033601, January 2018.

[131] G. O. Olaofe, "Diffraction by Gaussian Apertures," *J. Opt. Soc. Am.*, vol. 60, pp. 1654–1657, December 1970.

[132] R. G. Schell and G. Tyras, "Irradiance from an Aperture with a Truncated-Gaussian Field Distribution," *J. Opt. Soc. Am.*, vol. 61, pp. 31–35, January 1971.

[133] P. Belland and J. P. Crenn, "Changes in the characteristics of a Gaussian beam weakly diffracted by a circular aperture," *Appl. Opt.*, vol. 21, pp. 522–527, February 1982.

[134] A. Senger, "A Mobile Atom Interferometer for High-Precision Measurements of Local Gravity," *PhD Thesis*, November 2011. Humboldt-Universität zu Berlin.

[135] S. Kuhr, W. Alt, D. Schrader, I. Dotsenko, Y. Miroshnychenko, A. Rauschenbeutel, and D. Meschede, "Analysis of dephasing mechanisms in a standing-wave dipole trap," *Phys. Rev. A*, vol. 72, p. 023406, August 2005.

[136] M. Himsworth, "Coherent Manipulation of Ultracold Rubidium," *PhD Thesis*, September 2009. University of Southampton.

[137] S.-w. Chiow, T. Kovachy, H.-C. Chien, and M. A. Kasevich, "102$\hbar k$ Large Area Atom Interferometers," *Phys. Rev. Lett.*, vol. 107, p. 130403, September 2011.

[138] H. Müller, S.-w. Chiow, Q. Long, S. Herrmann, and S. Chu, "Atom Interferometry with up to 24-Photon-Momentum-Transfer Beam Splitters," *Phys. Rev. Lett.*, vol. 100, p. 180405, May 2008.

[139] J. M. McGuirk, M. J. Snadden, and M. A. Kasevich, "Large Area Light-Pulse Atom Interferometry," *Phys. Rev. Lett.*, vol. 85, pp. 4498–4501, November 2000.

[140] T. Lévèque, A. Gauguet, F. Michaud, F. Pereira Dos Santos, and A. Landragin, "Enhancing the Area of a Raman Atom Interferometer Using a Versatile Double-Diffraction Technique," *Phys. Rev. Lett.*, vol. 103, p. 080405, August 2009.

[141] M. Jaffe, V. Xu, P. Haslinger, H. Müller, and P. Hamilton, "Efficient Adiabatic Spin-Dependent Kicks in an Atom Interferometer," *Phys. Rev. Lett.*, vol. 121, p. 040402, July 2018.

[142] D. Boiron, C. Triché, D. R. Meacher, P. Verkerk, and G. Grynberg, "Three-dimensional cooling of cesium atoms in four-beam gray optical molasses," *Phys. Rev. A*, vol. 52, pp. R3425–R3428, November 1995.

[143] S. Rosi, A. Burchianti, S. Conclave, D. S. Naik, G. Roati, C. Fort, and F. Minardi, "Λ-enhanced grey molasses on the D_2 transition of Rubidium-87 atoms," *Scientific Reports*, vol. 8, January 2018.

[144] A. B. Deb, T. McKellar, and N. Kjærgaard, "Optical runaway evaporation for the parallel production of multiple Bose-Einstein condensates," *Phys. Rev. A*, vol. 90, p. 051401, November 2014.

[145] J. Rudolph, W. Herr, C. Grzeschik, T. Sternke, A. Grote, M. Popp, D. Becker, H. Müntinga, H. Ahlers, A. Peters, C. Lämmerzahl, K. Sengstock, N. Gaaloul, W. Ertmer, and E. M. Rasel, "A high-flux BEC source for mobile atom interferometers," *New Journal of Physics*, vol. 17, no. 6, p. 065001, 2015.

[146] Y. Shin, M. Saba, T. A. Pasquini, W. Ketterle, D. E. Pritchard, and A. E. Leanhardt, "Atom Interferometry with Bose-Einstein Condensates in a Double-Well Potential," *Phys. Rev. Lett.*, vol. 92, p. 050405, February 2004.

[147] R. Grimm, M. Weidemüller, and Y. B. Ovchinnikov, "Optical Dipole Traps for Neutral Atoms," vol. 42 of *Advances In Atomic, Molecular, and Optical Physics*, pp. 95 – 170, Academic Press, 2000.

[148] M. A. Kasevich, E. Riis, S. Chu, and R. G. DeVoe, "RF Spectroscopy in an Atomic Fountain," *Phys. Rev. Lett.*, vol. 63, pp. 612–615, August 1989.

[149] K. Gibble and S. Chu, "Laser-cooled Cs frequency standard and a measurement of the frequency shift due to ultracold collisions," *Phys. Rev. Lett.*, vol. 70, pp. 1771–1774, March 1993.

[150] H. J. Metcalf and P. van der Straten, *Laser Cooling and Trapping.* Springer, 1999.

[151] V. S. Letokhov, V. G. Minogin, and B. D. Pavlik, "Cooling and capture of atoms and molecules by a resonant light field," *Soviet Journal of Experimental and Theoretical Physics*, vol. 45, p. 698, April 1977.

[152] S. Chu, L. Hollberg, J. E. Bjorkholm, A. Cable, and A. Ashkin, "Three-dimensional viscous confinement and cooling of atoms by resonance radiation pressure," *Phys. Rev. Lett.*, vol. 55, pp. 48–51, July 1985.

[153] P. D. Lett, W. D. Phillips, S. L. Rolston, C. E. Tanner, R. N. Watts, and C. I. Westbrook, "Optical molasses," *J. Opt. Soc. Am. B*, vol. 6, pp. 2084–2107, November 1989.

[154] P. D. Lett, R. N. Watts, C. I. Westbrook, W. D. Phillips, P. L. Gould, and H. J. Metcalf, "Observation of Atoms Laser Cooled below the Doppler Limit," *Phys. Rev. Lett.*, vol. 61, pp. 169–172, July 1988.

[155] A. Ashkin and J. P. Gordon, "Stability of radiation-pressure particle traps: an optical Earnshaw theorem," *Opt. Lett.*, vol. 8, pp. 511–513, October 1983.

[156] E. L. Raab, M. Prentiss, A. Cable, S. Chu, and D. E. Pritchard, "Trapping of Neutral Sodium Atoms with Radiation Pressure," *Phys. Rev. Lett.*, vol. 59, pp. 2631–2634, December 1987.

[157] D. S. Weiss, E. Riis, Y. Shevy, P. J. Ungar, and S. Chu, "Optical molasses and multilevel atoms: experiment," *J. Opt. Soc. Am. B*, vol. 6, pp. 2072–2083, November 1989.

[158] A. M. Steane, G. Hillenbrand, and C. J. Foot, "Polarization gradient cooling in a one-dimensional σ^+-σ^- configuration for any atomic transition," *Journal of Physics B: Atomic, Molecular and Optical Physics*, vol. 25, no. 22, p. 4721, 1992.

[159] J. Dalibard and C. Cohen-Tannoudji, "Dressed-atom approach to atomic motion in laser light: the dipole force revisited," *J. Opt. Soc. Am. B*, vol. 2, pp. 1707–1720, November 1985.

[160] A. Aspect, J. Dalibard, A. Heidmann, C. Salomon, and C. Cohen-Tannoudji, "Cooling Atoms with Stimulated Emission," *Phys. Rev. Lett.*, vol. 57, pp. 1688–1691, October 1986.

[161] B. Sheehy, S.-Q. Shang, P. van der Straten, S. Hatamian, and H. Metcalf, "Magnetic-field-induced laser cooling below the doppler limit," *Phys. Rev. Lett.*, vol. 64, pp. 858–861, February 1990.

[162] J. Söding, R. Grimm, and Y. B. Ovchinnikov, "Gravitational laser trap for atoms with evanescent-wave cooling," *Optics Communications*, vol. 119, no. 5, pp. 652 – 662, 1995.

[163] Y. B. Ovchinnikov, I. Manek, and R. Grimm, "Surface Trap for Cs atoms based on Evanescent-Wave Cooling," *Phys. Rev. Lett.*, vol. 79, pp. 2225–2228, September 1997.

[164] C. Huang, P.-C. Kuan, and S.-Y. Lan, "Laser cooling of ^{85}Rb atoms to the recoil-temperature limit," *Phys. Rev. A*, vol. 97, p. 023403, February 2018.

[165] G. Nienhuis, P. van der Straten, and S.-Q. Shang, "Operator description of laser cooling below the Doppler limit," *Phys. Rev. A*, vol. 44, pp. 462–474, July 1991.